PASSIVE MATERIALS FOR HIGH FREQUENCY PIEZOCOMPOSITE ULTRASONIC TRANSDUCERS

by

RHIANNON ALYS WEBSTER

A thesis submitted to
The University of Birmingham
for the degree of
DOCTOR OF PHILOSOPHY

Department of Metallurgy and Materials
The University of Birmingham
September 2009

Abstract

High frequency ultrasound is receiving increased attention for medical imaging in areas such as ophthalmology and dermatology. Recent advances in the manufacture of fine scale piezocomposite materials mean there is great potential for commercial transducers far superior to conventional devices currently in clinical use.

This Thesis reports the fabrication and characterisation of passive materials suitable for use in high frequency piezocomposite transducer devices. Epoxy composites have been fabricated using tungsten and alumina as filler material with volume fractions up to 0.4. Acoustic impedance and attenuation has been determined for different filler volume fractions to provide data for modelling to aid transducer design and also determine the filler volume fraction required to provide optimal results. Acoustic impedance values of 3-15MRayl were measured for the materials made in this work and the influence of filler particle size and shape is also discussed.

Piezocomposite transducers have been constructed using material developed in this work and compared to devices made with more conventional passive materials. In addition to the fabrication of the composite samples for characterisation a process for incorporating material into transducers is described showing how the fabrication can be a part of the transducer construction resulting in an efficient and neat package.

Acknowledgements

This work was funded with a studentship from ESPRC and also financially sponsored by Applied Functional Materials (AFM) Ltd. The author would also like to acknowledge the support from the project supervisors, Tim Button and Sandy Cochran and thank the following people for their help with practical work in Scotland and in Birmingham; Carl Meggs (University of Birmingham), Christine Demore (University of Dundee) and Duncan MacLennan (University of Strathclyde).

Contents

Nomenclature

The following is a list of symbols used throughout this Thesis. Other expressions are defined in the text as appropriate.

f	frequency
c / V	speed / velocity
λ	wavelength
k_t	electromechanical coupling coefficient
v	volume fraction
ρ	density
K	bulk modulus
G	shear modulus
d	distance / sample thickness
t	time
Δt	time of flight
A	amplitude
Z	acoustic impedance
R	reflection coefficient
T	transmission coefficient
α	attenuation coefficient

Conference Presentations and Publications

The following is a list of conference presentations and publications incorporating this work.

Proceedings:

R.A. Webster, T.W. Button, C. Meggs, D. MacLennan, S. Cochran, “Passive materials for high frequency ultrasound components,” IEEE Ultrasonics Symposium, OCT 28-31, 2007, New York, NY, IEEE Ultrasonics Symposium Proceedings, Vols 1-6, 1925-1928, 2007.
T. W. Button, S. Cochran, K. J. Kirk, D. MacLennan, A. MacNeil, K. McDonald, C. Meggs, D. Rodriquez-Sanmartin, R. Webster, and D. Zhang, "Net-shape ceramic manufacturing as an aid to realize ultrasonic transducers for high-resolution medical imaging," Proceedings 2005 IEEE Ultrasonics Symposium, vol. 3, pp. 1625-1628, 2005.

Presentations:

S. Cochran, J. Bamber, A. Bernassau, N. Bush, T.W. Button, C. Démoré, L. Garcia-Gancedo, D. Hutson, D. MacLennan, P. Maher, C. Meggs, R.A. Webster “Utilisation of ceramic micromoulding techniques for high frequency ultrasound transducers and arrays,” 6th International Conference on Ultrasonic Biomedical Microscanning, Malibu, California, USA, 23 – 26 September 2008.

S. Cochran, J. Bamber, A.L. Bernassau, N. Bush, T.W. Button, C.E.M. Démoré, L. Garcia-Gancedo, D. Hutson, D. MacLennan, P. Maher, C. Meggs, R.A. Webster, “Progress Towards Transducers and Arrays for Real-time High Frequency Biomedical Ultrasound Imaging,” Acoustics, Paris, 29 June – 4 July 2008.

C.E.M. Démoré, S. Cochran, J.C. Bamber, A.L. Bernassau, N.L. Bush, T.W. Button, L. Garcia-Gancedo, D. Hutson, D. MacLennan, P. Maher, C. Meggs, R.A. Webster, “Progress Towards Piezocomposite Transducers and Arrays for Real-time High Frequency Biomedical Ultrasound Imaging,” US Navy Workshop on Acoustic Transduction Materials and Devices, Pennsylvania State University, USA, 13-16 May 2008.

S. Cochran, T.W. Button, A.L. Bernassau, T. Clipsham, C.E.M. Démoré, G. Dolman, J. Elgoyhen, H. Hughes, D. Hutson, D. MacLennan, C. Meggs, G. O'Hare, R.A.Webster, “A holistic approach to ultrahigh frequency ultrasonic arrays,” 8th Annual Ultrasonic Transducer Conference, Los Angeles, USA, 4-6 April 2007 (Invited).

CHAPTER 1

Introduction

1.1 Background

Ultrasound is defined as high frequency sound waves with frequencies greater than 20kHz. Ultrasonic testing is widely used in applications such as medical imaging and non-destructive testing (NDT). The conversion of electrical pulses to mechanical vibrations and the conversion of returned mechanical vibrations back into electrical energy is the basis for ultrasonic testing using a transducer device with a piezoelectric material as the active element. [(1)]

Most current commercial medical imaging systems operate at frequencies less than 20MHz, this upper limit being partly defined by manufacturing techniques. High frequency ultrasound (>30 MHz) is desirable for medical imaging because increasing the frequency increases the resolution of the image, although the depth of penetration is reduced. At a conventional imaging frequency of 3.5MHz a typical transducer can resolve structures in the region of 1mm at a depth of 10-20cm. If the frequency is increased to 50MHz the resolution improves to 75μm but the depth of penetration is limited to less than 1cm. [(2)] Therefore high frequency ultrasound imaging has applications where resolution is critical but depth of penetration requirements are small, such as in ophthalmology and dermatology. [(3)] High frequency ultrasound imaging is now an accepted procedure for imaging the eye [(4-5)] and has great potential in differentiating common benign skin lesions from melanoma. [(6-7)] Research has shown that when high frequency ultrasound is used in combination with optical non invasive methods the referral of benign tumours can be potentially reduced by 65% without missing melanoma, [(6)] which has cost implications as referral can be avoided as well as the patients being safely reassured at an early stage.

High frequency requires fine scale active elements; the required thickness is less than 50μm, meaning that fabrication of the active material is difficult. Composite materials consisting of piezoceramic pillars upstanding in a polymer matrix have many performance advantages over traditional monolithic ceramic [8-11] and other developments with fine scale ceramic fibre manufacture [12,13] and moulding techniques [14-17] have produced fine scale structures with great potential. Work being undertaken at the time of writing at the University of Birmingham by the Functional Materials Group and Applied Functional Materials Ltd (AFM Ltd), a spin-off company of the group, is focused on developing high frequency transducers made with composite structures for commercialisation. [18- 23] This thesis will focus on the construction of the transducer, including investigating passive materials in the device and optimising the package as a whole.

The construction of a transducer begins with the piezoelectric active element with thin films, usually of gold or silver, on both sides acting as electrodes. A matching layer is placed on one face of the active element to improve the energy transfer to and from the patient or load. [1] A backing layer is placed behind the other electrode to reduce ringing (continued vibration) of the element. The whole assembly is then housed in a casing which provides electrical insulation and structural support as shown in Figure 1.1. A single element transducer can be focused either by attaching a concave lens to the planar face of the transducer (like an optical lens) or by curving the active element into a convex shape, as shown in Figure 1.2. The focal length, F will depend on the radius of curvature and the beam width, w, in the focal zone will depend on the aperture, a, focal length, F, and the ultrasound wavelength.

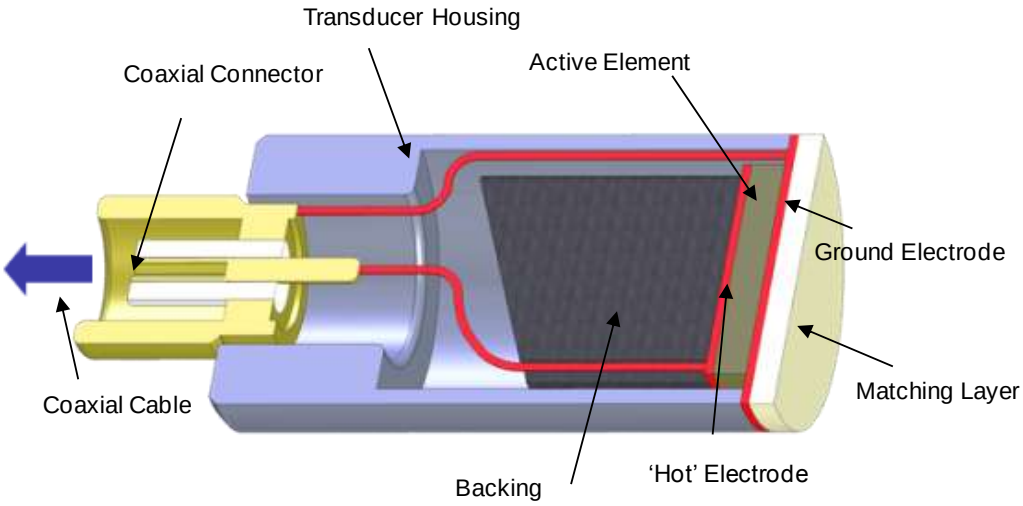

Figure 1.1 *Schematic of transducer construction with active element wired to coaxial connector*

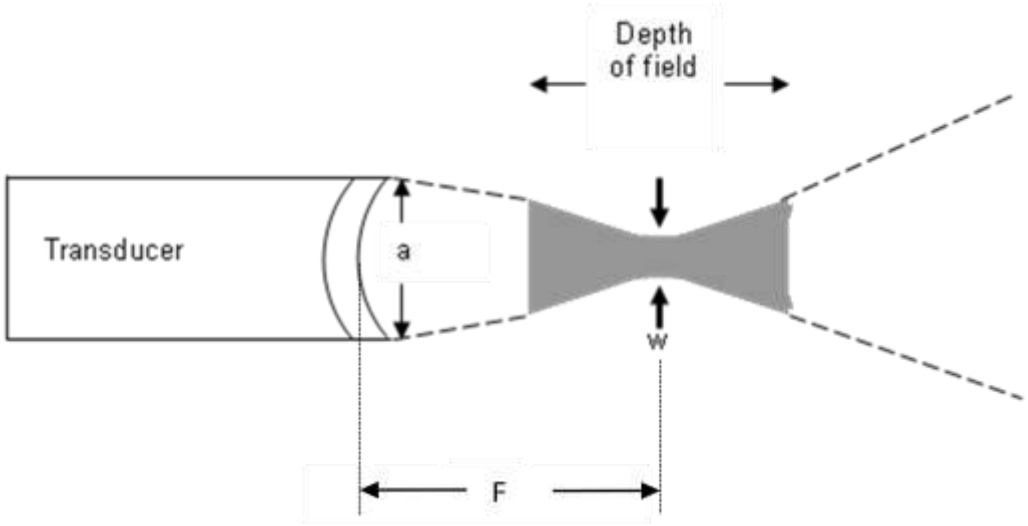

Figure 1.2 *Schematic of focused transducer with curved element. The focal length, F depends on the radius of curvature of the curved active element. The beam width, w, in the focal zone depends on the aperture, a, the focal length, F and the ultrasound wavelength.*

A transducer has a finite usable frequency range and the bandwidth is the difference between low and high operational frequency limits. The bandwidth is generally proportional to the centre frequency of the transducer and the term fractional bandwidth is therefore commonly used to express the bandwidth as a fraction of the centre frequency. Quality factor, Q, or mechanical coefficient is a related concept. It has two definitions related to the energy stored and lost per cycle and also the centre

frequency and bandwidth. A broadband transducer has a large fractional bandwidth. There is an inverse relationship between bandwidth and pulse length (duration). Short pulse duration implies a high axial resolution resulting in a high image quality, which is a major advantage of broadband transducers. [24] A high-Q transducer loses very little energy each cycle producing a long pulse and a low-Q transducer generates a short pulse. Diagnostic ultrasound uses low-Q transducers and high-Q transducers are good for continuous wave ultrasound. The operating frequency of a transducer is determined by the electro-acoustic properties and thickness of the active material; a thinner element generally means increased frequency. [25,26]

Several material factors of the active element are important for ultrasonic transducer performance, including the electromechanical coupling coefficient, dielectric constant, electrical and mechanical losses, and acoustic impedance. The electromechanical coupling coefficient, k_t, defines how efficiently the material converts electrical stimuli from the transmitting circuit into ultrasonic energy and received ultrasonic energy into electrical signals. A high k_t value ($k_t \rightarrow 1$) is desirable for transducer applications. The dielectric constant, ε_r, describes the relative strain that the piezoelectric material undergoes when an electric field is applied to it. A high dielectric constant ($\varepsilon_r \geq 100$) is desirable in ultrasonic applications to match the electrical impedance of the imaging system [26] (typically 50Ω), minimising electronic noise from cabling and amplifiers. Low mechanical ($Q \geq 10$) and electrical losses ($\tan\delta \leq 0.10$) are also required for good sensitivity giving a short pulse. The acoustic impedance of the material, Z, (product of velocity and density) influences the energy transfer across the transducer-tissue interface. The Mega Rayl is the unit of acoustic impedance and is equivalent to $10^6 kg/m^2/s$. The specific acoustic impedance of the active element should be close to that of tissue ($Z \approx 1.5$MRayl). Matching acoustic

impedance values of tissue and piezoelectric element enhances the transmission of ultrasound between the body or load, which is where passive materials are key. Passive materials have an important role in the transducer performance in addition to the active material for enhancing energy transfer and preventing unwanted resonances in the transducer. [27] The important properties for passive materials are acoustic impedance and attenuation. The desired acoustic impedance values for the backing and matching components will depend on the acoustic impedance of the active material to be matched. The acoustic impedance of piezocomposite is much lower than that of monolithic ceramic, depending on the volume fraction of ceramic in the composite; [28] therefore the acoustic impedance value requirements for passive materials in piezocomposite transducer devices are different to those for standard ceramic transducers.

1.2 Project Aims

The principle aim of this work is to investigate passive materials suitable for use in high frequency piezocomposite devices. The focus is on single element transducers but the potential for use in transducer arrays is also considered. The key objectives of the project are

- select suitable materials for use as backing and matching in piezocomposite transducers
- develop fabrication procedures to achieve passive materials with a range of acoustic impedance values
- develop an acoustic characterisation technique to characterise acoustic properties of the passive materials, including velocity and attenuation at relevant frequencies.

- obtain results to aid transducer design creating a database of impedance and attenuation values for the passive materials at a specific frequency.
- consider the design and fabrication of the backing in terms of the whole transducer package, to allow the passive materials made to be incorporated into commercial transducer probes.

1.3 Thesis Content

Chapter 2 gives more background to the project, including an introduction to ultrasound and piezoelectric transducers and a more in depth overview of what properties are important for passive materials, how the acoustic properties can be modelled and candidate materials suitable for use as backing and matching for piezocomposite transducer devices. Chapter 3 goes on to review acoustic characterisation techniques before introducing the technique used in this work and giving an analysis of how the velocity and attenuation of both longitudinal and shear waves through the sample material can be determined. The experimental materials and methods are explained in Chapter 4, including the fabrication development, final procedures used, and the characterisation techniques including the acoustic characterisation set up. Chapters 5 and 6 present the results and discussion of the two types of materials made. The results are divided into powder characterisation and material characterisation which includes SEM microstructure analysis and acoustic velocity and attenuation results. Chapter 7 shows how material made in this work has been incorporated into single element transducers and is compared to other materials used previously. Two approaches to fabricating the material as a transducer component are presented as well as some measured transducer properties of devices incorporating the material as backing. The final Chapter summarises the work, giving conclusions and some discussion for further work.

CHAPTER 2

Ultrasound, Piezoelectricity and Transducer Materials

2.1 Fundamentals of Ultrasound Imaging

Ultrasound is defined as high frequency sound waves that humans cannot hear, mechanical waves with frequencies greater than 20 kHz. [29] The frequency of a wave (f) is the number of cycles (pressure oscillations) occurring at a given point within it in one second. Although sound waves are mechanical in nature they do not only propagate through air; generally a deformable medium is required for propagation, which could be gas, liquid or solid. The velocity of sound or ultrasound remains constant in a particular medium if the temperature is fixed. The velocity (c) is equal to the frequency times the wavelength (λ). [1]

$$c = f\lambda \qquad \textbf{Equation 2.1}$$

This is the most important equation used in ultrasound. Because the velocity is constant for a particular medium, increasing the frequency causes the wavelength to decrease.

There are two types of waves; longitudinal and shear (or transverse) as shown in Figure 2.1. Longitudinal waves are those in which particle motion is along the direction of the wave propagation; the molecules oscillate in the same direction as the wave is travelling. Shear waves are those in which the particles oscillate perpendicular to the direction of wave propagation. Sound waves in liquids and tissues are generally considered to be all longitudinal as shear waves are not supported except in unusual circumstances; bone is the only biological tissue that can support propagation of shear waves easily. [30]

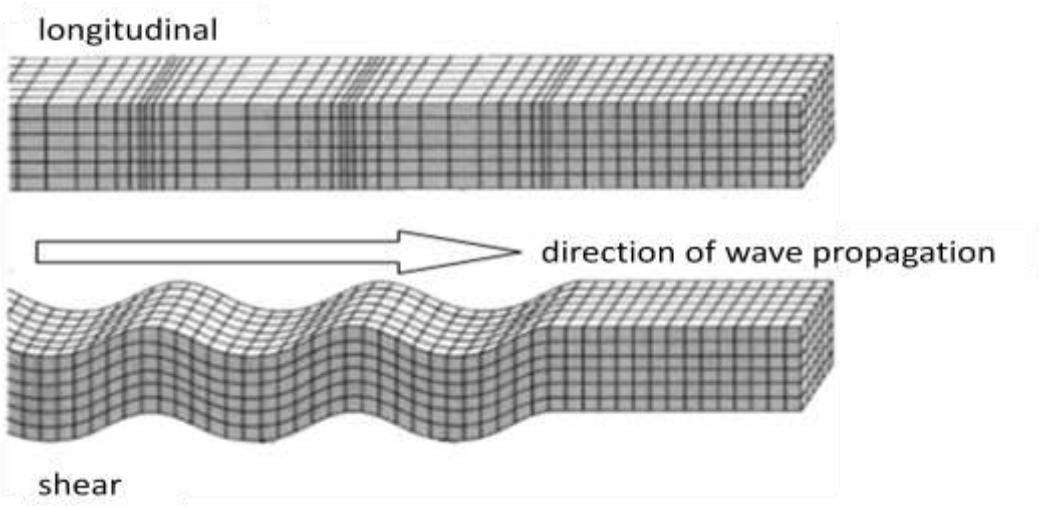

Figure 2.1 *Illustration of longitudinal and shear (transverse) wave modes*

A transducer is a device that converts one form of energy into another. [31] The active element is the heart of an ultrasonic transducer as it converts the electrical energy to acoustic energy and vice versa. In most transducers it is a piezoelectric material. [32] In diagnostic ultrasound, an ultrasonic wave is transmitted into the body, strikes an interface (where there is an acoustic mismatch between two media), and it is partially reflected back to the transducer. [29,31] This describes the technique of echo ranging which involves a system that can generate an ultrasonic pulsed wave and detect the reflected echo after a measured time so the distance to an interface can be determined (as the velocity of the wave through a particular media is constant – taken to be about 1540ms^{-1} in soft tissue). [1]

There are at least five advantages of ultrasound energy in medical diagnostic imaging: [33]

1) ultrasound can be directed in a beam

2) ultrasound obeys the laws of reflection and refraction

3) ultrasonic waves are reflected off small objects

4) at low amplitudes ultrasound has no known deleterious health effects

5) ultrasound uses simpler hardware than many other imaging techniques.

There are two principle disadvantages of ultrasound for medical imaging: ultrasound waves propagate poorly through a gaseous medium. [31] Thus ultrasonic transducers must have airless contact with the body and it is difficult to image parts of the body that contain air (such as the lungs) using ultrasound. The second disadvantage is that ultrasound images are relatively noisy, and have poorer contrast than X-ray and magnetic resonance (MR) techniques. This means that ultrasound is a heavily operator-dependent technique that requires extensive training and a long learning curve. [29]

2.2 Piezoelectricity

Piezoelectricity describes the phenomenon of the generation of an electric charge in a material, which is proportional to an applied mechanical stress. [34,35] This is described as the direct piezoelectric effect and the indirect or converse effect describes the development of a strain directly proportional to an applied electric field. For the piezoelectric effect to occur, the absence of a centre of symmetry in the material structure is necessary. [31,35] Several ceramics exhibit the piezoelectric effect including lead zirconate titanate, known as PZT, ($Pb(Ti_{1-x},Zr_x)O_3$), lead titanate ($PbTiO_3$), lead zirconate ($PbZrO_3$) and barium titanate ($BaTiO_3$). [31,32] A typical piezoelectric ceramic structure is a mass of perovskite crystals, each consisting of a small tetravalent metal ion, B^{4+}, (titanium/zirconium), in a lattice of larger divalent metal ions, A^{2+}, (lead/barium) and O^{2-} ions. Above a critical temperature, the Curie point (T_c), each perovskite crystal in the ceramic element exhibits simple cubic symmetry with no dipole moment. At temperatures below T_c each crystal has tetragonal or rhombohedral symmetry and a dipole moment as shown in Figure 2. 2.

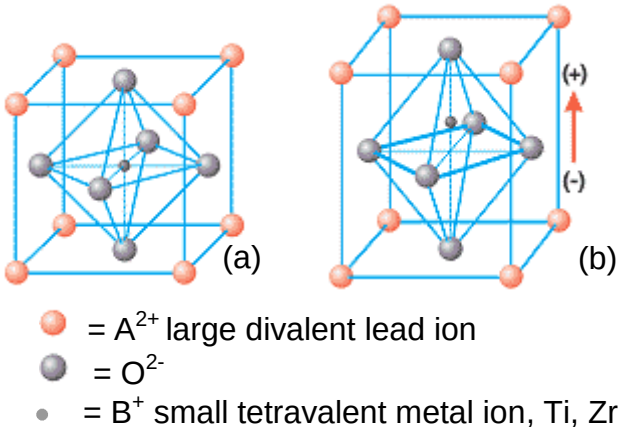

Figure 2.2 *(a) Perovskite structure of piezoelectric ceramic above Curie temperature: cubic lattice, symmetric arrangement of positive and negative charge (b) Tetragonal structure of piezoelectric ceramic below Curie temperature: crystal has electric dipole*

A ceramic is a multi crystalline structure made up of large numbers of randomly orientated crystal grains. The random orientation of the grains results in a net cancellation of the dipole effect so there is no overall polarisation. [31] The ceramic must be polarised to align a majority of the individual grain effects with a poling technique. In poling an electric field is applied with sufficient strength to orient the polarisation vector to the crystallographic direction which is the nearest to the direction of the applied field. After the field is removed the dipoles cannot easily return to their original positions so the ceramic has a permanent polarisation and exhibits piezoelectricity. [34]

The magnitudes of piezoelectric constants vary with direction of electrical and mechanical measurement and the direction of poling, so subscripts referring to direction are added to symbols. [34] The 3 direction is defined as the direction of poling and 1 and 2 are the perpendicular directions as shown in Figure 2.3a. Rotation about the axes 1, 2 and 3 is also shown and noted by the subscripts 4, 5 and 6 respectively. The piezoelectric constant, d, is the charge or strain constant, where in actuator mode

d (m/V) is the strain developed per unit of applied field, and in sensor mode d (C/N) is the electrical displacement generated per unit of applied stress. Therefore the d_{31} coefficient relates the strain developed in the 1 direction to the electrical field applied along the direction of poling (the transverse effect), and d_{33} relates the strain developed in the direction of poling to the electrical field applied in this direction.

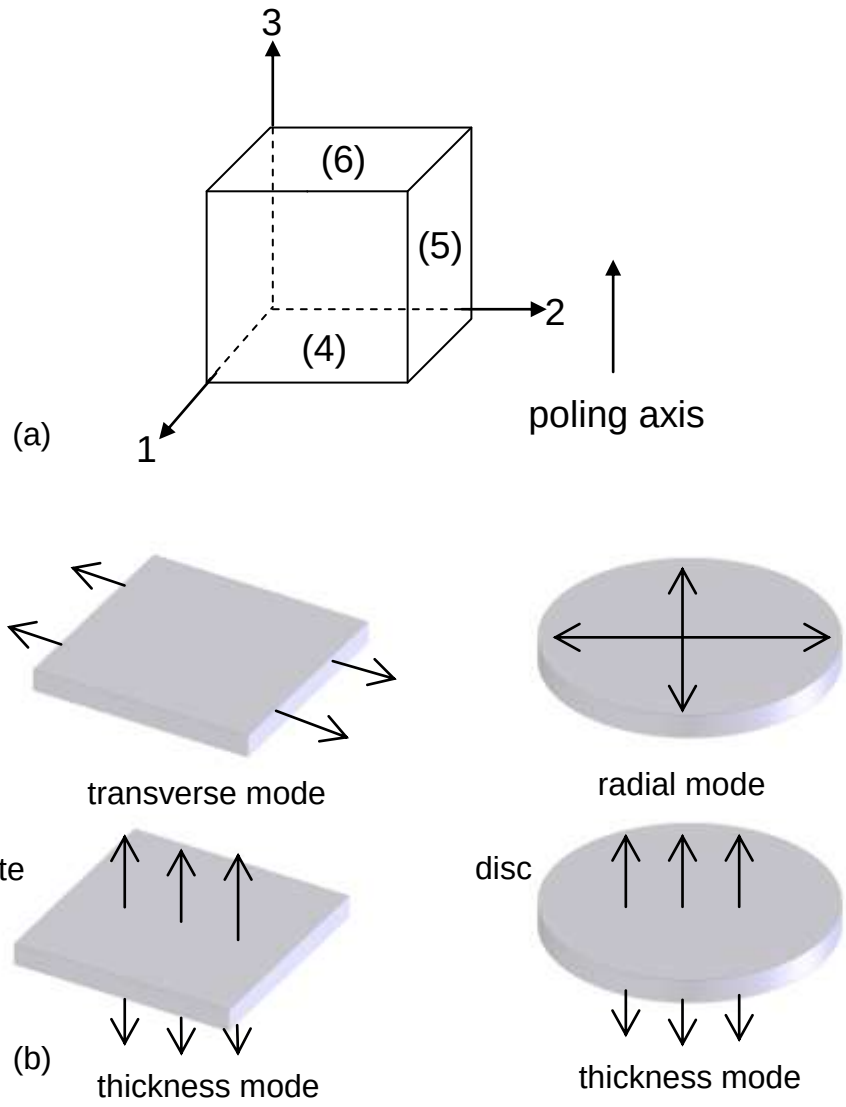

Figure 2.3 *(a) Axes and planes for piezoceramics (b)Resonance modes for plate and disc shapes*

The modes of vibration, or resonance modes, of a component made with piezoelectric material depend on the geometry and dimensions of the component. Figure 2.3b shows the modes of vibration for a plate and a disc. The thickness mode is most

commonly utilised in ultrasonic transducers so is the most important for transducer materials. The material is poled in the thickness direction and the voltage is also applied in the 3 axis. The electromechanical coefficient, k_t (for a plate), or k_{33} (for a bar) relates the mechanical strain in the thickness direction to the applied field in the same direction so is a critical property of piezoelectric transducer materials, where the thickness mode is important. [26]

2.3 Ultrasonic Transducers

2.3.1 Piezoelectric Materials for Ultrasonic Transducers

Active elements can be piezoceramic, monolithic single crystal, piezopolymer or piezocomposite materials. The most common piezoceramic material used as active material in ultrasonic transducers is lead zirconate titanate (PZT), [31,32,36] as it has good electromechanical properties including a high electromechanical coupling coefficient and a high dielectric constant. Its properties can also be adjusted by doping with other elements. [35] The main disadvantage of PZT is its large acoustic impedance of approximately 35MRayl compared to tissue (~1.5MRayl). Other disadvantages are its brittleness and that it contains lead. Other transducer materials include lithium niobate and potassium niobate, which are single crystals and can be cut in different ways to give different properties. These materials have been used in high frequency single element transducer design [37-40] but have small dielectric constants and are also brittle, cracking when curved to form focused transducers. Piezoelectric polymers also have application as transducer materials. A common piezoploymer is polyvinylidene fluoride (PVDF) which is a semicrystalline polymer material. [41,42] Its advantages include the fact that it is flexible which is useful for focusing, it is broadband and has a lower acoustic impedance than ceramic that is

more matched to human tissue. Although the advantages of a low acoustic impedance value close to tissue and flexibility are better than ceramic for transducer applications its disadvantages are that its piezoelectric properties are not as good as PZT: it has a fairly small k_t value compared to other materials, a very small transmitting constant, its dielectric loss is large and the dielectric constant small. Therefore it is not an ideal transmitting material, although its receiving properties are better leading to its commercial use in receiving hydrophones.

Table 2.1 Properties of some transducer materials [43]

Material	Type	Acoustic Impedance Z (MRayl)	Dielectric Constant	Elecomechanical coefficient, k_t	Mechanical loss %	Dielectric Loss %
PZT	piezoceramic	35	800	0.5	2.7	2.5
$LiNbO_3$	single crystal	34	28	0.49	0.01	0.1
PVDF	piezopolymer	4.6	4.1	0.29	4.0	6.9

Table 2.1 compares some relevant properties of some of the materials discussed here, showing that an ideal active material is difficult to find and a series of trade-offs must exist in transducer design. Therefore there is a need for a flexible material with low acoustic impedance and good electro-acoustic properties for high frequency transducer applications.

Composite materials consisting of piezoelectric ceramic in a flexible non-piezoelectric epoxy polymer matrix have advantages over other materials mentioned here, including a higher k_t value (up to 0.7) [8] and lower acoustic impedance that is closer to human tissue than the figures for ceramic materials. [44] It is also flexible when it is sufficiently thin so can be curved easily and is less likely to fracture. [45] These properties can be tailored by adjusting the ceramic volume fraction in the matrix material. [28] The main disadvantages are that piezocomposite has a lower

dielectric constant than some ceramics, there are difficulties with manufacture and cost, and the maximum operating temperature is limited to around 100°C. [32]

A 1-3 composite is shown in Figure 2.4 consisting of piezoceramic pillars upstanding in a polymer matrix. The 1-3 notation describes the connectivity of the composite; the ceramic is connected in one direction and the polymer matrix in all three orthogonal directions. [34]

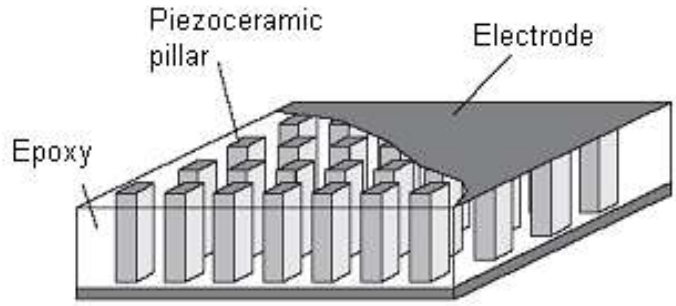

Figure 2.4 *Schematic of 1-3 piezocomposite*

In a disc or plate of 1-3 material, three resonant modes exist; the planar mode, the thickness mode, and various inter-pillar lateral modes caused by the regular arrangement of pillars in the material. [46] The 1-3 piezocomposite arrangement is the most promising for transducer applications as a high aspect ratio of the pillars within the structure causes the thickness resonance mode to be dominant above the planar mode and the polymer absorbs most of the lateral mode resonance. The aspect ratio of the pillars should be greater than 2 and ideally about 5 to achieve optimal results. [20]

The volume fraction of ceramic in composites can easily be manipulated in principle by changing the size and spacing of pillars and influences many performance factors, including the electromechanical coupling coefficient, k_t, and the acoustic impedance,

Z, although this is limited by manufacture techniques. The thickness mode resonance properties of 1-3 composites have been modelled by Smith and Auld [11,28] and Figure 2.5 shows how the density, velocity and k_t of a 1-3 composite vary with increasing ceramic volume fraction according to this model. It can be seen that k_t is high over a large range of ceramic volume fractions and the increasing density means that acoustic impedance, Z, will increase almost linearly with volume fraction of ceramic.

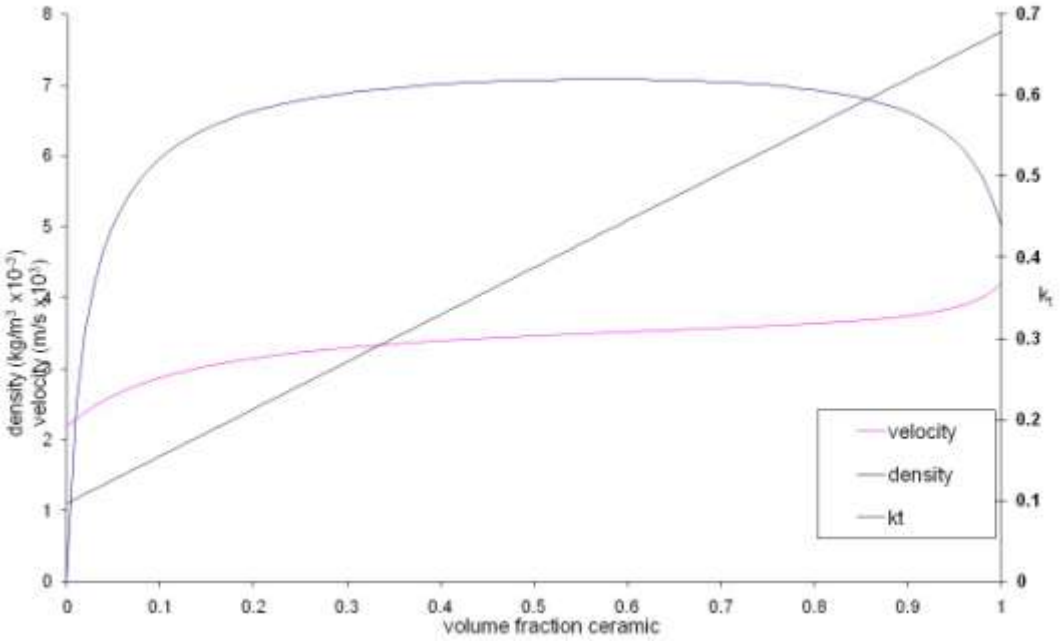

Figure 2.5 *Influence of ceramic volume fraction on density, velocity and k_t of 1-3 composite* [11,28]

Therefore, relative to monolithic and standard piezoelectric ceramics, composites can be designed with a higher thickness coupling coefficient, their acoustic impedance can be more closely matched to human tissue and low frequency lateral resonances can be suppressed. These improvements can lead to a higher sensitivity and bandwidth in the transducer and reduced ringing or unwanted resonances. The traditional monolithic piezoceramic material has other limitations as discussed, including low fracture strength, high stiffness, high density and difficulty in producing complex shapes. Composite materials are less brittle and the flexibility of some polymers allows

composite to conform more easily to curved surfaces when lapped thin enough, which is a great advantage for focused transducers. Therefore it is generally accepted that piezocomposite is superior to piezoceramic as the active element in ultrasonic transducers and they have been extensively studied for use in a range of applications. [9,47,48]

2.3.2 High Frequency Transducer Design

High frequency single element transducer design has been reported incorporating a range of active materials including piezoceramic, piezocrystal, piezopolymer and piezocomposite materials. [41] Generally the active material is lapped to thickness and electrodes are applied before being potted into an electrical housing (typically SMA or BNC) with insulating and conductive epoxy where appropriate. SMA (SubMiniature version A) connectors are coaxial RF connectors used as a minimal connector interface for coaxial cable with a screw type coupling mechanism. The BNC connector is another type of RF connector used for terminating coaxial cable and is commonly used for plugs and sockets for audio and video applications. The active element has electrodes on both faces which are electrically connected to the housing so a coaxial cable can be attached.

Aristizabel and Turnbull [49] describe the fabrication of a 44MHz planar lithium niobate transducer. Circular discs of $LiNbO_3$ plate were mounted in SMA connectors with silver epoxy and then potted with insulating epoxy. A Cr-Au layer was then evaporated onto the front surface to create a ground electrode. Cr-Au is commonly used for conducting electrode applications; a thin layer (~10nm) of Cr is used for adhesion and a thicker layer of Au (~200nm) is used as the electrical conductor as it has lower resistivity. [50] Both materials are also chemically inert. The transducer

reported here was air backed; other studies [51-53] have reported using a conductive epoxy as backing. A schematic of the curved and lens focused devices reported by Cannata [39] is shown in Figure 2.6 where a conducting epoxy backing is used and silver epoxy and parylene used for matching. Using a conductive backing means that wire bonding is not required to electrically connect the rear face of the active element. The lithium niobate was pressed into a curved shape to focus the transducer and it was reported that the material cracked during this process. The design of the curved element transducer is also similar to a curved PZT transducer housed in a SMA housing reported by Lockwood [54]

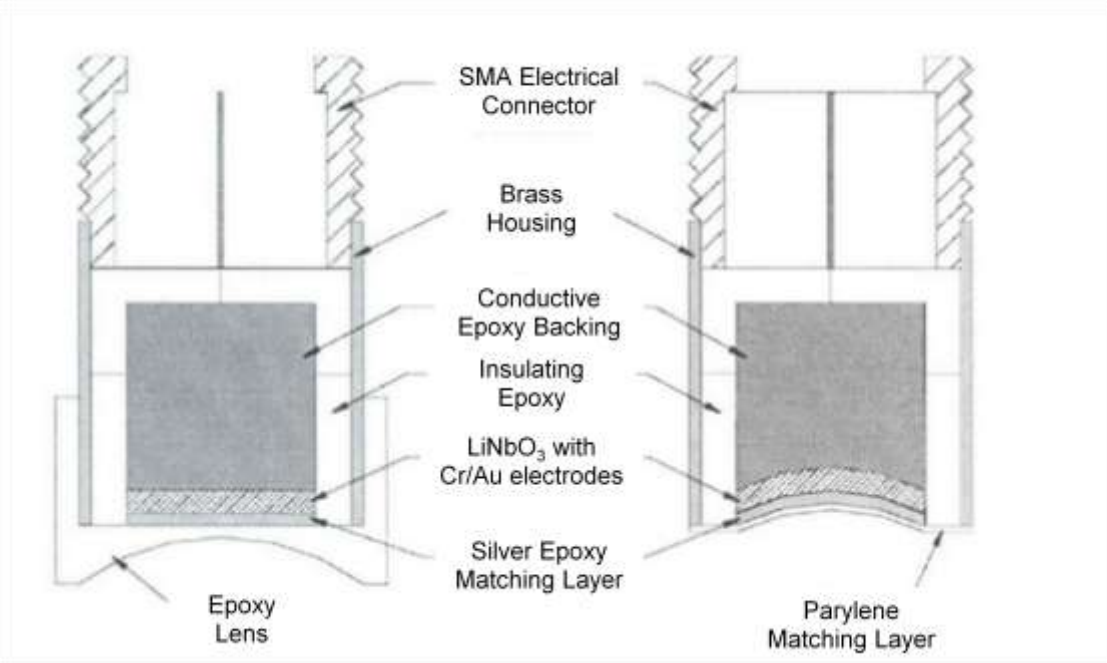

Figure 2.6 *Schematic of lens focused and press focused transducers reported by Cannata* [39]

The conductive epoxy backing reported in the literature can be commercial conductive epoxy adhesive such as E-Solder, a silver epoxy adhesive, or Epotek 430, a copper filled epoxy used for adhesive bonding in electronics. [39,55] Other work has reported fabricating backings using tungsten filler in an epoxy base [56,57] where conductive backings are achieved with centrifugation producing 'heavy' backings.

Alumina-filled epoxy has also been reported for use in matching applications, [57,58] as well as other polymer materials, such as parylene [59] and silica gel. [60] The required thickness of the matching layer is related to the wavelength of the ultrasound (typically ¼ wavelength) so high frequency operation requires thin matching layers. This limits matching material selection to materials that can be applied in thin layers easily or those that can be lapped down easily, although lapping bulk material down can be expensive and is impossible on curved surfaces. [61]

2.3.3 Piezocomposite Manufacture for High Frequency Operation

High frequency operation requires the thickness of the piezoelectric active element to be as thin as 50μm at 30MHz. Lapping down bulk ceramic can be difficult due to the the brittleness and poor mechanical strength of ceramics and is also time consuming and expensive. The challenge now is to manufacture ultra-fine scale composite structures.

The standard method for fabricating 1-3 composites is dice-and-fill, first reported by Savakus, [62] where a ceramic block is diced in one direction and then again perpendicular to the first direction, creating a 'bristle block' of square pillars attached to the remaining ceramic stock. The block is then back filled with epoxy and the remaining stock and excess epoxy removed. Dice-and-fill is not ideal for high frequency composites as saw blades have a finite minimum thickness (typically 10μm) and the weakness of the ceramic means that small pillars can break easily during cutting.

High frequency operation requires fine lateral scales in addition to the aspect ratio requirement of 2-5. In particular, the spacing between the pillars (kerf) must be

narrow enough (<15μm) to prevent the frequency of inter-pillar acoustic modes coinciding with the operating frequency so the lateral modes are moved outside the transducer bandwidth. For example, a 1-3 piezocomposite operating at 50MHz would require ceramic pillars approximately 20μm wide and a kerf less than 10μm. [20] Composite devices fabricated via traditional dice-and-fill with square pillars have been reported operating up to 30MHz. [53] Other fine scale 1-3 fabrication dicing methods have also been reported including interdigital pair bonding, [63] where two ceramic sheets are diced and then interdigitally inserted and the surfaces are then lapped away to produce a 1-3 composite, as shown in Figure 2.7. This requires elaborate machining and the dimensions are still limited so transducer designs are compromised, therefore these dicing methods have not been adopted for commercial production.

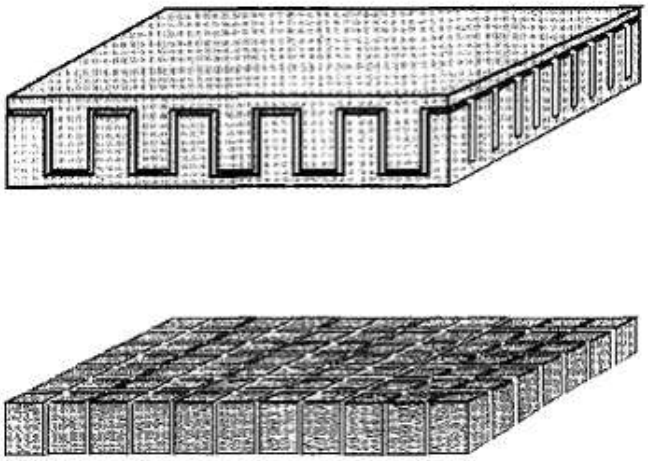

Figure 2.7 *Interdigital pair bonding: two ceramic sheets are diced in two directions, then interdigitally inserted and the surfaces are then lapped away to produce a 1-3 composite* [63]

Transducers with triangular shaped pillars operating up to 40MHz have been manufactured with a dice and fill technique. [55] The geometry of the triangular pillars helps spread the lateral modes over a broad spectrum of frequencies. The composite

design is still limited by the blade thickness on a micro-dicing saw so the ceramic volume fraction is also limited to 25% or less.

More specialised methods to manufacture fine scale 1-3 composites utilising moulds have been investigated with more success and suitable structures for commercial production have been developed.[18-23] This technique is based on viscous polymer processing (VPP) combined with a 'lost mould' method.[20] The fabrication route has four main process steps; production of ceramic 'paste', embossing of the 1-3 structure into a mould, mould removal and heat treatment, and finally piezocomposite assembly and finishing. Using this fabrication technique different shaped and sized pillars can be produced depending on the mould dimensions. Examples of sintered pillars manufactured via this technique are shown in Figure 2.8. This net shape manufacture has demonstrated that it is possible to mould 1-3 structures suitable for high frequency operation in ultrasound transducer devices, and the technique has the potential to extend the frequency range of piezocomposite materials beyond existing limits.

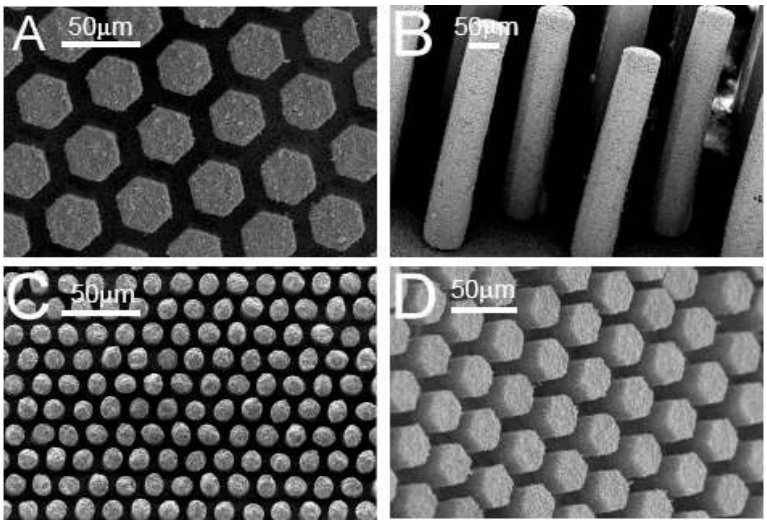

Figure 2.8 *Sintered 1-3 Structures made by embossing VPP ceramic into polymer moulds*[20]
A Hexagonal, 30µm width, 10µm kerf, aspect ratio 3
B Circular, 50µm pillar width, 100µm kerf, aspect ratio 8
C Circular, 12µm pillar width, 7µm kerf, aspect ratio 3
D Hexagonal, 30µm pillar width, 10µm kerf, aspect ratio 3

2.3.4 Passive Transducer Materials

2.3.4.1 Backing and Matching Requirements

The fundamental desired characteristics of an ultrasound transducer for diagnostic imaging are a wide bandwidth, which gives short echoes and thus high resolution, and a low transmission loss, which gives good sensitivity. The main problem with transducers used for medical applications is the large acoustic mismatch between the active element and the load (tissue), resulting in most of the acoustic energy being reflected back and forth between the front and rear faces of the element; the transducer consequently has a small bandwidth, the pulse transmitted into the load is long, and the axial resolution is poor. These oscillations may be dampened by positioning a lossy backing material behind the piezoelectric element to absorb a large proportion of the energy and increase the bandwidth. [27]

In imaging, a pulsed wave system is used; the transducer sends out a short burst of ultrasound followed by a period of silence to allow for detection of returning echoes (receiving mode) before another pulse is generated. Ideally the backing material should absorb all the energy except for one cycle of sound produced from the front face of the transducer to avoid false echoes. [27] For maximum transfer of energy to occur into the backing, the backing material must have an acoustic impedance value identical to that of the active element; [64] the pulse length will be short when transmitted and received after reflection. However, most of the ultrasonic energy will be coupled into the backing and, as a result, the transducer will have a shorter pulse duration at the expense of sensitivity. [27] By using a backing with lower acoustic impedance than the active element, greater sensitivity is achieved because less energy is absorbed into the backing. Unfortunately the transmitted and received pulses are

longer due to increased ringing (continued vibration of the element after excitation) in the transducer, therefore a compromise must be made in choosing the acoustic impedance of the backing. The backing material should also have a high absorption coefficient (attenuation) to prevent ultrasonic energy from returning to the piezoelectric element. (65)

The acoustic mismatch between the transducer and load can be reduced by placing a matching material on the face of the transducer, with this material having an intermediate acoustic impedance value so that the effective difference in impedance values at the interface is reduced and the energy transfer across the interface is improved as reflection is reduced. (27) This material must have the desired acoustic impedance value tailored to match the active element to the load and must also have low loss properties as high attenuation would prevent the desired function of providing high transmission between the element and the load and vice versa. The required acoustic impedance of the matching layer can be calculated by taking the geometric mean of the impedance values of the active element and tissue. (66)

$$Z_{matching} = \sqrt{Z_{element} Z_{load}} \qquad \textbf{Equation 2.2}$$

A specific thickness of the matching layer is also helpful. A thickness equal to integer multiples of a quarter of the wavelength in the matching layer gives maximum reinforcement of the wave reflected from the transducer – matching layer interface enhancing the intensity of the ultrasound transmitted into the body. A one quarter wavelength layer is preferred to other integer values as a thicker layer increases attenuation. (67) The wavelength at the centre frequency of the transducer is considered to design the matching layer thickness so at high transducer operating frequencies matching layer thickness is very small (¼ wavelength ~12μm for 50MHz).

Multiple matching layers can be used to taper the acoustic impedance between the transducer material and the load providing additional performance improvement; it has been reported that a transducer with a single matching layer has a 40-50% fractional bandwidth and that a transducer with double matching layers has a fractional bandwidth of about 70%. [68] It has also been suggested that wider bandwidth characteristics can be obtained using triple matching layers. The quarter wavelength matching layer allows maximum transmission for a single frequency of an ultrasound wave. However, pulsed wave systems produce ultrasound waves across a range of frequencies – described by the bandwidth – and each frequency has its associated wavelength, making the optimal single matching layer difficult to design. Multiple matching layers alter the frequency distribution towards a broader bandwidth enhancing sensitivity and axial resolution. [68]

2.3.4.2 Material Selection

Epoxies loaded with suitable fillers are used as backing and matching materials in many commercial NDT and medical imaging probes. Epoxies provide the necessary toughness so backings are capable of withstanding high pressures. The acoustic impedance and attenuation characteristics of the backing material can be tailored depending on the amount of filler. Composites containing a small amount of filler in a polymer matrix have a 0-3 connectivity pattern, in which the "0" phase is the filler material which is not connected in any dimension and the "3" phase is the polymer matrix that is interconnected in all three dimensions. [34] Commonly fillers such as tungsten, iron, magnesium and aluminium are used to obtain high acoustic impedance and fillers such as glass, microspheres, wood and cork are used for low acoustic impedance backings. As previously discussed, tungsten and alumina are commonly

used as filler material for transducer passive materials, manufacture being limited by the maximum solid loading for backings and the thin matching layers required for high frequency operation. Table 2.2 shows some acoustic properties of possible fillers and epoxies compared with the properties of human tissue and some common transducer materials.

Table 2.2 Acoustic properties of candidate fillers and epoxies compared with the properties of tissue and some common transducer materials [69; 70]

Material	**Longitudinal Velocity, V_L m/s**	**Density, ρ g/cc**	**Acoustic Impedance, Z MRayl**
Human skin	1540	1.11-1.19	1.71-1.83
Human breast tissue	1430-1570	0.99-1.06	1.42-1.66
Epoxy Epotek 301	2640	1.08	2.85
Epoxy CY1301/HY1300	2482	1.15	2.85
Parylene C	2150	1.40	3.0
Silver epoxy	1900	2.71	5.14
PZT-5H	4440	7.43	33.0
Gold	3240	19.7	63.8
Glass	5660	2.49	14.09
Iron	5900	7.69	46.4
Magnesium	5800	1.74	10.0
Nickel	5600	8.84	49.5
Platinum	3260	21.40	69.8
Silicon Carbide	13060	3.22	42.0
Silver	3600	10.6	38.0
Tungsten	5200	19.4	101.0
Alumina	10520	3.86	40.6

From Table 2.2 it can be seen that tungsten has a very high acoustic impedance, mostly due to its high density and this is the main reason tungsten is commonly used

as filler in backing materials. Tungsten-filled composites can also be electrically conducting at high volume fractions. Table 2.2 shows that gold and platinum also have high acoustic impedance values due to their high density. These materials are, however, expensive and so are not suitable for filler in backing materials for commercial devices. Although alumina does not have a very high density, the velocity is very high so it has a reasonably high acoustic impedance. Therefore low volume fractions of alumina filler in epoxy is used as matching material but higher volume fraction alumina epoxy may be suitable for backing composite transducers and also array transducers, as alumina is non-conducting and less expensive than tungsten. In order to match the PZT acoustic impedance of ~35MRayl, about 60-70% volume tungsten is usually needed, [56,65] resulting in a heavily loaded backing.

The acoustic impedance of piezocomposites is lower than that of PZT, depending on the volume fraction of ceramic in the composite, therefore the required acoustic impedance of the backing will be lower than that required to match a monolithic PZT ceramic active element. The relationship between acoustic impedance and ceramic volume fraction is shown in Figure 2.9 showing how acoustic impedance varies almost linearly with ceramic volume fraction for a 1-3 piezocomposite of PZT5/Spurr epoxy according to the Smith and Auld model, [28] so a composite with about 50% volume ceramic has an acoustic impedance value of approximately 15MRayl. This also has implications for matching design as the geometric mean of tissue and PZT is approximately 7MRayl compared with 4.7MRayl for tissue and a 50% volume fraction ceramic composite, which means that some composite transducers may not require matching, or may be matched reasonably well with unfilled polymer.

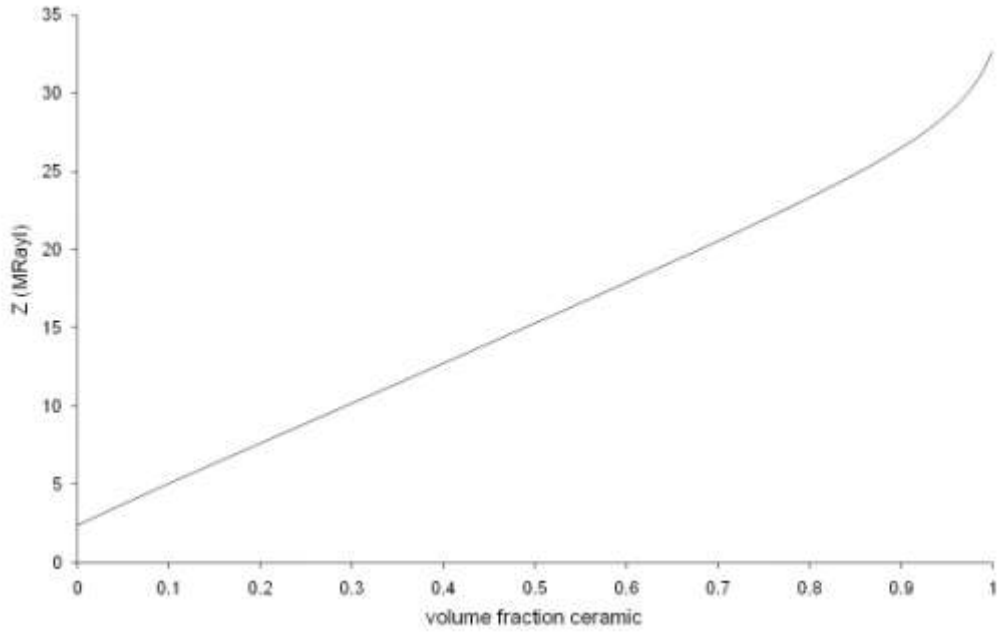

Figure 2.9 *Influence of volume fraction ceramic in 1-3 composite on acoustic impedance* [28]

2.3.5 Transducer Simulation and Modelling

2.3.5.1 Transducer Modelling

Modelling transducer and material properties is important for transducer design in order to predict how a device will perform, as there are many possibilities and combinations of layer thicknesses and impedances. There are, however, many factors in the manufacturing process that could influence performance so a device does not behave as predicted by the model. These include thick bond lines, air bubbles in backing material and cracks in the ceramic material, so modelling is important to ensure that experimental results are due to the selection of material properties and dimensions and not manufacturing problems. The Mason model, a one dimensional analysis of the wave equation on transducer materials, shown in Figure 2.10, was developed to calculate the transfer function for a transducer. It is an electromechanical equivalent circuit valid for a thin lossless disc operating only in the thickness mode, separating the piezoelectric transducer into an electrical port and acoustic ports representing the different transducer components. [71,72]

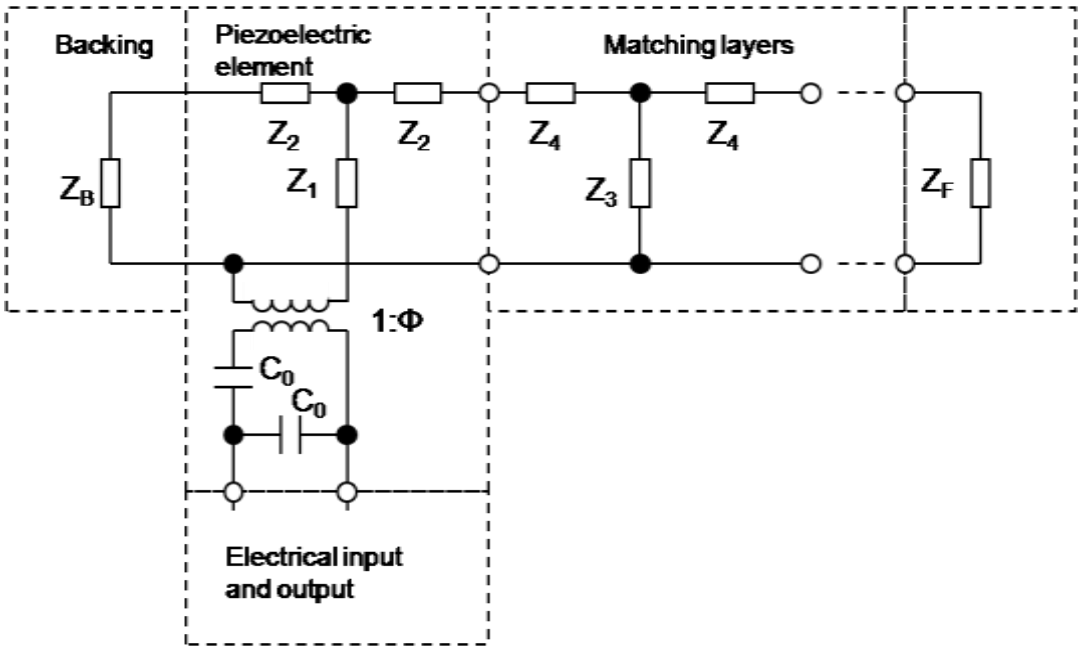

Figure 2.10 Mason *Equivalent Circuit* [71]

Another commonly used 1D equivalent circuit is the KLM model, however as both these models are one dimensional (only describe the thickness mode) they do not describe the whole system as some factors are not taken into account; the piezoelectric, dielectric, and elastic constants are represented by complex quantities to account for loss in the material but other losses due to absorption and diffraction are ignored. [72] These models require a precise knowledge of the electrical and mechanical properties of the transducer and can be quite inaccurate. Transducer designers generally now employ more comprehensive and accurate finite element modelling (FEM) solutions for 2D and 3D analyses rather than relying exclusively on 1D analytical models and experimental prototypes. [73,74] The accuracy of the simulation still relies on the accuracy of material properties that are input into the models but the more comprehensive analysis represents the real situation better than one dimensional models. These properties are often not specified in manufacturer specifications so characterisation of transducer material properties at the frequencies

of interest is required to ensure simulation and modelling can give a good representation of the transducer performance in reality. FEM modelling can be performed using different approaches. Currently there are two major FEM software packages available commercially designed for the analysis of piezoelectric resonators; ANSYS (ANSYS Inc. PA, US), a frequency domain modelling package and PZFlex (Weidlinger Associates, CA, US), a time domain modelling package. [75]

2.3.5.2 Acoustic Modelling of Passive Materials

To model the acoustic properties of transducer passive components such as backing and matching materials, scattering and bulk elastic properties must be considered. Medical ultrasound relies greatly on the fact that biological tissues reflect or scatter incident sound. It also relies on the transmitted part of the sound wave; if all the transmitted energy is reflected at a particular interface no sound penetrates further to show underlying structures. This occurs in the body at the boundary between tissue and air which is why ultrasound cannot image tissue within or under the lung.

The two physical processes of reflection and scattering are closely related but scattering refers to the interaction between sound waves and particles much smaller than the wavelength and reflection occurs with interaction between particles or objects larger than the wavelength. If the incident wavelength is much smaller than the dimensions of the object the reflection process can be estimated by analysing conceptual rays incident on the object. The reflected wavefront is a replica of the object shape and is reflected by a reflection factor due to the impedance mismatch between the propagating medium and the sphere. [76] This is known as specular scattering, as illustrated in Figure 2.11(a). Scattering by small sub-wavelength particles, known as diffusive scattering [76] and shown in Figure 2.11(b) is important in

medical imaging as this is how tissue is often modelled. As the object size gets closer to the wavelength the radiation pattern becomes more complex and progressively more directional.

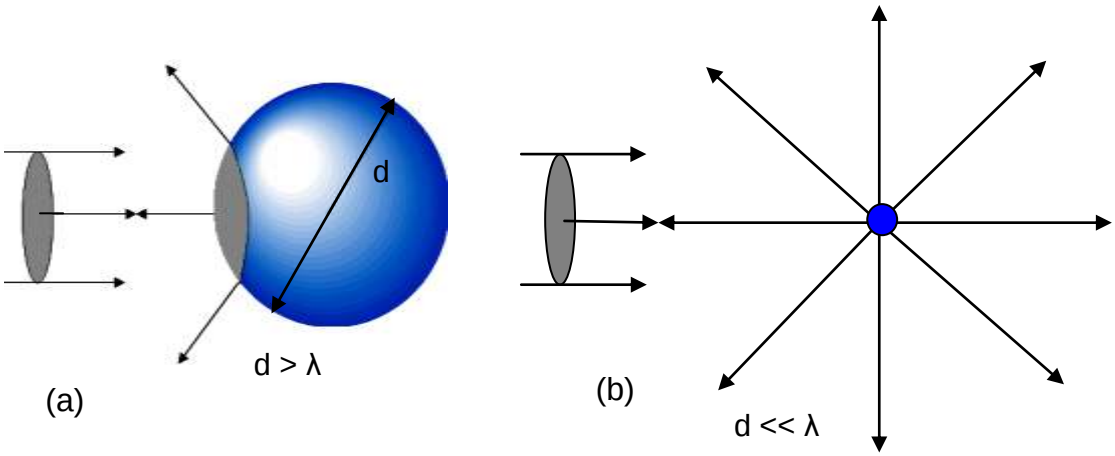

Figure 2.11 *Illustration of specular and diffusive scattering (a) sound incident on spherical particle much bigger than wavelength (specular scattering) (b) sound incident on spherical particle much smaller than wavelength (diffusive scattering)* [76]

Scattering or reflection of sound waves can be caused by inhomogeneities in the density or compressibility of the medium, such as filler particles in an isotropic matrix. The amount of scattering or reflection is usually proportional to the difference in the mechanical properties of the medium, therefore the scattering or reflection process can be modelled. In the 19th century Raleigh derived an expression for scattering from a sphere much smaller than the wavelength and with different elastic properties, density and compressibility, and since then many other elastic models have been formulated. For simple geometric shapes it is possible to give explicit expressions for the scattering cross-sections. Solutions for a limited range of other object shapes do exist but spheres and cylinders can be used to estimate a large number of scattering objects found in tissue. Therefore if the scattering particles in transducer materials are assumed to be spherical and much smaller than the wavelength, the elastic properties can be modelled to show how the amount of

scatterers (volume fraction of filler) affects velocity. These types of models will be used to describe the acoustic properties of backing and matching material consisting of 0-3 composites. Acoustic modelling of materials is related to the elastic properties of the material. [77] Elasticity is related to the ability of a material to return to its original shape after a force ceases to act on it. An ultrasonic wave travelling through an elastic material causes deformations by the separation and compression of neighbouring molecules or atoms in the lattice. The velocity of sound through a material is related to the material stiffness and scattering due to the inclusions affect the material attenuation. Therefore the velocity and acoustic attenuation in 0-3 composites can be estimated using the filler and matrix mechanical properties. [78] Many models have been formulated to describe the bulk properties of random heterogeneous composite materials as considered here.

The velocity of a longitudinal sound wave, V_L, is related to the mechanical properties of the medium by

$$V_L = \left(\frac{K + \frac{4}{3}G}{\rho} \right)^{1/2} \qquad \textbf{Equation 2.3}$$

where K is the elastic bulk modulus, G is the shear modulus and ρ is the density. [79] The composite density is calculated by

$$\rho_{composite} = \rho_1 v_1 + \rho_2 v_2 \qquad \textbf{Equation 2.4}$$

where ρ is the density and v is the volume fraction of each phase denoted by subscripts 1 and 2. Common models to describe the elastic properties of two phase composites include Reuss and Voigt. [79] The Reuss model assumes constant stress throughout the material and is defined by

$$K_{composite} = \frac{K_1 K_2}{v_1 K_1 + v_2 K_2} \qquad \textbf{Equation 2.5}$$

The Voigt model assumes constant strain throughout the material and is defined by

$$K_{composite} = v_1 K_1 + v_2 K_2 \qquad \textbf{Equation 2.6}$$

These two models are the simplest models applied to two phase composites and lead to extreme upper and lower limits (Reuss gives the lower limit and Voigt the upper). These models make simplifying assumptions concerning geometry and physical behaviour of the two phases.

A better approach is the model proposed by Hashin and Shtrikman. [80] This model is based on energetic considerations and results in more restrictive limits. This model evaluates the strain energy stored in the material, and determines limits using the principle of minimum complementary energy and the principle of minimum potential energy to obtain maximum and minimum conditions. The disadvantage of using this model to predict acoustic properties is that the difference between the upper and lower bounds is still fairly large so accurate specific predictions cannot be made. More accurate predictions can be made using scattering models.

Scattering effects must be considered to fully understand acoustic properties of 0-3 composites. Most of the theoretical understanding of ultrasonic propagation in composite materials is based on the scattering properties of a single inclusion or void. At very low concentrations multiple scattering can be neglected and each scatterer can be treated as independent, but it is not known at what concentration the single scatter approximation remains useful, [81] and multiple scattering effects are important in many practical situations where concentrations range from 1% to 60%. [82] Therefore accurate models must be based on multiple scattering effects. [83]

Kuster and Toksoz's 1974 model [84] is based on multiple scattering of waves and is identical to the lower bound of Hashin and Shrikman at low volume fractions. The Devaney model [85] is based on a self-consistent formulation of multiple scattering theory. According to this model the moduli K and G of the composite are given by Equations 2.7 and 2.8. [85]

$$K = K_1 + v_2 \frac{(3K + 4G)(K_2 - K_1)}{3K + 4G + 3(K_2 - K_1)} \qquad \textbf{Equation 2.7}$$

$$G = G_1 + v_2 \frac{5(3K + 4G)G(G_2 - G_1)}{(15K + 20G)G + 6(K + 2G)G_2 - G_1)} \qquad \textbf{Equation 2.8}$$

Where wavelengths are much larger than the particle size, and the concentration of filler is low, the Devaney model reduces to the coherent potential approximation (CPA), a single scatterer model where multiple scattering effects are not taken into account [79] Therefore it may be assumed that the lower bounds of the Hashin and Shtrikman model and single scattering models are valid at low volume fractions but multiple scattering effects become more important as the volume fraction of filler increases.

Using the moduli from the models discussed here and Equation 2.3 the longitudinal velocity and acoustic impedance have been calculated for 0-3 composites using the common transducer filler materials of tungsten and alumina in CY1301/HY1300, a common two-part engineering epoxy. The velocity results are plotted in Figure 2.12 showing how these models describe the variation of longitudinal velocity with volume fraction tungsten and alumina in epoxy. The Devaney model has agreed best with experimental data in the literature. [57,86,87] However, when the volume fraction of filler is one, the Devaney model velocity is different from the bulk velocity in the filler material (as it is in the Kuster and Toksov model). This is due to the fact that

this approach does not place the matrix and the filler on equal footing and the situation where $v_2 = 1$ is not taken into account by these models. Therefore at very high volume fractions these scattering models are not likely to be accurate. The corresponding acoustic impedance values according to the models are shown in Figure 2.13. According to the Devaney model, a volume of 45% tungsten would be required to match a piezocomposite with a 50% volume ceramic, compared to above 60% volume tungsten needed to match PZT.

It has been found experimentally that the velocity, acoustic impedance and elastic stiffness of 0-3 composites is independent of frequency. [56] Therefore the elastic models should be valid at high frequencies. The scattering models assume the scattering particles to be spherically shaped. They also assume the particle size to be sufficiently small so that diffusive scattering is occurring instead of specular scattering, as described in Figure 2.11, therefore the particle size of the filler becomes more important with high frequency operation. Another problem using these models is related to the material parameters for the particle filler phase, as values are usually taken from literature data on bulk samples and it is not known how this applies to powder materials. [88]

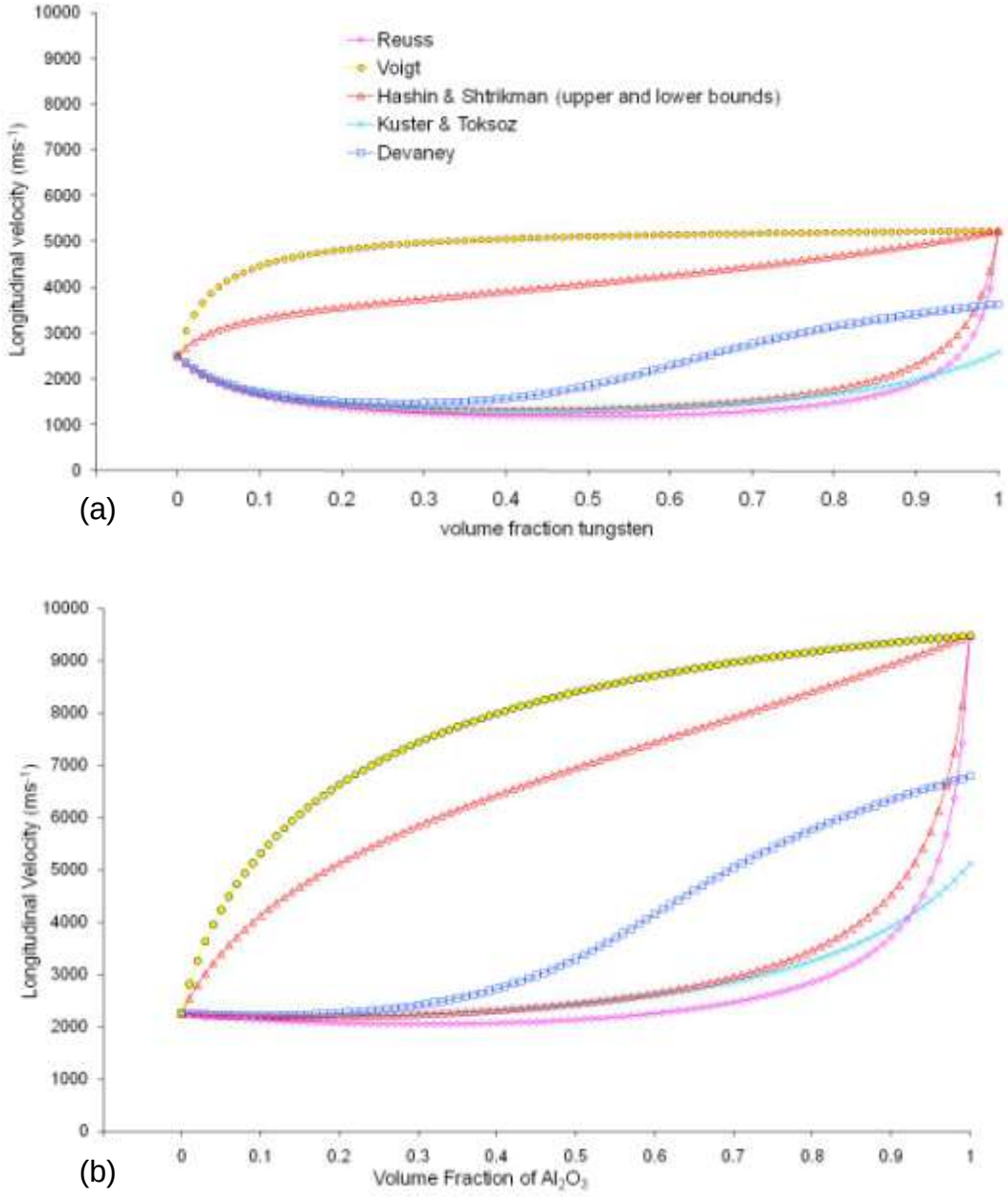

Figure 2.12 *Effect of filler volume fraction on longitudinal velocity of (a) tungsten epoxy material and (b) alumina epoxy material according to different elastic and scattering models*

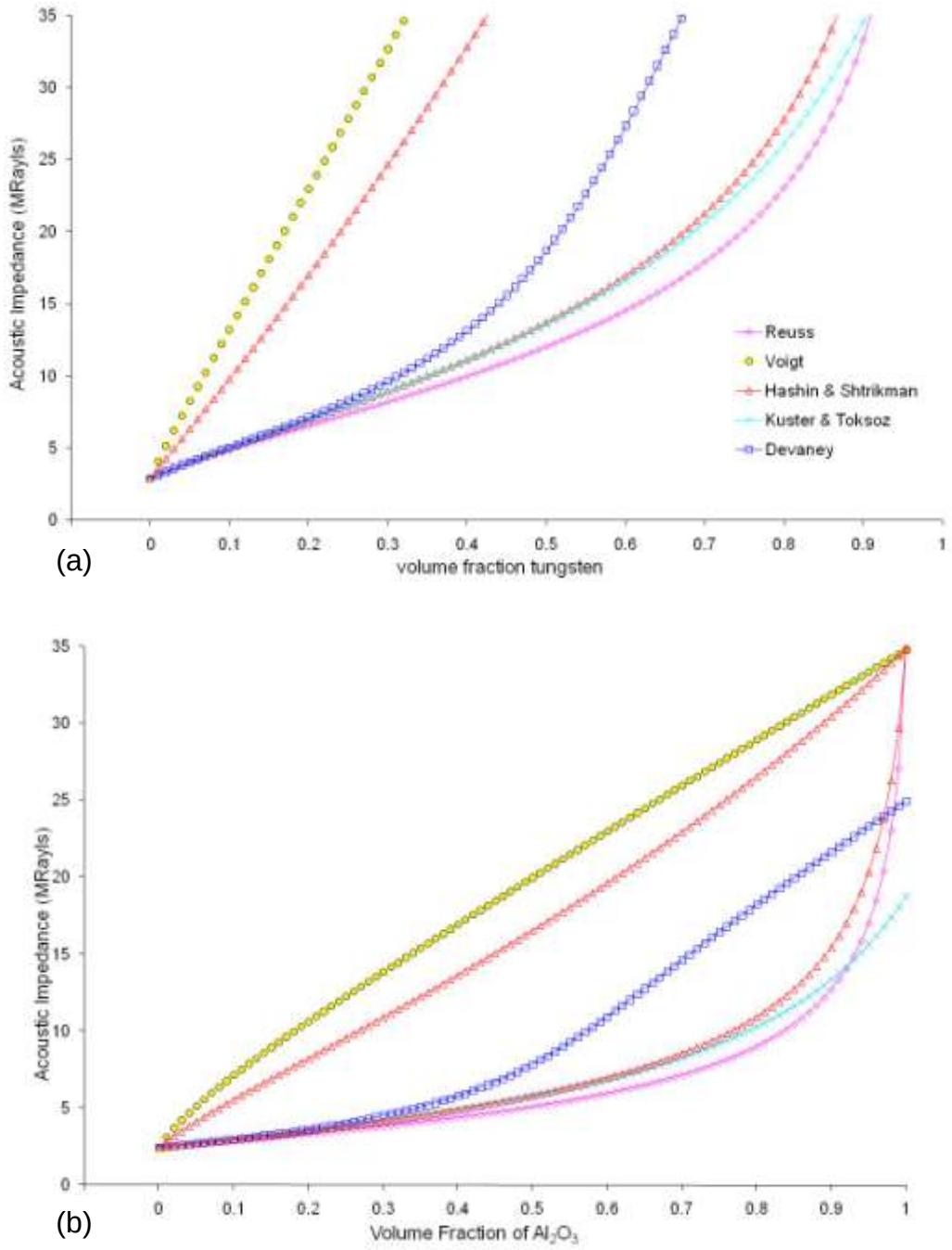

Figure 2.13 *Effect of filler volume fraction on acoustic impedance of (a) tungsten epoxy material and (b) alumina epoxy material according to different elastic and scattering models*

2.3.5.3 Additional High Frequency Considerations for Passive Materials

In addition to tailoring the backing and matching to the acoustic impedance of the piezocomposite material acting as the active element there are additional considerations for high frequency operation. As previously stated, the most important are the particle size of the filler and the thickness of the matching layer. This stems from the fact that ultrasound through solids around 100MHz typically has wavelengths in the order of a few tens of microns. This means that the filler particles must be at least ten times smaller than the wavelength to act properly as scatterers so that the velocity properties can be accurately modelled.

Such small wavelengths mean that a ¼ wavelength matching layer would be very thin and would limit the materials that could be used for the matching material. Typically thin layers of solids such as composite epoxy materials are laminated onto the front of transducers operating at lower frequencies but lapping these materials thin can be difficult. [61] Thin polymer films, such as parylene can be vapour deposited onto the front of a transducer. Parylene is useful for the front face material of a transducer, i.e. the final matching layer, as parylene coatings have a uniform thickness and are pinhole free so components with sharp edges, points, flat surfaces or crevices are coated uniformly without voids. [89] It is also chemically inert and biocompatible and is used to coat many medical devices and components.

The use of nanoparticles as filler has been reported in high frequency transducer passive materials to adjust impedance and attenuation properties and create thin matching layers.[58,90-92] Epoxy filled with alumina nano particles has been investigated for matching applications. [91] The alumina was dispersed in a solvent then added to epoxy which was spin coated onto a silicon substrate creating layers

2-8μm thick. The measured acoustic impedance ranged from 2.8-4.8MRayl and the attenuation 1.5-12dB/mm. The attenuation was found to be dependent on the smoothness and quality of the coating layer, therefore the optimal production process must be investigated further to obtain material with predictable attenuation properties. Other work has reported fabrication of high volume fraction TiO_2-polymer composite matching layers. [92] The filler was a nanopowder in the range of 20-40nm. The material was coated on a substrate with a doctor blade technique producing 8-15μm thick films. The specific volume fraction of the composite is not known but the material appears to be well packed without trapped air bubbles. Curing the epoxy at different temperatures resulted in material with different measured acoustic impedance values ranging from 5.3-7.2MRayl, although this material was fabricated onto a substrate. The characterisation of matching materials on a substrate can be difficult depending on the thickness of the substrate and additional charaterisation techniques may have to be developed. [67] In addition to matching applications, nanopowder filler has been investigated for use in lens material. [90] In this study the acoustic impedance and attenuation of silicone rubber was altered by adding different amounts of metal oxide nanopowders. The method of dispersing the nanopowder in the silicone was not reported and agglomerations of 1μm were observed. Therefore optimal mixing processes must be investigated as the dispersion of nanopowders in polymer is difficult. A clear particle size dependence on acoustic attenuation was found so that material with smaller filler particles had a lower attenuation, other factors were also suggested to affect the attenuation including particle shape, distribution, agglomeration and uniformity. [90]

2.4 Summary

The active part of a transducer probe is usually a piezoelectric material that converts electrical energy into mechanical waves and vice versa. Common piezoceramic materials used in ultrasound transducers include PZT and lithium niobate. Piezocomposite materials consisting of piezoceramic pillars upstanding in a polymer matrix offer superior properties than conventional monolithic materials, including a higher electromechanical coefficient k_t. High frequency operation requires thin active material and composite material is also easier to lap down thin and is less likely to fracture when curved to form focused transducers than other materials, such as lithium niobate.

Conventional manufacture of 1-3 piezocomposite is limited for high frequency operation as fine scale structures are required. Materials fabricated via a VPP moulding route have created composite structures with great potential, with feature sizes as small as 12µm, allowing operation above 50MHz. These piezocomposite materials have different acoustic impedance values than conventional transducer material so the requirements for passive materials are changed.

Transducer passive materials involve a backing material placed behind the active material to absorb ultrasonic energy preventing false echoes and continued vibration (ringing) in the active material and a matching layer which is placed on the front face of the transducer to improve the energy transfer from the transducer to the load by reducing the acoustic mismatch at the interface. Passive materials are usually a composite material consisting of filler particles randomly arranged in a polymer matrix. Common filler materials for transducer applications include alumina and tungsten and the overall composite properties can be tailored by adjusting the amount

of filler. The velocity and acoustic impedance can be predicted from multiple scattering models.

The additional requirements for passive materials for high frequency applications are related to the ultrasound wavelength. The filler particle size must be sufficiently smaller than the wavelength for diffusive scattering to occur and the matching layer thickness is optimal at ¼ wavelength, which can be approximately 10μm at 50MHz. Therefore there are additional fabrication issues for high frequency passive materials. The use of nanoparticles as matching filler has been reported recently but fabrication issues with dispersion and agglomeration still need to be optimised.

CHAPTER 3

Wave Propagation and Acoustic Measurement Techniques

3.1 Propagation of sound: Velocity and Attenuation

As mentioned in the previous Chapter, the key properties for transducer passive materials are acoustic impedance and attenuation. Acoustic impedance is the product of velocity and density, therefore both impedance and attenuation can be determined by measuring the velocity and attenuation of an ultrasound wave through a material of known density. This Chapter will present the theory of sound propagation through a medium showing how velocity and attenuation can be calculated, and various acoustic measurement techniques will be reviewed. As mentioned previously the speed of ultrasound is constant in a medium and it is determined by the elastic properties of that medium, its modulus and density. [77]

The main mechanisms of attenuation are based on scattering and absorption. Scattering decreases ultrasonic intensity by redirecting the energy of the beam. Scattering occurs when interfaces are small, with dimensions approximately the same size or smaller than the ultrasound wavelength. Each interface effectively acts as a new sound source as the sound is reflected in all directions independent of the direction of the original wave. Scattering by particles much smaller than the wavelength is called Rayleigh (diffusive) scattering; this has a strong frequency dependence which makes it useful for tissue characterisation, as other types of reflections do not have a frequency dependence.

Absorption is the process where ultrasonic energy is transformed into other energy forms, mainly heat, and it is the only process where sound energy is dissipated in a material. It is influenced by the ultrasound frequency and the viscosity and relaxation time of the material. The relaxation time describes the rate at which molecules return

to their original positions after being displaced; if a material has short relaxation time the molecules return to their original position before the compression phase of the next wave.[1] In a material with a long relaxation time the molecules are still moving when the compression phase of the next wave arrives, so more energy is required to stop and reverse the direction of the molecules, thereby producing more heat. Viscosity also has an effect, so a highly viscous fluid has more absorption than a low viscosity fluid. Frequency affects absorption in relation to both relaxation time and viscosity; when the frequency is increased the molecules move more often generating more heat from the drag caused by friction (viscosity). There is also less time between waves for the molecules to recover in the relaxation process so the molecules remain in motion and more energy is necessary to stop and redirect them, producing more absorption.

Attenuation includes scattering and absorption in describing how the amplitude of a wave is reduced as it propagates through a material. [93] As the frequency is increased the attenuation increases so consequently the intensity of the ultrasound decreases with increasing distance, which is why the depth of penetration in medical imaging is reduced as the operating frequency increases.

A common method to measure the key acoustic properties of acoustic impedance and attenuation is to first determine the time of flight through a material to calculate velocity. [94,95] The amplitude of a pulse transmitted through the sample is compared to a pulse without the sample in place. The transmitted signal is then corrected for reflection losses at any interfaces to determine the attenuation.

3.2 Potential Characterisation Methods

Ultrasonic measurement methods for characterising materials are well established and there are a number of different techniques possible using both continuous wave and pulsed systems, as reviewed by McSkimmin for pulsed waves [96] and Bolef and De Klerk for continuous wave methods. [97] A pulsed system is the most appropriate characterisation technique for transducer materials as this technique is used in medical imaging. Continuous wave methods have disadvantages including being subject to errors due to reflections, mode conversions or other interfering signals [98] and they also tend to be time consuming. A broadband pulse technique offers a more attractive approach as the transmitted pulse can be isolated in the time domain from unwanted signals, such as reflections and reverberations. The experimental technique is relatively simple and Fourier analysis can be performed quickly to determine velocity and attenuation. [99]

The pulsed method can be used with a reverberation path using one transducer device as a transmitter and receiver or a through technique using two separate devices acting as a transmitter and a receiver. [100] These techniques will be discussed and the relative merits and disadvantages identified.

3.2.1 Reverberation Method

3.2.1.1 Underwater Configuration

The reverberation method as described by Selfridge [69] allows the longitudinal velocity and attenuation to be measured. In this method a single transducer acts as a transmitter and receiver; it is positioned normal to the sample surface and the distance between the transducer and sample is chosen so that the transit time of an ultrasonic

pulse between the transducer and sample is about four to five times the transit time though the sample, as illustrated in Figure 3.1. [69] The transducer is then excited in a pulse or toneburst mode and a train of echoes due to the reverberation of ultrasound in the sample and the water path between the sample and transducer should be observed.

The received echoes are shown in Figure 3.2; the pulses labelled A_1, A_2, A_3 and A_4 are due to the wave that has travelled once through the water between the sample and specimen. A_1 is due to the reflection off the front face of the sample, A_2 is due to the reflection off the back face of the sample and A_3 and A_4 are due to reverberations within the sample.

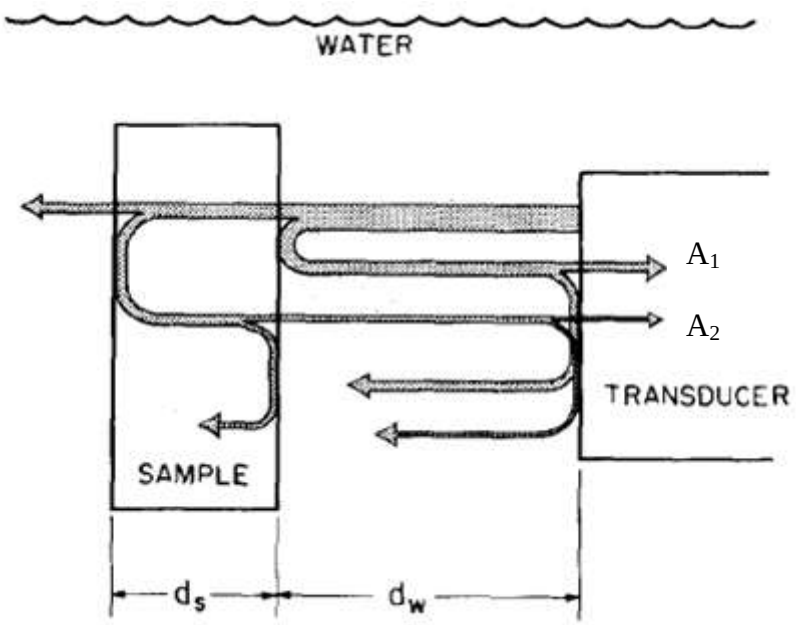

Figure 3.1 *Illustration of reverberation paths, from Selfridge pulse-echo characterisation method* [69]

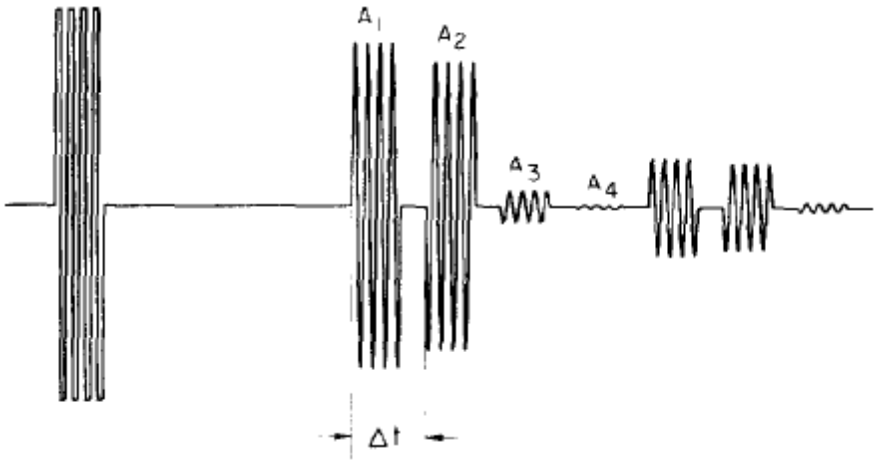

Figure 3.2 *Measurement signal showing received echoes from Selfridge pulse-echo method* [69]

This method was used by Selfridge to determine the longitudinal wave properties of a number of different materials. The longitudinal velocity is calculated by

$$V_L = \frac{2d}{\Delta t} \qquad \textbf{Equation 3.1}$$

where d is the thickness of the sample and Δt is the time between the signals reflected from the front and back faces of the sample.

The attenuation is determined by calculating what the relative amplitudes of A_2/A_1 should be with no loss in the sample by looking at transmission and reflection coefficients. The reflection coefficient, R is given by

$$R = \frac{Z_s - Z_w}{Z_s + Z_w} \qquad \textbf{Equation 3.2}$$

where Z_s is the acoustic impedance of the sample and Z_w is the acoustic impedance of water.

The amplitude of the transmitted wave into the sample at the front face is given by T_1

$$T_1 = \frac{2Z_S}{Z_S + Z_W} = 1 + R \qquad \textbf{Equation 3.3}$$

When this portion of the ultrasound reaches the back face some is reflected back into the sample and some is transmitted into the water. The reflection coefficient at the back face is –R and the transmission coefficient T_2 is given by

$$T_2 = \frac{2Z_W}{Z_S + Z_W} = 1 - R \qquad \textbf{Equation 3.4}$$

The calculated ratio between A_2 and A_1 without any loss is given by

$$\text{calculated}\frac{A_2}{A_1} = T_1 \times T_2 = 1 - R^2 \qquad \textbf{Equation 3.5}$$

Therefore the actual loss in the sample is found by comparing the measured ratio to the calculated ratio as in

$$\text{Loss in dB/m} = 20\log\left(\frac{Calculated\frac{A_2}{A_1}}{Measured\frac{A_2}{A_1}}\right)/2d \qquad \textbf{Equation 3.6}$$

This method is quite a simple method of determining longitudinal wave velocity and attenuation and has been used to characterise various materials by Selfridge and other researchers, [87] including some of the materials shown in Table 2.2. The main disadvantage of this technique is that shear waves cannot be characterised in this configuration. Shear waves are generated when longitudinal waves are incident on a boundary at an oblique angle so shear wave properties are generally more important for matching materials than for backing as piezocomposite active materials primarily use the thickness mode and lateral resonances are suppressed. However, both longitudinal and shear waves propagate through solids and determining both mode properties will fully characterise the material.

3.2.1.2 Direct Contact Configuration

The analysis from Selfridge [69] described in the previous section is valid for underwater experiments where water is used as the coupling medium. It is also possible to perform similar reverberation experiments using direct contact of the transducer and sample with the aid of an appropriate acoustic couplant, [101] as shown in Figure 3.3. The acoustic mismatch between the sample and air is greater than with water so a couplant is required with a strong physical contact between the transducer and sample.

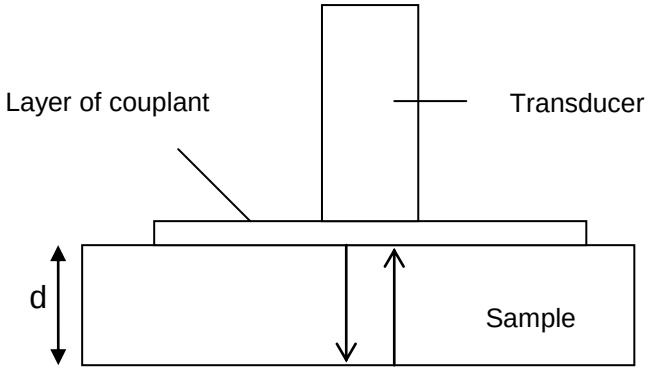

Figure 3.3 *Diagram of direct contact method where a couplant is used to help transfer the ultrasonic energy between the transducer and sample material*

The longitudinal velocity and attenuation can then be calculated as shown previously with Equations 3.1 and 3.6 respectively.

This method can be used to generate both longitudinal and shear waves within a sample material, but different experimental arrangements are required using different transducers as a shear transducer is required to generate shear waves. A technique where one experimental arrangement can be used to measure the velocity and attenuation of both wave modes would be more suitable for the characterisation of materials. Additionally, another disadvantage of both these reverberation methods is

that the wave has to travel through the sample twice. The sample must be thick enough that the reflections from both faces can be easily distinguished in the time domain, but thin enough so that the signal is not lost completely in very lossy (attenuative) materials.

3.3 Non-Contact Through-Transmission Method

A suitable approach for the acoustic characterisation of materials is a non-contact through-transmission method. This technique uses two devices, a transmitter and a receiver, separated by a coupling medium i.e. water. A sample is positioned between these devices and both longitudinal and shear waves can be excited in the sample material by rotating the sample and therefore adjusting the angle of incidence. The following sections will show how the velocity and attenuation can be determined using this method. The analysis will start with the situation of normal incidence where only longitudinal waves propagate through the sample. Then it will be shown how adjusting the angle of incidence results in mode conversion so both longitudinal and shear waves are transmitted through the sample material enabling shear wave properties to also be analysed.

3.3.1 Determination of Longitudinal Velocity at Normal Incidence

The longitudinal velocity through a material can be determined by measuring the time of flight of a reference signal in water and then measuring the signal through the sample and water in a non-contact transmission mode; the time difference between the two signals can be used to calculate the velocity.

Consider two transducers set up to transmit and receive an ultrasound signal a distance D apart in water as shown in Figure 3.4. When a sample of thickness d is placed between the transducers the transmitted signal will arrive at a different time to the reference signal in water, depending on the speed through the sample and its thickness.

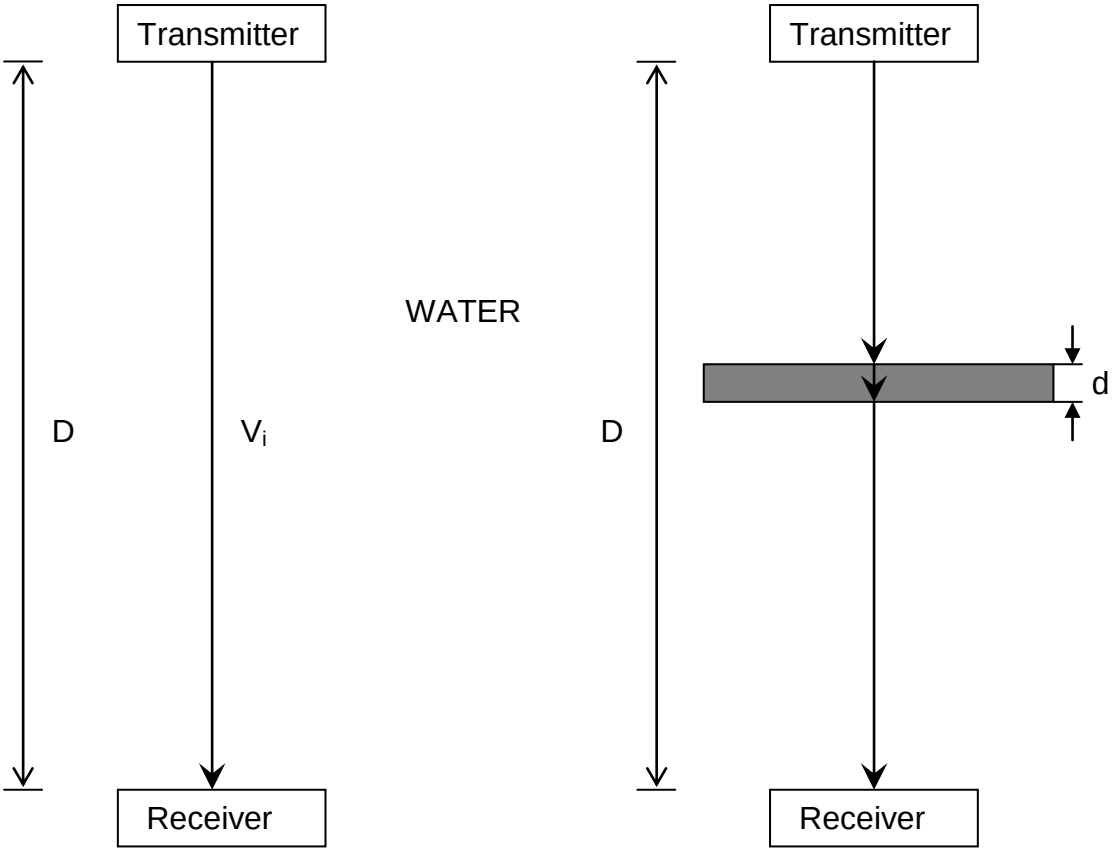

Figure 3.4 *Diagram of through transmission technique under normal incidence with and without sample present*

The time difference between the two signals, Δt, is determined such that it is positive when the transmitted signal arrives before the reference signal and negative when the transmitted signal is later than the reference signal. The analysis to calculate the longitudinal velocity V_L just has to consider the propagation through the sample, of

length d, and compare it to the reference signal propagation through the same distance of water, so the distance D does not need to be known. Velocity is calculated by distance/time and the velocity through distilled water is taken as 1483ms^{-1} at 20°C. [76] Therefore the time taken for the reference signal to travel distance d through water can be calculated as

$$t_w = \frac{d}{V_i}$$ **Equation 3.7**

and the time for the transmitted signal to travel distance d through the sample is

$$t_s = \frac{d}{V_i} - \Delta t$$ **Equation 3.8**

so the velocity V_L through the sample is found with Equation 3.9.

$$V_L = \frac{d}{\left(\frac{d}{V_i}\right) - \Delta t}$$ **Equation 3.9**

O'Leary also derived the same equation for the longitudinal velocity through the sample by considering the whole path length of the transmitted and reference waves, D. [101]

3.3.2 Calculating Time of Flight, Δt

The time difference between the two signals, Δt, can be measured by inspection of the pulses and finding the difference in arrival times. However, different times can be recorded depending on the experimental criteria used resulting in a variation in the calculated velocity. [98] The pulse can change shape when transmitted through the material, especially in lossy (highly attenuative) materials, so it can be difficult to assess the arrival time accurately and the process can become somewhat subjective.

Three different criteria for assessing the transit time have been presented, [98] as shown in Figure 3.5 and are as follows;

1. **first arrival -** in which the time marker is placed at the point of first apparent deviation from the horizontal (time) axis
2. **thresholding -** in which the amplitude of the first half cycle of the received wave is measured and the time marker positioned at a point on the rising edge of the signal corresponding to 10% of that amplitude
3. **first zero crossing –** in which the time marker is placed at the point where the received waveform first crosses the time axis

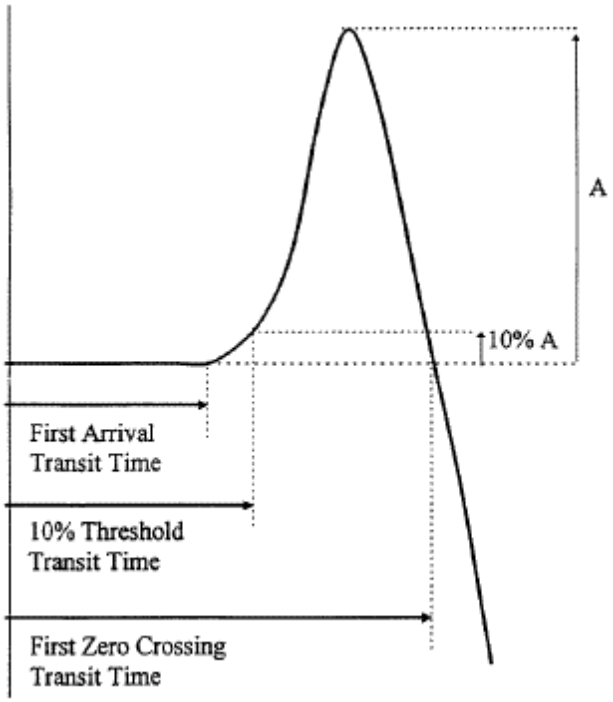

Figure 3.5 *Different criteria suggested to assess the arrival time of ultrasound pulses by Nicholson et al* [98]

These different criteria result in highly significant differences in the calculated velocities, which mean it is important to state which technique and criteria are used. The three criteria presented here still involved some subjective assessment and therefore results obtained with these criteria could differ.

Another mathematical analysis has been used to determine the transit time with the cross correlation function in MATLAB (Mathworks Inc., MA). This approach is preferred to other criteria such as threshold detection, as it has been shown to be more accurate and performs better in low signal to noise ratio environments, especially in highly attenuative materials. [101]

In this technique the reference signal (with no sample present) and the transmitted signal are compared. The signals are made the same length, so that the entire transmitted signal can be correlated against the entire reference signal. In the correlation algorithm the sum of the product of the two signal vectors is found before the transmitted signal is moved along the time axis by one discretisation point and the sum of the product of the two signals calculated again. The point of maximum correlation is equal to the number of discretisation points the transmitted signal has been shifted to overlap with the reference signal. This is found using the MATLAB syntax:

$$[x\ y] = \max(corr) \qquad \textbf{Equation 3.10}$$

where y is the number of discretisation points the signals were moved relative to each other to obtain maximum correlation and corr is the vector describing the correlation function in MATLAB. The corresponding time difference between the signals, Δt, is then calculated with

$$\Delta t = refdelay - txdelay + [timestep\ (y-2000)] \qquad \textbf{Equation 3.11}$$

where refdelay is the first time point of the reference signal, txdelay is the first time point of the transmitted signal, timestep is the time difference between adjacent data points in the recorded signals and 2000 is the number of points in the recorded signals. The longitudinal velocity can then be calculated using Equation 3.9.

An example of the correlation technique is shown in Figure 3.6. The blue line in Figure 3.6a shows the reference signal and the black line shows the transmitted signal through a 2.5cm thick block of Perspex®. The transmitted signal arrives before the reference signal and the amplitude is reduced. Figure 3.6b shows the correlated signals when the transmitted signal has been shifted along the time axis by Δt, calculated with Equation 3.11. The accuracy of the correlation technique depends on the timestep of the recorded signals and if this is small it is much more reliable than other more subjective techniques

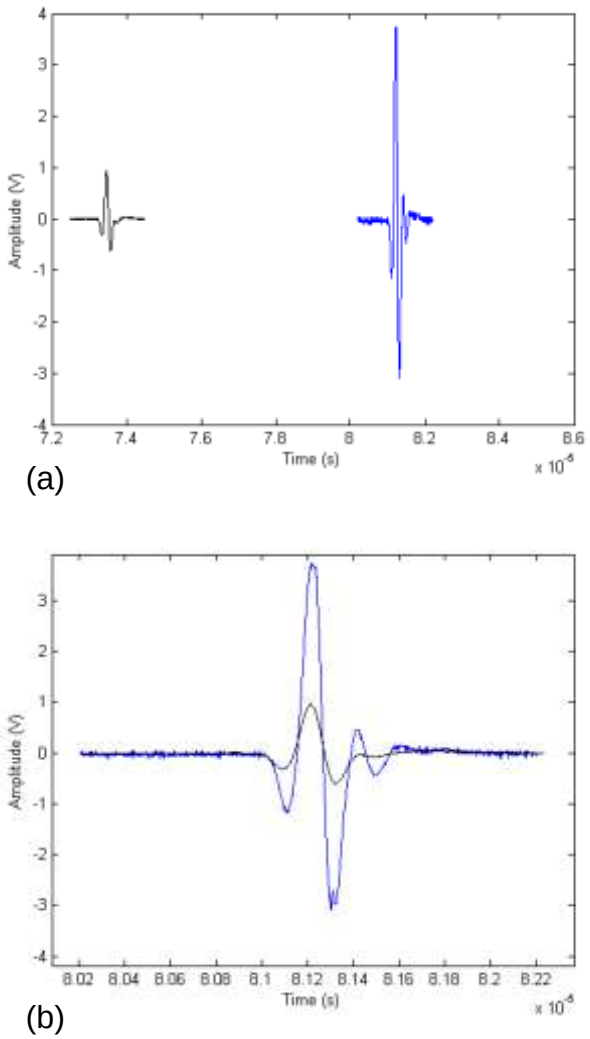

Figure 3.6 *(a) Transmitted and reference signals through a 2.5cm thick sample of Perspex® at normal incidence (b) Correlated signals after calculating Δt. Blue line depicts reference signal and the black line depicts the transmitted signal*

3.3.3 Calculating Longitudinal Attenuation

As attenuation is related to the loss in intensity of an ultrasound wave as it propagates through a material, the same type of measurement to calculate the velocity can be done to determine the attenuation, only with the amplitudes of the signals now compared. Transmission coefficients have to be considered when calculating the attenuation as some ultrasonic intensity will be lost via reflection when transmitted through a material; the remainder is due to attenuation in the material. The fractions of ultrasound energy reflected and transmitted at the sample-water interface are related to the acoustic impedance of each material so when the velocity and hence acoustic impedance of the sample (found by multiplying calculated velocity with measured density) has been determined, the attenuation, α, in dB/mm can be calculated with Equation 3.12.

$$\alpha_l = \log\left(\frac{T_L A_w}{A_S}\right) / d \qquad \textbf{Equation 3.12}$$

where A_w is the amplitude of the reference signal through water, A_S is the amplitude of the transmitted signal through the sample, d is the sample thickness in mm and the total longitudinal transmission coefficient, T_L, through both interfaces of the sample is

$$T_L = \frac{4 Z_w Z_L}{(Z_w + Z_L)^2} \qquad \textbf{Equation 3.13}$$

where Z_w is the acoustic impedance of the wave in water and Z_L is the longitudinal acoustic impedance of the wave in the sample material. The derivation of T_L is shown in Appendix 1.

3.3.4 Oblique Incidence

The previous discussion has only considered ultrasonic pulses at normal incidence to the sample, therefore only longitudinal waves are transmitted for characterisation. Isotropic solids are capable of propagating more than one wave mode, including longitudinal and shear wave modes. Under suitable conditions of oblique incidence, mode conversion occurs at the boundary, resulting in propagation of a longitudinal and a shear wave into the sample. Since fluids cannot generally support shear wave propagation, only a longitudinal wave is reflected back from the interface into the fluid as shown in Figure 3.7. The angle between the incoming wave and the normal to the first interface is labelled θ_i, and the transmission angles of the longitudinal and shear waves in the solid are θ_L and θ_S respectively. These angles are then the incident angles for the next interface and the transmitted waves emerge at angles θ_{LL} and θ_{LS} to the normal of the second interface and are each a longitudinal wave in the fluid, one generated from the transmission of the longitudinal wave and the other a longitudinal wave converted from the transmitted shear wave as shown in Figure 3.7 where the solid lines depict longitudinal waves and the dashed lines represent shear waves.

The angles and wave velocities are related by Snell's Law:

$$\frac{V_i}{\sin\theta_i} = \frac{V_L}{\sin\theta_L} = \frac{V_S}{\sin\theta_S} \qquad \textbf{Equation 3.14}$$

where V_S is the velocity of shear waves in the material.

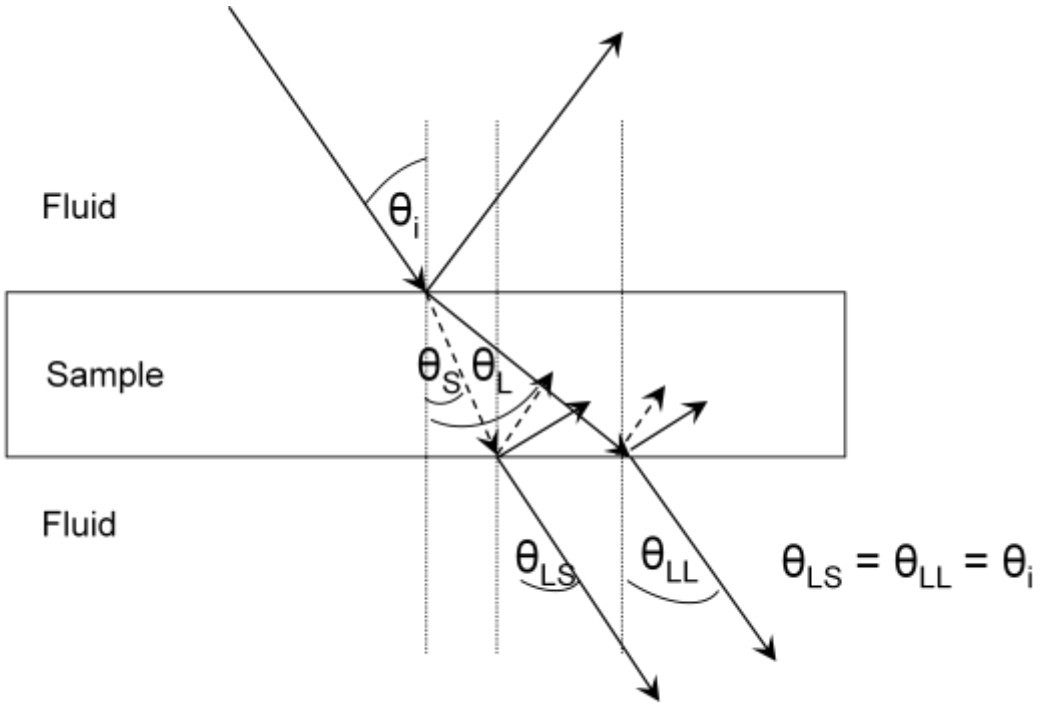

Figure 3.7 *Diagram of mode conversion at oblique incidence. Solid lines depict longitudinal waves, dashed lines depict shear waves*

There are two critical angles of incidence where waves are refracted along the surface of the sample. Normal incidence ($\theta_i = 0$) results in propagation of longitudinal wave modes only in the sample. Changing the value of θ_i to the first critical angle θ_{c1} causes total refraction of the longitudinal wave mode along the surface of the sample so θ_L is 90° and only a shear wave mode propagates through the sample. θ_{c1} is defined by

$$\theta_{c1} = \sin^{-1}\frac{V_i}{V_L} \qquad \textbf{Equation 3.15}$$

Increasing θ_i to the second critical angle θ_{c2} causes total refraction of the shear wave so all the ultrasonic energy propagates along the surface of the sample in the form of a Rayleigh wave. θ_{c2} is defined by

$$\theta_{c2} = \sin^{-1}\frac{V_i}{V_S}$$ **Equation 3.16**

When V_i is greater than V_L the first critical angle is not reached and the shear wave is not refracted into the material and when V_i is greater than V_S the second critical angle is not observed.

Based on these principles it is possible to excite longitudinal and shear modes separately in the sample and perform time of flight measurements to determine longitudinal and shear velocity, V_L and V_S. Alternatively the velocities can be determined by measuring the critical angles. The rotation of the sample must be very accurate to determine the velocities from critical angles. There is also a subjective element when determining when the signal amplitude is equal to zero; this will depend on the signal-to-noise ratio.

3.3.5 Shear Wave Velocity Determination at Oblique Incidence

The analysis to determine shear velocity is more complex than the longitudinal analysis as the path length under oblique incidence is not the sample thickness, and the measurement of Δt is more complex due to the difference in the distances travelled by the reference signal transmitted through the fluid alone and the transmitted signal transmitted through the fluid and the sample. An analysis for determining Δt for shear wave propagation at oblique incidence has been presented by O'Leary [101] and expressions to calculate the shear velocity have been published by Wang et al [86] and Wu. [102]

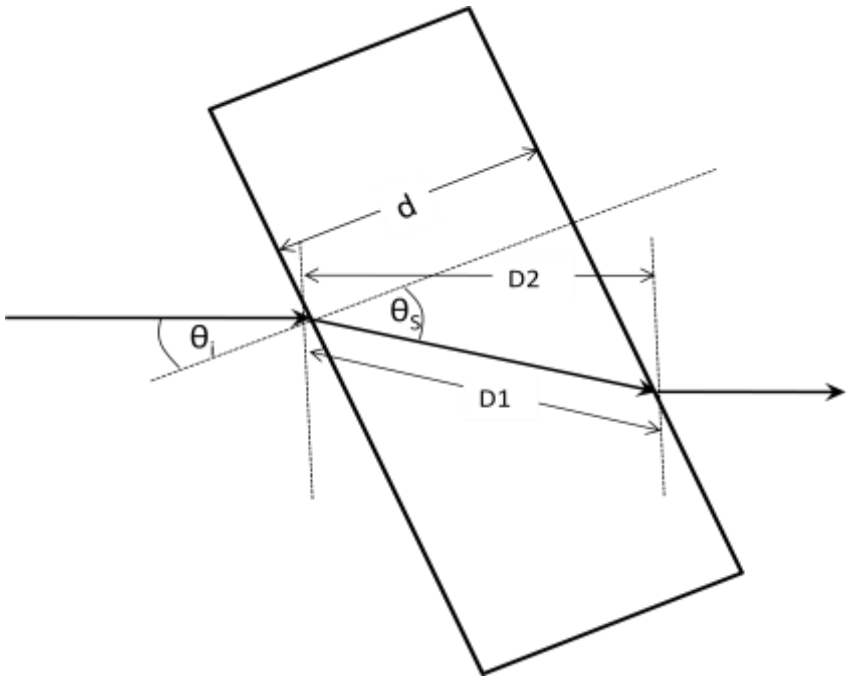

Figure 3.8 *Diagram showing geometry used to determine shear wave path length, from O'Leary.* [101] *D1 is distance shear wave travels through sample and D2 is the equivalent distance the reference signal would travel without the sample present*

Consider the situation shown in Figure 3.8 where a shear wave is propagated in a sample of thickness d. The distance the shear wave travels in the sample is D1 and the distance the reference signal would travel without the sample present is D2. D1 is found with

$$D1 = \frac{d}{\cos\theta_S} \qquad \textbf{Equation 3.17}$$

The time t_1 for the wave of velocity V_S to travel distance D1 is

$$t_1 = \frac{d}{V_S \cos\theta_S} \qquad \textbf{Equation 3.18}$$

The distance the reference signal would travel when the sample is replaced with fluid, D2, is found with

$$D2 = D1\cos\left(\theta_S - \theta_i\right)$$
$$D2 = \frac{d\cos\left(\theta_S - \theta_i\right)}{\cos\theta_S} \qquad \textbf{Equation 3.19}$$

The time t_2 for a wave of velocity V_i to travel distance D2 is

$$t_2 = \frac{d\cos(\theta_S - \theta_i)}{V_i \cos\theta_S} \qquad \textbf{Equation 3.20}$$

And the time difference Δt, between the reference signal and the transmitted shear wave is then found by

$$\Delta t = t_1 - t_2 = d\left[\frac{\cos(\theta_S - \theta_i)}{V_i \cos\theta_S} - \frac{1}{V_S \cos\theta_S}\right] \qquad \textbf{Equation 3.21}$$

giving an expression for the time of flight through the sample at oblique incidence similar to that for normal incidence. However there is more than one unknown so substitutions from Snell's Law must be used.

From Snell's Law

$$\sin\theta_S = \frac{V_S \sin\theta_i}{V_i} \qquad \textbf{Equation 3.22}$$

$$\cos^2\theta_S = 1 - \frac{V_S{}^2 \sin^2\theta_i^2}{V_i^2} \qquad \textbf{Equation 3.23}$$

and from trigonometry

$$\cos(\theta_S - \theta_i) = \cos\theta_S \cos\theta_i + \sin\theta_S \sin\theta_i$$

$$\cos(\theta_S - \theta_1) = \cos\theta_i \sqrt{1 - \frac{V_S{}^2 \sin^2\theta_i^2}{V_i{}^2}} + \frac{V_S \sin^2\theta_i^2}{V_i} \qquad \textbf{Equation 3.24}$$

Therefore making substitutions into Equation 3.21 gives an expression for Δt where there is only one unknown.

$$\Delta t = d\left[\frac{\cos\theta_i \sqrt{1 - \frac{V_S{}^2 \sin^2\theta_i^2}{V_i^2}} + \frac{V_S \sin^2\theta_i^2}{V_i}}{V_i \sqrt{1 - \frac{V_S{}^2 \sin\theta_i^2}{V_i^2}}} - \frac{1}{V_S \sqrt{\frac{V_S{}^2 \sin\theta_i^2}{V_i^2}}}\right]$$

Equation 3.25

This expression for Δt is used here with an iterative approach to determine the shear velocity as described by O'Leary [101] or it can be rearranged to give an expression for V_S as reported by Wang et al [57] and Wu. [102] These researchers have reported using the phase difference between the two signals instead of the time difference to calculate velocity with Equation 3.26.

$$V_S = \frac{V_i}{\sqrt{\sin^2\theta_i + \left[\frac{V_i(\phi_S - \phi_W \pm 2m\pi)}{2\pi f d} + \cos\theta_i\right]^2}} \qquad \textbf{Equation 3.26}$$

Where Φ_S is the phase of the signal transmitted through the sample and Φ_W is the phase of the reference signal through water. The expression ±2mπ is to account for the ambiguity of the phase spectrum calculated from the arctangent function where m is an integer. The time difference can be obtained from the phase difference of two sine waves as follows:

$$\Delta t = \Delta\phi \times \frac{\Gamma}{2\pi} \qquad \textbf{Equation 3.27}$$

Where ΔΦ is the phase difference in radians and Γ is the period of the wave in seconds. The period is the reciprocal of frequency (Γ = 1/f)

Therefore the expression $\frac{\phi_S - \phi_W \pm 2m\pi}{2\pi f}$ in Equation 3.26 is equivalent to -Δt calculated with the cross correlation described in Section 3.3.2 and the shear velocity V_S can be found using Equation 3.28.

$$V_S = \frac{V_i}{\sqrt{\sin^2\theta_i + \left[\frac{-\Delta t V_i}{d} + \cos\theta_i\right]^2}} \qquad \textbf{Equation 3.28}$$

3.3.6 Transmission Coefficients at Oblique Incidence

The attenuation of both longitudinal and shear waves can be determined with an analysis of the relative amplitudes of the incident and transmitted waves compared to transmission coefficients. The analysis of the situation shown in Figure 3.7 must be broken down so each interface, fluid-solid and solid-fluid is analysed separately.

3.3.6.1 Fluid-Solid Interface

As illustrated in Figure 3.7, when a sound wave is incident from a fluid upon a fluid-solid interface at an angle θ_i, a longitudinal wave and a mode converted shear wave are transmitted through the solid and a longitudinal wave is reflected back into the fluid. The proportions of the magnitude of the original sound wave that are reflected or transmitted as longitudinal or shear waves are found with transmission and reflection coefficients and are related to the acoustic impedances of the fluid and the solid. The transmission coefficients T_{L1} and T_{S1} of the refracted longitudinal and shear waves respectively can be found with the Equations 3.29 and 3.30 derived by Brekhovskikh [103]

$$T_{L1} = \frac{\rho}{\rho_1} \frac{2Z_L \cos 2\theta_S}{Z_L \cos^2 2\theta_S + Z_S \sin^2 2\theta_S + Z} \qquad \textbf{Equation 3.29}$$

$$T_{S1} = -\frac{\rho}{\rho_1} \frac{2Z_S \sin 2\theta_S}{Z_L \cos^2 2\theta_S + Z_S \sin^2 2\theta_S + Z} \qquad \textbf{Equation 3.30}$$

where Z is the acoustic impedance of the fluid, Z_L and Z_S are the acoustic impedances associated with the longitudinal and shear waves respectively and ρ and ρ_1 are the densities of the fluid and the solid respectively. The derivation of these equations is given in Appendix 1. It can be shown from Equation 3.30 that no shear wave is transmitted into the solid at normal incidence, when θ_i is equal to zero.

3.3.6.2 Solid-Fluid Interface

Solid materials support both longitudinal and shear wave propagation. O'Leary [101] has shown that the total transmission coefficients for each wave mode can be calculated by combining the transmission coefficients at each interface given by Brekhovskikh. The two wave types will be now analysed separately to determine the transmission coefficients for the solid-fluid interface and hence the total combined coefficients across both interfaces.

3.3.6.2.1 Longitudinal Wave Incident at Solid-Fluid Interface

The longitudinal wave impinging on the solid-fluid interface results in three waves: reflected longitudinal and (mode converted) shear waves and a refracted longitudinal wave, as shown in Figure 3.9. The angle of refraction of the longitudinal wave transmitted into the fluid is equal to the angle of incidence of the original wave incident onto the solid.

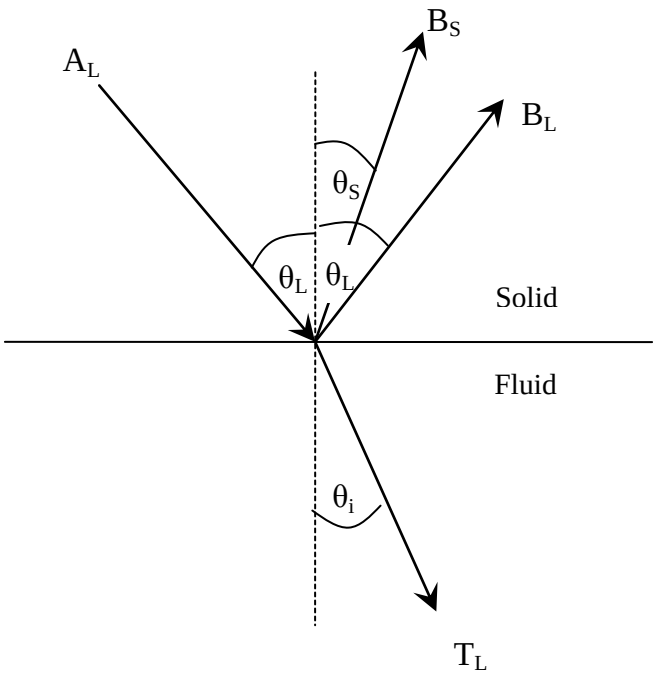

Figure 3.9 *Oblique incidence of a longitudinal wave at a solid-fluid interface*

The wave amplitudes are labelled A_L, B_L, B_S and T_L for the incident longitudinal wave, the reflected longitudinal wave, the reflected shear wave and the refracted (transmitted) longitudinal wave respectively. The amplitude of the incident longitudinal wave, A_L is described by T_{L1} in Equation 3.29, and the total longitudinal transmission coefficient, T_L can be written as

$$T_L = T_{L1}\frac{V_i \cos\theta_L}{V_L \cos\theta_i \cos^2 2\theta_S}\left(1-\frac{Z+Z_S \sin^2 2\theta_S - Z_L \cos^2 2\theta_S}{Z+Z_S \sin^2 2\theta_S + Z_L \cos^2 2\theta_S}\right) \quad \textbf{Equation 3.31}$$

3.3.6.2.2 Shear Wave Incident at Solid-Fluid Interface

Figure 3.10 illustrates the shear wave incident from a solid onto the solid-fluid interface. As before, three waves result: a reflected shear wave, a reflected longitudinal wave and a refracted longitudinal wave.

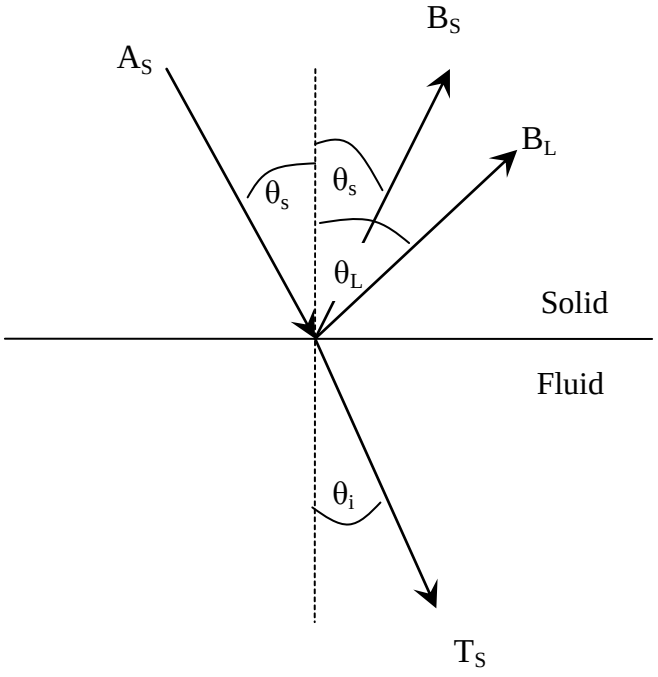

Figure 3.10 *Oblique incidence of a shear wave at a solid-fluid interface*

The wave amplitudes are labelled A_S, B_S, B_L and T_S for the incident shear wave, the reflected shear wave, the reflected longitudinal wave and the refracted (transmitted) longitudinal wave respectively. As in the analysis of the longitudinal wave, the amplitude of the shear wave incident on the solid-fluid interface can be considered to be T_{Sl}, defined in Equation 3.30, and the total shear transmission coefficient, T_S, can be written as

$$T_S = T_{S1}\frac{\tan\theta_i}{2\sin^2\theta_S}\left(1-\frac{Z+Z_L\cos^2 2\theta_S - Z_S\sin^2 2\theta_S}{Z+Z_L\cos^2 2\theta_S + Z_S\sin^2 2\theta_S}\right)$$

Equation 3.32

In this situation the specific acoustic impedances are used:

$$Z = \frac{Z_{water}}{\cos\theta_i}$$
$$Z_L = \frac{Z_{longitudinal}}{\cos\theta_L}$$
$$Z_S = \frac{Z_{shear}}{\cos\theta_S}$$

Equation 3.33

The derivations of the transmission coefficients T_L and T_S in Equations 3.31 and 3.32 are shown in Appendix 1.

3.3.7 Transmission Coefficients as a Function of Incident Angle

Using Equations 3.31 and 3.32 the longitudinal and shear transmission coefficients can be plotted against the incident angle to illustrate the critical angles and transmission of the waves through the solid in the non contact through transmission method considered here.

The longitudinal and shear transmission coefficients have been plotted as a function of the angle of incidence for a sample of CY1301/HY1300 hard setting epoxy with water as the coupling medium as shown in Figure 3.11. The data was plotted using Equations 3.31 and 3.32 with incident angles up to 90° using material parameters as follows; ρ =1.149g/cm^3, V_L =2500m/s, V_S =1170m/s, taken from CUE materials database, University of Strathclyde [104]. Figure 3.11b illustrates the description of the critical angles discussed previously. The longitudinal transmission coefficient is equal to zero at the first critical angle, θ_{c1}, where θ_L is equal to 90° and the energy of the longitudinal wave is reflected along the surface of the epoxy sample. Similarly, the shear wave transmission is zero at the second critical angle, θ_{c2}. In the example shown in Figure 3.11 it would not be possible to observe θ_{c2} experimentally as $\frac{V_i}{V_S} > 1$, and θ_{c2} is greater than 90°. Coupling with other mediums, such as air, would allow θ_{c2} to be experimentally observed. [101]

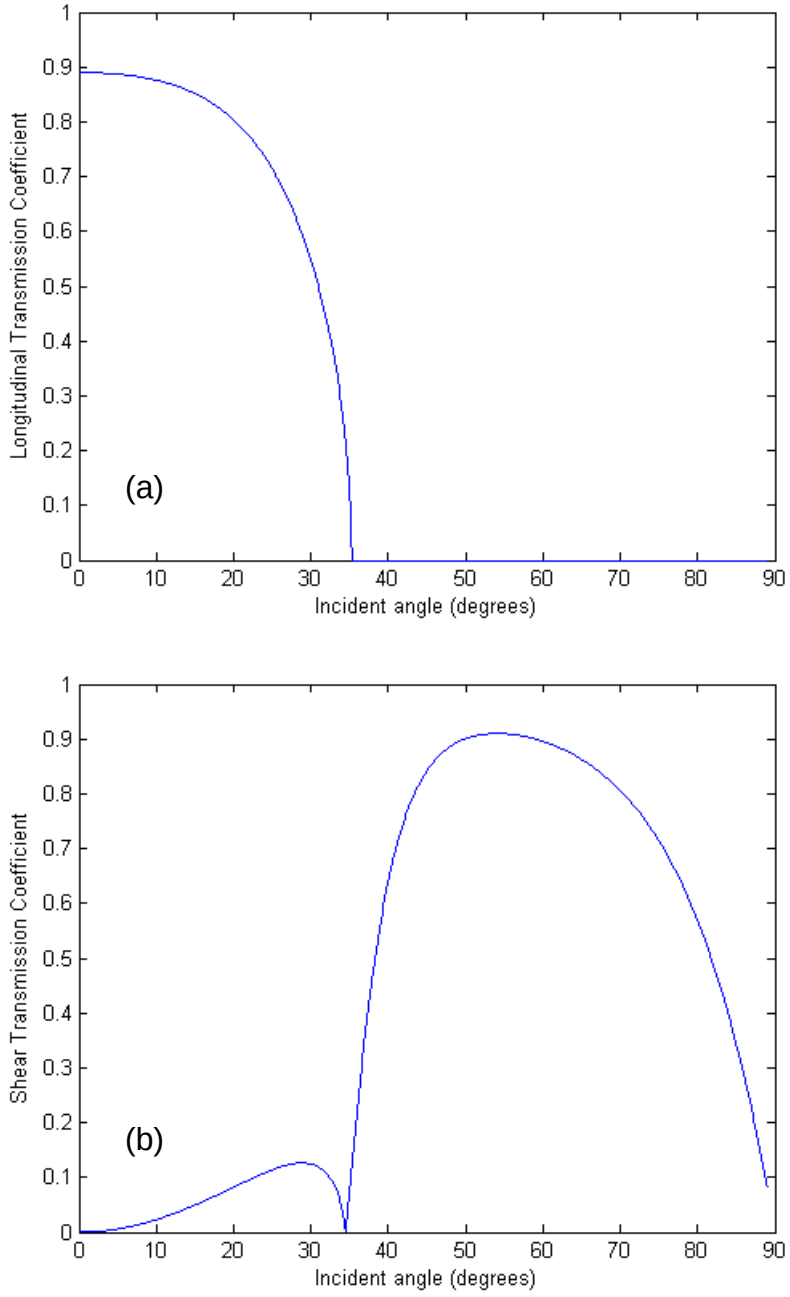

Figure 3.11 *Transmission coefficients for CY1301/HY1300 epoxy at oblique incidence (a) longitudinal wave calculated with Equation 3.31(b) shear wave calculated with Equation 3.32*

3.3.8 Determination of attenuation as a function of incidence angle

The analysis discussed in the previous section can be used to calculate the losses due to reflection and transmission at the interfaces; attenuation has not yet been considered. The transmission coefficients shown represent only the losses due to reflection and mode conversion and attenuation has been ignored. The transmitted waves propagating through the material are attenuated by the mechanisms described previously resulting in a reduction in energy of the waves. To deal with this mathematically it is possible to modify Equations 3.31 and 3.32 to include attenuation as an exponential loss term: [101]

$$T_L = T_{L1} \exp\left(\frac{-\alpha_L d}{\cos\theta_L}\right) \cdot \frac{V_i \cos\theta_L}{V_L \cos\theta_i \cos^2 2\theta_S} \left(1 - \frac{Z + Z_S \sin^2 2\theta_S - Z_L \cos^2 2\theta_S}{Z + Z_S \sin^2 2\theta_S + Z_L \cos^2 2\theta_S}\right)$$

Equation 3.34

$$T_S = T_{S1} \exp\left(\frac{-\alpha_S d}{\cos\theta_S}\right) \cdot \frac{\tan\theta_i}{2\sin^2 \theta_S} \left(1 - \frac{Z + Z_L \cos^2 2\theta_S - Z_S \sin^2 2\theta_S}{Z + Z_L \cos^2 2\theta_S + Z_S \sin^2 2\theta_S}\right)$$

Equation 3.35

where α_L and α_S are the attenuation factors in nepers per metre of the longitudinal and shear waves respectively at a specific frequency (the neper describes a logarithmic loss in amplitude due to attenuation and is equivalent to -8.686dB). Therefore the attenuation factors can be determined by calculating the relative amplitudes of the signals with and without the sample and comparing to the theory in Equations 3.34 and 3.35 via curve fitting.

3.4 Summary and Experimental Considerations

A number of techniques to measure the velocity and attenuation of ultrasonic waves through material samples have been introduced and discussed. A pulsed wave technique is probably the most appropriate in this work as it is the technique used in medical imaging and it is relatively easy to use in pulse echo and transmitted wave modes and the reflected or transmitted pulse can be easily isolated from other unwanted signals. A transmitted wave technique has advantages over a pulse-echo or reverberation method as the wave only has to travel through the sample once so highly attenuative materials can be characterised easily. Direct contact methods require a strong physical contact between the sample and transducer with a suitable couplant, therefore underwater set-ups where water is the coupling medium and no contact is needed may be a better approach. If the sample can be rotated relative to the transmitting transducer shear waves can be excited in the material, so both longitudinal and shear waves can be characterised using the same experimental set-up and transducers.

Therefore the non-contact through transmission technique described in this chapter is the most appropriate way to characterise the acoustic properties of material samples at high frequencies as the same experimental set up can be used to determine both longitudinal and shear wave properties by simply rotating the sample between the transmitter and receiver. Important practical considerations are:

- **Velocity in Water (V_i)** – A method of measuring the speed of ultrasound in water must be incorporated into the technique so the calculations can be done accurately.

- **Incident Angle (θ_i)** – Accurate angular resolution of the rotation of the sample is required to determine shear velocity and attenuation accurately.
- **Sample Geometry** – The sample surfaces must be flat and have parallel sides to measure the time of flight correctly. Selfridge [69] has suggested that the sample should have a thickness approximately ten times the wavelength and lateral dimensions at least ten times the thickness. It may be necessary to have thinner samples than this in the case of highly attenuative materials so a transmitted signal is observed, but it is important that the transmitted longitudinal and shear waves can be isolated in the time domain and they can be differentiated from internal reflections in the sample.
- **Lateral Movement of Transmitter/Receiver** – Figure 3.7 shows the ultrasound being refracted in the sample so that the beam exiting the sample is not in line with the incident beam. Therefore if the transmitter and receiver are facing each other a reduction in amplitude of the received signal could occur due to the beam missing or only partly impinging on the receiver (depending on the thickness of the sample). To overcome this error, either the transmitter or receiver must be moved laterally to ensure maximum signal amplitude during measurements.

CHAPTER 4

Experimental Materials and Methods

This Chapter details the experimental materials and techniques used in this work, including the characterisation of potential filler materials, the development of the fabrication procedures and the characterisation of the composite materials. Tungsten and alumina were identified as suitable filler material for passive materials. As discussed in previous chapters these powder materials are commonly used in a polymer matrix for transducer passive material applications. Tungsten has a high acoustic impedance and is inexpensive compared to other high impedance materials, such as platinum, so is used for backing applications. Alumina has a lower acoustic impedance but alumina materials with a high solid loading can be used as backing materials. The advantage of using alumina materials over tungsten materials is that it is not electrically conducting so can be used in array devices where the separate elements must not have electrical contact. Alumina materials with a low solid loading are also suitable for matching applications to slightly increase the acoustic impedance of the polymer phase. The relatively high attenuation value of tungsten makes it unsuitable for matching.

Table 4.1 shows the tungsten and alumina powders available to be used as potential fillers for backing and matching applications in this work, with information known from the manufacturers. There were two tungsten powders available with particle sizes 1-5μm and 0.5μm and four alumina powders with particle sizes ranging from 20nm to 5μm. The purity of all powders is greater than 99%. The nano grade alumina was described as gamma alumina by the manufacturer, NaBond (Shenzhen, China), while the major phase of all the other alumina types is stated as alpha alumina in the manufacturer specifications. Alpha alumina is usually hexagonal and occurs as the mineral corundum and is the stable high-temperature modification of alumina. Cubic-gamma alumina is less stable and can be formed by the dehydration of most of

the known aluminium oxide hydrates, above a critical temperature alpha alumina will begin to be formed. [105]

Table 4.1 Available Filler Materials

Material	Grade/ Manufacturer	Purity	Particle Size (μm)	Specific Surface Area (m^2/g)
Tungsten	Alpha Aesar, Heysham, UK	99.9%	1-5	-
	Ventron, MA, USA	-	0.5	-
Alumina	MA95, BACo, London, UK	99.2%	5 (median)	1.0
	CR15, Baikowski, PA, USA	99.9%	0.4 (d50)	15
	CT3000SG, Alcoa, PA, USA	99.8%	<1 (d50)	-
	Nano, NaBond, Shenzhen, China	≥99%	20nm	≤200

Epoxies are commonly used as the polymer phase in transducer passive materials as they are simple to use and incorporate with filler materials. They have a relatively long shelf-life as they are typically two part materials where a hardener is added to the resin to initiate the setting reaction so the material cures within 24 hours after preparation. There are a number of different epoxies available with different physical properties that make them useful for various applications. Table 4.2 shows the various epoxies used to fabricate the samples. They each are two part resin and hardener epoxies and have similar densities but different properties such as viscosity and shrinkage during curing. [106]

Table 4.2 Available Epoxy Materials

Epoxy	Manufacturer	Type	Cured Density (g/cc)
RX771C/HY1300	Robnor Resins, Swindon, UK	Two part resin/hardener	1.049
EpoFix	Struers, Solihull, UK	Two part resin/hardener	1.087
Epotek 301	Epoxy Technology, MA, USA	Two part resin/hardener	1.094

4.1 Powder Characterisation

4.1.1 Particle Size Analysis

The particle size of the potential filler materials was analysed using a Sympatec HELOS particle size analyser, with WINDOX software (Sympatec, Pulverhaus, Germany). This uses a laser diffraction particle sizing technique with the size of the particles affecting the position of the diffracted beam, thus enabling the particle size distribution of a powder to be analysed. The measurement range of the instrument is 0.45 – 87.5µm, but if the particles are not well dispersed the agglomerate size rather than the size of the particles is measured.

A standard method was used to analyse the powder samples in the particle size analyser. The procedure is as follows:

- Sample preparation - a small amount of the powder to be analysed was placed into a test tube which was then filled with de-ionised water and a drop of dispersant (0.1 molar $Na_4P_2O_7$, Sympatec).
- Sample analysis - the stirrer on the Sympatec machine was set to 50% speed and the sonication turned on for 10 minutes and the pump set to forward.

- The correct sample names and trigger conditions were selected in the WINDOX software and a reference analysis run to determine the background count with no sample present.
- The sample was then introduced into the chamber and the output monitored on the computer so a concentration near to the optimal concentration of 28% was reached.

The analysis takes place automatically and the results recorded as a graph of density distribution and cumulative distribution against particle size. The procedure was repeated two more times for each sample to ensure the result was an accurate representation of the material.

4.1.2 X-Ray Diffraction (XRD)

The alumina powders were characterised using X-ray diffraction analysis. The powder samples were analysed with a Philips X'Pert machine (Philips Analytical, Almelo, Netherlands) scanned over the whole 2θ range of 10-140°.

4.2 Sample Fabrication Development

4.2.1 Tungsten Epoxy Composites

Tungsten epoxy samples were fabricated with the Alpha Aesar tungsten powder and RX771C/HY1300, a common two part engineering epoxy equivalent to Araldite CY1301/HY1300. The larger particle size powder was chosen to achieve a high level of mixing. Initially the epoxy was added to the tungsten in a 30mm diameter sample holder (or mould) under vacuum in a vacuum impreganation unit (Epovac®, Struers, UK). The Epovac® allows the epoxy to be introduced into the mould under atmospheric pressure. The mould was then sealed and rotated during curing to mix together the epoxy and powder. This method prevented the tungsten being evenly

dispersed in the epoxy as the two phases were not mixed sufficiently. It was found necessary to mix the powder and epoxy together first and degas the mixture before transferring to a mould. During degassing the mixture would expand when foaming so a large container was required for this process. At low volume fractions of tungsten the powder tended to settle out and form a sediment at the bottom of the sample due to the high density of tungsten. To overcome this problem a lid was put over the mould and the mould was rotated during curing to prevent the tungsten settling out. A problem encountered using this method was that the mould was not completely full so there was air in the mixture which resulted in a void in the centre of the sample after the epoxy had cured while being rotated. Some examples of tungsten samples with evidence of the tungsten not evenly dispersed in the sample and samples with large air bubbles observed are shown in Figure 4.1.

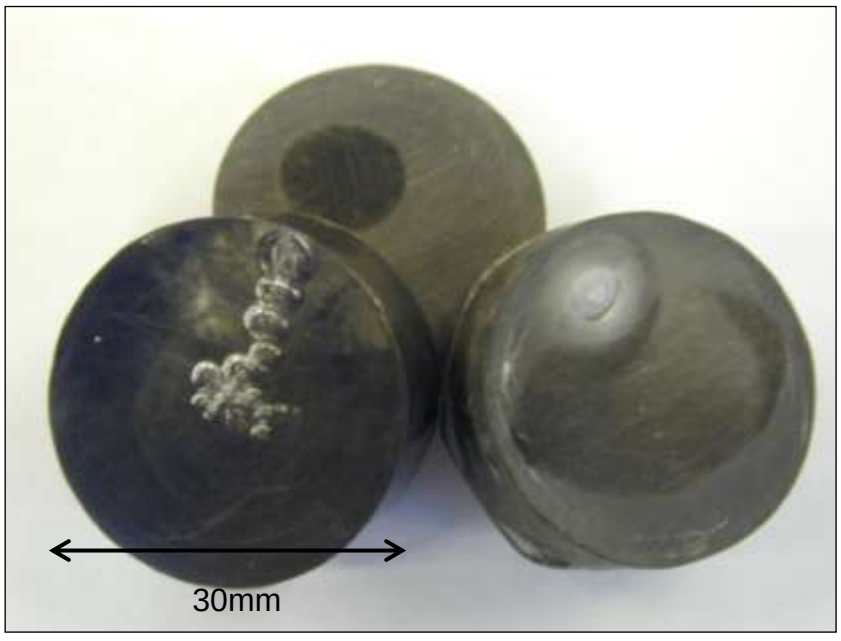

Figure 4.1 *Photograph of tungsten-epoxy samples showing large air bubbles and uneven dispersion of tungsten due to inefficient mixing and rotation of closed containers not properly filled*

A procedure was finally developed to create samples evenly dispersed with tungsten, properly degassed without voids. The desired quantities of epoxy and tungsten powder were weighed out and mixed together by hand with a spatula to make approximately 20cm^3 of material, which was degassed under vacuum in a desiccator until all bubbles were removed. The mixture was then drawn up into a closed container (a syringe of diameter 12mm) and then placed in a hole in a polystyrene ball which was rotated on a ball mill for 24 hours during curing. The material was rotated to prevent the tungsten separating out into sediment due to its high density, as described in other work. [79] Photographs showing the tungsten epoxy in the syringe and the ball container that was rotated on the mill are shown in Figure 4.2. After curing the cast material was removed from the syringe and post cured at 80°C for 1 hour. 1mm thick sample discs were then cut for characterisation.

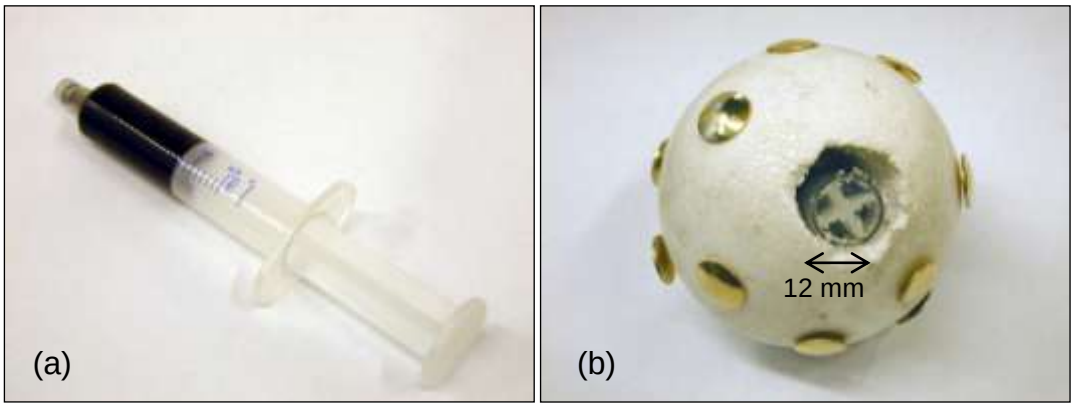

Figure 4.2 *Photographs of some fabrication steps of tungsten-epoxy composites (a) mixture in syringe (b) syringe in ball*

This procedure prevented the tungsten settling that was observed at low volume fractions, although swirling patterns were observed when the epoxy sample was cut as shown in Figure 4.3a. The speed of the ball mill was reduced one speed setting (from approximately 60rpm to approximately 36rpm) and these patterns were no longer observed as shown in Figure 4.3b There was still an problem with small air bubbles

but this was avoided if the mixture was pulled into the syringe carefully, ensuring no air was trapped.

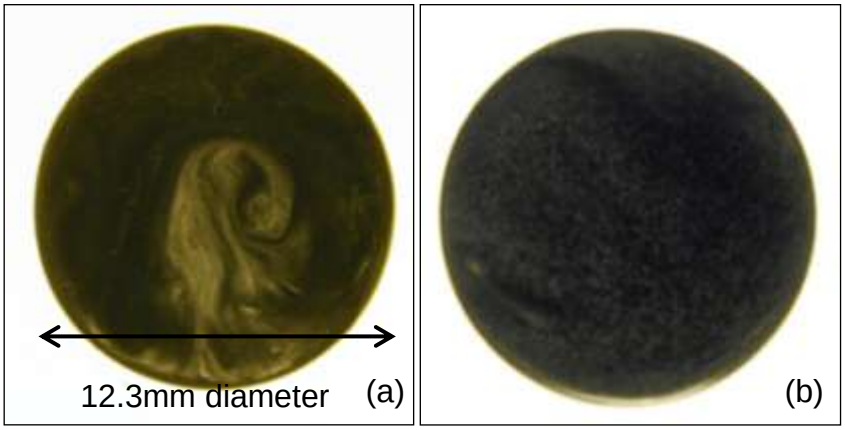

Figure 4.3 ***(a)*** *Cut disc showing tungsten dispersion with swirl pattern when rotated at 60rpm (b) Disc showing reasonable dispersion when rotation speed reduced to 36rpm*

This procedure was successful in fabricating samples up to 0.3 volume fraction. At higher volume fractions the viscosity became too high to draw the mixture up into the syringe. To try to overcome this problem, initially the mixture was just packed into the syringe, degassed, then put in the ball as before. This produced a porous sample with many tiny air holes, as the mixture was too viscous to degas effectively. Therefore, a solvent (ethanol) was added to the mixture to reduce the viscosity so the mixture could be degassed. The mixture with the solvent was then poured into the syringe and placed in the vacuum with a funnel inserted into a syringe with the end cut off to account for the expansion of the material during degassing. In addition to the material foaming and expanding, material was also spat out as the solvent evaporated in a volatile manner during degassing. The material was then left at room temperature for 24 hours to cure before demoulding. Finally, the sample was heated to 80^{o}C for 1 hour after demoulding; it was assumed that the tungsten would not settle out in such a viscous mixture and no sedimentation was observed. It was noted that

the time taken for the solvent to evaporate away was much shorter than the usual time required to degas epoxy effectively so all air bubbles are removed. It is therefore predicted that the material was not degassed properly with this method as the material left after the solvent has been removed is too viscous. Air holes were observed in the cured material and more solvent had to be added for higher volume fractions, resulting in a larger volume of tungsten epoxy being spat out as the solvent evaporated in the vacuum, and therefore a smaller overall sample volume.

An alternative fabrication method was also used to fabricate material with a high tungsten loading, exploiting a technique used in the manufacture of rubbers and ceramics. Epoxy was combined with tungsten powder in a twin roll mill which employs high shear mixing so a higher tungsten volume fraction could be produced. The high viscosity of the material meant it could not be degassed so it was pressed instead and sections were cut for testing. Another sample was made by employing a viscous polymer technique normally used in the processing of ceramic. Tungsten powder was mixed with solvent and polymer binder (PVB) and other additives in the following proportions.

Tungsten	150g	(Alpha Aesar, APS 1-5 micron 99.9%)
PVB (Polyvinyl Butyral)	2.6g	(Wacker, Pioloform® BS18)
Cyclohexanone	2.0g	(BDH, GPR Grade)
DBP (Dibutyl phthalate)	1.2g	(BDH, GPR Grade)
Steric Acid	0.1g	(BDH, GPR Grade)

The mixture was then milled with the twin roll mill until a tape was formed. The tape was then calendered to about 1.2 mm thickness then left in an oven at 80^{o}C for several days to dry out the solvent. The tungsten volume fraction of this sample was then estimated by measuring the density and using Equation 2.4. Density measurements of

all samples were carried out by weighing a section and calculating the volume of the material by measuring its dimensions, and additionally using the Archimedes method.

4.2.2 Alumina Epoxy Composites

Initial trials were undertaken mixing CR15 and CT3000 SG alumina grades with epoxy using a method similar to that carried out previously with the tungsten powder. The grades were chosen as they were readily available and both had a similar particle sizes. The powder and epoxy was mixed together in a beaker by hand with a spatula and the mixture was drawn into a syringe and left to cure. It was not found necessary to rotate the mixture as the alumina was observed not to settle out like the tungsten powder. Sections were sliced out of the samples to assess the dispersion of alumina powder in the material. Photographs of the resulting samples cut down their length, taken on a light box are shown in Figures 4.4 and 4.5 so the overall alumina particle distribution in the epoxy can be seen clearly; the dark areas in the photographs are large agglomerates of alumina.

The alumina powders tended to agglomerate together more than the tungsten powder, making mixing difficult. The pictures in Figures 4.4 and 4.5 clearly show that the method of mixing the powder into the epoxy by hand does not break up agglomerates present in the powder resulting in uneven distribution in the epoxy. The agglomerates in the CT3000 SG alumina grade are larger than those in CR15 and it can be seen these have settled to the bottom of the epoxy sample. Attempts to improve the mixing by gradually adding the powder did not result in improved alumina distribution and reduced agglomeration within both grades.

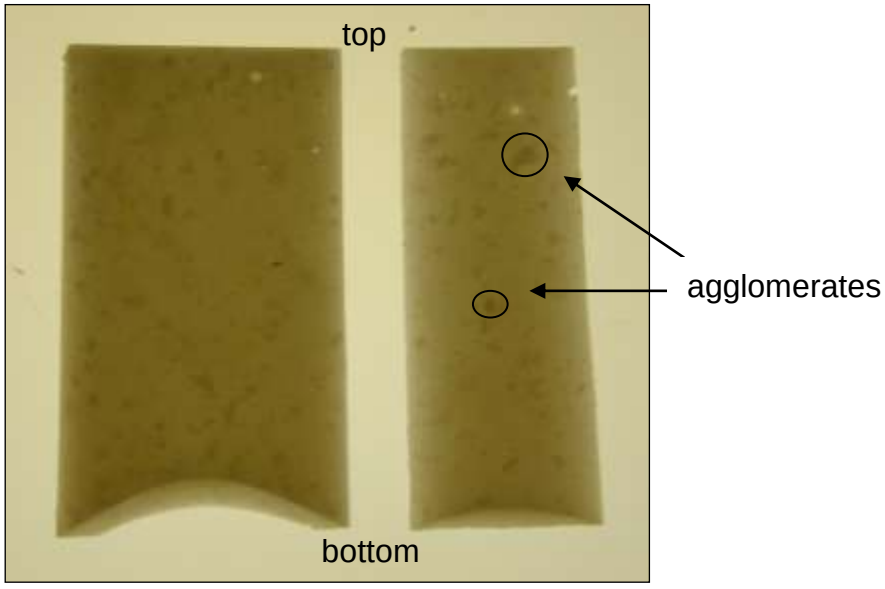

Figure 4.4 *Photograph of epoxy filled with CR15 grade alumina mixed by hand*

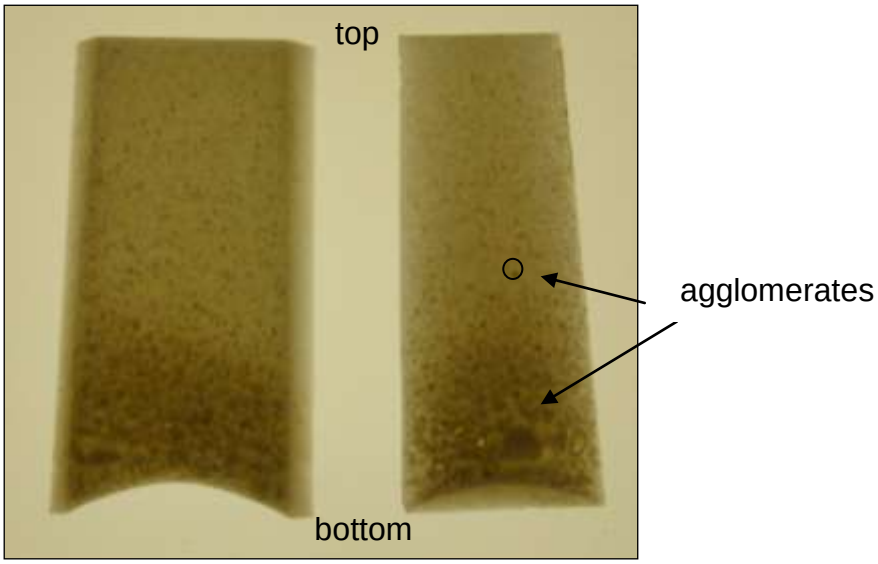

Figure 4.5 *Photograph of epoxy filled with CT3000 SG grade alumina mixed by hand*

Photographs of alumina epoxy samples mixed with a magnetic stirrer are shown in Figures 4.6 and 4.7. This new mixing technique showed good results with the CR15 grade alumina as no large agglomerates are seen in Figure 4.6, although there is an additional problem with trapped air bubbles. Agglomerates are still observed in Figure 4.7 with the CT3000 SG grade alumina, although the mixing is improved as there is no settling of alumina particles at the bottom of the sample. Additional trials

using a magnetic stirrer and applying a low heat to the material to reduce the viscosity of the epoxy further showed good results and air bubbles were removed by degassing the material more carefully.

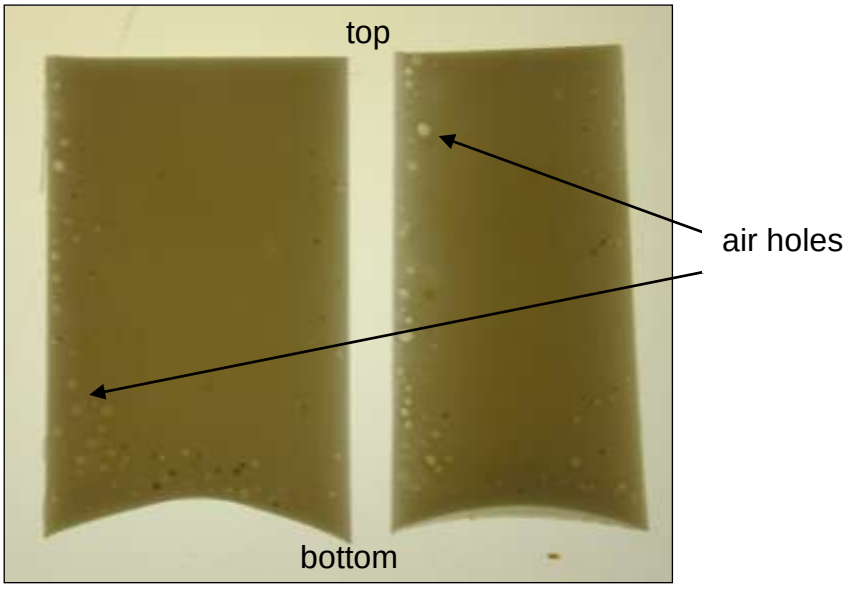

Figure 4.6 *Photograph of epoxy filled with CR15 grade alumina mixed with stirrer*

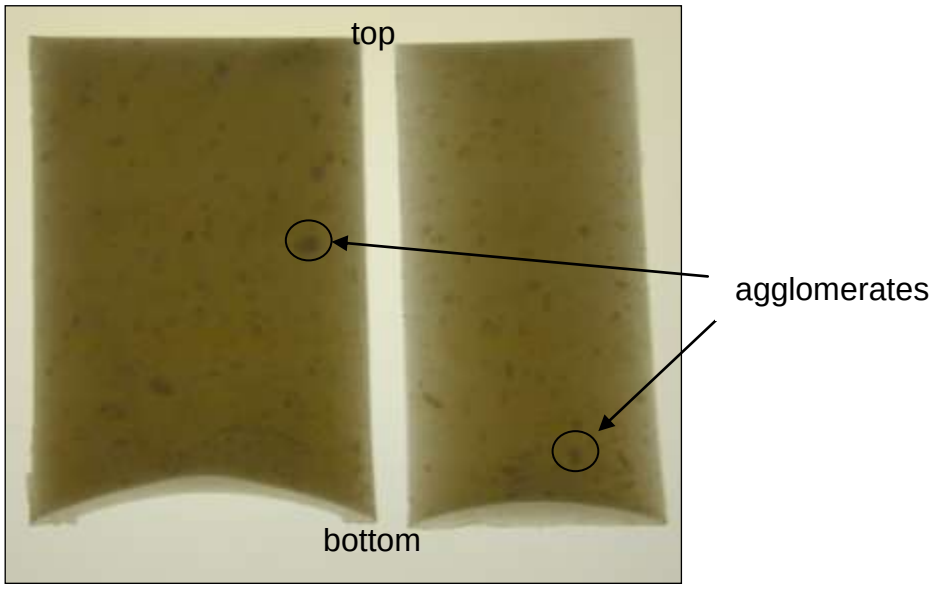

Figure 4.7 *Photograph of epoxy filled with CT3000 SG grade alumina mixed with stirrer*

Three different alumina grades and two epoxies were used to make the final alumina epoxy composite samples. Alumina grades MA95, CR15 and alumina nanopowder were mixed with Epofix and Epotek 301. These epoxies were chosen as Epofix has similar properties to RX771C/HY1300 used previously, but does not shrink during curing and Epotek 301 has a very low pre-cure viscosity, similar to water so a higher solid loading can be achieved. [106] The alumina grades were chosen after the initial mixing trials so CT3000SG was not used as it tended to agglomerate more and could not be dispersed. The desired amount of alumina powder was weighed out and added to the epoxy resin and mixed by hand with a spatula (approximately 20cm^3 volume of material). The mixture was then put on to a hot plate in a cardboard container and was mixed again with a magnetic stirrer under a low heat for about 2 minutes. The hardner was then added and the mixture stirred again at a high speed before being degassed and drawn into a syringe of 14.2mm diameter. The epoxy was then left to cure overnight before demoulding and no post curing was necessary. Sample discs were then cut for characterisation. It was observed in the initial trials that no settling occurred when the alumina was fully dispersed as the density of alumina is much smaller than that of tungsten, so no rotation during curing was necessary as with the tungsten material.

Higher alumina volume fractions were attempted using the viscous polymer process described for the tungsten epoxy material with the CR15 alumina grade to produce materials suitable for matching applications. The particle size of this alumina powder is smaller than the tungsten powder which meant that the milling of the material was more difficult as it did not wet up sufficiently due to the increased surface area of the alumina compared to the tungsten powder and, therefore, this approach was unsuccessful at fabricating high alumina volume fraction material.

4.3 Material Characterisation

4.3.1 Scanning Electron Microscopy (SEM)

SEM images were taken using a JEOL 6060 microscope of all tungsten and alumina powders. The dry powders were placed onto a SEM stub and then sputtered with a thin layer of gold for examination. Images were also taken of cut surfaces of the filled epoxy samples to determine the dispersion of the filler particles in the epoxy and look for any evidence of porosity.

4.3.2 Low Frequency Acoustic Measurements

Initial measurements of acoustic impedance for the tungsten epoxy samples were made at 5MHz using the non-contact-through transmission set up described in Section 3.3. Two 5 MHz flat immersion transducers (Panametrics-NDT, MA, USA) were used as the transmitter and receiver respectively and clamped in position facing each other, but separated by a small space, and connected to a pulser receiver (DPR300, JSR Ultrasonics, NY, USA) and an oscilloscope (Agilent 54641A, Agilent Technologies, South Queensferry, UK), as shown in Figure 4.8.

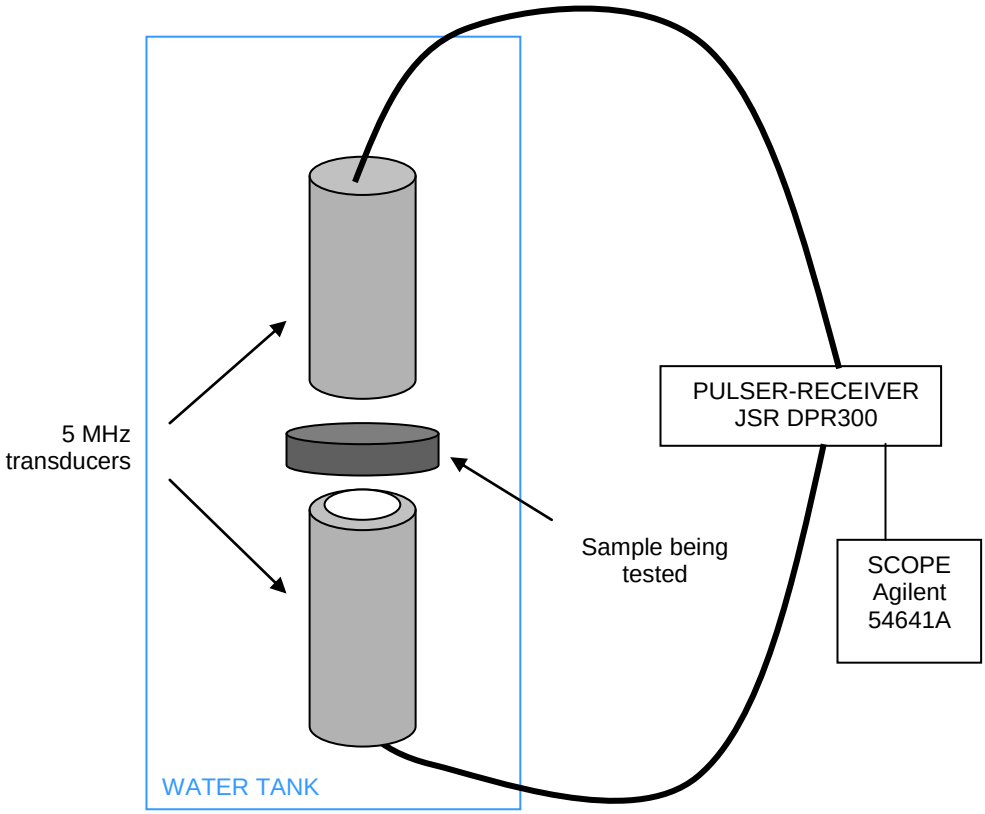

Figure 4.8 *Schematic diagram of the experimental set up for longitudinal velocity measurements*

A pulse was transmitted by one transducer upon excitation by the pulser-receiver and the time scale was adjusted on the oscilloscope so that the pulse from the receiving transducer was clear and the edge could be seen, thus enabling the time taken for the wave to travel between the transducers to be observed. This pulse was then saved so it could be seen in the background on the oscilloscope. The sample was then carefully placed on top of the bottom transducer, ensuring that the transducers were not moved at all. The pulse transmitted through the sample could then be compared to the original pulse and the time difference, Δt, could be calculated from the difference of the first arrival times of the two signals. Between each sample measurement the reference pulse (without a sample present) was checked and compared to the original

saved trace on the oscilloscope, ensuring that the system had not changed. The longitudinal velocity through the sample was then calculated using Equation 3.9 and the acoustic impedance was found by multiplying the velocity by the measured density of each sample.

4.3.3 High Frequency Acoustic Measurements

4.3.3.1 Characterisation Jig

A jig was custom designed and constructed to accommodate the transmitter, receiver and sample for acoustic measurements of both longitudinal and shear wave properties at high frequencies, used courtesy of Duncan MacLennan. [107] The jig was designed to hold a membrane hydrophone as a receiver and a transmitting transducer attached to a remote pulser. The jig allows alignment of the transducer and hydrophone; the platforms on which the hydrophone and sample holder are positioned can be finely adjusted so they are parallel and the remote pulser is attached to a goniometer and an x-y stage so the angle in two directions and the x-y position can be finely adjusted. The sample holder is attached to a gear and worm allowing it to be rotated. A photograph of the whole jig, showing the key components and functions is presented in Figure 4.9.

The sample holder had to be modified initially to accommodate samples that were not 10mm by 10mm squares as shown in Figure 4.10. A layer of plastic tape was positioned at the edges of the sample to provide an inference fit. Consequently another sample holder was made that included a removable fixture so it would be possible to hold samples of varying size and shape in following experiments; the design of this sample holder is shown in Figure 4.11.

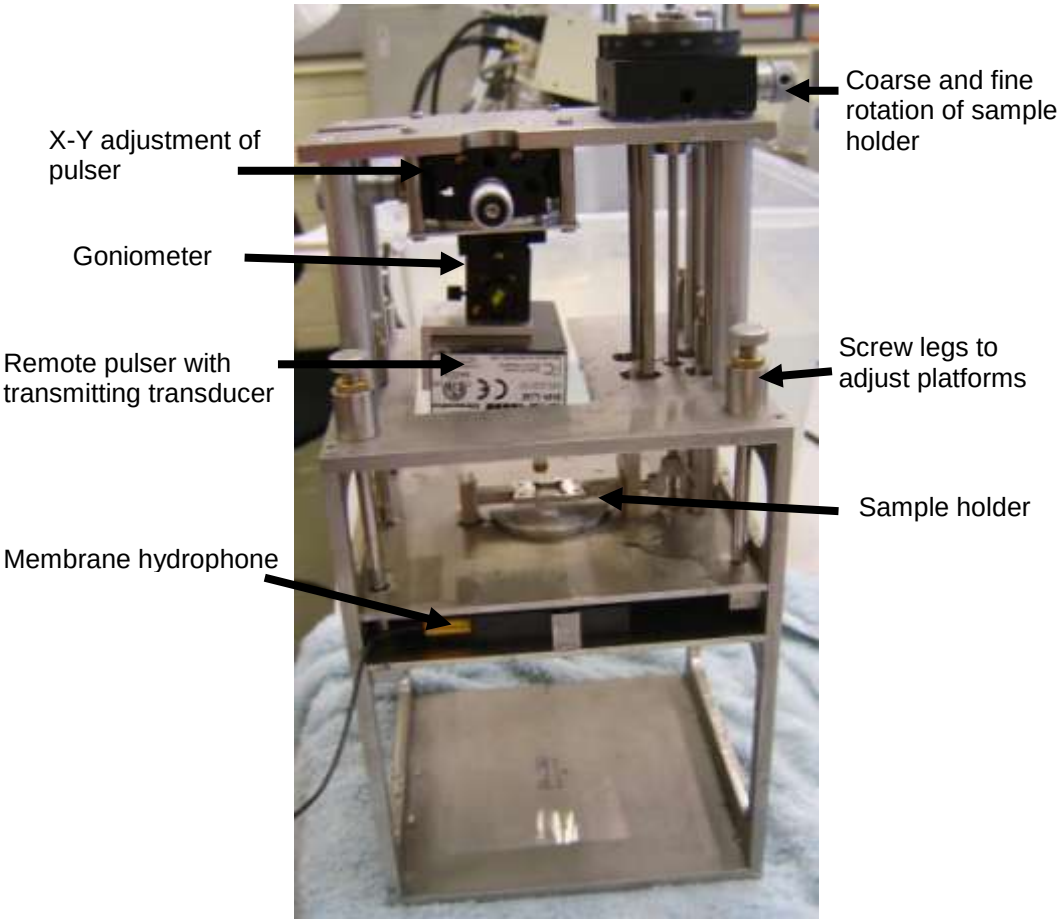

Figure 4.9 *Photograph of acoustic characterisation jig*

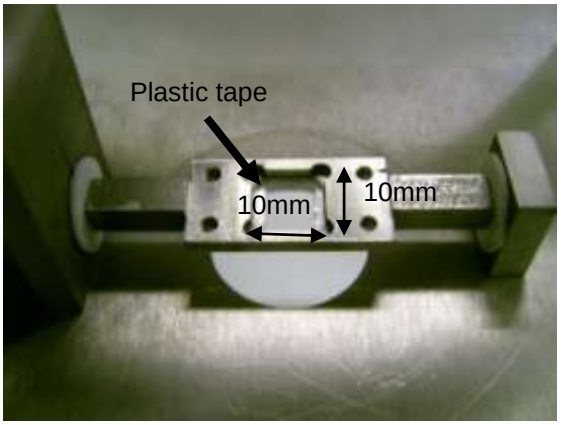

Figure 4.10 *Photograph of original sample holder modified with plastic tape*

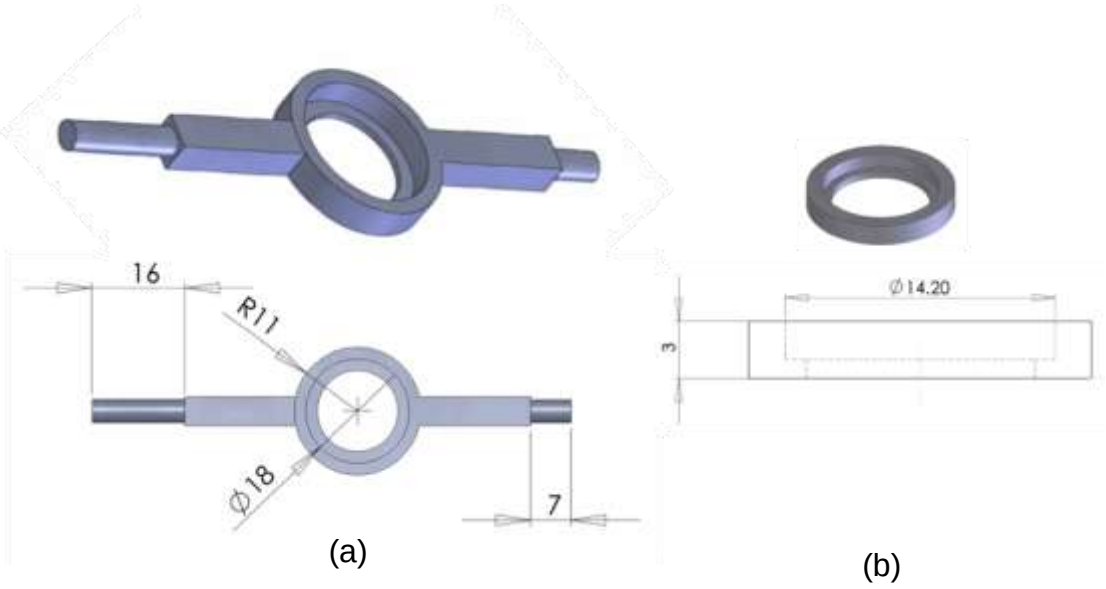

Figure 4.11 *CAD schematic of (a) alternative sample holder with (b) removable fixture to accommodate disc shaped samples of 14.2mm diameter*

4.3.3.2 Experimental Set Up and Procedure

The initial experimental setup is illustrated in Figure 4.12 with the characterisation jig in a container of degassed water with the tip of the transmitting transducer just submerged. A 35MHz focused piezocomposite transducer (AFM Ltd, Birmingham, UK) was used as a transmitter and a membrane hydrophone (16µm gold PVDF film, Precision Acoustics, Dorchester, UK) was the receiver. The transmitter directly connected to a computer-controlled remote pulser (DPR500, JSR Ultrasonics, NY, USA) and the hydrophone was connected directly to the Agilent 54641A oscilloscope via its preamplifier and a 50Ω cable.

The transducer and receiver were first characterised by recording both the pulse-echo response of the transducer off the steel plate of the characterisation jig and also the through reference signal. The signals were then analysed using fast fourier transform (FFT) to look at the frequency characteristics of the received echo and through signals.

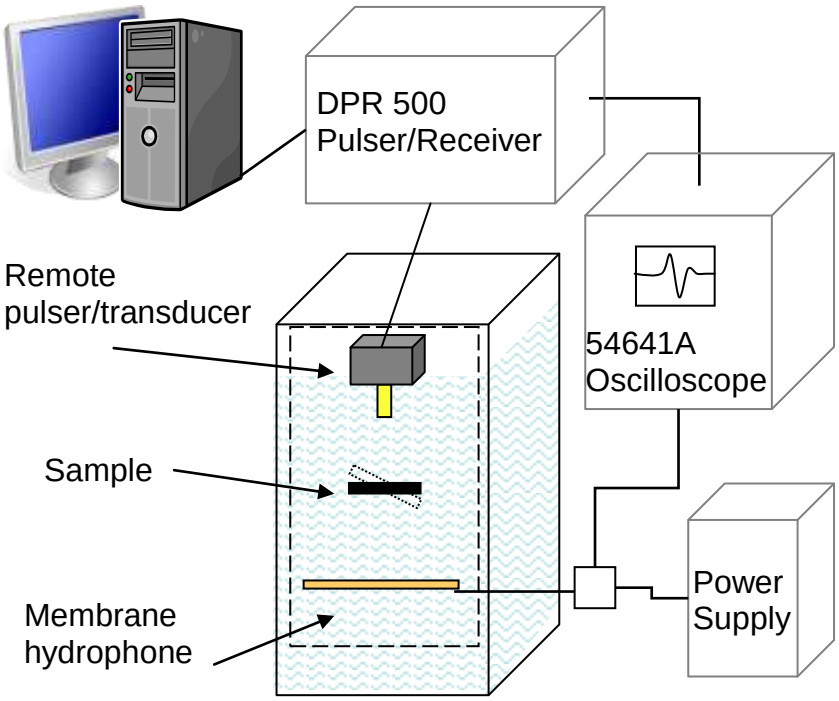

Figure 4.12 *Schematic diagram of experimental set up with membrane hydrophone. Characterisation jig represented by dotted lines*

The experimental procedure was as follows: the platforms of the characterisation jig were adjusted so that they were level using a spirit level. The remote pulser was used to generate a pulse with the PRF (Pulse Repetition Frequency) set to 2.9kHz and the damping value set to 100Ω (standard values). The output from the hydrophone was sampled by the oscilloscope. The position of the transmitter was adjusted using the goniometer and the x-y stage so that the received signal amplitude without the sample in place was maximised. The reference signal was then recorded and the sample placed in the sample holder, without moving the jig. The transmitted signal was then recorded for normal incidence. Then the sample was rotated stepwise and the signal recorded for a number of incident angles. The pulser was moved laterally as appropriate to account for the wave being refracted in the sample so the maximum signal was observed. This was necessary for thicker samples but was not done when

measuring thin samples (~250-500μm) as the signal was easily lost with any small movement.

The experimental set up, as illustrated in Figure 4.12, was used to characterise the first tungsten epoxy samples fabricated. Later, the alumina epoxy samples were measured using a slightly different set up, as shown in Figure 4.13. Two transducers were used as transmitter and receiver; the transmitter was a focused 35MHz composite transducer (used courtesy of Jeremy Brown, Sunnybrook Health Sciences Centre, Toronto, Canada) which was connected to the remote pulser. The receiver was a 26MHz flat piezocomposite transducer (AFM Ltd, Birmingham, UK) which was clamped in place. The receiving transducer was then connected to a pulser/receiver (DPR300, JSR Ultrasonics, NY, USA) set to a gain of 40dB to amplify the signal. The redesigned sample holder (Figure 4.11) was used so that disc shaped samples could be accommodated without needing further machining. The measurement procedure was then unchanged as the signal was recorded with and without the sample present and the sample rotated through a range of incident angles and the signal recorded every 2°. Both transducers were also characterised as described before in pulse-echo mode and also the through signals were analysed with one transducer acting as transmitter and the other as receiver and vice versa.

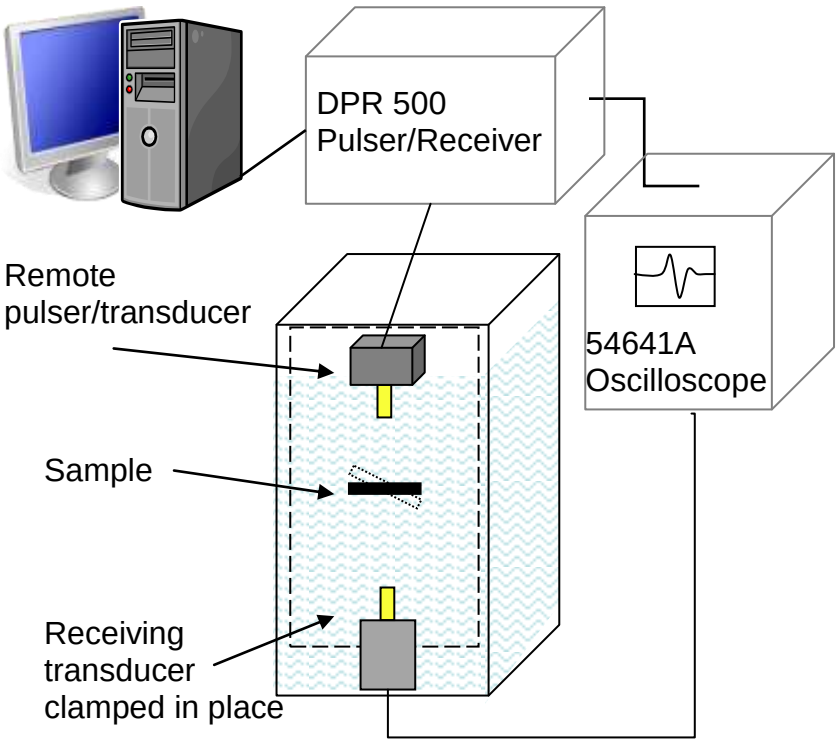

Figure 4.13 *Schematic diagram of experimental set up with transmitting and receiving transducers. Characterisation jig represented by dotted lines*

4.3.3.3 Determination of Experimental Errors

The error associated with the density measurements of the samples was calculated using the resolutions of the equipment used to weigh and measure the sample dimensions and also using the difference of the densities of the individual samples measured. The velocity and attenuation of the longitudinal and shear waves through the samples were calculated as described in Section 3.3. The experimental errors were then determined by calculating the maximum and minimum values obtained when the measurement errors of the time, sample thickness, sample density and the resolution of the oscilloscope were taken into account. The maximum velocity was calculated using the smallest pathlength and shortest time, and the minimum velocity was calculated using the longest pathlength and longest time. The errors associated

with the measured density and velocity values were then combined to give a total error for acoustic impedance. The errors were also found for the attenuation data in the same way, using the combined error in the acoustic impedance values and the error in the amplitude measurement due to the resolution of the oscilloscope.

CHAPTER 5

Tungsten-Epoxy Composites

This Chapter presents the results for the tungsten epoxy materials, including characterisation of the filler material, as well as acoustic results at 5MHz and 35MHz to determine the frequency dependence of velocity through the materials. Attenuation results measured at 35MHz are then presented and compared to other published work in the literature.

5.1 Powder Characterisation

5.1.1 Particle Size Analysis

The particle size results obtained for the Alpha Aesar and Ventron tungsten powders are shown in Figures 5.1 and 5.2. The graphs show density distribution and cumulative distribution against particle size, and indicate quite broad size distributions in both powders. The mean sizes of both powders according to these results are very similar. The mean size (d50) of the Alpha Aesar powder is approximately 6μm, and the mean size of the Ventron powder is approximately 7μm. Both graphs also show a secondary peak around 20μm indicating a broad distribution, suggesting agglomeration in both powder types. As mentioned previously, using the laser diffraction technique the agglomerate size is measured if the powder is not well dispersed. Table 5.1 also compares the d10, d50 and d90 values for the powders (cumulative undersize values, eg. d10 is the average particle diameter where the powder particles reach a cumulative particle number of 10% in a cumulative undersize particle distribution). The d50 values for both grades are higher than the specification suggesting that the powders may be agglomerated.

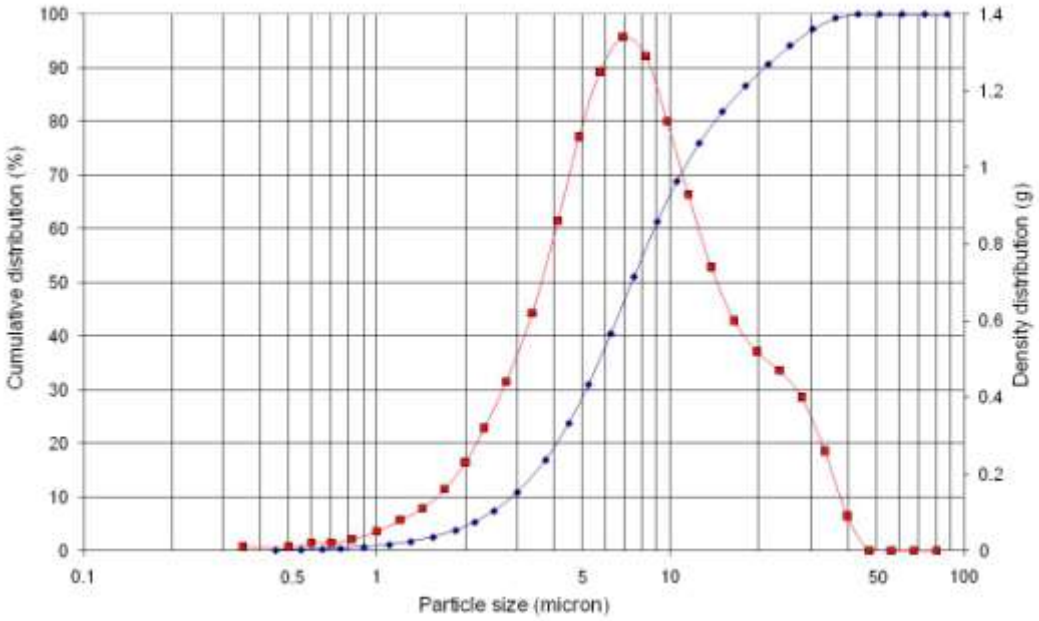

Figure 5.1 *Particle size results for Alpha Aesar tungsten powder*

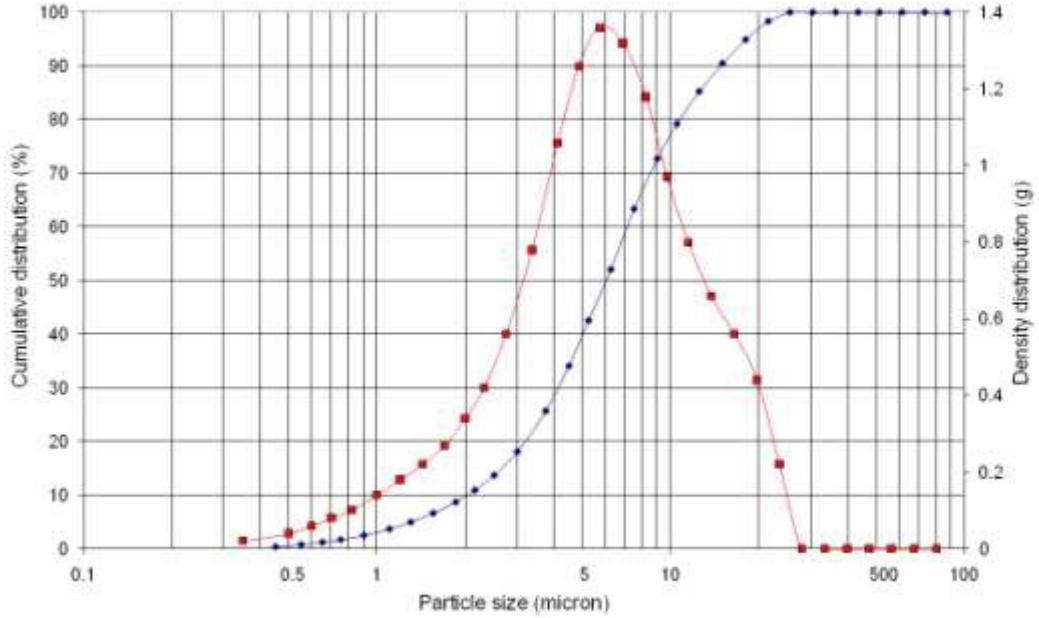

Figure 5.2 *Particle size results for Ventron tungsten powder*

Table 5.1 Particle Size Data for Tungsten Powders

Tungsten Powder Type	Particle Size (μm)		
	d10	d50	d90
Alpha Aesar (1-5μm)	2.78	7.41	21.86
Ventron (0.5μm)	2.02	5.97	14.78

5.1.2 Scanning Electron Microscopy (SEM)

SEM images were taken of the dry powders, without any kind of dispersant to separate the individual particles. SEM images of the tungsten powder types discussed are shown in Figure 5.3. Figure 5.3a shows that the particles of the Alpha Aesar powder do range in size from approximately below 1μm to 5μm and agglomerates are visible in the image consisting of clusters of the smaller particles. The SEM image shows that most of the particles are approximately spherical in shape making them suitable as a scattering filler material. The corresponding SEM image of the Ventron powder is shown in Figure 5.3b. Again it is clear that the primary particle size is ~0.5μm, with an apparently narrow distribution, but the particles are agglomerated to approximately 10-15μm. The picture shows large clusters of tungsten particles forming shapes that are not spherical and these agglomerates also look like they are fused together, in contrast to the Alpha Aesar powder which looks like the particles may be broken up more easily. The Alpha Aesar grade was initially chosen as the filler for backing materials to achieve a reasonable level of loading, as it would be more difficult to wet all the particles with a smaller size. The shape of the Alpha Aesar particles is also more suitable to use as filler so that the scattering models described in Chapter 2 are valid.

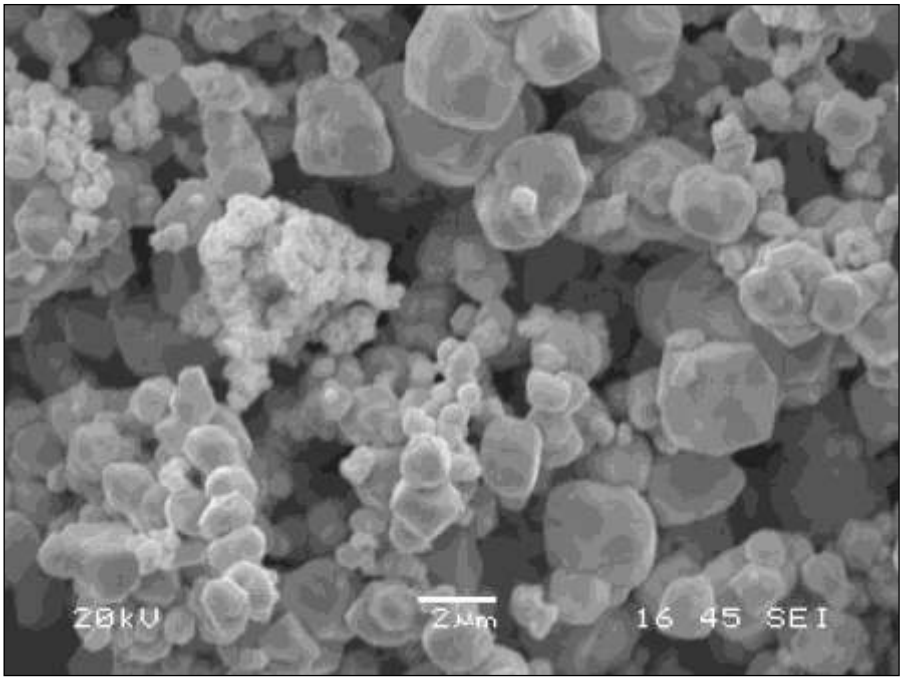

(a)

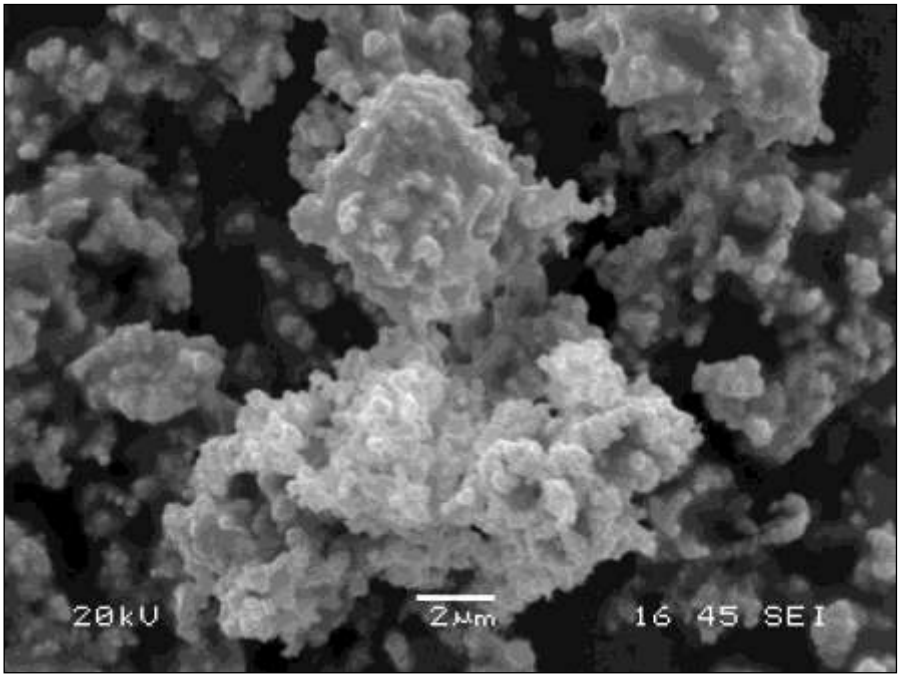

(b)

Figure 5.3 *(a) SEM image of Alpha Aesar tungsten powder (b) SEM image of Ventron tungsten powder*

5.2 Composite Characterisation

Using the fabrication methods described in Chapter 4 samples were made with volume fractions shown in Table 5.2. It is clear that the samples made with the solvent are a lot lower than the design volume fraction; suggesting all the solvent is not removed or tungsten powder is removed from the epoxy as the solvent evaporates away. Another reason for the density of the samples to be lower than the theoretical density is due to porosity arising from incomplete bonding and adhesion between the particles and epoxy; this problem has been reported experimentally elsewhere. [65]

Table 5.2 Tungsten loaded epoxy samples

Design Volume fraction	Number of discs	Average disc density (g/cm^{-3}) ±0.02	Actual volume fraction (to nearest 0.01)	
0	10	1.15	0	
0.01	10	1.29	0.01	
0.05	9	2.00	0.05	
0.10	10	2.92	0.10	
0.15	10	3.68	0.14	
0.20	10	4.52	0.19	
0.25	10	5.47	0.24	
0.30	10	6.08	0.29	
0.35	9	6.67	0.31	processed with solvent
0.40	10	7.23	0.33	
0.45	6	7.54	0.35	
0.50	5	7.37	0.34	

To determine whether all the solvent was removed from the epoxy during degassing, samples were fabricated with and without solvent and the densities compared. The velocity through the samples was also measured at 5MHz using the experimental set

up described in Section 4.3.2. Table 5.3 shows the densities and velocities of epoxy made with and without solvent. The values are the average of 10 sample discs cut from the material made ± the standard deviation. The values are not significantly different indicating that the solvent is removed during the degassing process or that the solvent has little effect on these properties

Table 5.3 Density and Velocity through Epoxy made with and without solvent

Sample	Density (g/cm^3)	Velocity @5MHz (m/s)
Epoxy	1.14 ± 0.02	2551 ± 130
Epoxy + Solvent	1.12 ± 0.02	2530 ± 65

5.2.1 Scanning Electron Microscopy (SEM)

'As cut', unpolished samples of the composite material were examined using SEM. The images show evidence of tungsten agglomeration and porosity in the material, although generally the tungsten is well dispersed in the epoxy.

The SEM image obtained from the of 0.01 tungsten volume fraction epoxy sample is shown in Figure 5.4. It can be seen in Figure 5.4a that the tungsten is generally well dispersed in the epoxy although Figure 5.4b shows some clusters of tungsten particles larger than 10μm. There is also some porosity observed but this may be due to a filler particle being pulled out of the epoxy during cutting, as the pore size is similar to the tungsten particle size. The SEM images obtained for the 0.05 and 0.10 volume tungsten epoxy are shown in Figures 5.5 and 5.6 with similar features visible.

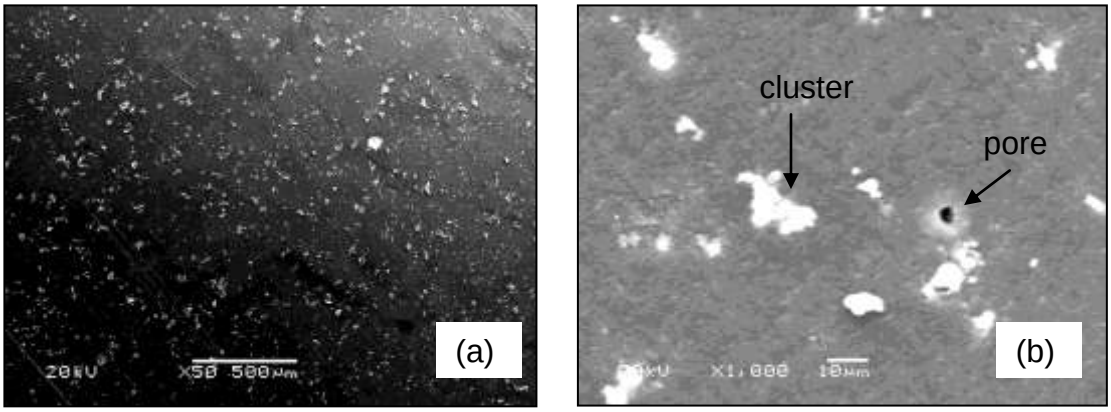

Figure 5.4 *SEM images of 0.01 tungsten volume fraction epoxy*

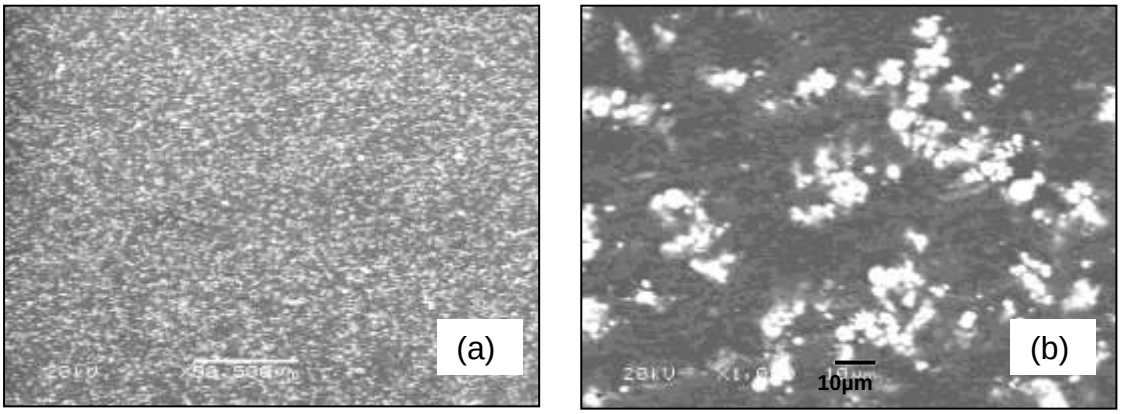

Figure 5.5 *SEM images of 0.05 tungsten volume fraction epoxy*

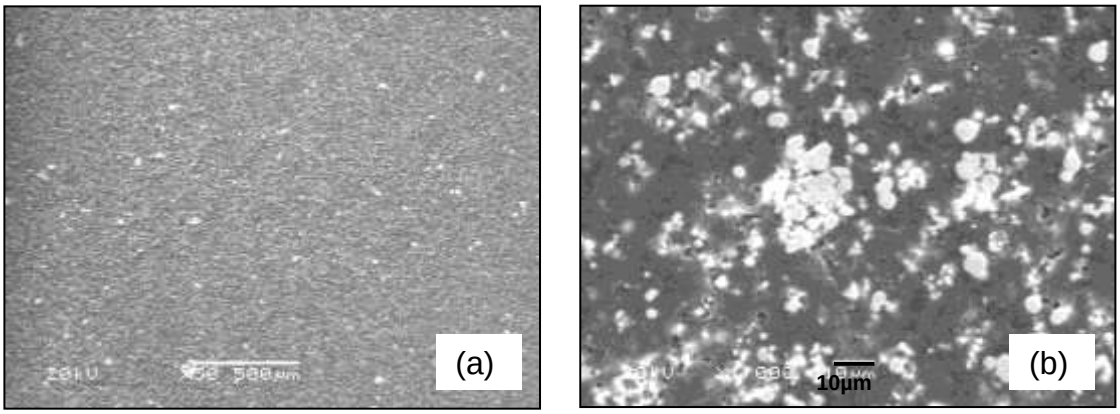

Figure 5.6 *SEM images of 0.10 tungsten volume fraction epoxy*

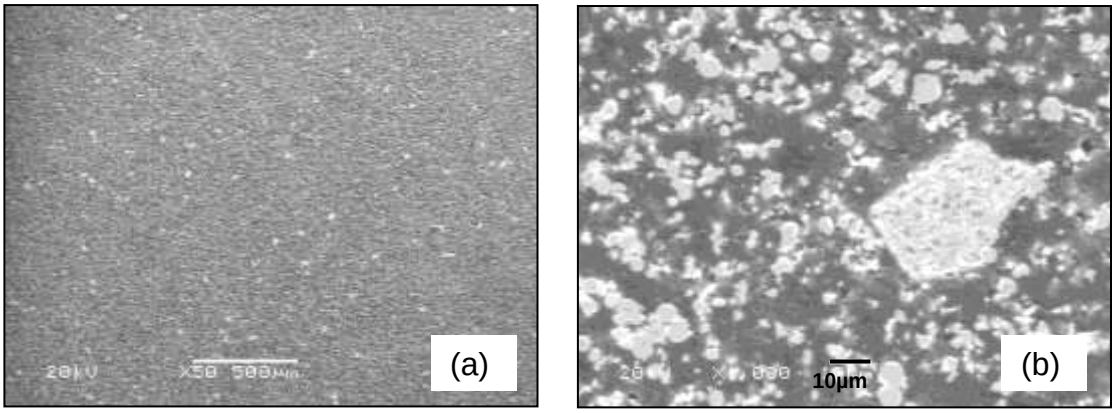

Figure 5.7 *SEM images of 0.15 tungsten volume fraction epoxy*

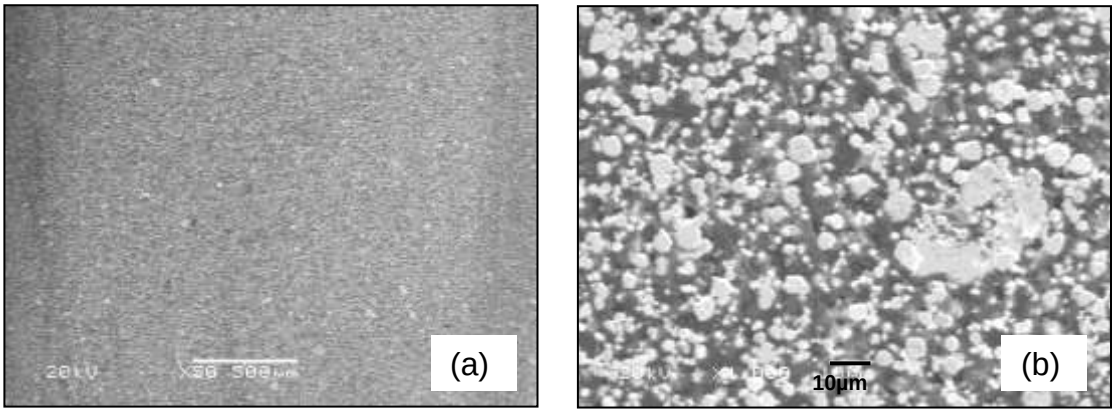

Figure 5.8 *SEM images of 0.20 tungsten volume fraction epoxy*

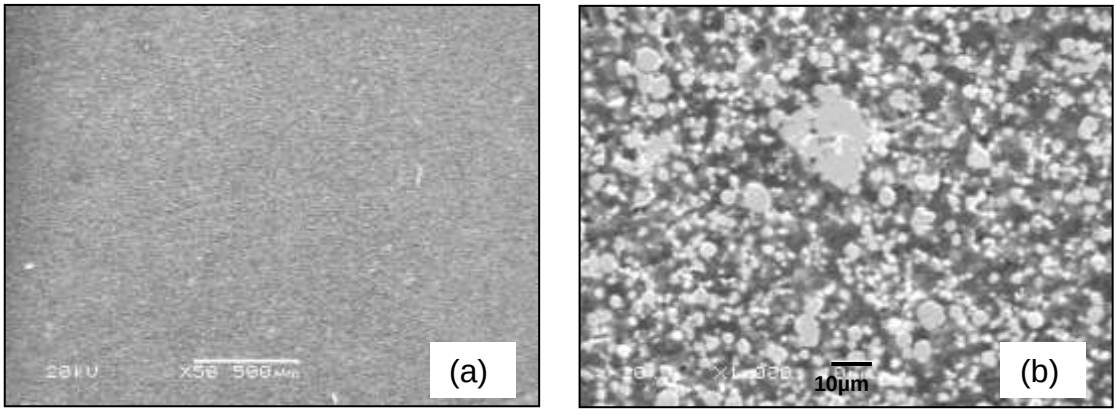

Figure 5.9 *SEM images of 0.25 tungsten volume fraction epoxy*

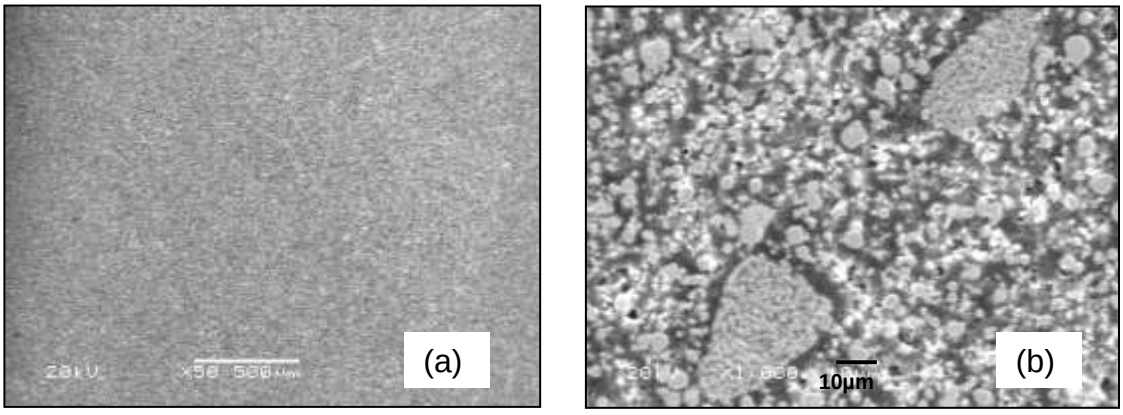

Figure 5.10 *SEM images of 0.30 tungsten volume fraction epoxy*

As the volume fraction of tungsten is increased in the epoxy the observed agglomerate size is increased as shown in Figures 5.7-5.10 which represent the tungsten epoxy samples of volume fractions 0.15-0.30. The SEM images in Figure 5.Xa for each volume fraction show general even distribution but at higher magnification shown in Figure 5.Xb for each sample, agglomerate sizes approximately 40μm in diameter can be observed, made up of clusters of relatively large particles in some cases (over 5μm in Figure 5.9b) and other clusters of smaller particles (approximately 1μm) shown in the 0.30 tungsten volume fraction epoxy in Figure 5.10b.

Large agglomerates as shown in Figure 5.10b are not desirable in backing materials as they can change the scattering properties of the material. Diffusive scattering occurs when the scattering object is smaller than the incident wavelength and specular scattering occurs when the object is larger than the wavelength, as described previously in Section 2.5. Diffusive scattering is required in backing materials so the ultrasound beam is not reflected back into the active element of the transducer; large agglomerates also act as scattering objects and may cause specular scattering. The agglomeration observed here in the higher volume fractions of tungsten epoxy would not be a problem in backing materials for conventional transducers operating at low frequencies. However, high frequency ultrasound has a smaller wavelength so these tungsten agglomerates may interfere with the sound wave causing specular scattering.

The samples fabricated by the milling technique do not show the same evidence of agglomeration as samples mixed by hand, as the high shear mixing process breaks down agglomerates. The SEM image obtained for the 0.40 volume fraction tungsten epoxy that was mixed together on the twin roll mill is shown in Figure 5.11. There is a lot of porosity observed as the material could not be degassed properly. The volume

of porosity can be estimated by calculating what the density of the material should be according to the proportions of epoxy and tungsten mixed together and measuring the actual density. The difference will give an indication of the porosity volume. No material was lost in fabrication using this technique so the estimates are reasonably accurate. The milled epoxy sample was made with 175g of tungsten powder and 13.3g of epoxy and the measured density is 95% of the theoretical density according to these proportions. Therefore the sample contains ~5% volume porosity. It is shown in Figure 5.11 that this porosity is made up of large pores up to approximately 30-50μm in diameter.

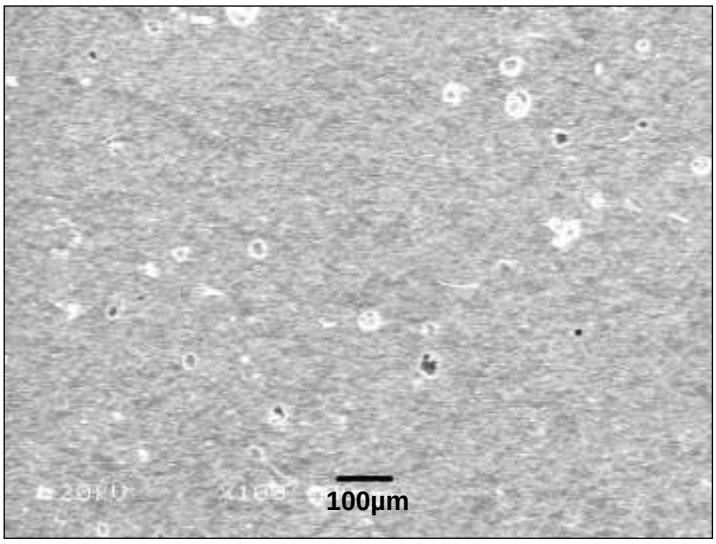

Figure 5.11 *SEM image of milled 0.40 tungsten volume fraction epoxy*

SEM images of the milled tungsten/PVB sample are shown in Figure 5.12. The high shear milling has broken down agglomerates so none are observed. The images do not show the porosity as clearly as the epoxy samples, although the material will not be fully dense; there are spaces between the tungsten and PVB particles. The volume porosity can be estimated as before, assuming that all the solvent was removed during drying and only the tungsten particles and PVB remains. The sample was made with 150g tungsten and 2.6g PVB and the measured density is 68% of the theoretical

density. Therefore the sample contains 32% volume porosity. This is a significant amount so the sample cannot be considered as a two phase material. The SEM image in Figure 5.12b, however, shows tighter packing than this porosity value suggests. The voids in the sample will affect the acoustic velocity through it so that the velocity cannot be estimated using two phase models. It is presumed that porosity would reduce the acoustic impedance of the material, thus resulting in a poorer matching to the piezocomposite transducer material. Porosity would also result in more specular scattering as the trapped air acts as a scatterer, just like the tungsten filler particles. These voids are quite large, but probably not as big as the wavelength in epoxy (~50μm at 50MHz) so would not cause diffusive scattering. The high shear milling technique allows a higher solid loading, hence a higher density resulting in a higher acoustic impedance, so it is a worthwhile technique, even though porosity exists.

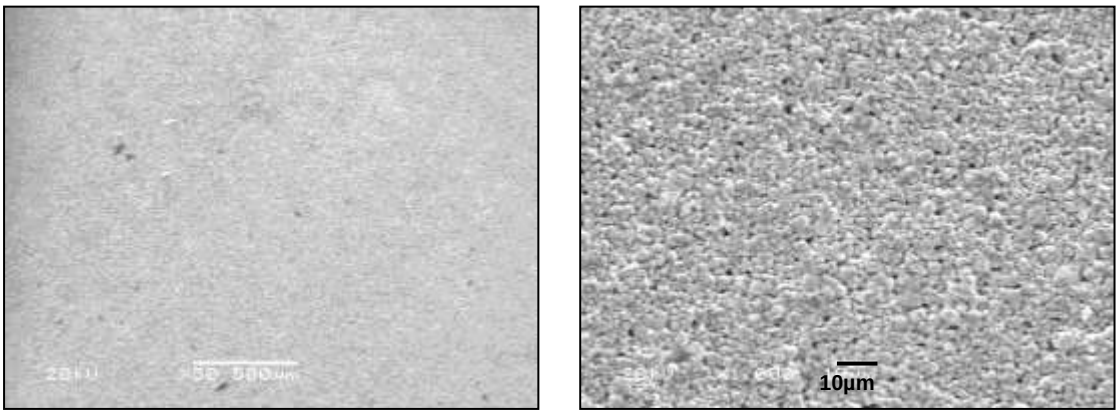

(a) (b)

Figure 5.12 *SEM images of 0.5 volume fraction tungsten/PVB*

The high solid loading also means that electrically conductive backing can be fabricated. Simple measurements with a multimeter showed that composites >0.30 tungsten volume fraction were conducting but material below this volume fraction was not. A conductive backing is commonly used in the manufacture of single element ultrasound transducers, such as E-solder 3022 [108] or Epotek 430. [55] Other reported work describes casting and centrifuging conductive epoxy onto the active

element to ensure conductivity throughout and increase the acoustic impedance. [39] Electrically conducting backing is not viable for array devices as the conductivity would short out array elements defined with separate electrodes. Non-conducting tungsten epoxy backings would be suitable for backing single element piezocomposite transducers as the requires acoustic impedance is lower compared with monolithic ceramic transducers, but the transducer design would have to incorporate a suitable method of electrically connecting the device, such as wiring.

5.2.2 Low Frequency Velocity Results

Initially the longitudinal velocity through the samples was measured at a frequency of 5MHz as described in Section 4.3.2. The time of flight, Δt, was recorded for each sample disc as described earlier and the velocity was then calculated using Equation 3.9. These results are shown graphically in Figure 5.13 compared with the Devaney and Kuster & Toksov scattering models.

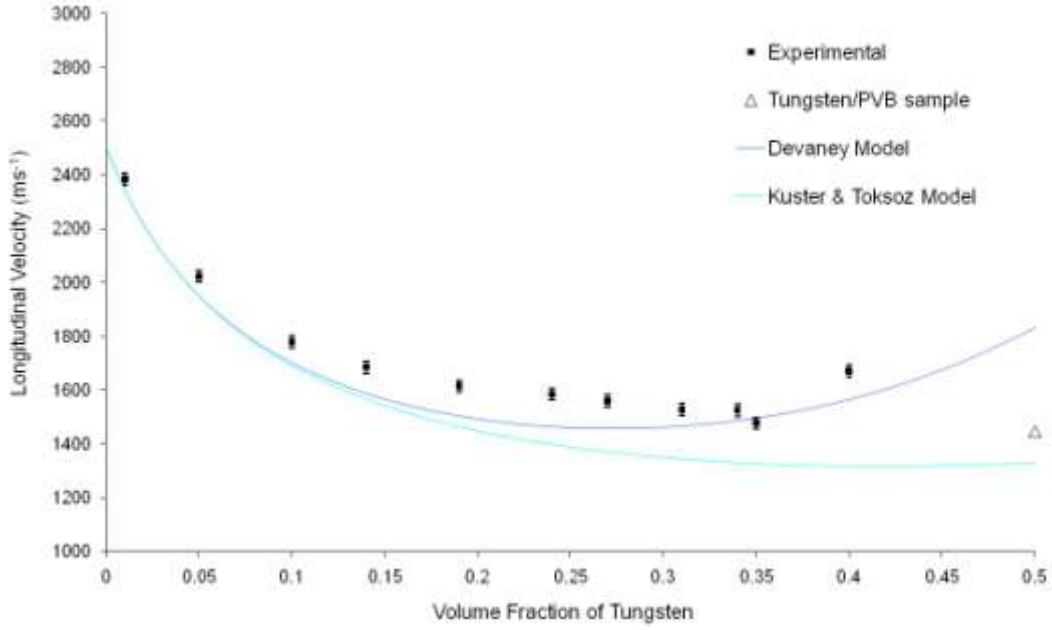

Figure 5.13 *Effect of volume fraction of tungsten loaded epoxy on longitudinal velocity at 5MHz*

These results suggest that the Devaney scattering model rather than the Kuster & Toksov model best describes the propagation of sound through the tungsten epoxy material, although both these scattering models describe the material properties better than any of the elastic models discussed earlier. The acoustic impedance is the product of velocity and density and is shown in Figure 5.14 with the Devaney and Kuster & Toksov scattering models. Both models are the same at volume fractions below 0.15 above which the models start to diverge. The experimental data fit well with the Devaney scattering model as shown, which agrees with other work; the Devaney model has shown the best fit out of the models previously discussed in reported work measured at both 5MHz and 30MHz. [86,87]

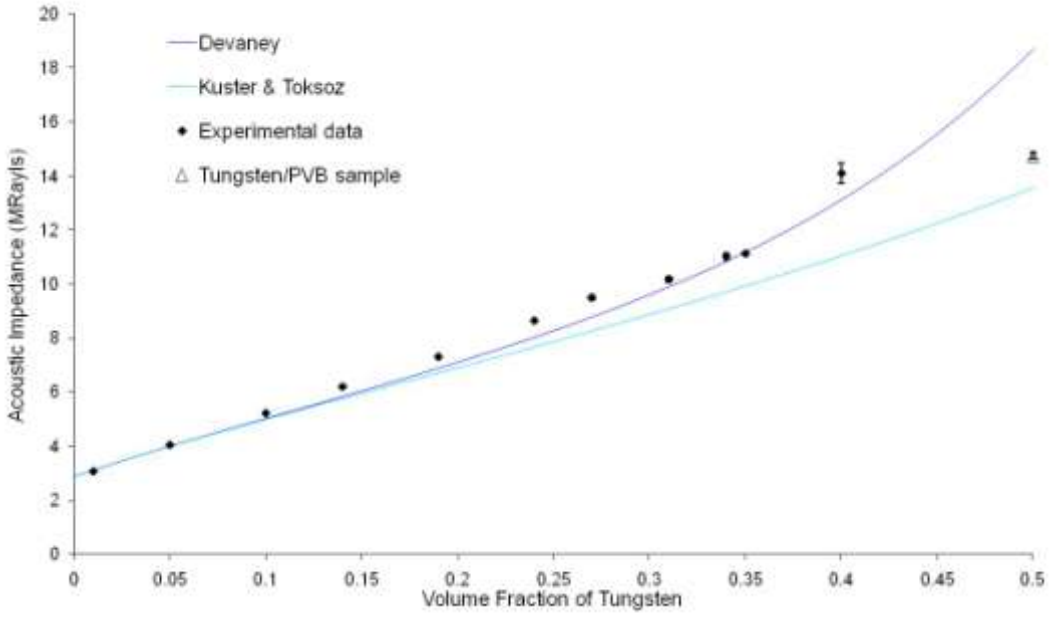

Figure 5.14 *Effect of volume fraction of tungsten loaded epoxy on acoustic impedance at 5MHz*

Reported velocity data for PVB is lower than that for the epoxy used here (V_L= 2350m/s) [69] so it may be expected that the velocity and acoustic impedance of a tungsten/PVB material should be lower than a tungsten/epoxy material of equivalent volume fraction. However, although the PVB/tungsten sample is closer to the Kuster

model this model would be slightly different with the material parameter inputs for PVB, also this sample cannot be described as a two phase material due to the porosity. Therefore the scattering models described in this work should not be used to explain the material properties.

5.2.3 High Frequency Acoustic Results

5.2.3.1 Transducer Characterisation

The transmitting transducer used in the initial set up to characterise the tungsten epoxy samples was known as AFMTH9. It is a 35MHz single element focused piezocomposite transducer housed in a SMA casing. The piezocomposite element has a diameter of 1.5mm and is curved, with a focal distance of 7mm. It was characterised as described in Section 4.3.3.2 in pulse-echo mode and the transmitted signal received from the hydrophone was also recorded for analysis.

The pulse-echo response of the transducer is shown in Figure 5.15, where the echo shown is reflected off the steel cover of the characterisation jig. Figure 5.15b shows the frequency response after carrying out a fast fourier transform (FFT) on the data showing the peak frequency to be approximately 35MHz. The through signal is simpler than the pulse-echo response, which should correspond to the through signal multiplied by itself in the frequency domain, however this may not be exact. The through signal transmitted by the transducer and received with the membrane hydrophone with no sample present is shown in Figure 5.16a. The alignment of the transducer and hydrophone affects the time the through signal arrives and can also affect the frequency response. Alignment was difficult as the focus of the transducer was not straight and the active area of the hydrophone is very small. This meant that the angle of the transmitting transducer had to be adjusted as well as the x and y

positions to obtain the maximum signal. The signal could also be easily lost with small movements of the transmitter due to the small active area of the hydrophone. The FFT shown in Figure 5.16b shows a relatively flat broadband response with a -3dB bandwidth of approximately 22MHz.

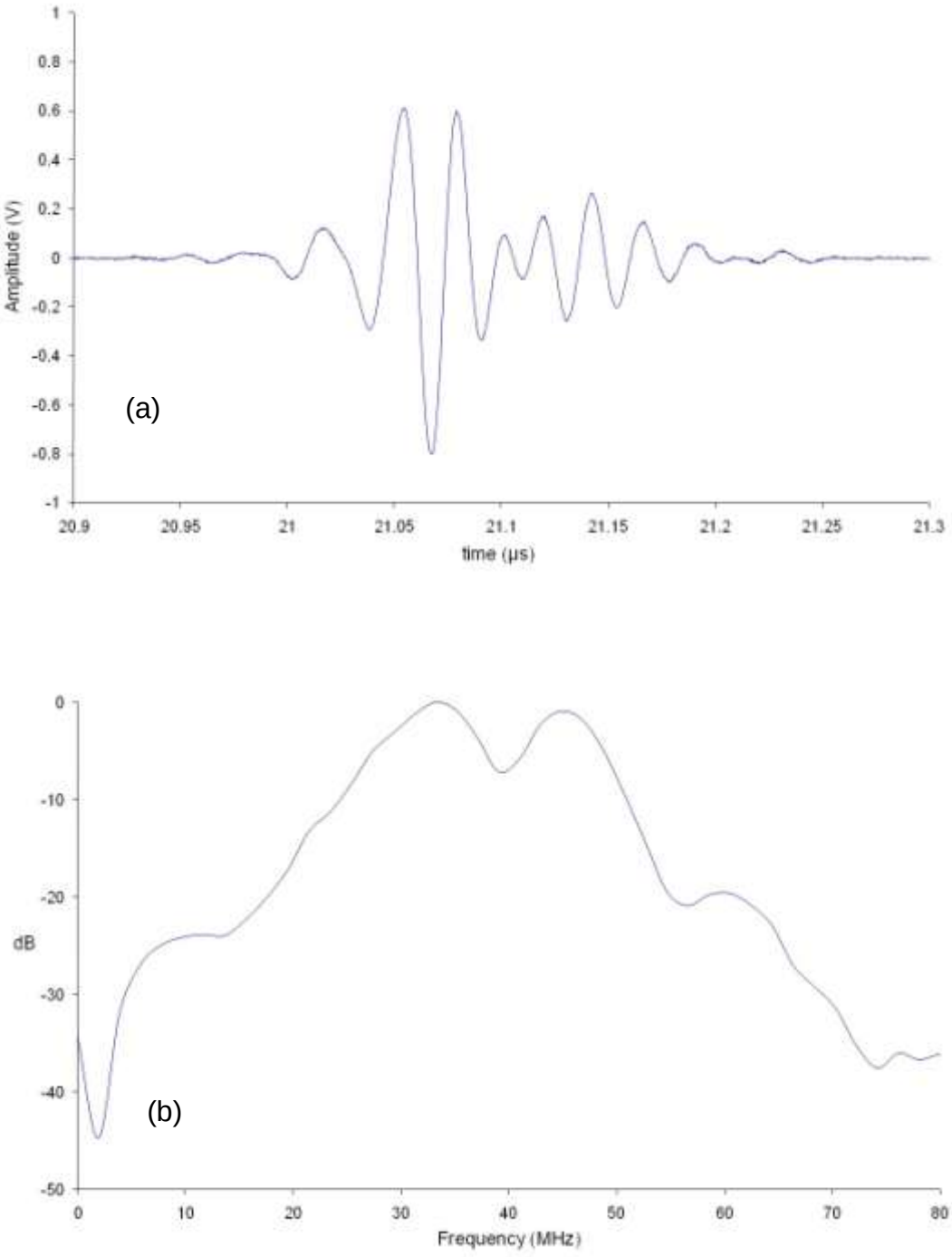

Figure 5.15 *(a) Echo from steel plate (b)FFT of echo*

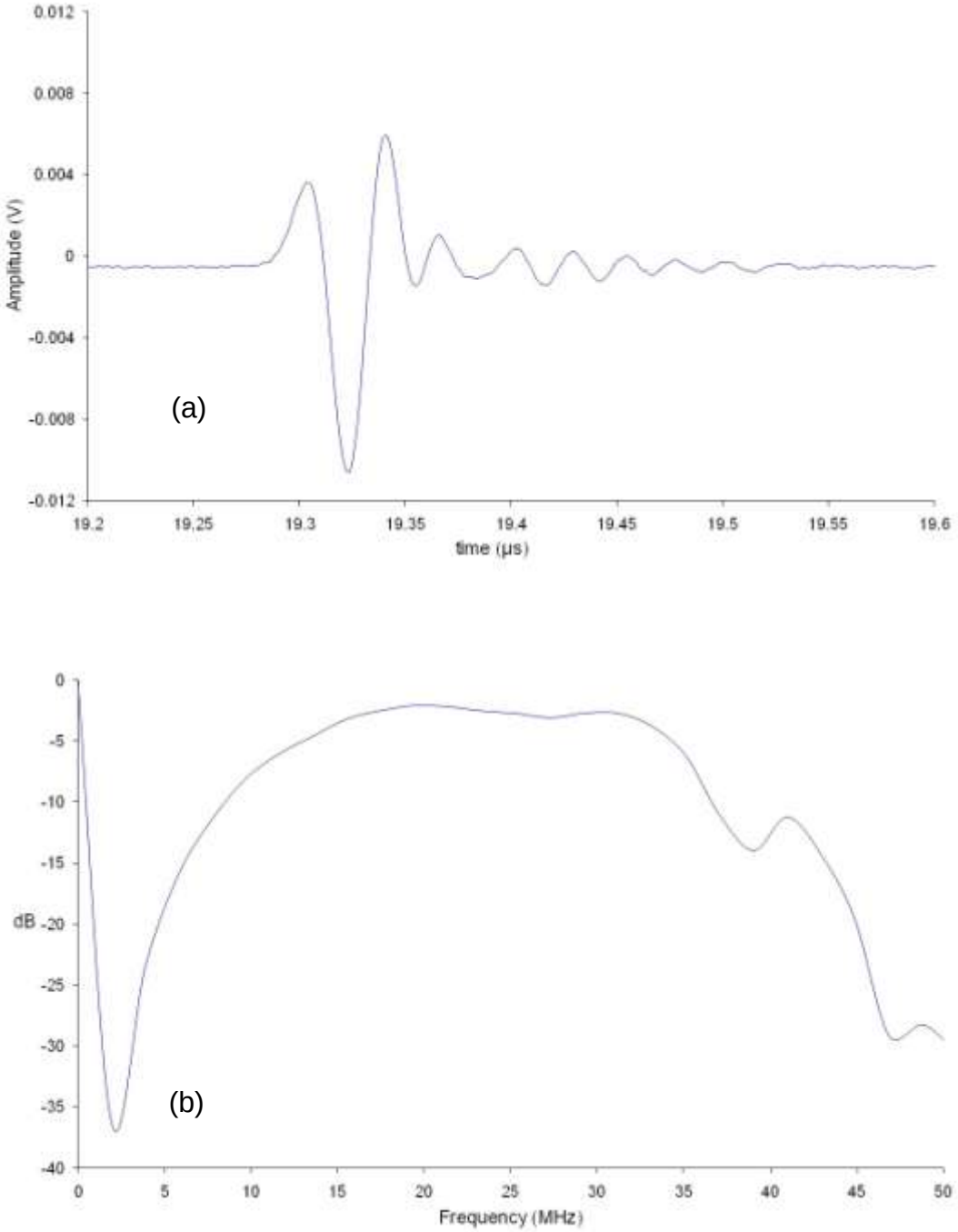

Figure 5.16 *(a) Signal transmitted through water received by hydrophone*

(b) Frequency response of through signal

5.2.3.2 Longitudinal and Shear Wave Velocity

The recorded data from the transmitted and reference signals at normal incidence from the measurements described in Section 4.3.3.2 are used to determine the longitudinal velocity and attenuation of ultrasound through the samples. Some of the measurements at normal incidence displayed pulses in the transmitted signal due to reverberations within the sample. The transmitted signal through the 0.10 tungsten volume fraction sample at normal incidence is shown in Figure 5.17. The sample thickness is 260μm. The pulse at approximately 19.5μs on the time axis is due to the echo from the far face of the sample. When rotating the sample to excite shear waves it was ensured that the transmitted signals due to the shear waves could be distinguished from any reverberations or echoes that might be observed. The samples were also thick enough for the reverberations not to impinge on the received directly transmitted signal. The transmitted wave and the echo can be clearly distinguished from each other in Figure 5.17 and the signals may be easily isolated for analysis.

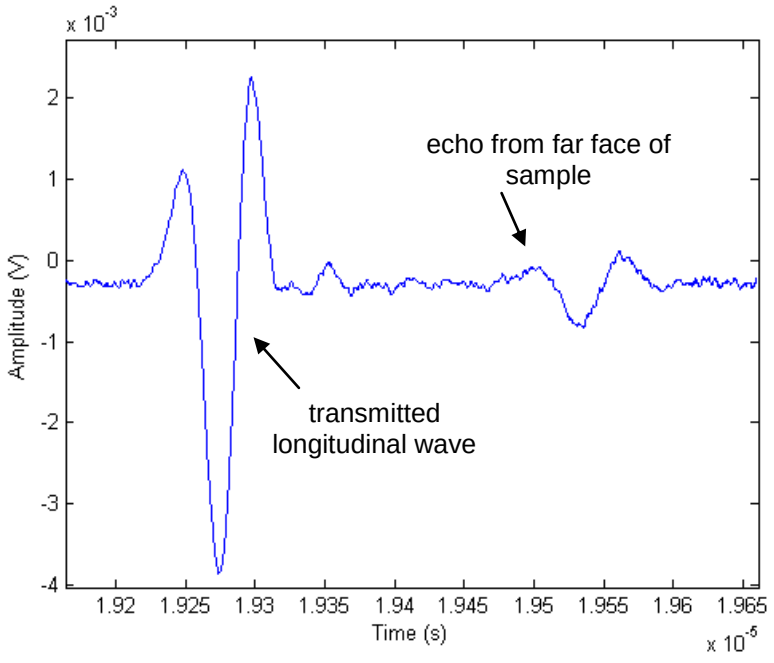

Figure 5.17 *Received output from signal transmitted through 0.10 tungsten volume fraction epoxy sample at normal incidence showing echo from rear face of sample*

The longitudinal velocity is determined by calculating the time delay between the reference signal and the received signal due to the transmitted longitudinal wave at normal incidence. Instead of recording the arrival times observed on the oscilloscope, both signals were recorded and Δt calculated using the cross correlation function in MATLAB as described in Chapter 3, giving a more accurate and less subjective result. The value obtained for Δt was validated for each data set by plotting the signals together with the transmitted signal shifted along the time axis so it corresponds to the reference signal. This is shown in Figure 5.18 for a 220μm thick sample of RX771C /HY1300 epoxy at normal incidence. The solid blue line is the reference signal without the sample present and the dotted line is the transmitted signal with the sample present arriving before the reference signal with a reduced amplitude.

At oblique incidence, when the sample is rotated, two transmitted waves can be received; one due to the longitudinal wave and one due to a transmitted mode-converted shear wave. All the tungsten epoxy samples transmitted shear waves at an incidence angle of 40° so this data set was used calculate the shear wave properties. The reference signal and the received output at 40° incident angle through the epoxy sample is shown in Figure 5.19a. At this incident angle, the longitudinal wave amplitude is almost zero as it is beyond the first critical angle. The first critical angle is higher for the tungsten epoxy samples so the two waves due to the transmitted longitudinal and shear waves are clear on the output, as shown in Figure 5.19b for the 0.25 tungsten volume fraction sample at the same incident angle of 40°. Therefore it is necessary to isolate the shear wave for analysis when the longitudinal wave has a greater amplitude than the shear wave.

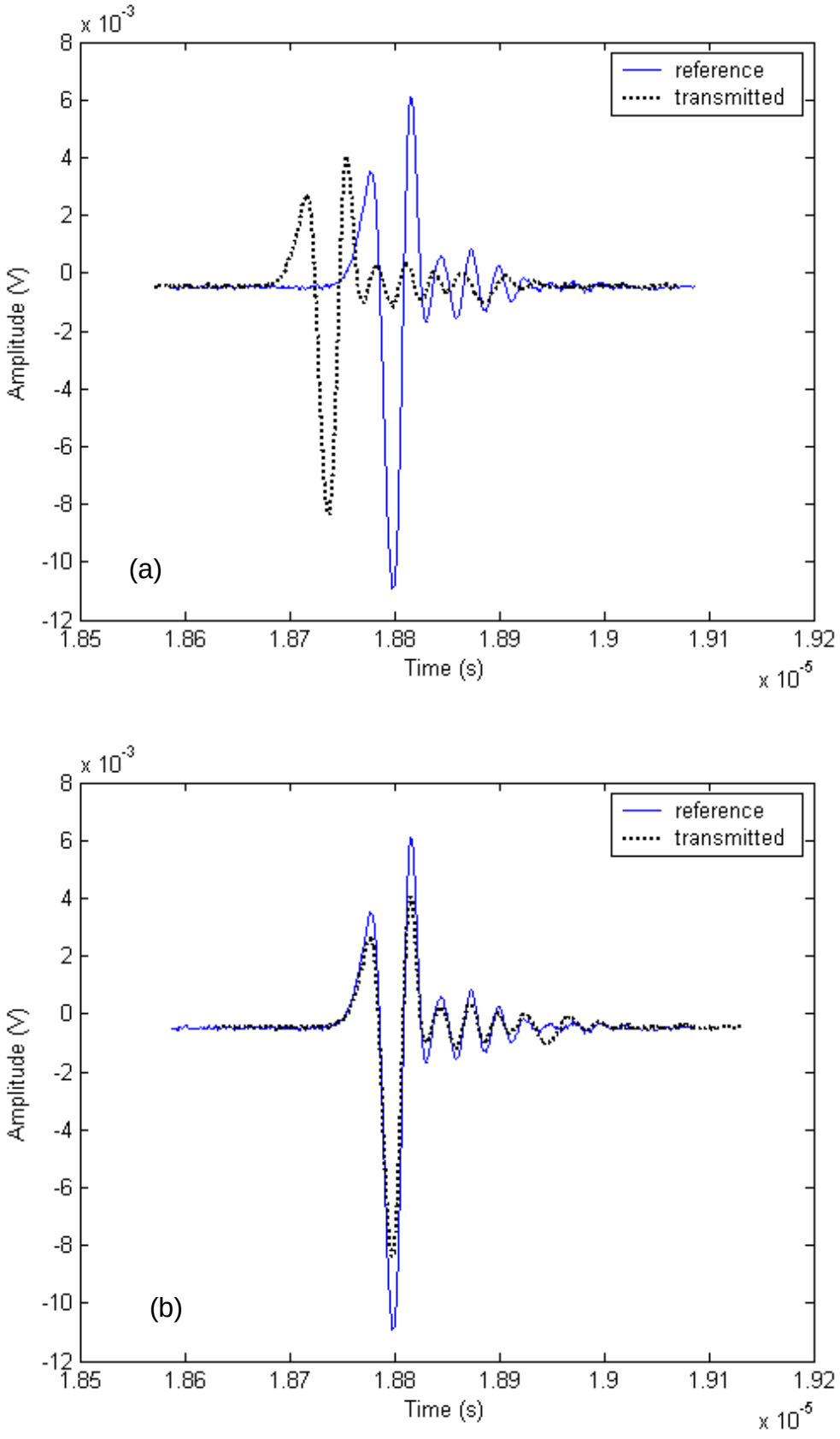

Figure 5.18 *(a) Transmitted and reference signals through 220μm thick sample of RX771C/HY1300 epoxy at normal incidence. (b) Correlated signals to allow calculation of Δt.*

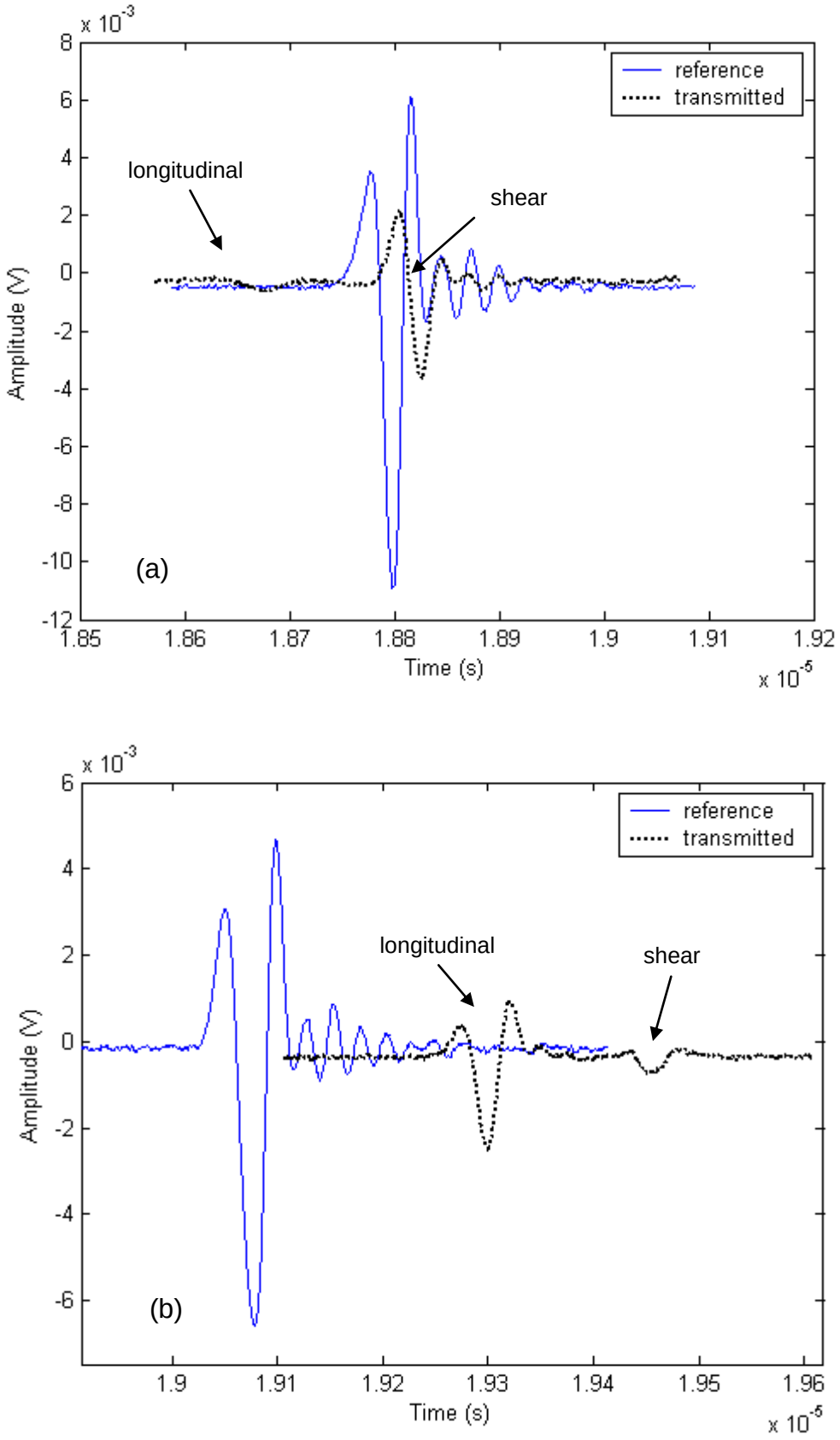

Figure 5.19 *Reference and transmitted signals through (a) 220μm thick sample of RX771C/HY1300 epoxy and (b) 265μm thick sample of 0.25 volume fraction tungsten epoxy both recorded at 40° incident angle*

The longitudinal and shear velocities were calculated using Equations 3.9 and 3.28 respectively and the acoustic impedances calculated by multiplying the velocity by the density of each sample from Table 5.2.

The variation of both longitudinal and shear wave velocity as a function of tungsten volume fraction in the composites is shown in Figure 5.20. The data is compared with the Devaney model, which was calculated using the material properties of the epoxy [104] and tungsten [109] as follows: $\rho_{tungsten}$ = 19.25kg/m^2, ρ_{epoxy} = 1.149kg/m^2, $K_{tungsten}$ = 310GPa, K_{epoxy} = 5.1GPa, $G_{tungsten}$ = 161GPa and G_{epoxy} = 1.57GPa. The dotted lines represent the variation of the Devaney model with a 10% error in the material properties input into the model. Whilst the model lies outside the measurements in some case even when errors are included, there is nevertheless clear correspondence.

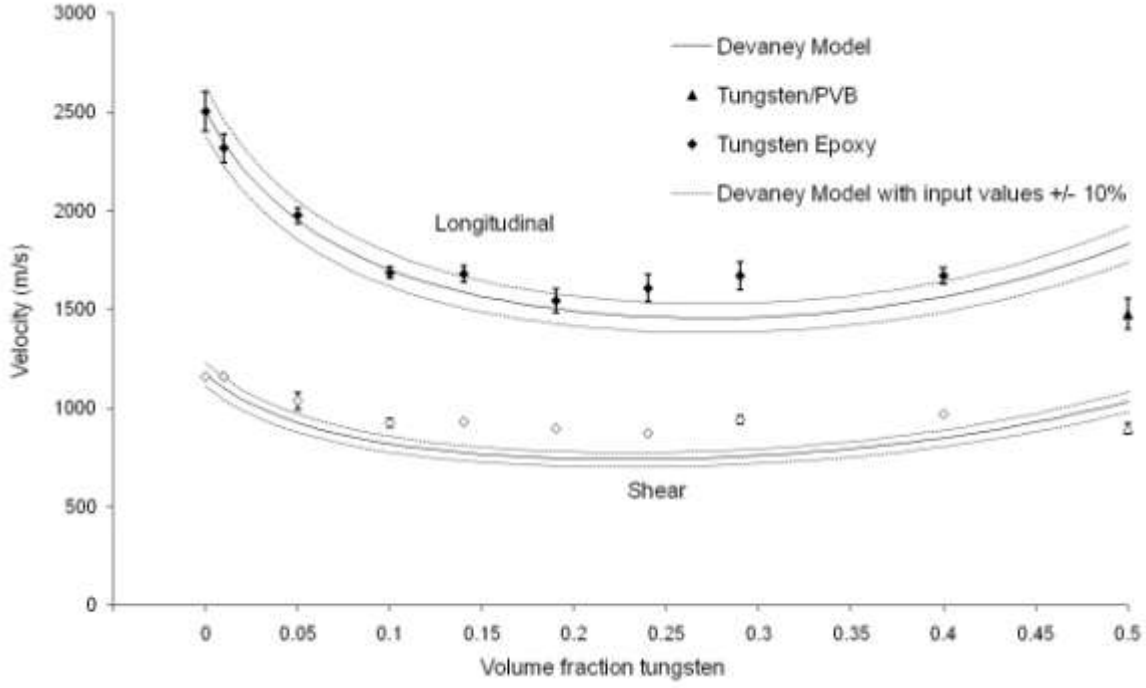

Figure 5.20 *Effect of tungsten volume fraction on longitudinal and shear wave velocity in epoxy measured at 35MHz*

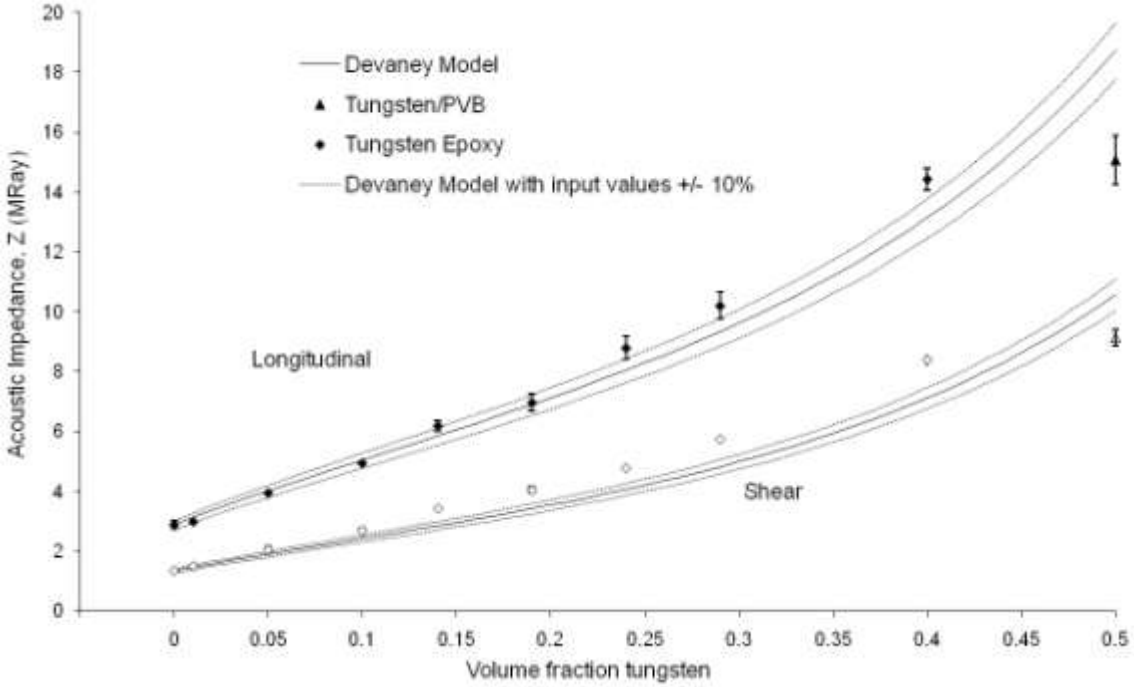

Figure 5.21 *Effect of tungsten volume fraction on longitudinal and shear wave acoustic impedance in epoxy measured at 35MHz*

The data in Figure 5.20 shows the velocity following the trend of the Devaney model. The longitudinal velocity initially decreases with the amount of filler and then begins to level off. As the number of scatterers in the material increases, the effective path length for the ultrasound increases, reducing velocity. Although the velocity decreases with increasing amounts of tungsten the density increases linearly with the amount of tungsten so the overall effect is a monotonic but non-linear increase in acoustic impedance, as shown in Figure 5.21.

Comparing the results measured at 5MHz in Figures 5.13 and 5.14 to these results measured at 35MHz it is clear that the velocity values do not significantly change (the difference between the two measurements is within 100m/s for each volume fraction and there is no trend showing the velocity being consistently higher or lower at a specific frequency), so it can be deduced that velocity is independent of frequency. This is useful because it means that the Devaney model can be used to approximate

the velocities at any frequency between the two measurement frequencies. It further confirms that the materials are acting in all cases in a diffusive scattering mode and not dispersive. The acoustic impedance values are also important for transducer design. It can be seen that to match the acoustic impedance of a 0.5 volume fraction ceramic piezocomposite (~15MRayl), a relatively high volume of tungsten is required. Therefore the volume fraction fabrication limit affects acoustic impedance and in turn affects the pulse length. However, a compromise must be made when considering the acoustic impedance value of a backing material to achieve a reasonably short pulse and a greater sensitivity. Therefore a backing with an acoustic impedance value between 5MRayl and 10MRayl would be desired to match the composite, depending on what is most important. A transducer with a backing with an impedance value close to the value of the piezocomposite will have a shorter pulse than a transducer with a lower impedance value backing but will have a reduced sensitivity. This is shown in Figures 5.22 and 5.23. ODM data showing how the acoustic impedance of the backing affects the pulse length of a 0.5 ceramic volume fraction composite transducer is shown in Figure 5.22. As expected the pulse length decreases as the backing impedance approaches the impedance value of the composite (~15MRayl). The reduced sensitivity of the composite is with a backing of 15MRayl compared to 5MRayl is shown in Figure 5.23, where the pulse amplitude is significantly reduced.

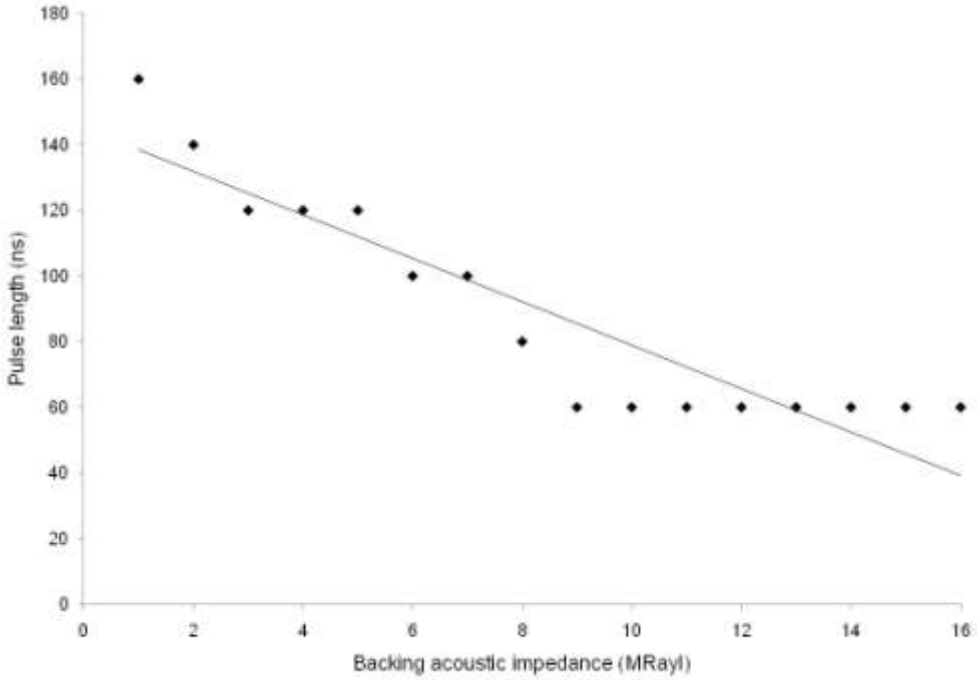

Figure 5.22 ODM data showing how backing impedance affects pulse length for a composite transducer

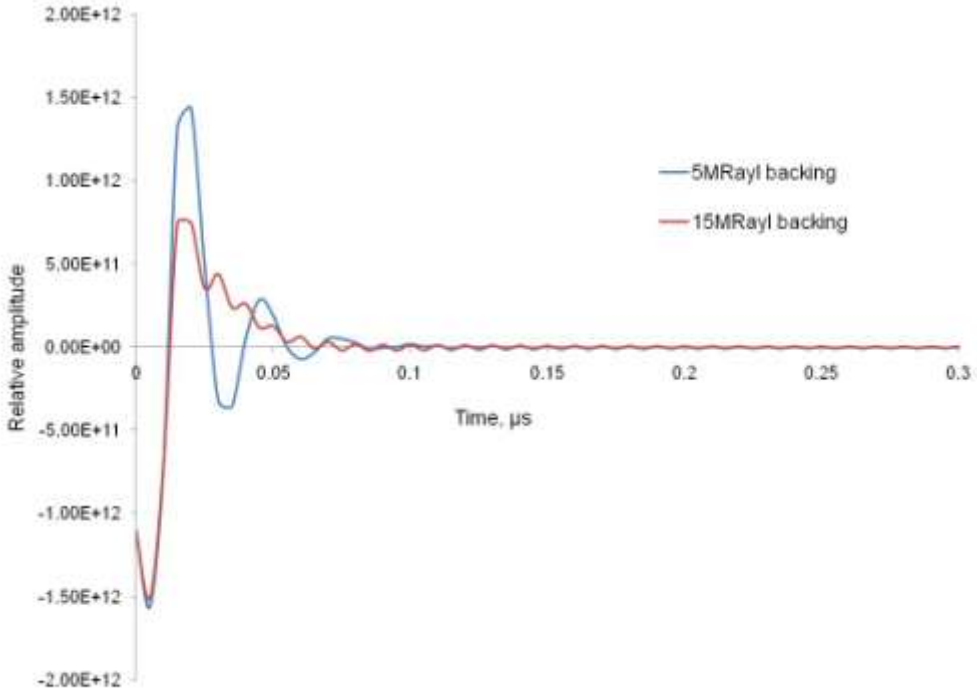

Figure 5.23 Pulse data generated from ODM showing reduced sensitivity of a composite transducer with 15MRayl backing compared to 5MRayl backing

5.2.3.3 Longitudinal and Shear Wave Attenuation

The amplitudes of the transmitted signals through the samples and reference signal without a sample present were recorded as described in Section 4.3.3.2. The attenuation of the transmitted longitudinal waves was calculated using Equation 3.12. The calculated longitudinal attenuation in dB/mm of the tungsten epoxy samples is shown in Figure 5.24. There is an attenuation peak observed at 0.05 tungsten volume fraction, which corresponds with other work where a peak was reported between 0.07 and 0.09 tungsten volume fraction with a particle size of 5μm measured at 30MHz. [86]

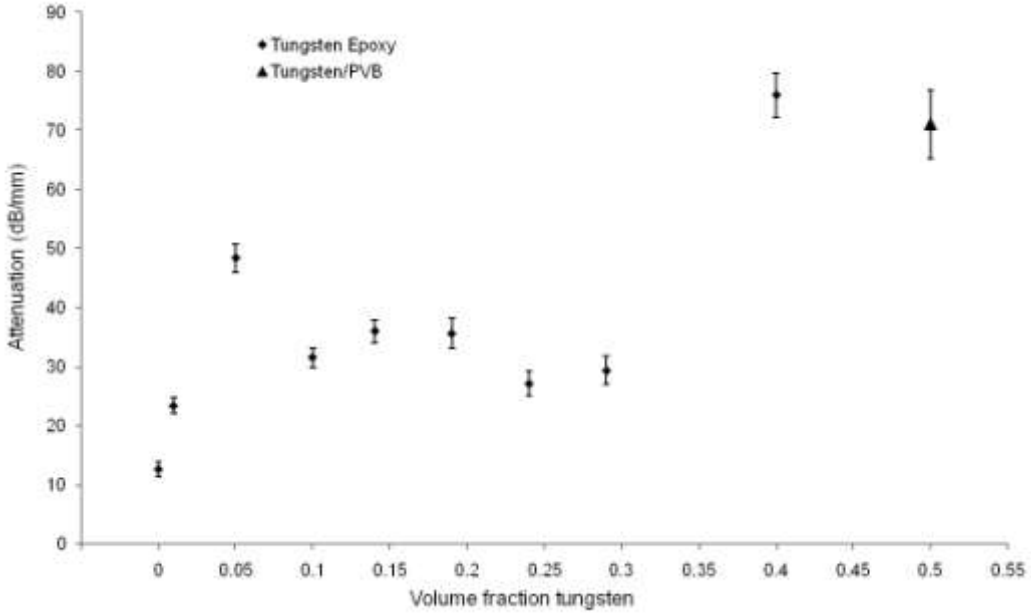

Figure 5.24 *Effect of tungsten volume fraction on the longitudinal attenuation through epoxy measured at 35MHz*

These attenuation results are comparable to other published work characterising tungsten epoxy at high frequencies where longitudinal attenuation values of 25dB/mm for 0.25 tungsten volume fraction epoxy at 30MHz have been reported, [86] compared to 27dB/mm measured here at 35MHz. The values measured here at 35MHz are also higher than measurements taken at lower frequencies, [56] showing that attenuation is dependent on frequency, as expected. A 0.10 tungsten volume fraction Spurr epoxy

composite was measured at 5MHz by Grewe et al [56] and the measured acoustic impedance is similar to the results here but the attenuation is considerably lower at 0.69dB/mm compared to 31dB/mm measured at 35MHz here. A high attenuation is required for acoustic backings so conventional backings used in low frequency devices will have a higher attenuation when operating at high frequencies. Knowledge of the attenuation values at specific operating frequencies is useful for transducer design. The backing material must be of a sufficient thickness that the sound is absorbed before it can be reflected back towards the transducer, whilst minimising the volume of backing for reasons of cost and physical transducer design convenience.

When the epoxy phase is more then 70% the tungsten epoxy composite can be assumed to have a 0-3 connectivity where each particle is surrounded by the epoxy matrix. [56] Microstructural examination of the materials produced here suggest that this is reasonable, as the tungsten particles are distributed well in the epoxy apart from some small areas of agglomeration. Therefore scattering effects will describe the attenuation behaviour of the tungsten epoxy samples up to 0.3 tungsten volume fraction, as each particle is acting as a scattering site. The scattering power of a particle is related to the difference in acoustic impedance values of the particle and epoxy matrix. Other factors have also been observed to affect attenuation including particle size and the adhesion between the epoxy and filler particle. [56] If the peak in attenuation observed at approximately 0.05 tungsten volume fraction is due to increased scattering at this particular volume fraction, the position of the peak will be affected by particle size. The surface to volume ratio decreases with increasing particle size so the peak could be expected to be at higher volume fractions with larger particle sizes.

At some higher volume fraction (>0.3) the composite cannot be described as having 0-3 connectivity. When filler particles are touching each other a network of connecting particles will be created. Therefore, attenuation will occur via processes other than scattering and may depend more on the actual attenuation coefficient of the filler material. This could explain the high attenuation values obtained for the 0.4 volume fraction milled epoxy sample and the tungsten/PVB sample. Tungsten has a high attenuation coefficient depending on the grain structure, and it is expected to be significantly higher than that of epoxy, which depends on the degree of crystallinity and cross-linking. [56] Additionally both the milled samples are not two phase structures as the porosity can be considered to act as a 'third phase'. The pores will affect both the acoustic impedance of the material and the attenuation values.

An alternative method of calculating the attenuation is curve fitting with the theoretical transmission coefficient graphs as described in Section 3.3.8. This method can give a greater degree of confidence in the result if the experimental data correlates well with the theory over a large range of incident angles. It also gives an indication how accurate the measurements are compared to the theory. A comparison of the experimental data for the longitudinal wave amplitude relative to the reference signal amplitude is compared with the theory in the following figures. The theoretical curve has been fitted with the experimental data by inputting a longitudinal attenuation value into Equation 3.34.

The curve fitting data for the RX771/HY1300 epoxy sample is shown in Figure 5.25. The experimental data increases first with incident angle as shown then follows the expected trend. The initial increase is likely to be because of small inaccuracies in the rotation of the sample. The theoretical curve was obtained by using the measured

velocity and density parameters input into Equation 3.34. The red line represents the attenuation calculated from the normal data shown in Figure 5.24. Over the full range of incident angles this value may not represent the experimental data fully therefore the value with the smallest mean square error (MSE) for each data point is also plotted.

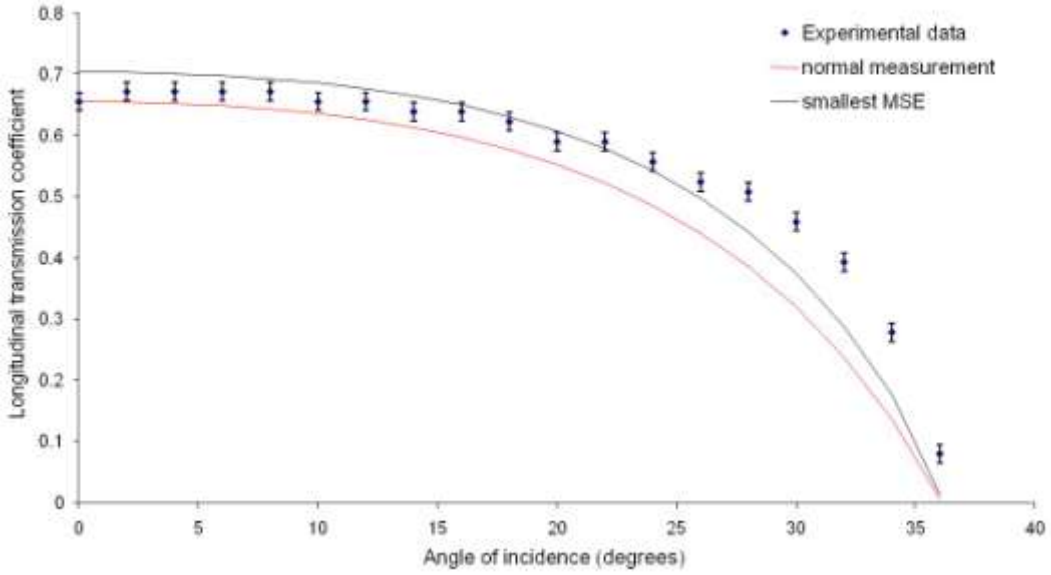

Figure 5.25 *Longitudinal attenuation curve fitting data for 220μm thick RX771/HY1300 epoxy sample.*

The ratio of longitudinal and shear velocities determines the first critical angle where the longitudinal transmission coefficient is zero. Therefore the correlation of the experimental data and theory at this point will be an indicator of the accuracy of the velocity measurements.

Table 5.4 shows the longitudinal attenuation values obtained with the normal measurement data and curve fitting with the whole incident angle range.

Table 5.4 Longitudinal attenuation values for tungsten epoxy samples

Tungsten Volume Fraction	Normal Measurement (Np/mm)	Smallest MSE (nearest 0.1Np/mm)
0	1.42	1.1
0.01	2.64	2.8
0.05	5.46	5.3
0.10	3.55	3.4
0.14	4.06	4.0
0.19	4.03	4.1
0.24	3.07	-
0.29	3.32	3.6
0.40 (milled)	8.57	7.7
0.50 (W/PVB)	8.02	9.9

The curves for the 0.01 and 0.05 tungsten volume fraction samples are shown in Figures 5.26 and 5.27 respectively. The experimental data for these samples generally compare well with the calculated curves, apart from where the data for the 0.05 tungsten volume fraction epoxy sample deviates by increasing after the expected decrease at approximately 30° shown in Figure 5.27. This is probably a problem with the rotation mechanism of the sample holder.

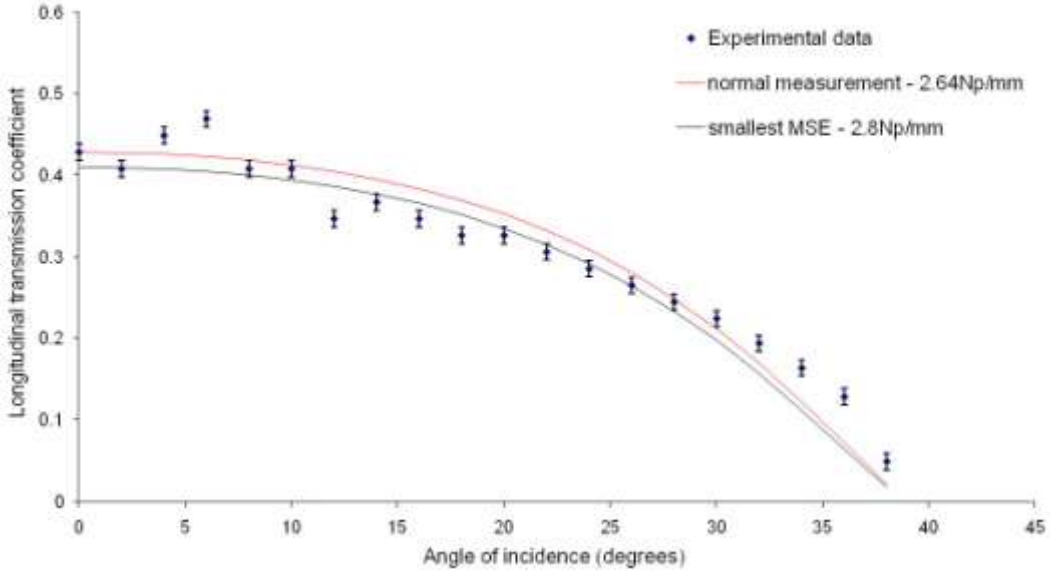

Figure 5.26 *Longitudinal attenuation curve fitting data for 0.01 tungsten epoxy sample*

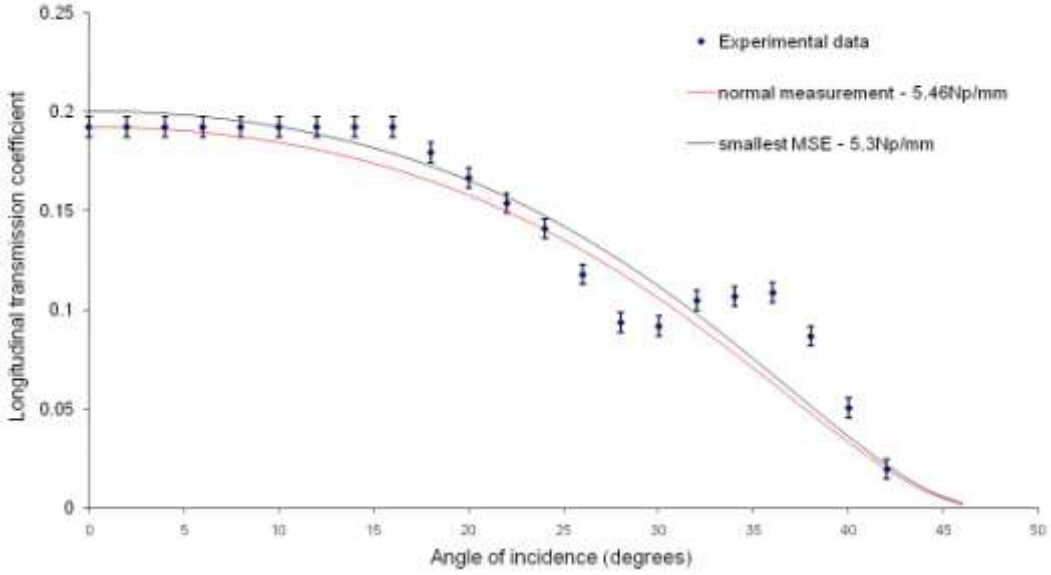

Figure 5.27 *Longitudinal attenuation curve fitting data for 0.05 tungsten epoxy sample*

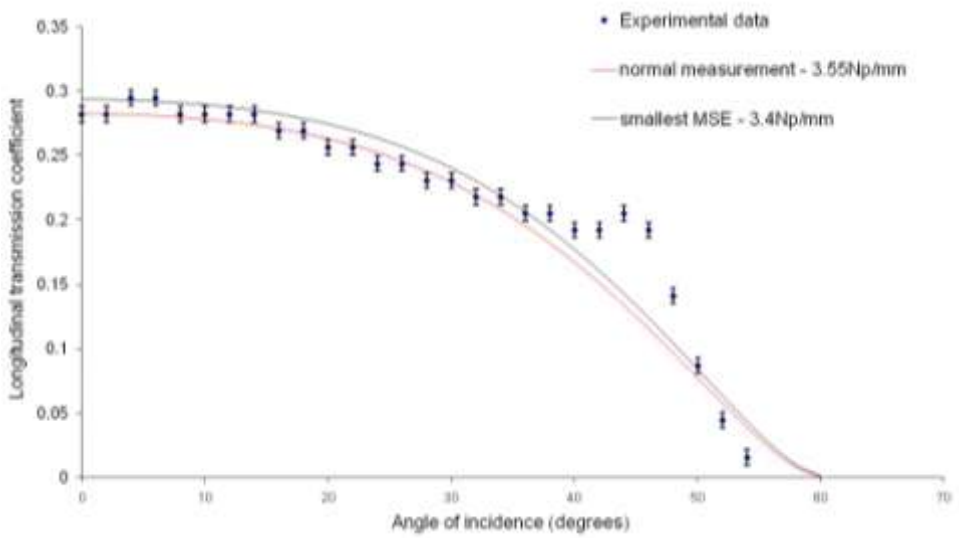

Figure 5.28 *Longitudinal attenuation curve fitting data for 0.10 tungsten epoxy sample*

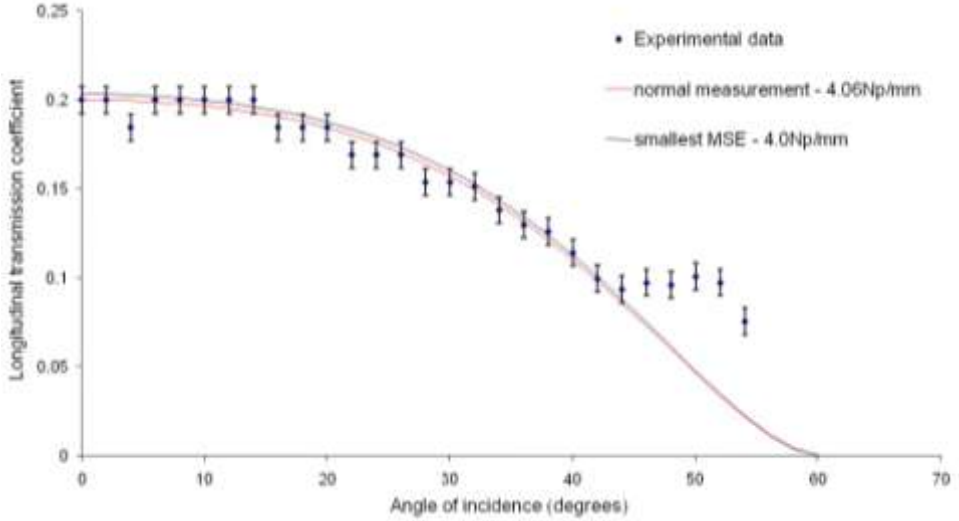

Figure 5.29 *Longitudinal attenuation curve fitting data for0.14 tungsten epoxy sample*

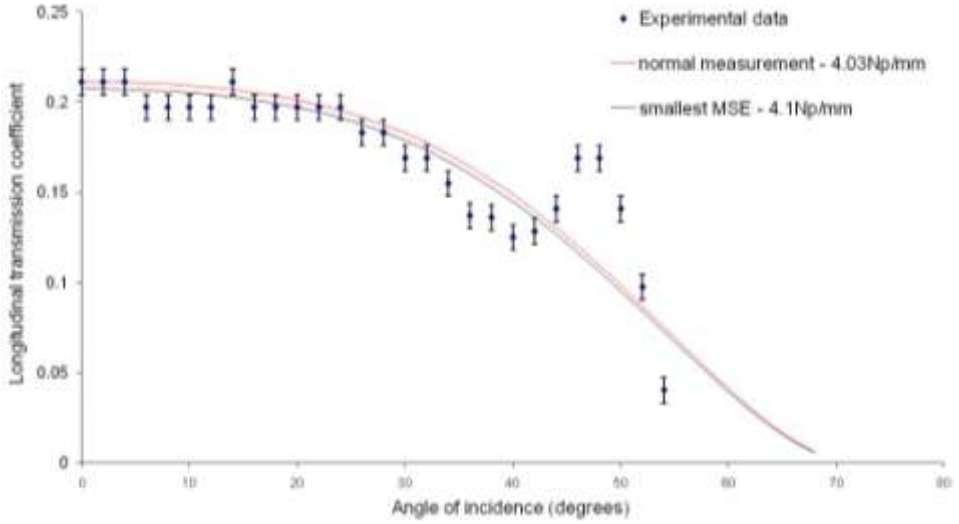

Figure 5.30 *Longitudinal attenuation curve fitting data for 0.19 tungsten epoxy sample*

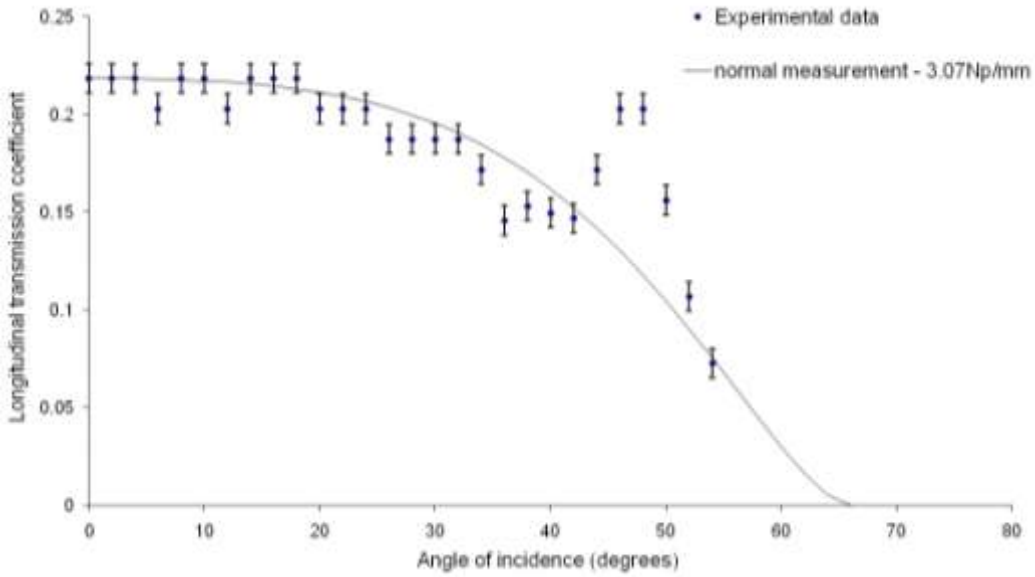

Figure 5.31 *Longitudinal attenuation curve fitting data for 0.24 tungsten epoxy sample*

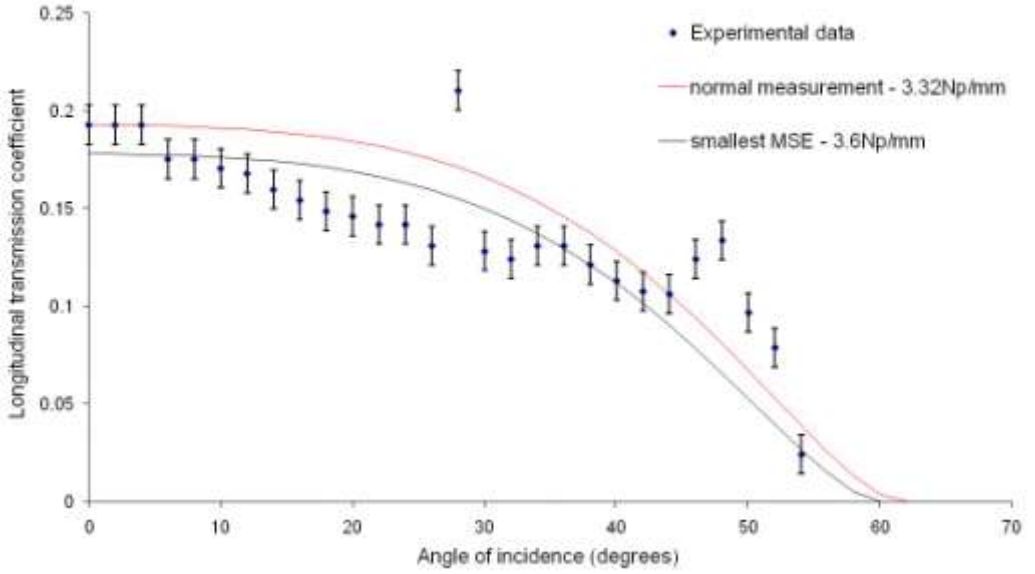

Figure 5.32 *Longitudinal attenuation curve fitting data for 0.29 tungsten epoxy sample*

The attenuation curves for the 0.10-0.30 tungsten volume fraction samples are shown in Figures 5.28-5.32. The experimental data again generally fit the calculated curves well apart from some minor anomalies up to approximately 42° where the experimental data generally deviates from the curve. As this seems to be a feature of many of the samples, it is most likely due to errors in the sample holder. As described in Section 4.3.3 the sample holder had to be modified by adding tape to support the

samples. As the sample holder was rotated through the incident angle range the signal was observed to be disrupted at an angle of approximately 60°, therefore it is possible that the modified sample holder affected the signal at a lower angle than that around 42º. A new sample holder was designed for further measurements with the alumina epoxy samples discussed in Chapter 6 to reduce these errors. The improved sample holder did seem to improve some of the problems, but there were additional problems with the rotation of the sample, which are described in the following chapter.

The attenuation curve for the milled 0.4 tungsten volume fraction sample is shown in Figure 5.33. Apart from one major anomaly at approximately 40º the experimental data fits the trend of the calculated curve well.

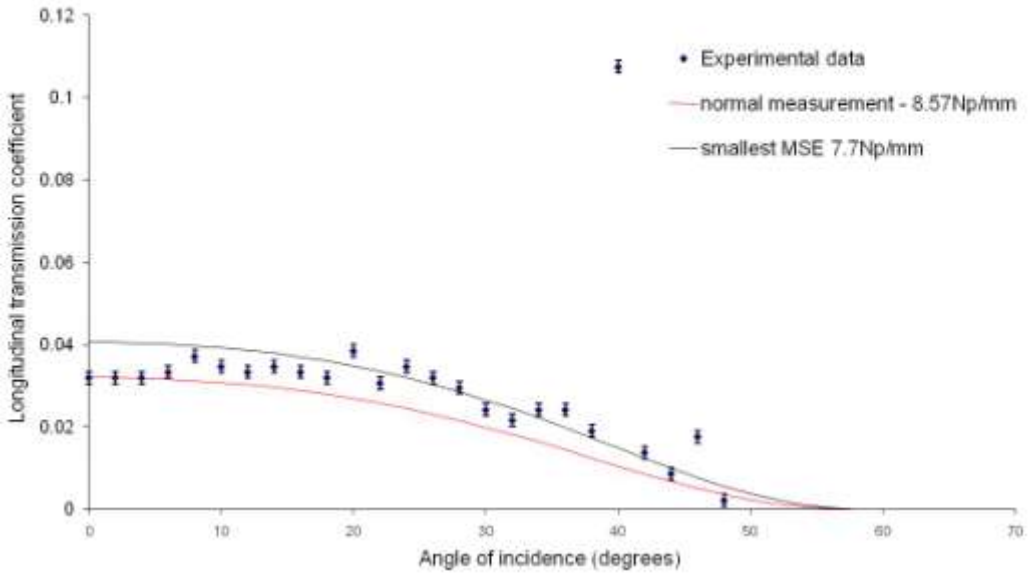

Figure 5.33 *Longitudinal attenuation curve fitting data for 0.4 milled tungsten epoxy sample*

The attenuation curve for the tungsten/PVB sample is shown in Figure 5.34. The experimental data does not match the calculated curve well after approximately 10º. The reduction in amplitude ratio after this angle means that the curve of "best fit"

found with the smallest mean square error for each data point is dramatically different to the attenuation value measured at normal incidence, so the confidence in this value is low. The poor correspondence if the experimental data with the theoretical attenuation curve could be due to the porosity in this sample, as air has a high attenuation, hence ultrasound travels poorly through air.

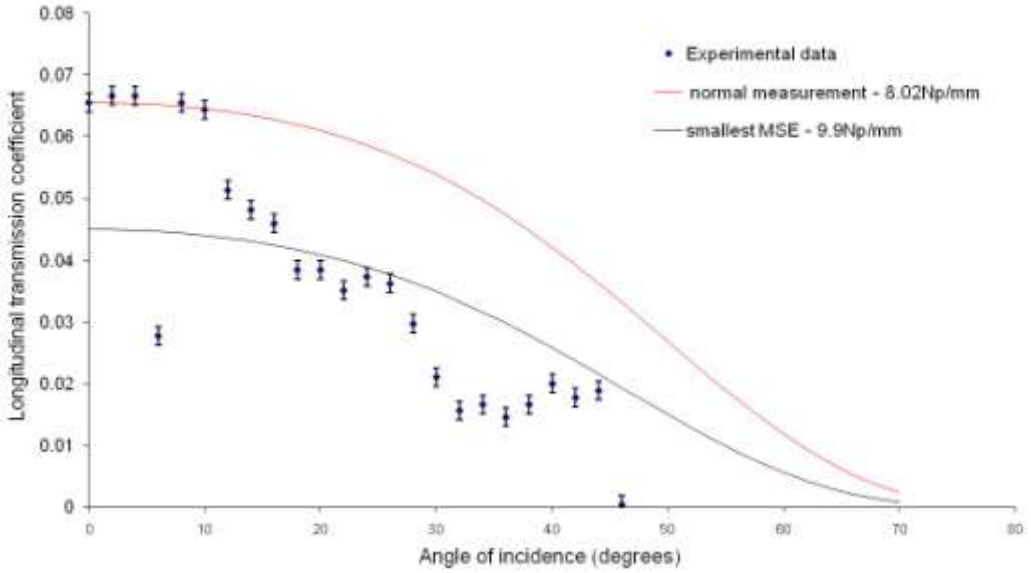

Figure 5.34 *Longitudinal attenuation curve fitting data for 0. 5 tungsten/PVB sample*

As mentioned previously the shear velocity calculations were done at an incidence angle of 40° for all samples. The first critical angle for epoxy is approximately 38° and this value increases with the amount of tungsten in the epoxy as the velocities decrease. The shear wave velocity at incident angles below the first critical angle is calculated by isolating the shear wave as two waves are transmitted through the sample due to both longitudinal and shear waves in the sample. The amplitude of the shear wave below the first critical angle is small and not significant enough to calculate the shear attenuation. Experimental data at incident angles greater than the first critical angle are much more appropriate to determine shear attenuation as the data amplitudes here are much larger as only a shear wave is transmitted through the

sample. The outcome of these issues is that the shear wave attenuation could be determined only for the epoxy and 0.01 volume fraction tungsten epoxy samples.

The curve fitting data for the shear attenuation of the epoxy sample is shown in Figure 5.35. The curve was plotted using Equation 3.35. The maximum shear peak was fitted with the calculated curve with a shear attenuation value of 3.55Np/mm. The experimental data points fit very well until approximately 46º where the data deviate from the curve. This is again likely to be because of the geometry of the sample holder interfering with the signal when rotated, effectively causing an incident angle limit for valid measurements.

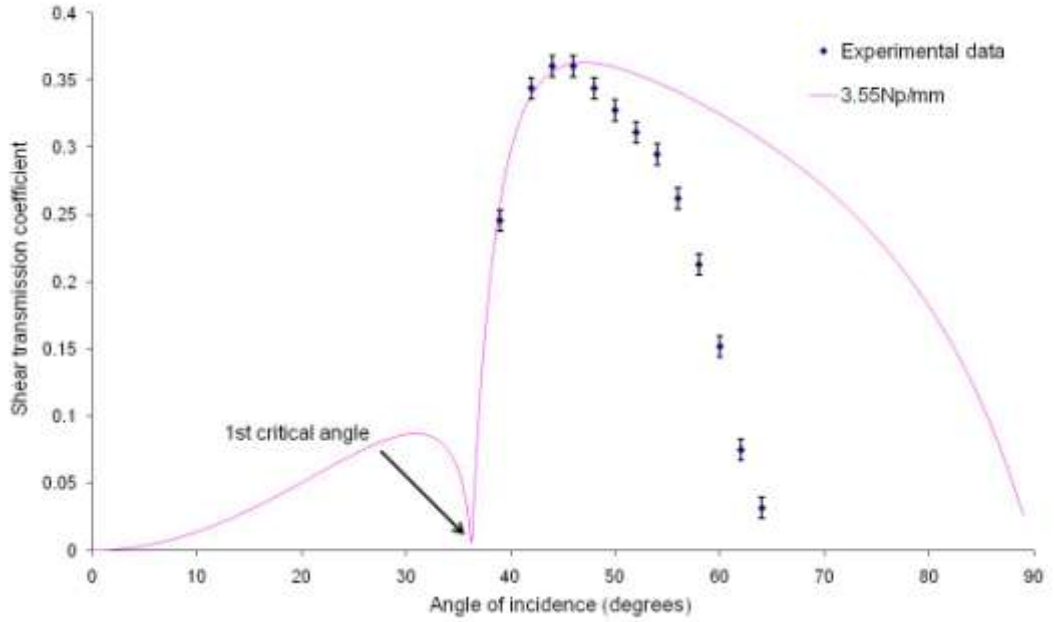

Figure 5.35 *Shear attenuation curve fitting data for RX771C/HY1300 epoxy sample.*

5.3 Summary

Tungsten epoxy samples were fabricated with Alpha Aesar powder with a reported particle size of 1-5μm to achieve a reasonable level of loading, although experimental particle size data indicates the real particle size distribution is different. Tungsten volume fractions up to 0.5 were achieved but only those up to 0.3 could be controlled. Other fabrication techniques were developed to fabricate higher volume fractions as the viscosity increased, but these techniques did not allow the amount of tungsten in the final sample to be controlled; using solvent to decrease viscosity and milling higher volume fractions resulted in porosity in the material. SEM analysis showed that the tungsten was generally well dispersed in the epoxy but there was agglomeration observed in higher volume fraction samples, although the sizes of the pores were not larger than the wavelength in the materials at 35MHz, as the velocity results indicate that specular scattering was occurring. Porosity was observed in the milled samples and was estimated to be 5% volume in the milled epoxy and 32% in the tungsten/PVB sample, although the SEM images obtained for this sample suggest the porosity value is lower than this. The porosity did not seem to affect the velocity results, and hence the acoustic impedance but there was evidence that the porosity may have significantly increased the attenuation in the high tungsten volume fraction samples.

The velocities measured through the samples at 5MHz and 35MHz were not significantly different and followed the expected trend of the Devaney scattering model. Attenuation data compares well with other reported work at high frequency and is significantly higher than other measurements taken at lower frequencies, showing that attenuation is frequency dependent. It was found that using a curve fitting approach to determine attenuation can give a greater degree of confidence in

the result. Shear attenuation could not be determined for all samples as the first critical angle where the shear amplitude significantly increases was not always in the measurement range so the shear amplitude was too low to determine attenuation.

These results show that tungsten epoxy is suitable for transducer backing applications and volume fractions up to 0.3 can be tailored to suit the application giving acoustic impedance values in the range of 3-10MRayl, which is suitable for backing composites as they have lower acoustic impedance than other ceramic elements. For Z values greater than this, higher volume fractions are required that can be centrifuged, resulting in conductive backings. An alternative method of electrically connecting the transducer is required to use non conducting backing, such as wiring, although this is required for array devices in any case.

CHAPTER 6

Alumina-Epoxy Composites

This Chapter presents the results for the alumina filled epoxy composite materials. The characterisation of the alumina powders is discussed including the rationale for choosing the powders that were finally used from the available powders presented in Table 4.1. Different grades of alumina were chosen to investigate the effect of particle size on the acoustic properties. Although tungsten materials perform well as acoustic backing materials alumina may be useful to avoid shorting in array devices and costs considerably less than tungsten. Alumina filled epoxy may also be used for matching layers, which require low attenuation values, and it is expected that using small filler particles will reduce the effect of increasing filler volume fraction on attenuation.

6.1 Powder Characterisation

6.1.1 Particle Size Analysis

The particle size data for the alumina powders measured are summarised in Table 6.1 and the particle size distribution data for the individual powders are shown in Figures 6.1-6.4.

Table 6.1 Particle Size Data for Alumina Powders

Alumina Type	Particle Size (μm)		
	d10	d50	d90
CT3000 SG	0.35	0.89	6.93
CR15	0.37	0.95	2.08
MA95	1.95	5.92	10.38
Nano	1.78	10.14	23.96

The data for both CT3000SG and CR15 correspond quite well to the manufacturer's data given in Table 4.1, with both grades having a d50 value around 1 micron. However, the particle size distribution plots shown in Figure 6.1 and 6.2 differ dramatically. A relatively narrow distribution is shown in Figure 6.1 for CR15 alumina, but the data for CT3000 SG however, shown in Figure 6.2, shows a broader distribution with a secondary peak between 10μm and 20μm, suggesting some agglomeration of the powder that has not been broken down in the laser diffraction instrument. CT3000 SG also has a relatively high d90 value compared to that for CR15. The particle size distribution of MA95, shown in Figure 6.3 also shows a relatively narrow distribution with a d50 around 7μm. From the alumina powders analysed here, the particle size data for this powder compares best to the corresponding data for the tungsten powder used to make samples in the previous chapter. The d50 value for the nano grade alumina powder clearly suggests that the powder is not fully dispersed. The mean particle size according to the manufacturer, NaBond (Shenzhen, China) is 20nm, but the data presented here suggests the powder consists of agglomerates between 1μm and 20μm, with a d50 value of 10.14μm, increasing the effective particle size considerably relative to the primary particle size.

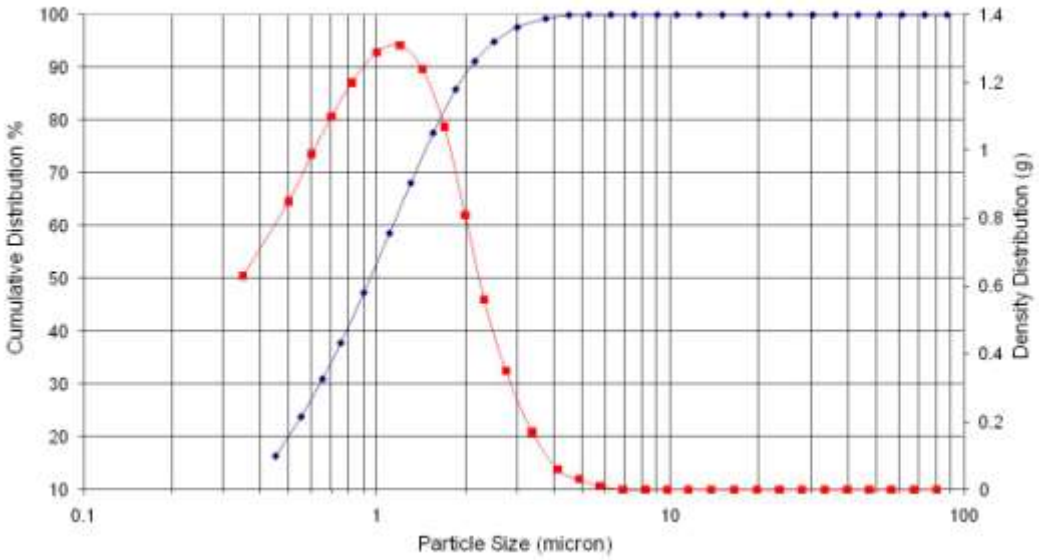

Figure 6.1 *Particle size distribution for CR15 grade alumina powder*

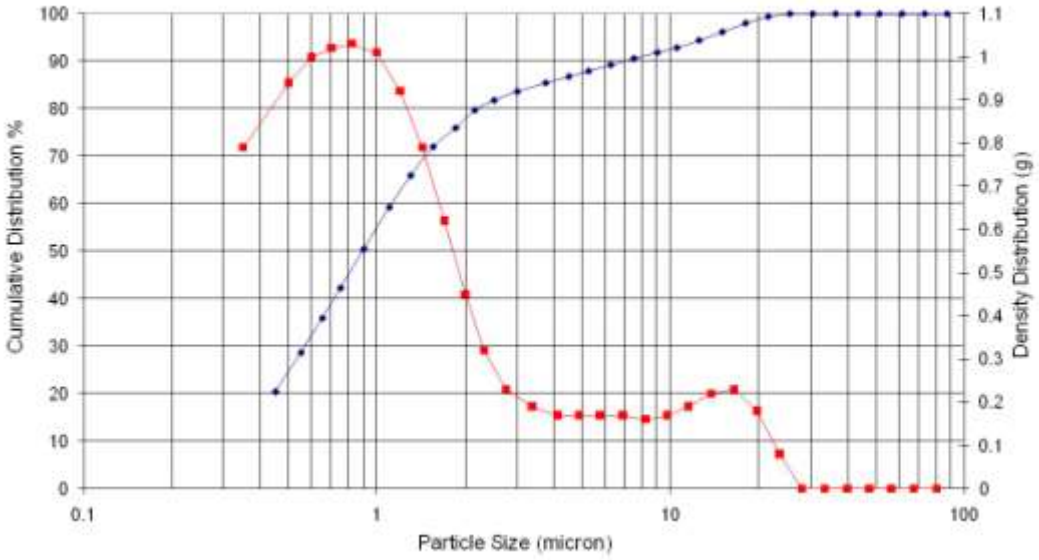

Figure 6.2 *Particle size distribution for CT3000 SG grade alumina powder*

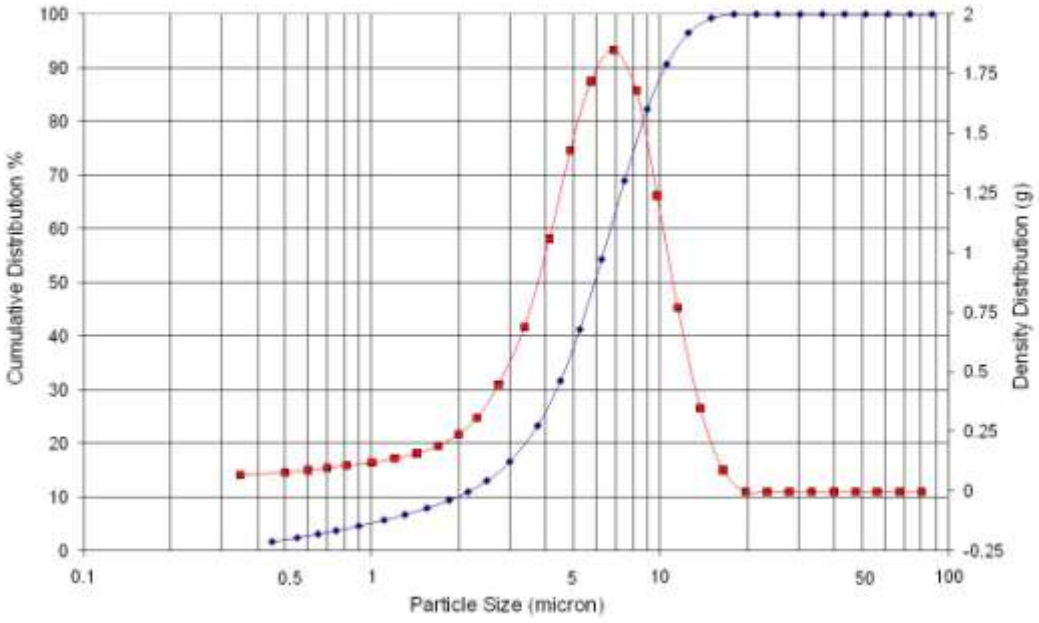

Figure 6.3 *Particle size distribution for MA95 grade alumina powder*

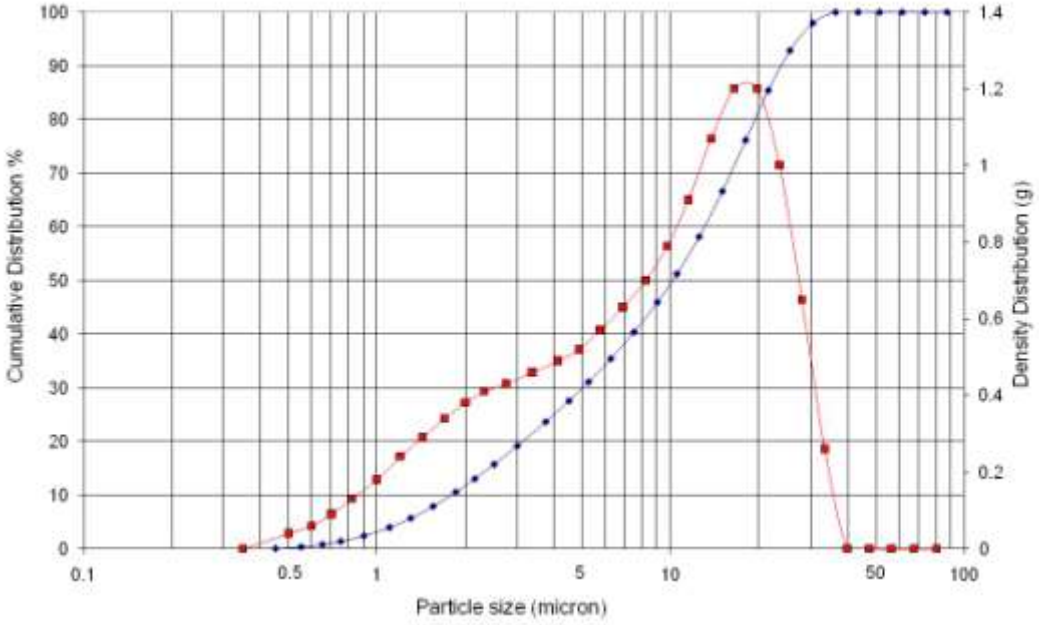

Figure 6.4 *Particle size distribution for nano grade alumina powder*

6.1.2 Powder Morphology

SEM images of the dry powders with no dispersant are shown in Figure 6.5.

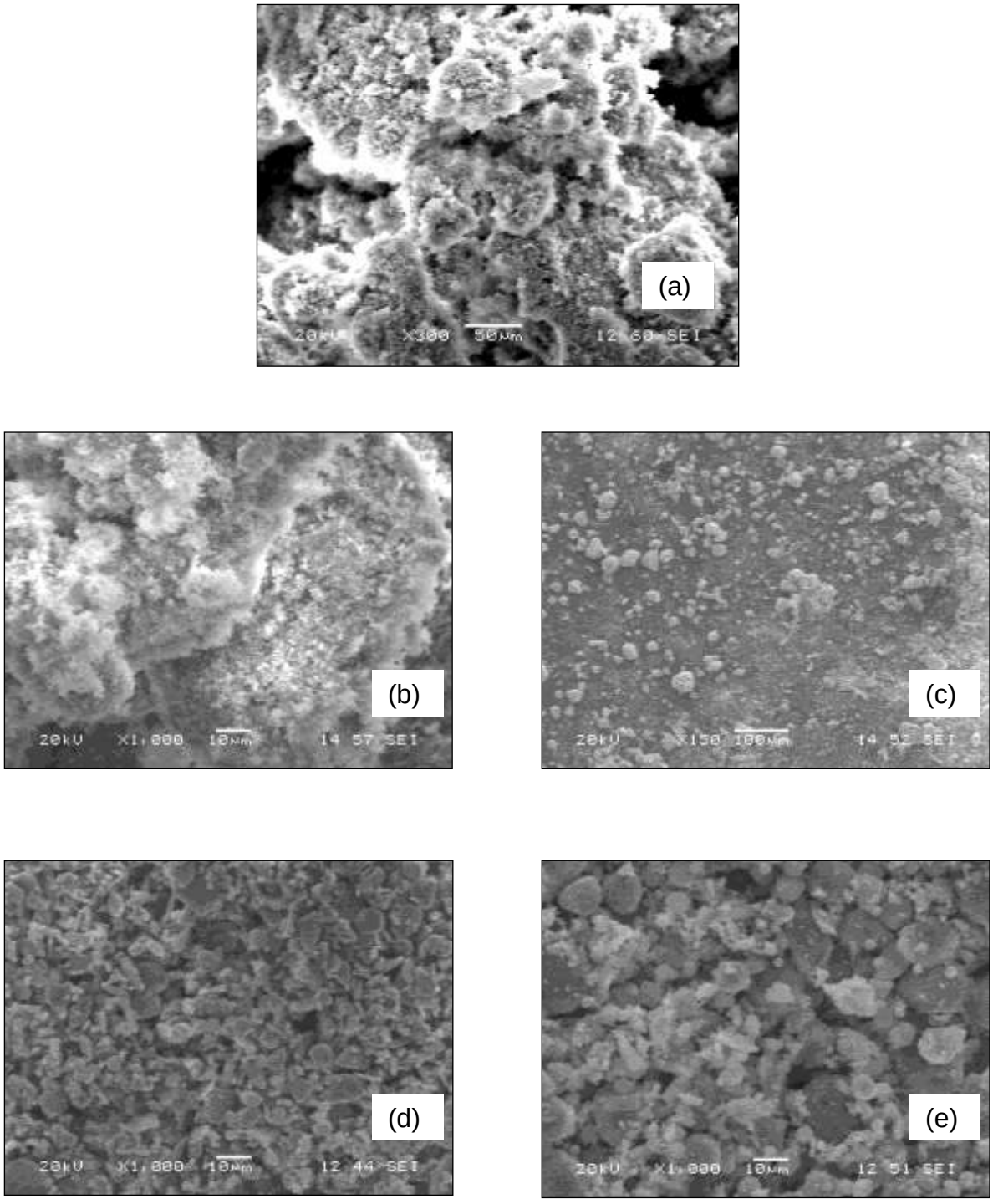

Figure 6.5 *SEM images of alumina powders (a) CR15 (b) CT3000SG x1000 (c) CT3000SG x150 (d) MA95 (e) nano grade*

The image of the CR15 grade in Figure 6.5a does not seem to correspond to the data shown in Figure 6.1 which suggests that the particles are being broken down in the Sympatec analyser. It can be seen that the primary particle size of the CR15 and CT3000SG grades is very fine shown in Figure 6.5a and 6.5b, but Figure 6.5c shows how the CT3000 SG powder tends to form rather large agglomerates, which must not be broken down in the particle size analyser resulting in the secondary peak of the density distribution on the particle distribution graph in Figure 6.2. The image of the MA95 grade alumina in Figure 6.5d shows the particle size to be less than 10μm. The particle shape seems to be platelets, with a thickness around 1μm and an aspect ratio ~5-10μm. The visible area of platelet shaped particles can change depending on the orientation of the particles, and this also influences the data for the laser diffraction measurement, as the particles are not spherically shaped with a fixed diameter. The SEM image of the nano grade alumina shown in Figure 6.5e corresponds with the particle size data presented in Figure 6.4 showing large agglomerates larger than 10μm in size and also some smaller agglomerates, all significantly larger than the primary particle size in the nanometre range, which is not dispersed, increasing the effective particle size.

6.1.3 XRD Analysis

The XRD results for the MA95 and CR15 grade alumina powders are shown in Figures 6.9 and 6.10 respectively. The peaks for a reference sample of alpha alumina (JPDS ref 00-042-1468, corrundum) are shown on each data set with the red markers, indicating a good match and allowing the peaks to be identified appropriately.

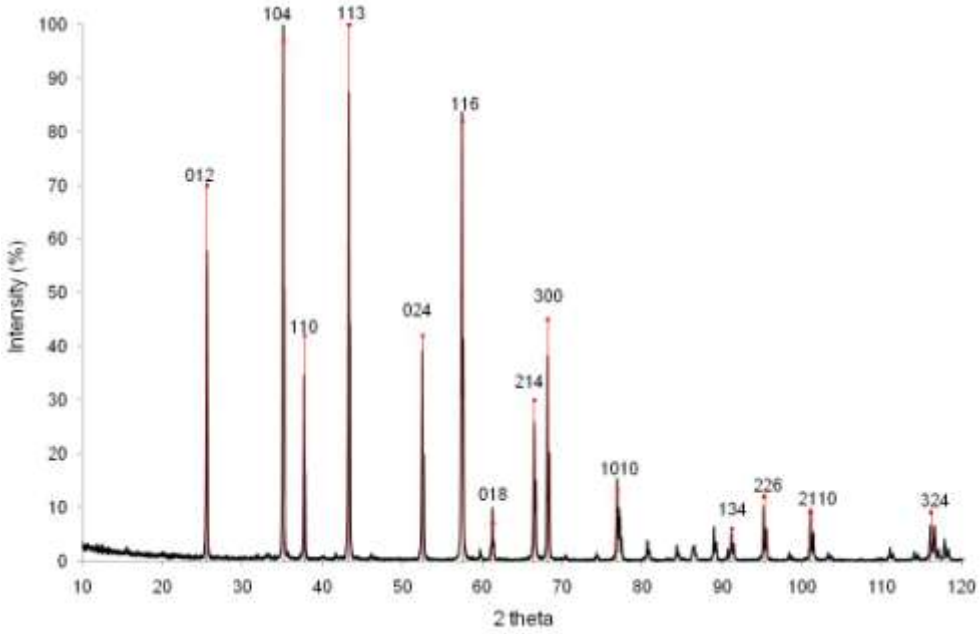

Figure 6.9 *XRD pattern for MA95 grade alumina with major peaks from powder diffraction file 00-042-1468*

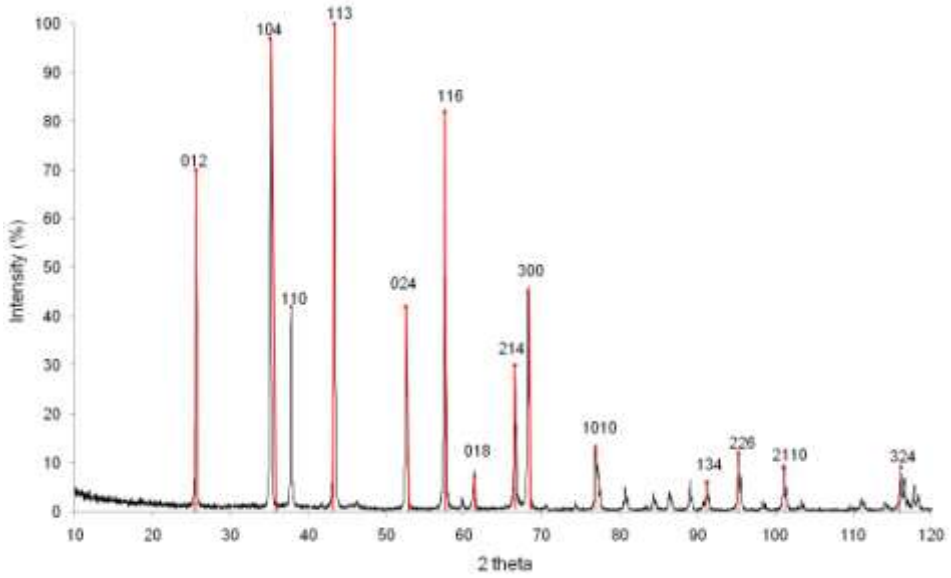

Figure 6.10 *XRD pattern for CR15 grade alumina with major peaks from powder diffraction file 00-042-1468*

The nano grade was scanned at a much slower speed as the initial data was poor showing the background count to be relatively high. The data count from a 36 hour scan time is shown in Figure 6.11. The background is still high and the peaks are not well defined. It is compared with the peaks of a standard gamma alumina sample (JPDS ref 00-029-0063). The experimental data does not compare as well to the reference data as do the other alumina grades. The experimental data indicates a lack of crystallinity within the sample but the peak width is affected by crystallite size, so this may be expected. Gamma alumina is also difficult to characterise by XRD. [105]

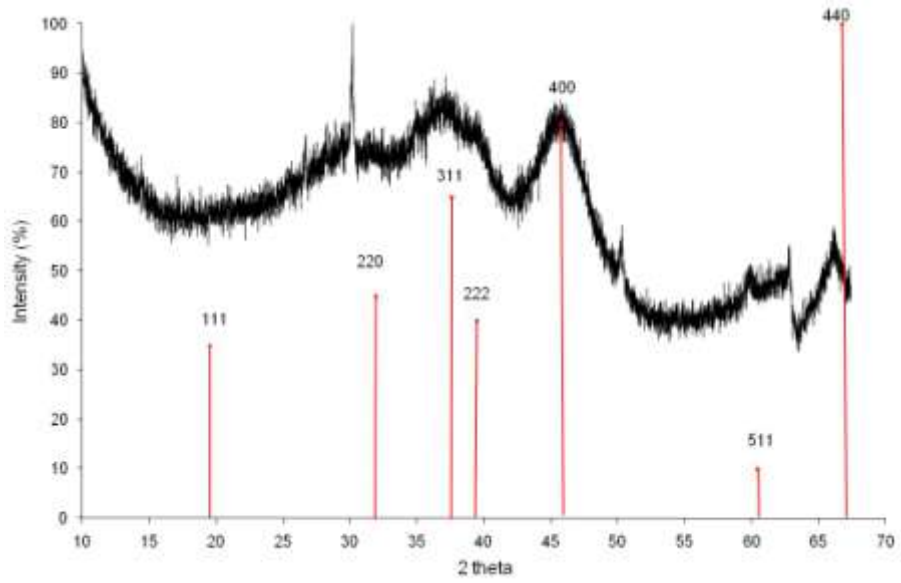

Figure 6.11 *XRD pattern for nano grade alumina with major peaks from powder diffraction file 00-029-0063*

Table 6.2 shows the alumina epoxy samples fabricated and the measured densities compared with the theoretical densities for those particular volume fractions. The measured densities compare well to the theoretical values except for with the nano grade, which suggests there is a greater level of porosity in these samples which increases with the amount of nanopowder in the epoxy.

The maximum possible solid loading of the epoxy is related to the viscosity of the mixture before curing. The viscosity increases with increasing amount of filler and there is a maximum viscosity where the material still flows enough to be degassed and drawn into the syringe. The maximum volume fraction achieved with MA95 was 0.25 in the Epotek epoxy and 0.20 in the Epofix, which has a slightly higher viscosity than the Epotek. Above these volume fractions the material could not be degassed properly so when it was drawn into the syringe there were large air bubbles. Therefore the maximum solid loading for smaller particle sizes, CR15 and nano grade, is a smaller volume fraction than for MA95 which has a higher particle size and thus a lower surface area. The maximum loading for the nano grade alumina is at the same volume fraction as the CR15 grade (0.15) showing that the particles are agglomerated. If the nano particles were fully dispersed in the epoxy the spacing between the particles would be smaller than with the CR15 grade as the surface area is greater and it would be expected that the maximum volume fraction achievable would be lower than 0.15.

Table 6.2 Measured densities of fabricated alumina filled epoxy samples

Epoxy / Grade	Volume Fraction	Measured Density (g/cm^3)	% Theoretical Density
Epofix / MA95	0.01	1.12	100
	0.05	1.23	100
	0.10	1.36	99
	0.15	1.51	99
	0.20	1.66	100
Epofix / CR15	0.01	1.12	100
	0.05	1.23	100
	0.10	1.37	100
	0.15	1.52	100
Epofix / Nano	0.01	1.09	97
	0.05	1.17	94
	0.10	1.25	90
Epotek301 / MA95	0.01	1.12	100
	0.05	1.23	100
	0.10	1.38	100
	0.15	1.50	99
	0.20	1.64	98
	0.25	1.79	99
Epotek301 / CR15	0.01	1.11	99
	0.05	1.22	99
	0.10	1.37	99
	0.15	1.51	99
Epotek301 / Nano	0.01	1.11	99
	0.05	1.20	97
	0.10	1.31	95
	0.15	1.40	92

6.2 Composite Characterisation

6.2.1 Scanning Electron Microscopy (SEM)

The alumina/Epotek epoxy samples were initially polished before being examined in the SEM microscope. However, polishing was very difficult because alumina particles were pulled out of the epoxy during the process and large agglomerates act as grinding media on the polishing plate resulting in further scratches on the sample. Therefore final SEM images were taken of the samples after they were cut with no further polishing. The surface of the epoxy is not flat but the alumina particles can be seen. The main features that were being investigated were the apparent distribution of alumina particles in the epoxy and observed porosity, and the images were generally suitable for this.

SEM images of Epotek 301 filled with MA95 alumina is shown in Figures 6.12 and 6.13. There is not much evidence of large amounts of agglomeration in the MA95 filled epoxy as shown in Figure 6.12a and 6.12b for 0.01 volume fraction alumina, although there is some porosity. The spherical nature of the pores, as shown in Figure 6.12d, suggests that the porosity is due to air bubbles trapped in the epoxy. Therefore, even though during the fabrication process the mixture seemed to be degassed properly and there are still air bubbles not effectively removed. The SEM image in Figure 6.12f shows how the orientation of the platelet particle shapes affects the exposed area in different directions. The particles can look like round particles or needle shaped particles depending on how they lie in the epoxy. Spherical shaped particles are ideal to allow prediction of scattering effects, which is not the case here.

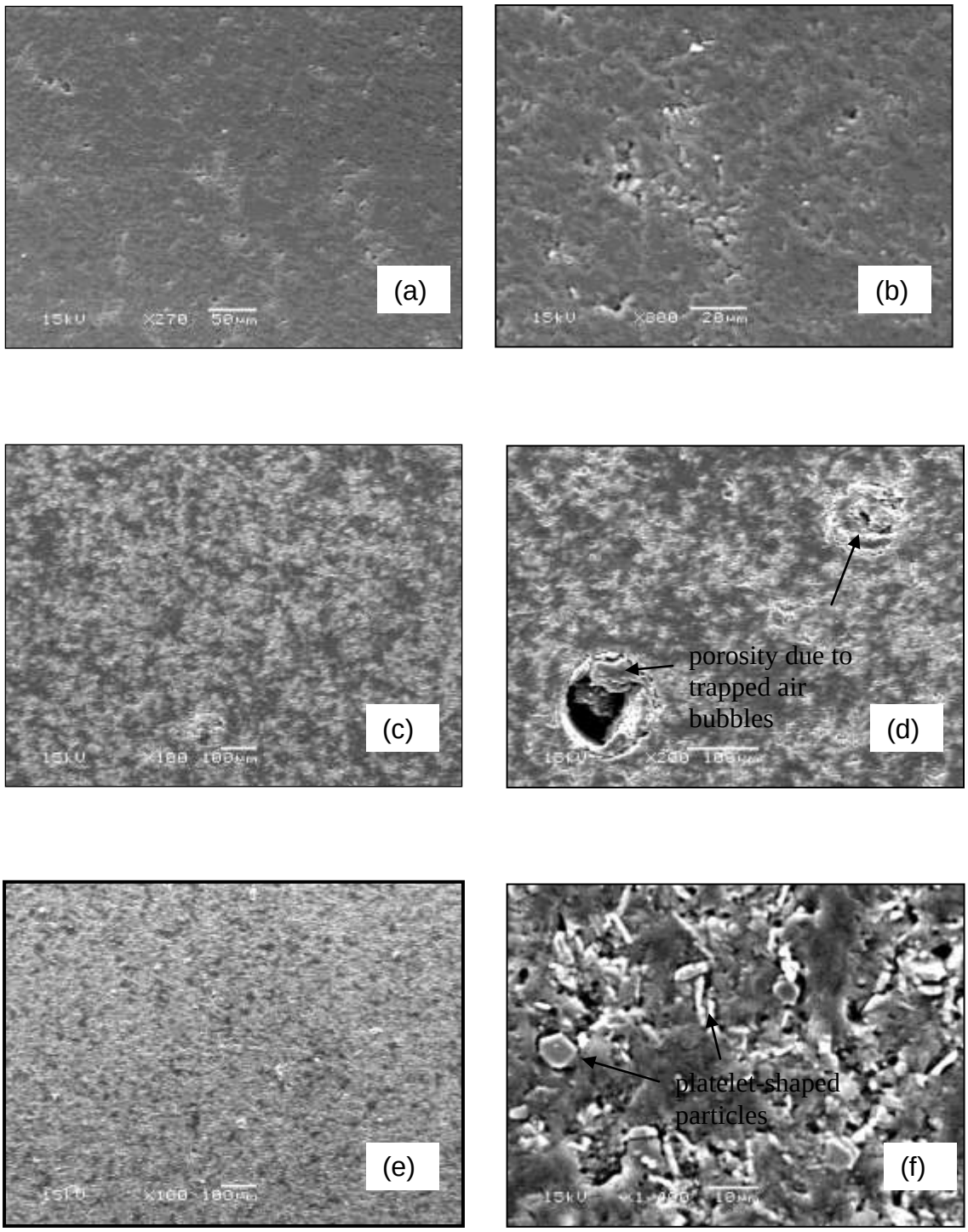

Figure 6.12 *SEM images of MA95 alumina/Epotek epoxy composites*
(a) 0.01 volume fraction x270 (b) 0.01 volume fraction x800
(c) 0.05 volume fraction x 100 (d) 0.05 volume fraction x200
(e) 0.10 volume fraction x 100 (f) 0.10 volume fraction x1400

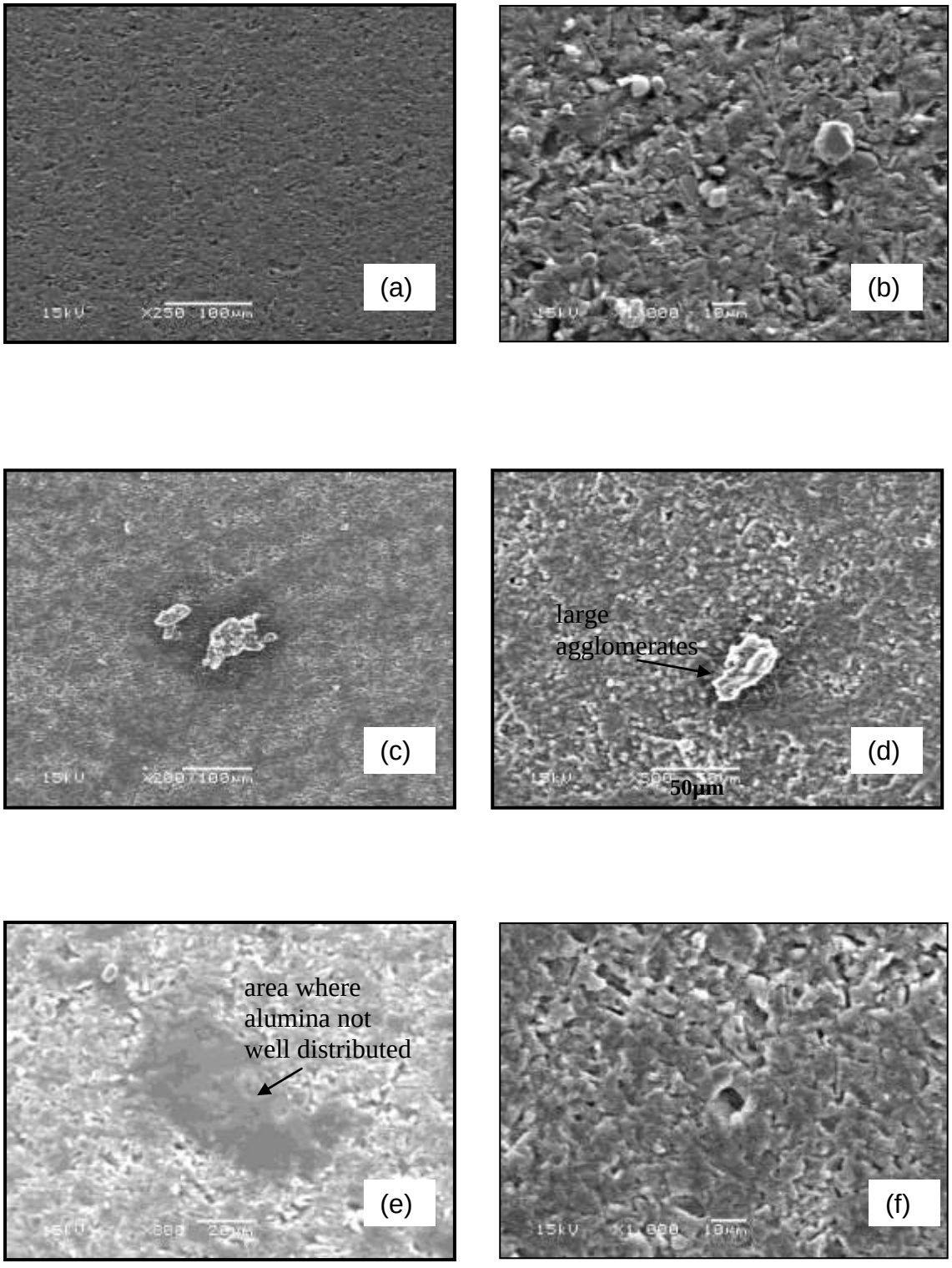

Figure 6.13 *SEM images of MA95 alumina/Epotek epoxy composites (a) 0.15 volume fraction x250 (b) 0.15 volume fraction x1000 (c) 0.20 volume fraction x 200 (d) 0.20 volume fraction x500 (e) 0.25 volume fraction x 800 (f) 0.25 volume fraction x1000*

SEM images of 0.15-0.25 volume fraction alumina with grade MA95 are shown in Figure 6.13. There seems to be an even distribution shown in Figure 6.13a but there is evidence of large agglomerates at higher magnification in Figure 6.13b, which is also shown in Figure 6.13c and 6.13d for 0.20 volume fraction. At the higher volume fractions mixing of the epoxy and powder was difficult so more agglomerations occur. The 0.25 volume fraction sample shows areas where the alumina is compacted together (Figure 6.13f) and other areas of epoxy where the alumina particles are not thoroughly distributed in the epoxy (Figure 6.13e) showing that the mixing is not optimised for the higher volume fraction materials.

SEM images of CR15 grade alumina epoxy are shown in Figure 6.14. The alumina particles seem generally well dispersed in the 0.01 volume fraction material, as shown in Figure 6.14a and discrete particles around one micron in size can be seen as well as some small areas of agglomeration in Figure 6.14b. Images of 0.05 volume fraction CR15 grade alumina are shown in Figure 6.14c and 6.14d showing some small areas of epoxy containing no alumina particles (dark area in 6.14c) and small agglomerates less than 10 micron in size (6.14d). The 0.10 volume fraction sample is shown in Figures 6.14e and 6.14f with much larger agglomerates and Figure 6.14g and 6.14h shows the 0.15 volume fraction sample, which was the highest volume fraction obtained with this alumina type. The distribution seems even at low magnification in Figure 6.14g, and at higher magnification in Figure 6.14h discrete particles are clearly visible but the epoxy surface appears broken up.

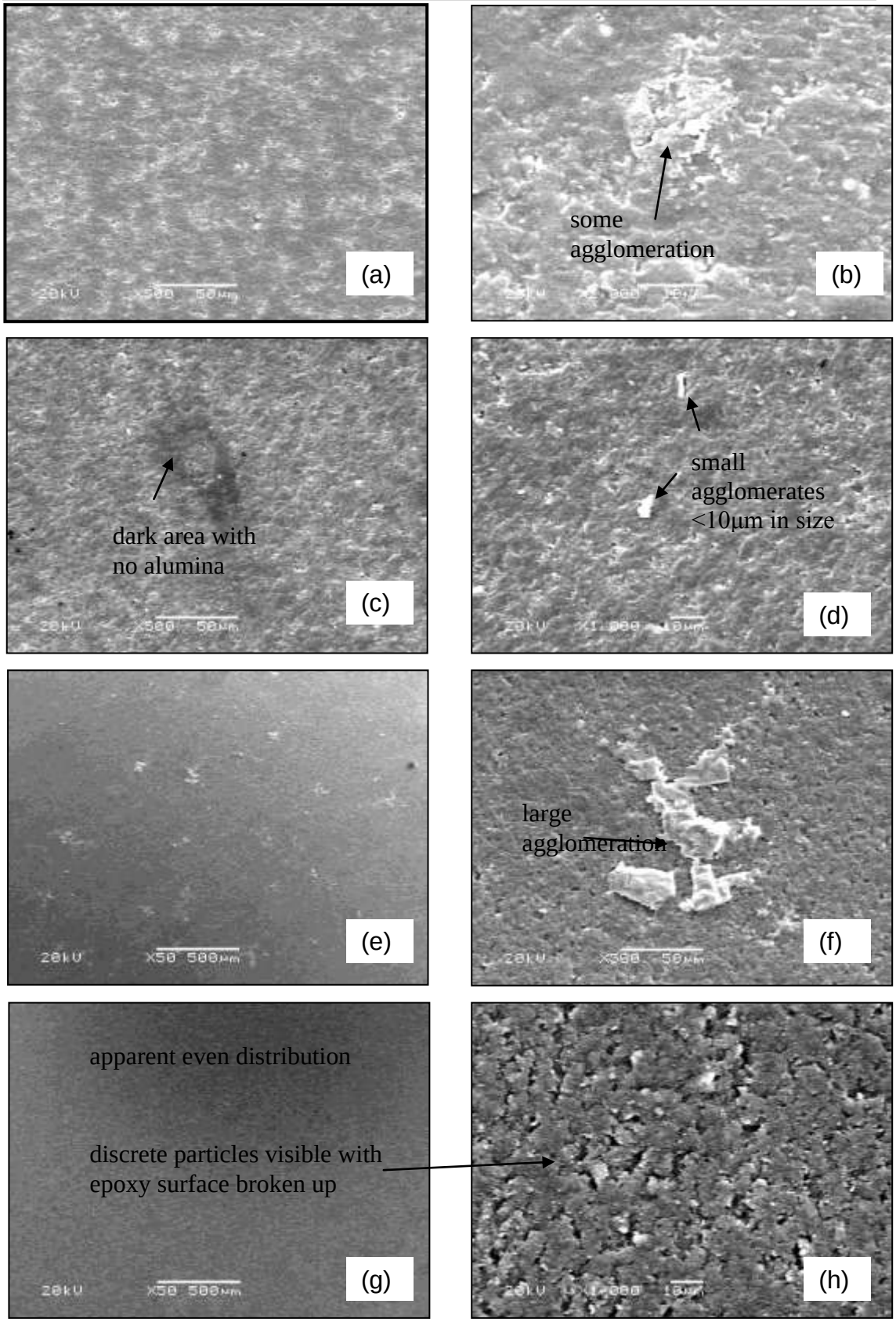

Figure 6.14 *SEM images of CR15 alumina/Epotek epoxy composites*
(a) 0.01 volume fraction x500 (b) 0.01 volume fraction x2000
(c) 0.05 volume fraction x 500 (d) 0.05 volume fraction x1000
(e) 0.10 volume fraction x 50 (f) 0.10 volume fraction x500
(g) 0.15 volume fraction x50 (h) 0.15 volume fraction x500

The epoxy samples filled with alumina nano powder show a large amount of porosity indicating that it is very difficult to obtain a non-porous filled alumina epoxy material, because porosity may exist on a scale that is impossible to determine during fabrication. Figure 6.15 shows SEM images of the nano alumina epoxy material showing porosity around the alumina particles. The porosity seems to only be located around the alumina agglomerates in all volume fractions, so is unlikely to be due to air being trapped in the epoxy during fabrication and is more likely to be affected by the agglomeration of the nano sized alumina particles.

The microstructure of the nano composites is complex. It seems to consist of large agglomerates over 10μm in size and smaller particles that have broken out of these agglomerates in the surrounding epoxy. There is porosity surrounding each large agglomerate, which could be due to nano particles from the surface of the agglomerates breaking away into the epoxy and leaving voids where the epoxy has not impregnated, resulting in a lower density than expected, as shown in Table 6.2. This also explains why the porosity increases with volume fraction of the nano type alumina.

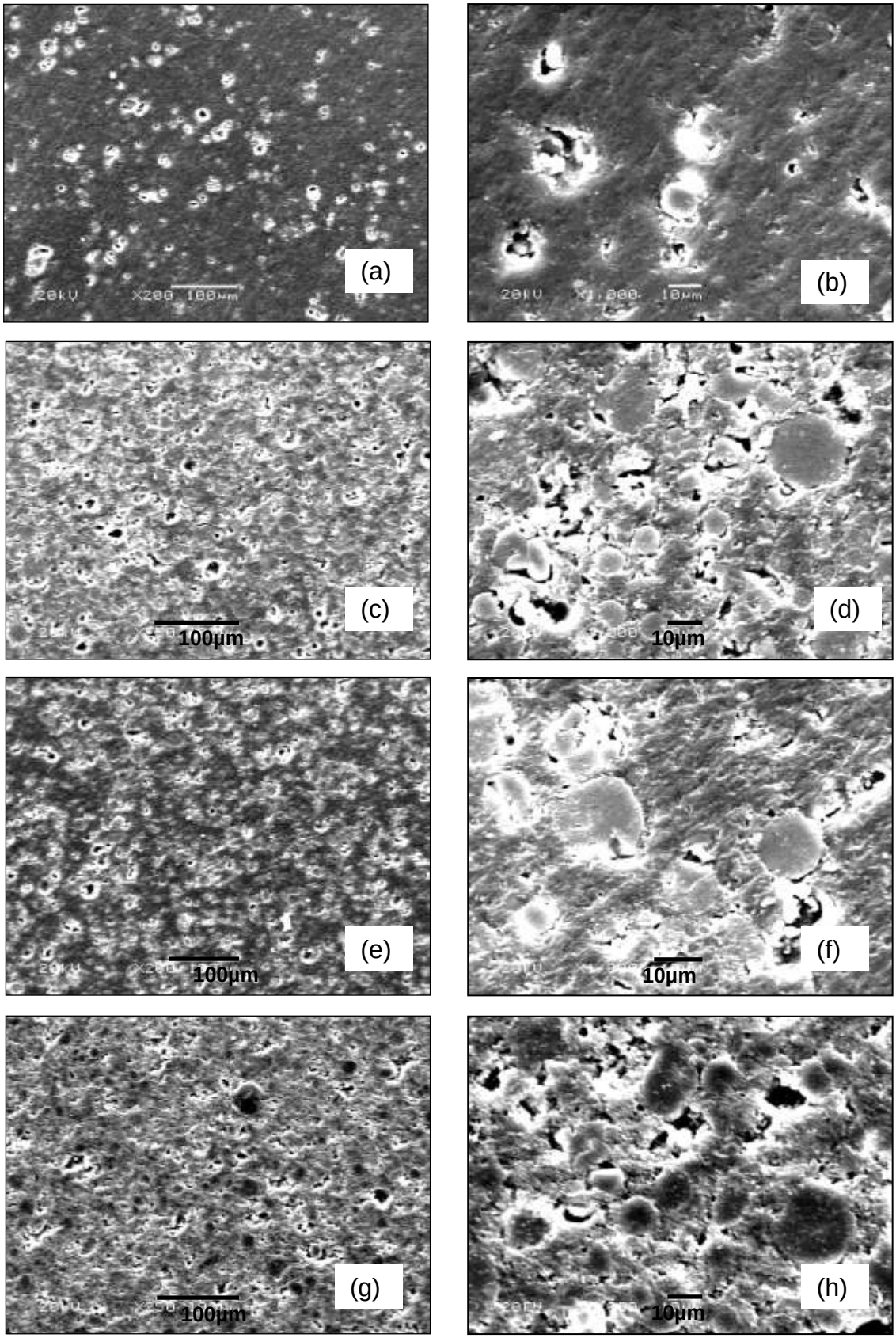

Figure 6.15 *SEM images of nano alumina/Epotek epoxy composites*
(a) 0.01 volume fraction x200 (b) 0.01 volume fraction x1000
(c) 0.05 volume fraction x 250 (d) 0.05 volume fraction x1000
(e) 0.10 volume fraction x 200 (f) 0.10 volume fraction x1000
(g) 0.15 volume fraction x250 (h) 0.15 volume fraction x1000

6.2.2 High Frequency Acoustic Results

The alumina epoxy composite samples were characterised acoustically using the set up described in Section 4.3.3.2. The transmitting and receiving transducers were different to those used for characterisation of the tungsten epoxy composite samples, therefore a brief characterisation of the transducers used in the set up was performed in pulse echo mode and in transmit and receive modes.

6.2.2.1 Transducer Characterisation

The transmitting transducer used in the experimental set up to characterise the alumina epoxy samples was a single element curved composite transducer, JB, (used courtesy of Jeremy Brown, Sunnybrook Health Sciences Centre, Toronto). The receiving transducer was known as AFMTH10, a flat piezocomposite transducer housed in a SMA case manufactured by AFM Ltd (Birmingham, UK). These transducers were used because of their availability at the time the measurements were made. Their slightly different characteristics, as outlined below for completeness, are not expected to have had any effect on the results.

The pulse-echo response of the transmitting transducer is shown in Figure 6.16a, where the echo shown is reflected off the steel cover of the characterisation jig. The frequency response after a fast fourier transform (FFT) analysis is shown in Figure 6.16b showing the peak frequency to be approximately 35MHz and the -6dB bandwidth to be approximately 20MHz. The equivalent data for the receiving transducer is shown in Figure 6.17. The peak frequency is at 26MHz.

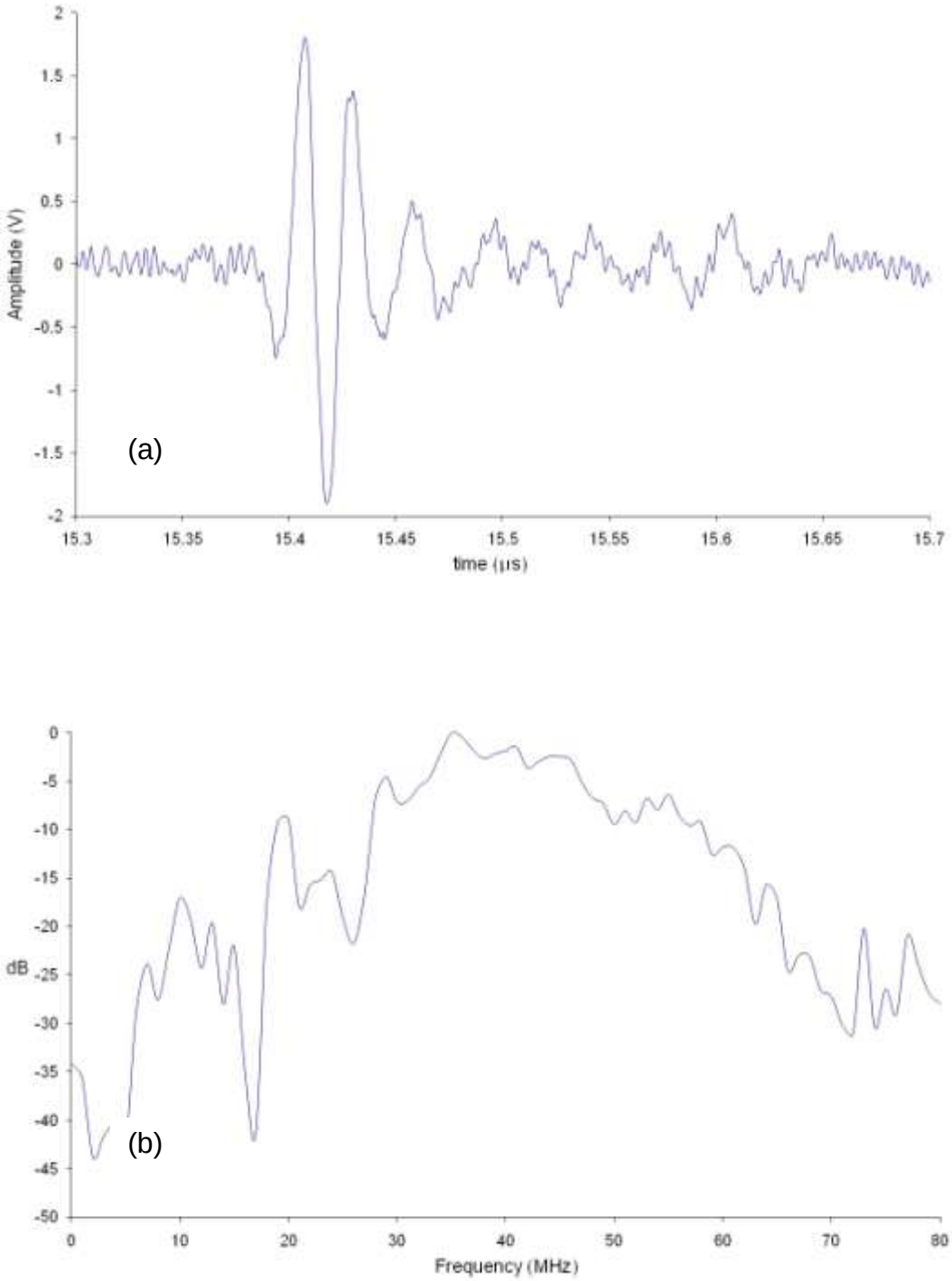

Figure 6.16 *Transmitting transducer (AFMTH10)*
(a) echo from steel plate (b) FFT of echo

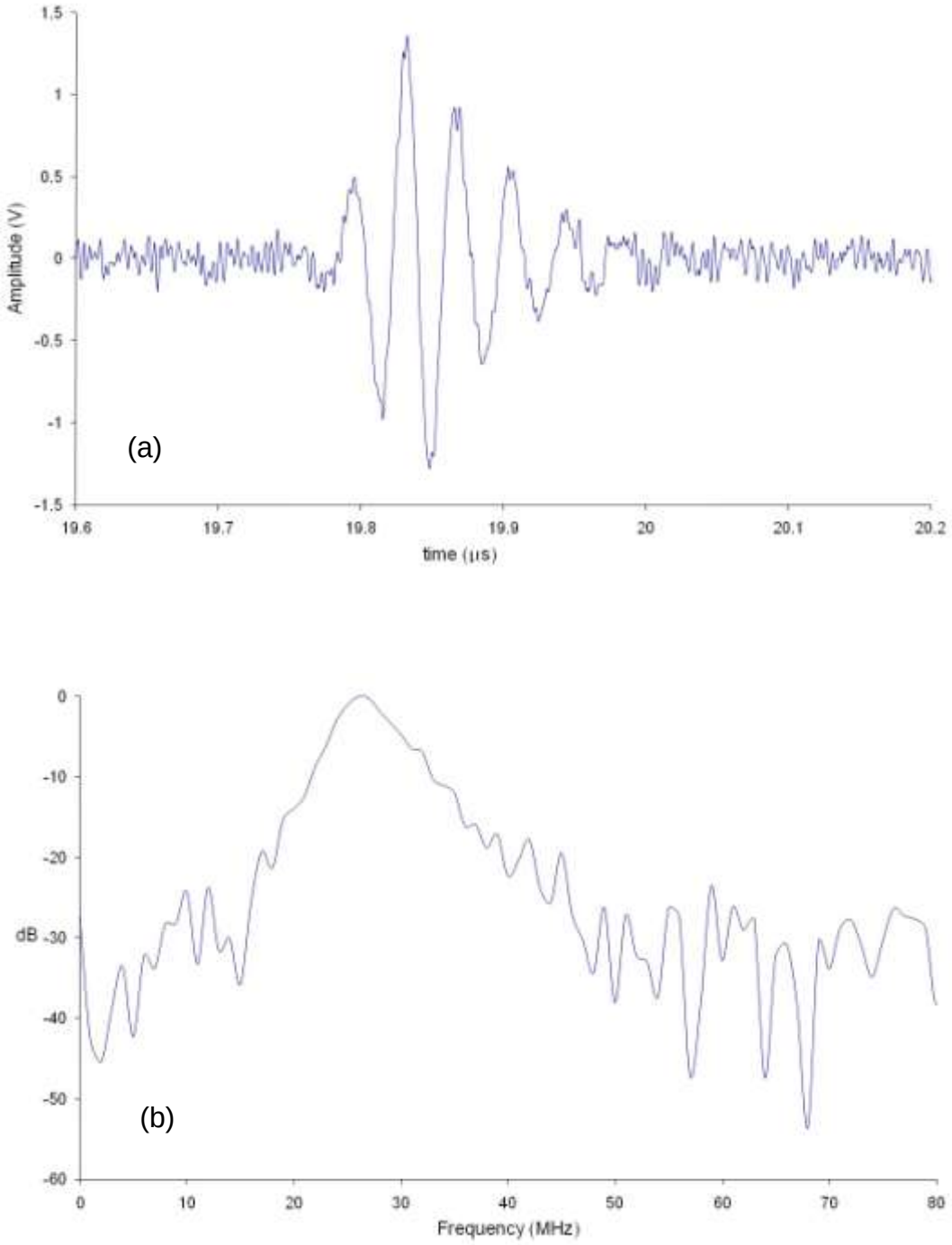

Figure 6.17 *Receiving transducer (JB)*
(a) echo from steel plate (b) FFT of echo

The through signal and FFT data for both transducers acting as receivers are shown in Figures 6.18 and 6.19. The signal in Figure 6.18 is transmitted by JB transducer and received by AFMTH10 and the signal in Figure 6.19 is the reverse. With ideal instrumentation there should be no difference in the FFT data for these transducer arrangements but it can be seen that there is a difference here. This may be due to the alignment of the transducers or the distance between them differing, as the JB transducer is focused. The signals are arriving at different times in Figures 6.18a and 6.19a so the distance is different. The implications of this are that the FFT is more broadband for the signal transmitted from AFMTH10 received by JB shown in Figure 6.19b than the for the signal received with the transducers in the other configuration shown in Figure 6.18, which was the configuration used for the measurements. It is also possible however, that the different characteristics of the transducers, when connected to non-ideal instrumentation, in terms of electrical impedance, may also have affected the results. Overall, the key issue is that the frequency range over which the two transducers operate in through transmission, as shown in Figures 6.16b and 6.17b, is similar to that used previously, when measuring the tungsten epoxy composite materials.

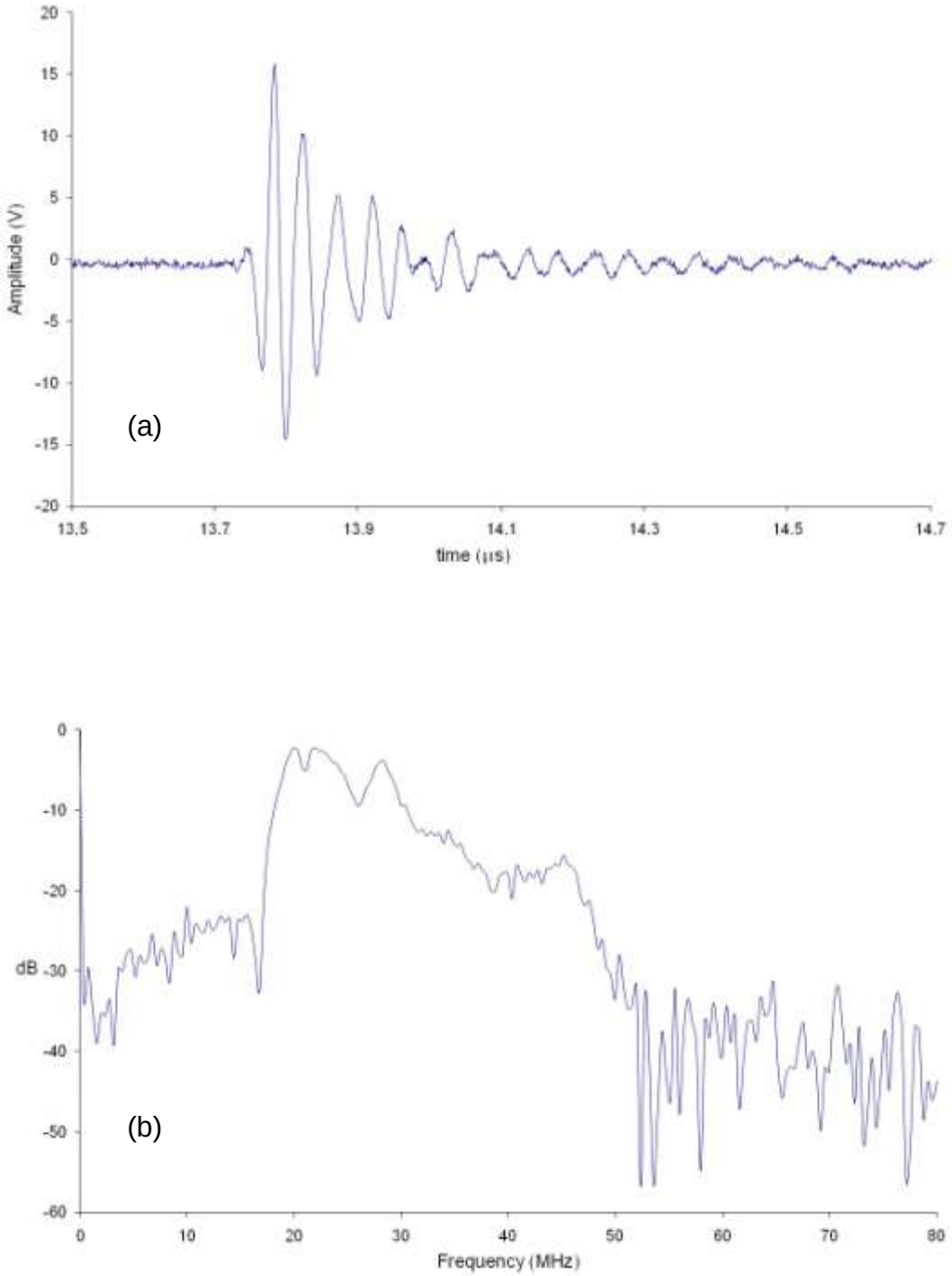

Figure 6.18 *(a) Signal transmitted through water by JB transducer and received by AFMTH10 transducer (b) Frequency response of through signal*

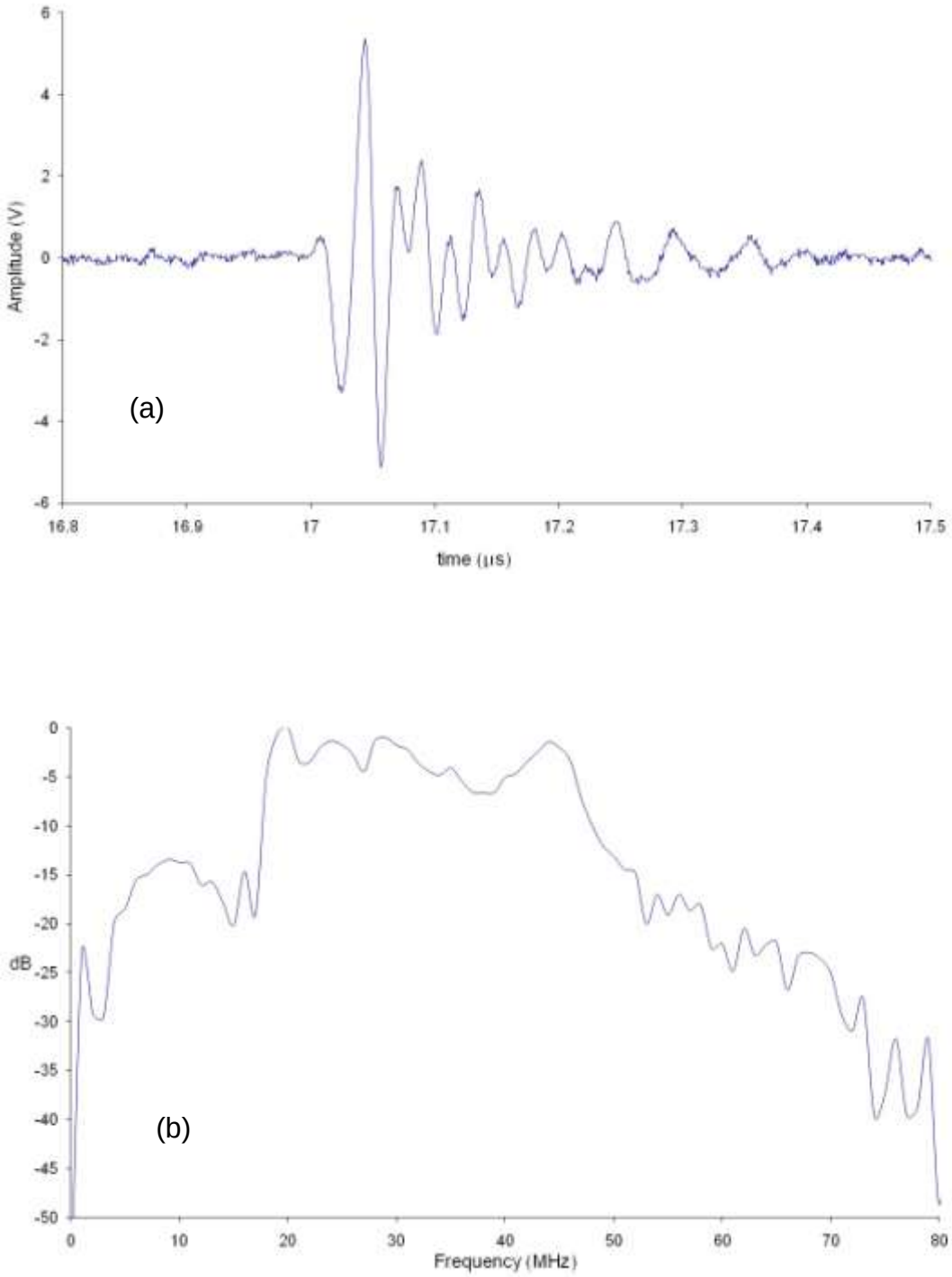

Figure 6.19 *(a) Signal transmitted through water by AFMTH10 transducer and received by JB transducer (b) Frequency response of through signal*

6.2.2.2 Longitudinal and Shear Wave Velocity

The longitudinal and shear wave velocities of the alumina epoxies were calculated as described previously in Section 3.3. The shear wave velocity was calculated from the data recorded at an incidence angle of 50°. The acoustic impedance values were then calculated by multiplying the velocity values with the measured densities of each sample. The data for each set of samples are plotted in Figures 6.20 and 6.21, which also show the Devaney model. The Devaney model was calculated here using Equations 2.7 and 2.8 and the standard density values for the epoxies and alumina; $\rho_{alumina}$ = 3.67g/cm^2, ρ_{epofix} = 1.087kg/m^3, $\rho_{epotek301}$ = 1.094g/cm^3 (from epoxy manufacturer's data). The standard moduli values for alumina were also used; $K_{alumina}$ = 165GPa, and $G_{alumina}$ = 124GPa [109] but the K and G values for the epoxies were calculated using the measured velocity values and rearranging Equations 6.2 and 6.3 below.

$$V_L = \sqrt{\frac{K + \frac{4}{3}G}{\rho}} \qquad \textbf{Equation 6.2}$$

$$V_S = \sqrt{\frac{G}{\rho}} \qquad \textbf{Equation 6.3}$$

The experimental results in Figures 6.20 and 6.21 generally show good agreement with the Devaney model. The longitudinal data for the Epofix samples seem to show a better correlation to the model than the shear data. The shear data for the Epotek 301 samples show a better fit with data points above and below the model. There does not seem to be trend involving particle size between both epoxy samples for the velocity results as there is no significant difference between the data for MA95

alumina, with a discrete particle size ~5μm and CR15 alumina with a particle size around 1μm.

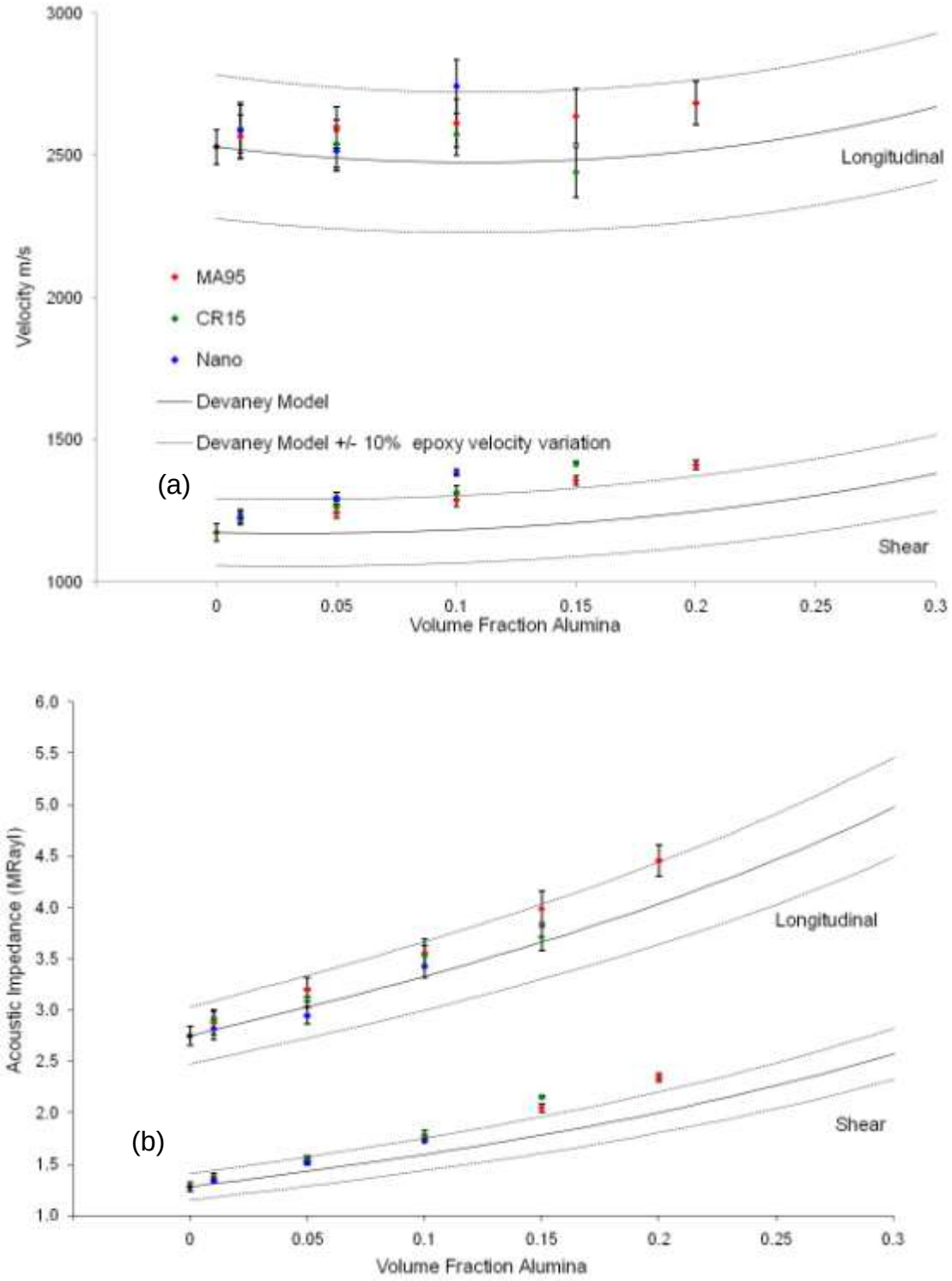

Figure 6.20 *(a) Longitudinal and shear wave velocities and (b) acoustic impedance values of alumina filled Epofix samples. Dotted lines represent how Devaney varies with ±10% epoxy velocity variation*

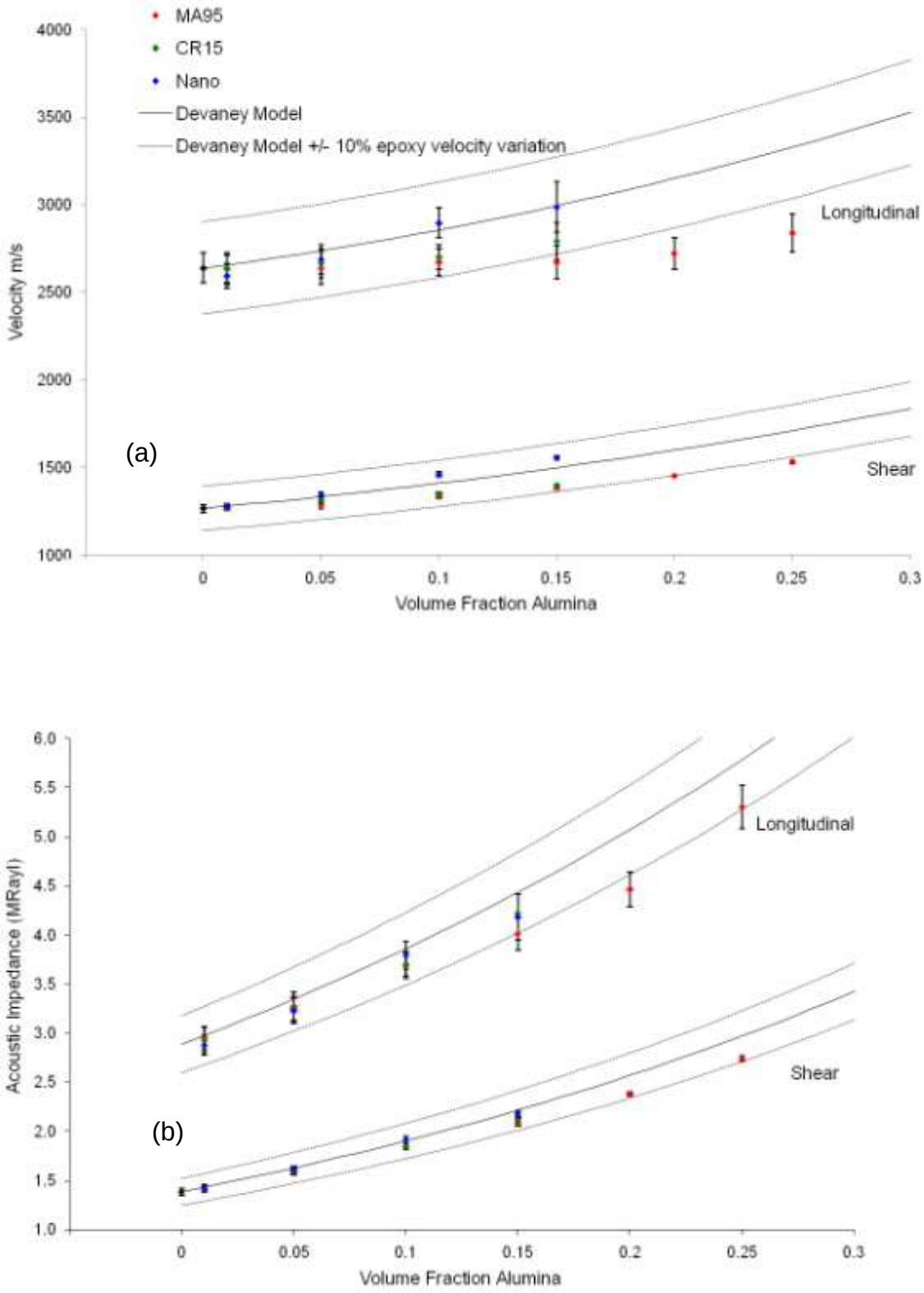

Figure 6.21 *(a) Longitudinal and shear wave velocities and (b) acoustic impedance values of alumina filled Epotek 301 samples. Dotted lines represent how Devaney varies with ±10% epoxy velocity variation*

A factor affecting the velocity may be the porosity in the sample, which is highest in the nano samples, increasing with the amount of alumina. Looking at the Epofix data in Figure 6.20 porosity may be considered to have an influence as the nano samples have higher longitudinal and shear velocities than the other grades. This trend also extends to the longitudinal and shear velocities of the Epotek 301 samples, but it is not as significant and here the nano data correlate better with the Devaney model. Other reported data for velocity in alumina filled epoxy has shown a tighter correlation with the Devaney model [86] but as with the tungsten data presented in the previous Chapter, the Devaney model describes the experimental data better than the other models described previously in Chapter 2.

The experimental data show that a high loading of alumina (≥0.25 volume fraction) is required to achieve an acoustic impedance value of ~5MRayl. Therefore for this material to be used as a backing material a high solid loading is necessary. This work has shown that this can be only achieved practically with a filler particle size of at least 5μm and an epoxy with a low viscosity, such as Epotek 301. As discussed in Chapter 4, high shear mixing may be possible to obtain a higher solid loading but it is difficult with the smaller particle sizes used. The acoustic impedance values obtained here show that alumina epoxy is suitable for matching material as the required acoustic impedance is an intermediate value between the active material and tissue (~1.5MRayl). The geometric mean calculated with Equation 2.2 using an impedance value of 15MRayls for the piezocomposite element is 4.7MRayl.

6.2.2.3 Longitudinal and Shear Wave Attenuation

As well as a suitable acoustic impedance optimised matching layers must also have a low attenuation so a high proportion of the ultrasound signal reaches the active part of the transducer. The longitudinal attenuation of the alumina filled samples was measured as described previously for the tungsten samples, in Section 3.3.3. The attenuation values obtained from the normal through measurements are shown in Figure 6.22 along with trendlines for each type of alumina.

The attenuation values for the two epoxies are different, with Epofix having a lower value than Epotek 301. It has been reported previously that the attenuation depends on the degree of crystallinity and the amount of cross-linking in a polymer material [56] so these factors may influence the results shown here. The shore D hardness values for Epotek 301 and Epofix are 80 and 75 respectively (from manufacturer's data), indicating that Epotek 301 may contain more cross links than Epofix, resulting in a higher degree of crystallinity. The Epotek 301 data compares well to other reported work where the attenuation increases with volume fraction alumina until a peak between 0.05 and 0.10 alumina volume fraction where the attenuation decreases with more alumina. [56,57,86] This pattern is generally followed by the MA95 and nano alumina grades with a polynomial trend, which suggests that this behaviour is due to the influence of particle size. The effective particle size of the MA95 and nano grades is much larger than the CR15 grade, which does not show this pattern. The CR15 samples do not show a significant variation in attenuation with volume of alumina as the other samples do, showing a more linear trend with a small gradient. This is to be expected, as if the particle size is significantly less than the wavelength, attenuation via scattering is minimised. Therefore the attenuation of the alumina filled epoxy depends on the particle size of the alumina and the attenuation of the epoxy.

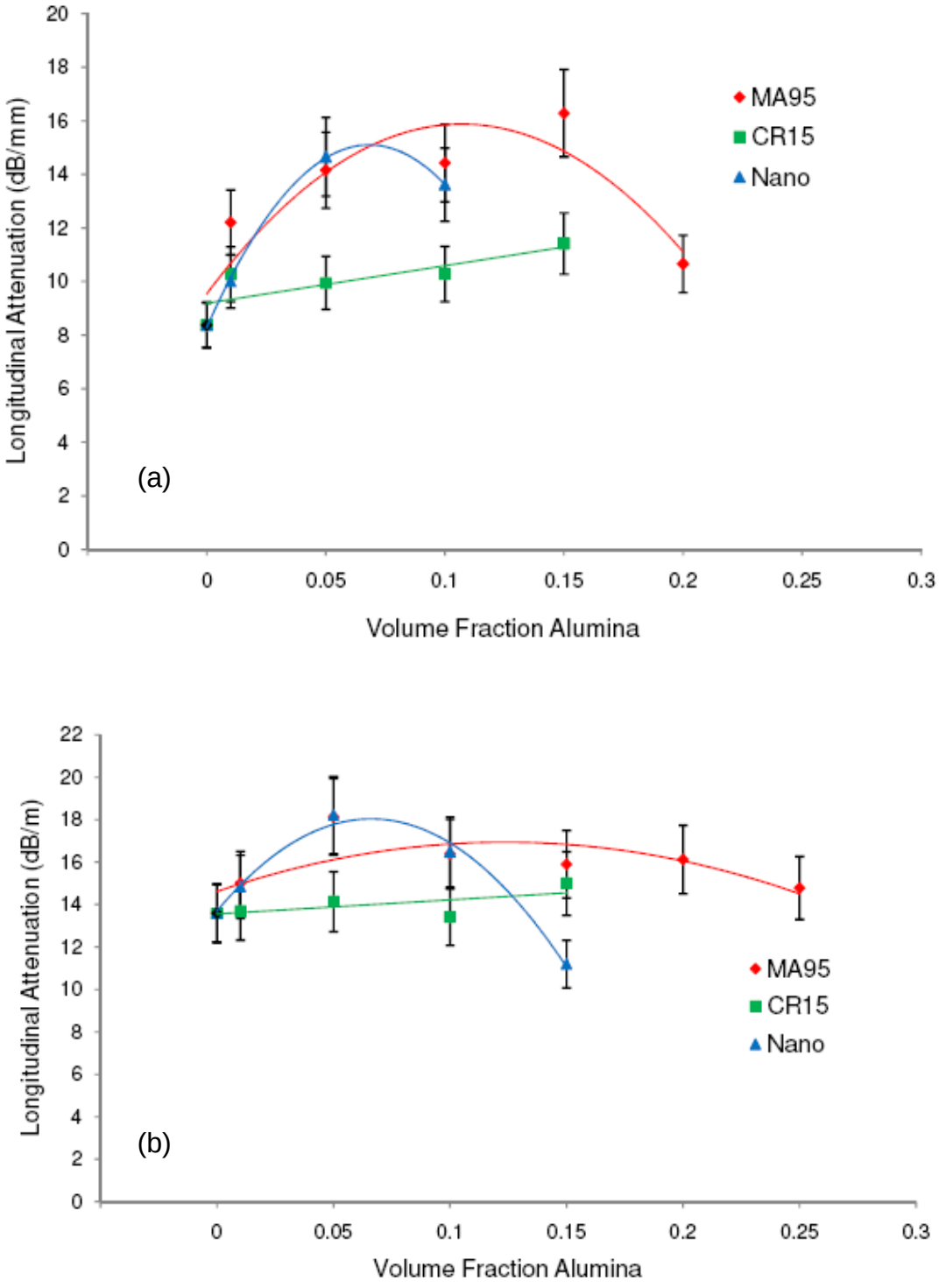

Figure 6.22 *Longitudinal attenuation calculated from normal measurement of (a) alumina filled Epofix samples (b) alumina filled Epotek 301 samples along with trendlines*

Curve fitting was also carried out to determine the accuracy of the measurements, as described previously with the tungsten epoxy data in Section 5.2.3.3, where the experimental data is compared with the calculated theory over a large range of incidence angles. The attenuation value with the smallest mean error for the experimental data was then found. Tables 6.3 and 6.4 show the attenuation values obtained from the normal measurements and the values with the smallest mean square error (MSE) from the curve fitting technique. The curves were calculated with the measured values of velocity and density.

Table 6.3 Epofix attenuation data determined via curve fitting

Grade	Volume fraction	Normal Measurement (Np/mm)	Smallest MSE (to nearest 0.1Np/mm)
-	0	0.94	1.1
MA95	0.01	1.38	1.5
	0.05	1.60	1.7
	0.10	1.62	1.7
	0.15	1.83	1.7
	0.20	1.20	1.2
CR15	0.01	1.16	1.16
	0.05	1.12	1.12
	0.10	1.16	1.4
	0.15	1.29	1.29
Nano	0.01	1.11	1.11
	0.05	1.64	1.64
	0.10	1.50	1.5

Table 6.4 Epotek 301 attenuation data determined via curve fitting

Grade	Volume fraction	Normal Measurement (Np/mm)	Smallest MSE (to nearest 0.1Np/mm)
-	0	1.53	1.5
MA95	0.01	1.69	1.5
	0.05	2.05	1.9
	0.10	1.85	1.8
	0.15	1.78	1.7
	0.20	1.81	1.81
	0.25	1.66	1.6
CR15	0.01	1.54	1.4
	0.05	1.58	1.5
	0.10	1.51	1.51
	0.15	1.68	1.7
Nano	0.01	1.67	1.6
	0.05	2.03	1.9
	0.10	1.86	1.6
	0.15	1.23	1.4

The calculated longitudinal transmission coefficient curve for the Epofix sample with the experimental data is shown in Figure 6.23. The shape and the value of the critical angle where the transmission coefficient is zero depends on the velocity values input into the calculation. The experimental data does not fit well here as it goes beyond

the critical angle expected from the theoretical curve calculated with the measured velocity values.

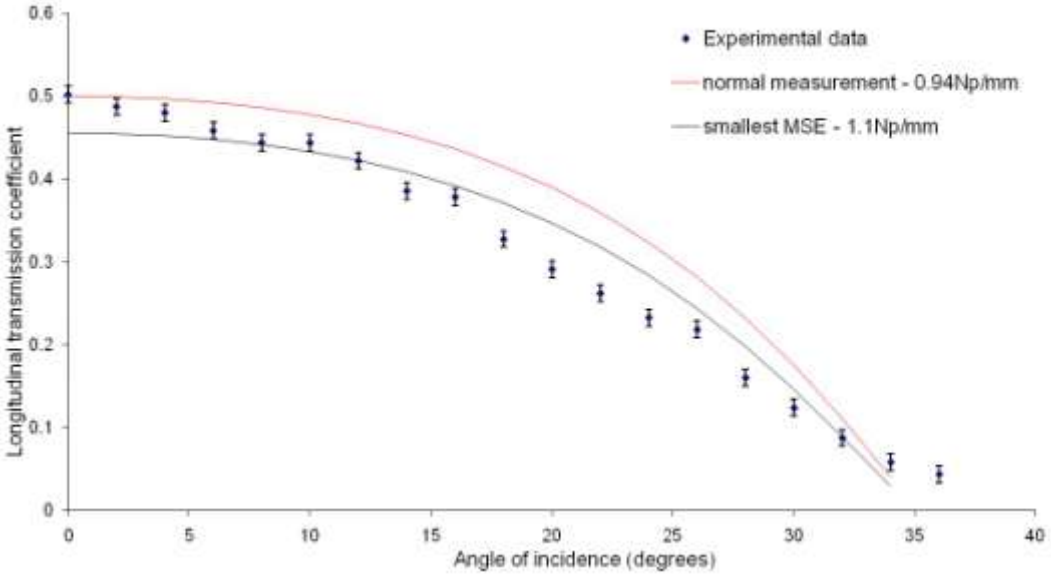

Figure 6.23 *Curve fitting data for Epofix sample.*

Repeat measurements showed that there was a backlash in the rotation of the sample holder so an error of up to 6° was observed between measurements of different samples. During the repeat measurements it was ensured that that the sample holder was normal to the jig before measurements were taken by using a small spirit level. However, it was observed that the alignment of the transducers could never be consistently repeated and the sample may not actually be normal to the ultrasound beam. The transmitting transducer was adjusted in the x and y positions so that the maximum signal observed was received for the measurements to be taken. These repeat measurements resulted in similar data to the original measurements, as shown in Figure 6.23. Other measurements were taken first recording the signal when the sample was rotated in one direction and then the signal recorded when the sample was

rotated back. Figure 6.24 shows the longitudinal wave data for the Epofix sample when rotated forward then back.

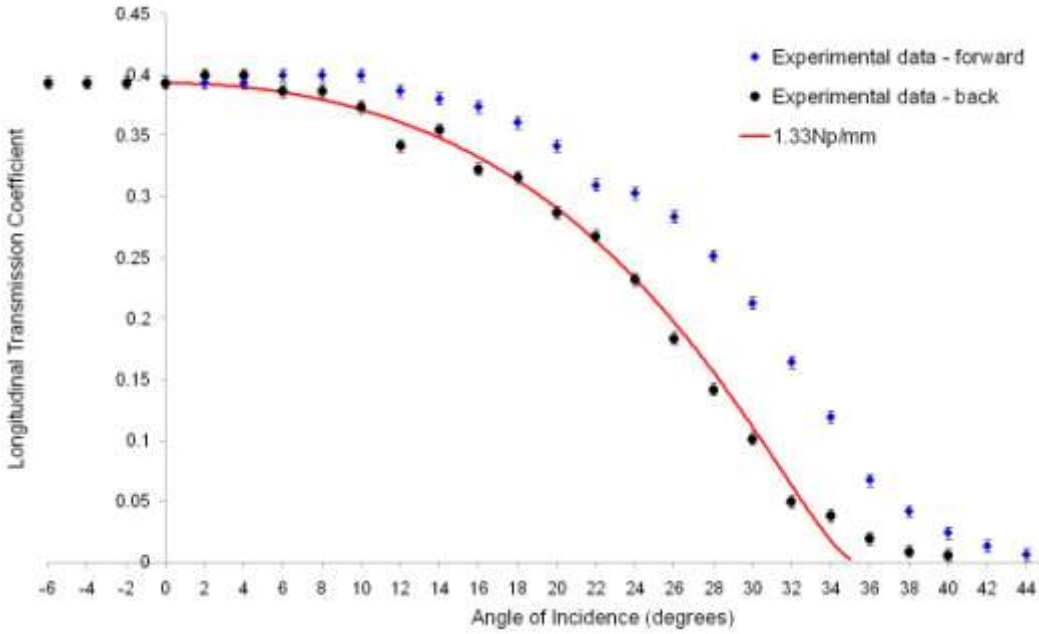

Figure 6.24 *Repeat measurement of longitudinal wave through Epofix sample. Signal recorded when sample rotated forwards then back*

The backlash is the difference in incident angle when rotated forwards and back and appears to be approximately 4°, although a difference of up to 6° was observed. Figure 6.25 shows the shear wave data for the Epofix sample when rotated forward and back.

It is shown in Figure 6.25 that a 3° angle shift in the theoretical curve results in a better fit to the data obtained from the forward rotation and the backlash is more clearly observed with the shear wave data when the amplitude does not change for a few degrees when rotated back. This observed backlash justifies the theoretical data being shifted up to 6° when curve fitting with the experimental shear attenuation data. The repeat measurements also resulted in slightly different attenuation values for both longitudinal and shear waves through the epoxy sample. However it was also

observed that the signal recorded from the receiver was significantly reduced compared to the signal from the original measurements, suggesting a loss in sensitivity from degradation of the transducers (the repeat measurements described here were taken four months after the original measurements). Therefore there is more confidence in the attenuation results from the original measurements which are presented here.

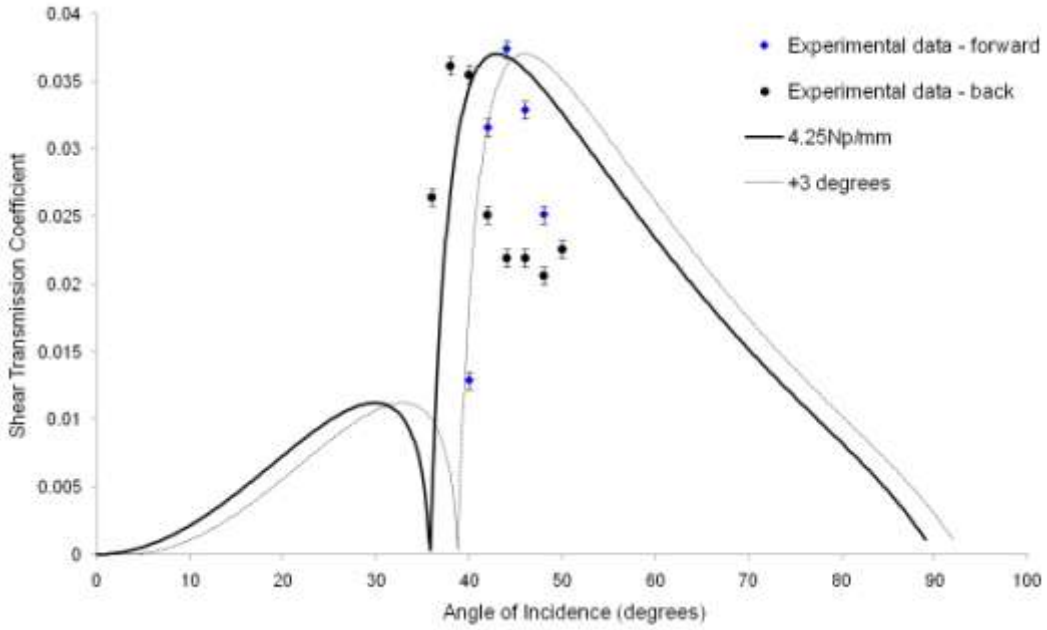

Figure 6.25 *Repeat measurement of shear wave through Epofix sample. Signal recorded when sample rotated forwards then back*

The original measurement data for the shear wave through the Epofix sample where the theoretical curve is shifted by 3° to fit the experimental data is shown in Figure 6.26. There was an additional problem with the resolution of the amplitude measurements taken so it was difficult to fit the data of some samples to a curve, as shown in Figure 6.27 for the 0.01 volume fraction MA95/Epofix sample. Therefore the shear attenuation was determined by fitting the theoretical curves to the maximum

experimental amplitude ratios for all the samples. The longitudinal and shear transmission coefficient curves for all other samples are shown in Appendix 2.

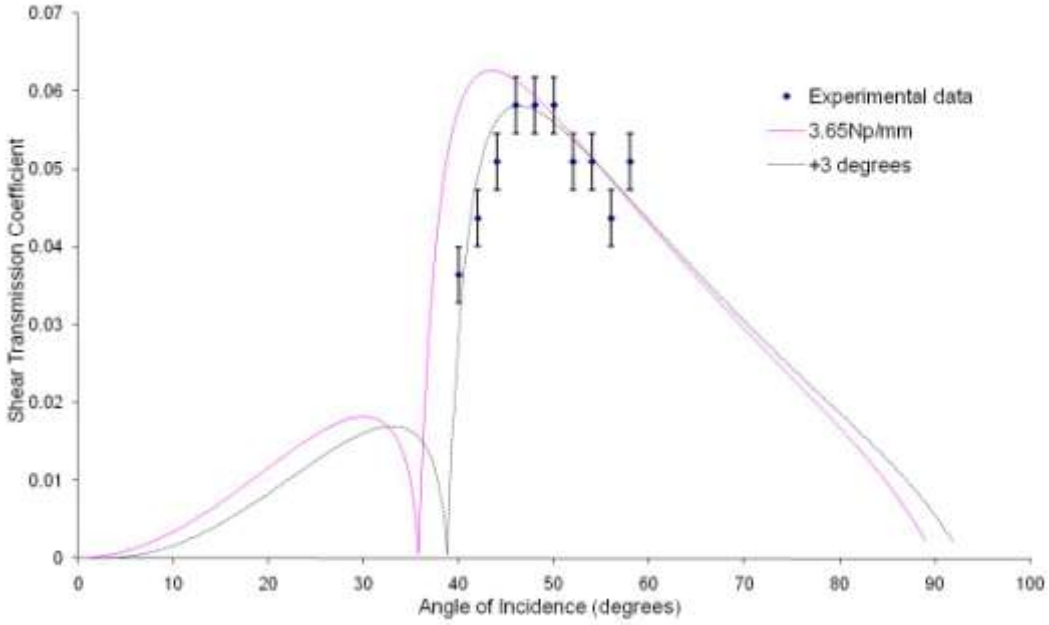

Figure 6.26 *Shear attenuation curve fitting data for Epofix sample.*

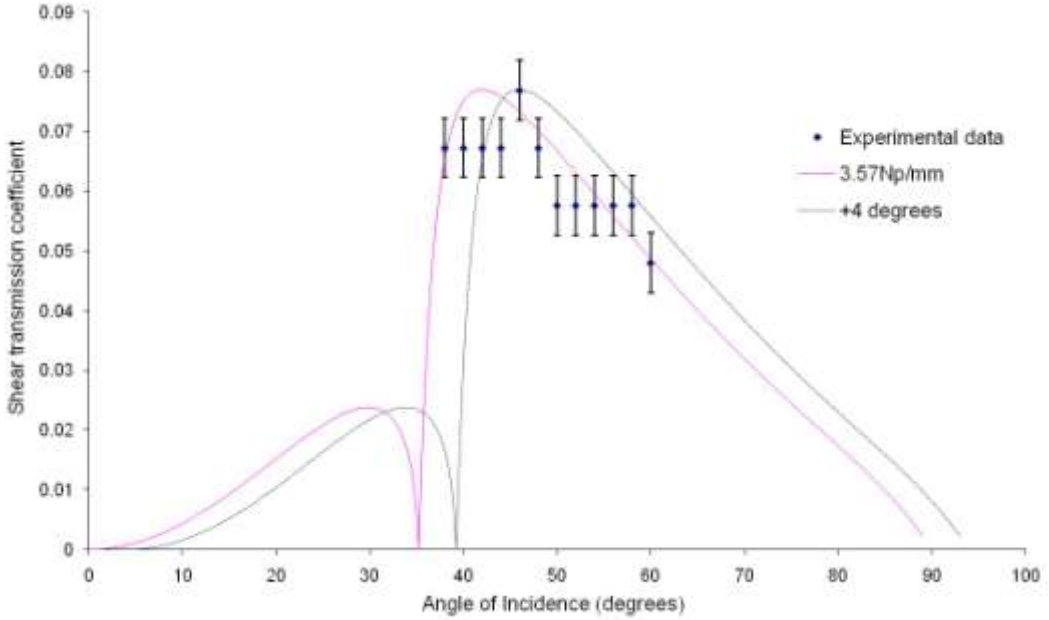

Figure 6.27 *Shear attenuation curve fitting data for 0.01MA95/Epofix sample*

The shear attenuation results are presented in Figure 6.28 in dB/mm. The values are significantly higher than the longitudinal attenuation values as expected and the Epotek 301 samples have a greater attenuation than the Epofix samples as before.

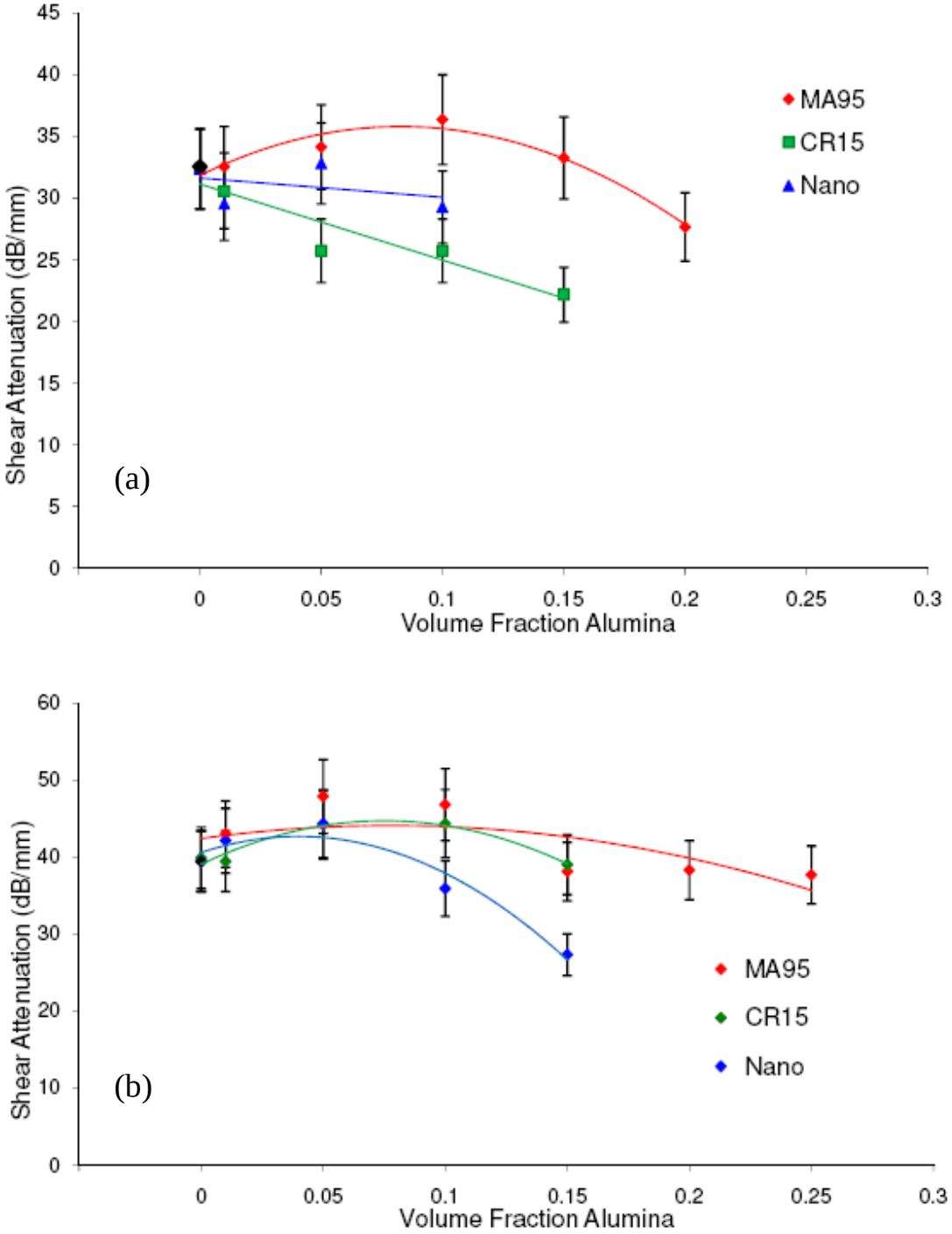

Figure 6.28 *Shear attenuation of (a) alumina filled Epofix samples (b) alumina filled Epotek 301 samples calculated from curve fitting*

Looking at the Epofix samples in Figure 6.28a the shear attenuation seems to follow a similar trend to the measured longitudinal attenuation where the CR15 grade with the smallest effective particle size has the lowest attenuation values. This is not the case with the Epotek 301 samples however, shown in Figure 6.28b where the CR15 samples have similar shear attenuation values to the MA95 samples. The Epotek301 samples also have higher shear attenuation valuations than the Epofix values, as with the longitudinal attenuation. The values are comparable to the only published data for shear attenuation of alumina filled epoxy measured at 30MHz [57,86], although the results here are a little lower. Shear attenuation values between 40dB/mm and 55dB/mm have been reported previously. [57,86]

As expected, the smaller particle size grade alumina (CR15) has the lowest longitudinal and shear attenuation values. When the particle size is smaller than the wavelength of the ultrasound reflective scattering is avoided. The nano grade alumina, which is made of large agglomerates around 20µm in diameter, shows similar attenuation properties to the larger grade MA95 alumina. The same trend is followed, in that a peak in attenuation is observed but the attenuation of nano grade does decrease at a lower volume fraction compared to the MA95 grade. This could be due to the large size of the agglomerates which are roughly spherical compared to the platelet shape of the MA95 grade, or to the increased porosity of the nano grade material.

As discussed in Chapter 5, attenuation values of passive materials are useful for high frequency transducer design. This work has shown that the longitudinal attenuation of alumina filled epoxy composites at a given frequency is dependent on the attenuation of the epoxy, which varies from epoxy to epoxy, and the particle size of

the alumina. A small particle size, ~1μm diameter, can minimise the longitudinal attenuation for the frequencies considered here, as shown by the CR15 grade samples in Figure 6.22. This pattern continues for shear attenuation only for the Epofix samples measured here, shown in Figure 6.28a. It is considered that the curve fitting technique is superior to a discrete angle measurement to obtain both longitudinal and shear wave attenuation because inaccuracies in the angle measurement can be taken into account.

For matching layer applications, the thickness of the layer is important in addition to the magnitude of acoustic impedance and minimisation of attenuation. The thickness relates to the operating frequency of the transducer because it has been found that optimal transducer performance factors, such as centre frequency, bandwidth, insertion loss and pulse length are achieved with a matching layer of ¼λ thickness. [110] This is around 25μm for 50MHz and 10μm for 100MHz operation with the material velocities considered here. Therefore an alumina filled epoxy matching layer would have to be lapped to thickness or applied to the transducer in a manner where the thickness can be controlled, such as spin coating. [58]

6.3 Summary

Alumina epoxy samples have been fabricated using three grades of alumina and two different epoxies. Particle characterisation with a particle size analyser and SEM showed the MA95 grade alumina to have platelet sized particles around 5μm in size, the CR15 grade to have spherically shaped particles that broke up to show discrete particles approximately 1μm in size and the nano grade alumina was found to be made up of large roughly spherical shaped agglomerates between 10μm and 20μm in size.

Higher volume fractions were achieved with the Epotek 301 epoxy as this has a slightly lower viscosity then Epofix, the other epoxy used. Volume fractions up to 0.25 were made using MA95, and up to 0.15 with both CR15 and the nano grade, although SEM images and density measurements indicated that the material made with the nano grade contained porosity. The porosity was located around the alumina agglomerates so increased with increasing volume fraction alumina. The other grades did not show the same level of porosity but some agglomeration was observed at higher volume fractions.

The velocity was measured through the alumina epoxy samples at 35MHz and the experimental data follows the Devaney model as expected. The porosity does not seem to affect the velocity through the nano grade alumina epoxy. Although the velocity is a little higher for the nano grade than the others, it is not a significant difference and it would be expected that there would be a decrease in velocity due to porosity as the ultrasound does not propagate in air and the air effectively acts as a scatterer.

Attenuation values were consistent with the relatively few other published values and the MA95 and nano grade alumina materials followed the same pattern as the tungsten filled epoxy, where there was generally a peak in attenuation around 0.05 volume fraction filler. The CR15 grade did not show this pattern as the attenuation was generally not affected by the volume fraction of alumina. This was expected as the particle size is significantly smaller than the ultrasound wavelength.

An improved sample holder was used to take measurements for the alumina epoxy samples, designed to accommodate discs. The changing of the sample holder may

have caused a problem with the rotation mechanism of the characterisation jig. A systematic error was found when using the curve fitting technique to determine attenuation values so that the theoretical curve had to be shifted to fit with the experimental data. There was found to be backlash in the rotation of the sample so that an error of up to 6° was observed, therefore shear attenuation was determined by matching the maximum amplitude ratio and shifting the theoretical curve up to 6° to fit the experimental data. An improved rotation mechanism must be realised for future measurements.

These results show that a high loading of alumina is required for it to be suitable for backing applications, and even then an acoustic impedance of up to only 5MRayl is possible. Alumina epoxy with lower volume fractions is suitable for matching layer applications where an intermediary acoustic value is required. For matching, the CR15 alumina grade would be most suitable as the particle size is small enough for increasing volume fraction alumina not to affect attenuation significantly. An additional problem to consider is the required thickness for matching high frequency devices. There are considerations for fabricating such thin layers as lapping bulk material is expensive and difficult so other techniques may have to be considered, such as spin coating.

CHAPTER 7

Fabrication of High Frequency Transducers Incorporating Tungsten Epoxy Backing

It is important to show that the material discussed in previous Chapters can be incorporated into practical transducers easily. This Chapter shows the development of transducer design to incorporate tungsten epoxy as backing. Firstly materials used in previous transducer designs are discussed and compared with the tungsten epoxy fabricated in this work and then transducer designs incorporating tungsten epoxy are presented and different fabrication routes for the backing to achieve the desired shape are illustrated.

7.1 Previous Transducer Design and SMA Fabrication

Previous work by the author at the University of Birmingham [111] has been based on fabricating piezocomposite transducers using a modified SMA connector as a housing, similar to some of the designs by other research groups reported in the literature previously described in Section 2.3.2 A schematic of a SMA-housed curved piezocomposite transducer illustrating all the components is shown in Figure 7.1. This design relies on the use of a conductive backing, in this case, a commercial silver epoxy. From Table 2.1 silver has an acoustic impedance value of 38MRayl, compared to 101MRayl for tungsten and 40.6MRayl for alumina.

Some of the fabrication steps in assembling the transducer are illustrated in Figure 7.2. The SMA connector was modified by mounting an IC (Integrated Circuit) socket pin onto the inner pin (Figure 7.2a). The socket was then filled with silver epoxy (186-3616, RS, UK) and the electroded piezocomposite disc set on top, as shown in Figure 7.2a. The composite was then surrounded with a electrically insulating and acoustically isolating mixture of epoxy and glass microballoons (3M, UK) in a ratio of 1:1 by weight (Figure 7.2c). Finally, the transducer was sputtered with gold to form the ground electrode, as shown in Figure 7.2d.

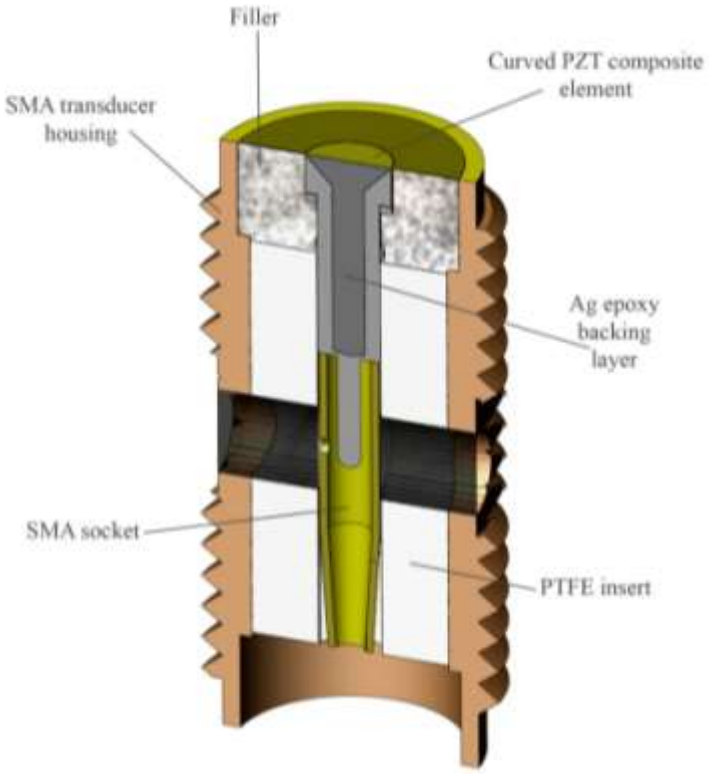

Figure 7.1 *Schematic of curved piezocomposite transducer in SMA housing*

Figure 7.2 *(a) Modified SMA connector with socket pin (b) Composite disc mounted on socket pin (c) After potting with insulating epoxy/glass micro-balloons (d) Complete transducer with ground Au electrode applied*

This fabrication procedure had some limitations as the SMA centre pin had to be modified. This involved removing the original SMA centre pin and soldering it to a trimmed socket pin before positioning the modified pin back into the casing. [112] The machined socket has a cavity which was filled with conducting silver epoxy, but

ensuring the cavity was completely filled was difficult. A photograph of the SMA housing and soldered pin is shown in Figure 7.3 and Figure 7.4 shows a cross section of a completed transducer.

Figure 7.3 *SMA Housing and soldered pin* [112]

There were problems with the fabrication described. As shown in Figure 7.4 the machined IC pin has an integral gripping mechanism in the cavity designed to grip the legs of the IC that would be inserted into it. Additional fabrication steps should be considered to improve the final transducer; drilling to remove the gripping system and using an epoxy backing that has a lower viscosity allowing flow may ensure that the cavity is filled and there are no air spaces, as shown in Figure 7.4. Additionally there were alignment problems with this transducer housing. The diameter of the IC pin leg is smaller than the SMA inner pin thus introducing potential alignment errors when soldering, and micrometer controlled tooling was required to ensure the top face of the transducer element was parallel and square to the end of the SMA housing.

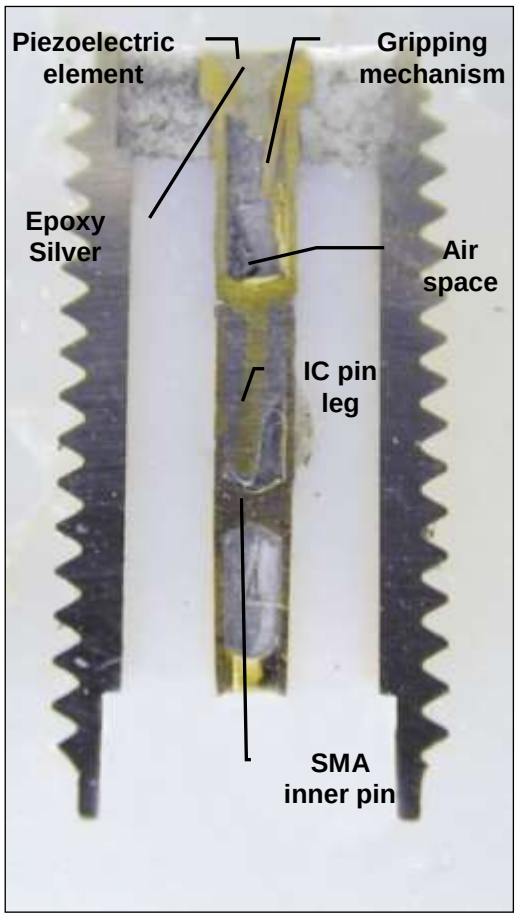

Figure 7.4 *Cross-section of piezocomposite transducer* [112]

SEM images of the silver loaded epoxy used as backing and for electrical contact in the work described are shown in Figure 7.5.

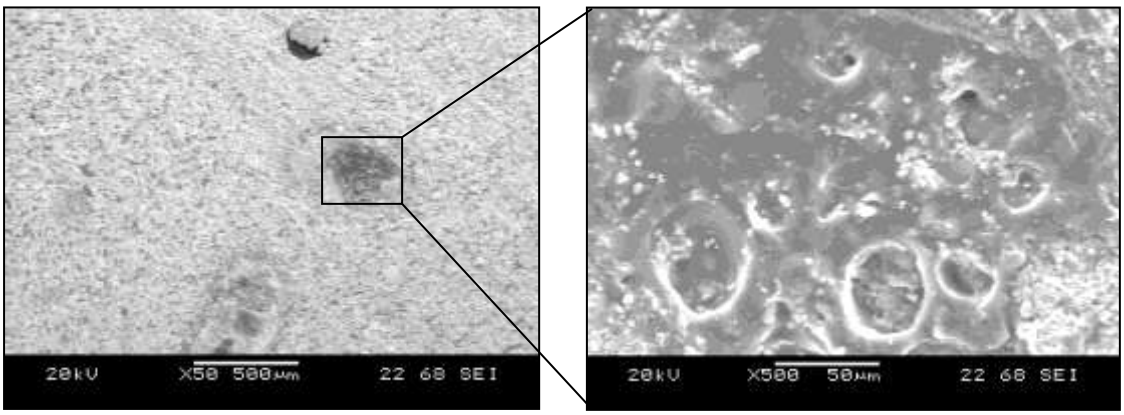

Figure 7.5 *SEM images of Ag-loaded epoxy*

This silver loaded epoxy is designed as a conducting adhesive to be used in small quantities. It is a two part thermosetting material with an epoxy resin base containing silver flakes. The high viscosity of the loaded epoxy means that cast shapes with no porosity are very difficult to achieve as it does not flow into a mould and porosity is still observed when the material undergoes degassing. Additionally the conductive epoxy has been found to be non-conducting sometimes in practice even when made to the manufacturer's instructions. The SEM images in Figure 7.5 show areas in the epoxy where the silver flakes are not fully dispersed in the epoxy, which may contribute to the epoxy not conducting.

A sample of the silver loaded epoxy was made for characterisation to compare with the other materials. Table 7.1 shows the measured acoustic properties.

Table 7.1 Measured acoustic properties of 186-3616 silver loaded epoxy

Velocity @5MHz (m/s)	Velocity @35MHz (m/s)	Acoustic Impedance, Z (MRayls)	Longitudinal Attenuation @35MHz (dB/mm)
1722	1755	4.35 ±0.05	60

The acoustic impedance of the silver epoxy is between that for the 0.05 and 0.10 tungsten epoxy material, but the longitudinal attenuation is higher than these materials at 60dB/mm. This attenuation value is higher than the materials under 0.30 tungsten volume fraction, being more similar to the conductive milled tungsten epoxy samples at approximately 70dB/mm, discussed in Section 5.2.3.3. Therefore in terms of attenuation it is suitable for backing, but it has a much lower acoustic impedance value compared to the conductive tungsten epoxy composite samples. The limitations of the material are that its higher viscosity means it cannot be made without some porosity and it is difficult to cast into shape. A piezocomposite transducer backed

with this silver epoxy would be lightly damped as the difference in acoustic impedance values is large. Using tungsten epoxy as backing has advantages over the silver as lower viscosities are achieved so the material can be cast into shape without any porosity and the amount of tungsten can be tailored to suit the damping needs of the transducer. It may be possible to overcome some of the problems encountered with this particular silver epoxy by fabricating a material and tailoring the silver volume fraction to adjust the viscosity and conductivity. However, as silver has a lower acoustic impedance value than tungsten and alumina, a higher loading of silver is required to achieve the same acoustic impedance value.

7.2 New Transducer Designs with Tungsten Backing

To overcome many of the transducer fabrication issues using the SMA housing a new customised casing was designed in this work. The electrical connections in the transducer had to be changed to incorporate the non-conducting tungsten epoxy backing fabricated in this work into the design. Although this complicates the fabrication somewhat, as miniature wire connections are necessary, it means that the composition of the backing can be altered easily within the design so transducers can be fabricated with backing acoustic impedance values tailored as required.

Two examples of curved composite transducer designs by Applied Functional Materialls Ltd. (AFM Ltd.) are shown in Figures 7.6 and 7.7. The backing is tungsten epoxy and the electrical connection is achieved using wiring. The wiring goes through the backing in the design in Figure 7.6. The backing material in Figure 7.7 includes a groove down one side which is designed to accommodate the wiring from the composite at the front face. The tungsten epoxy is shaped to accommodate the wiring and the curved face of the composite. Both designs include a

wedge-shaped backing to assist with the prevention of reflection straight back towards the composite. In both these designs the backing is required to be pre-fabricated and used as an 'insert'.

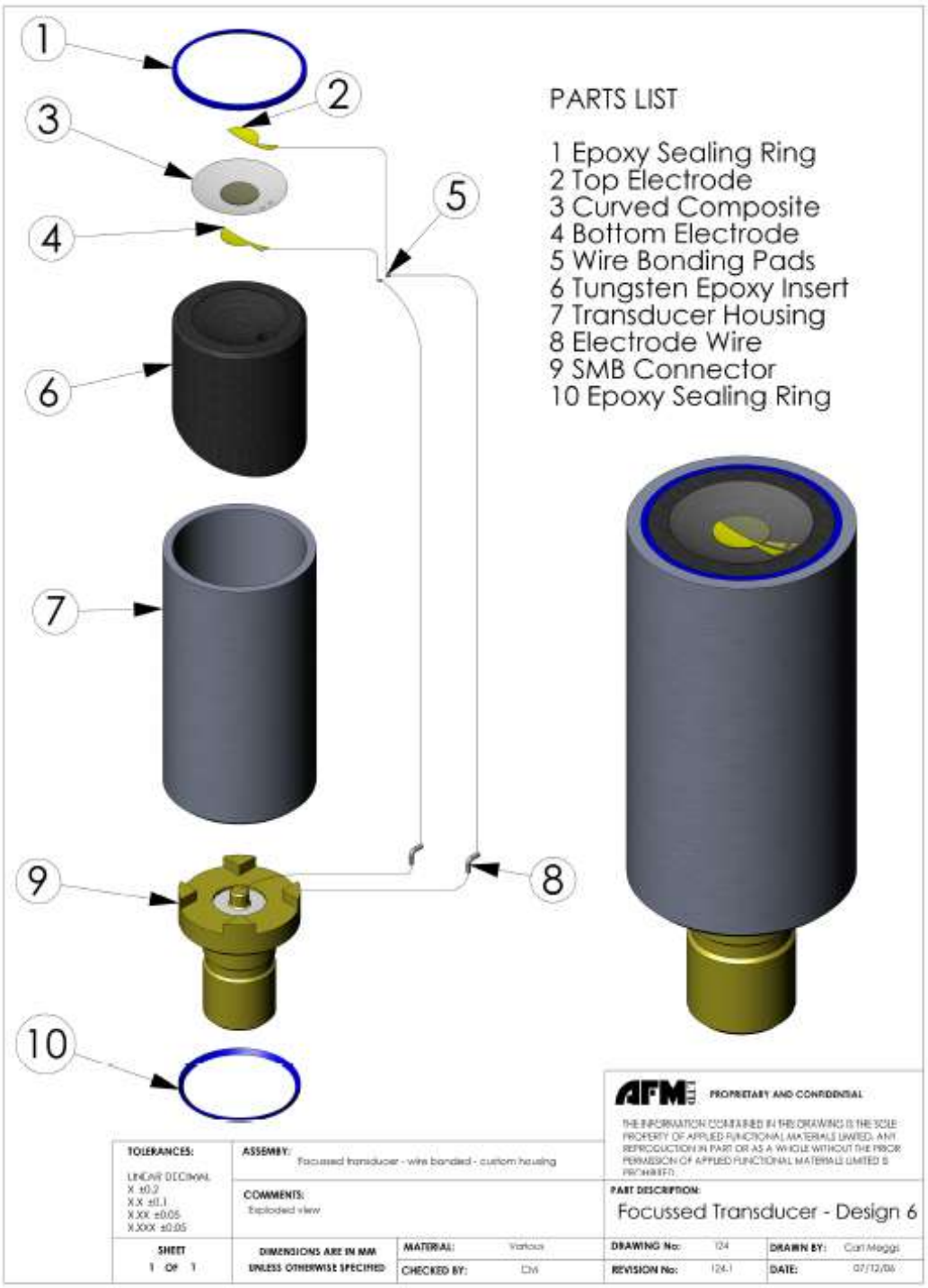

Figure 7.6 *AFM curved composite transducer design*

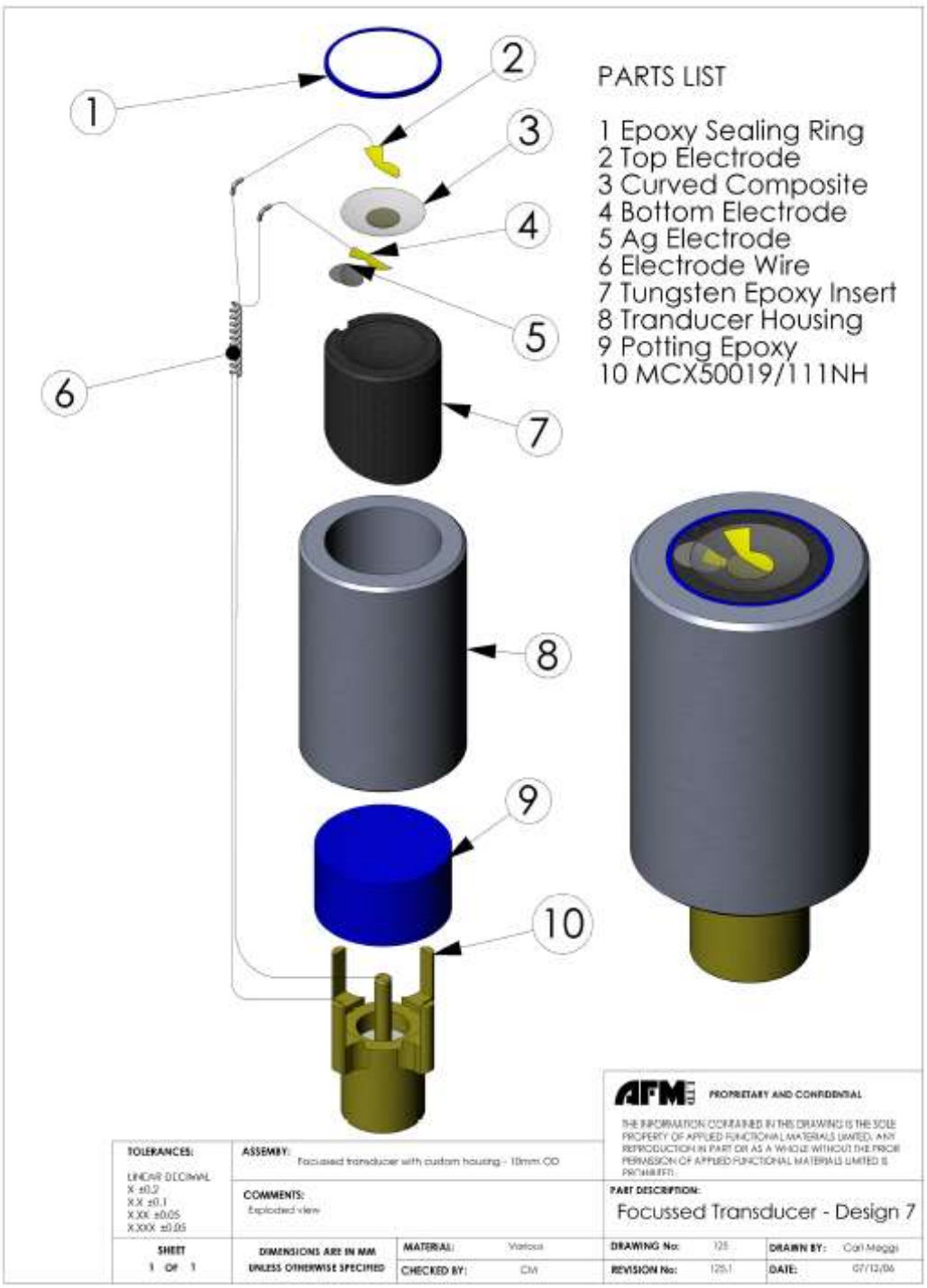

Figure 7.7 *AFM curved composite transducer design*

7.2.1 Fabrication Routes for Tungsten Epoxy Backing

There are two main fabrication routes for the tungsten epoxy backing insert; machining the insert out of a larger block or casting the epoxy directly into shape. Detailed designs can be drawn up in a computer aided design (CAD) program, such as Solid Works™ (Solidworks Corp., MA, US) and micro machining can be carried out to achieve the desired shape. A picture of the CAD design and a photograph of the finished insert produced by machining are shown in Figure 7.8.

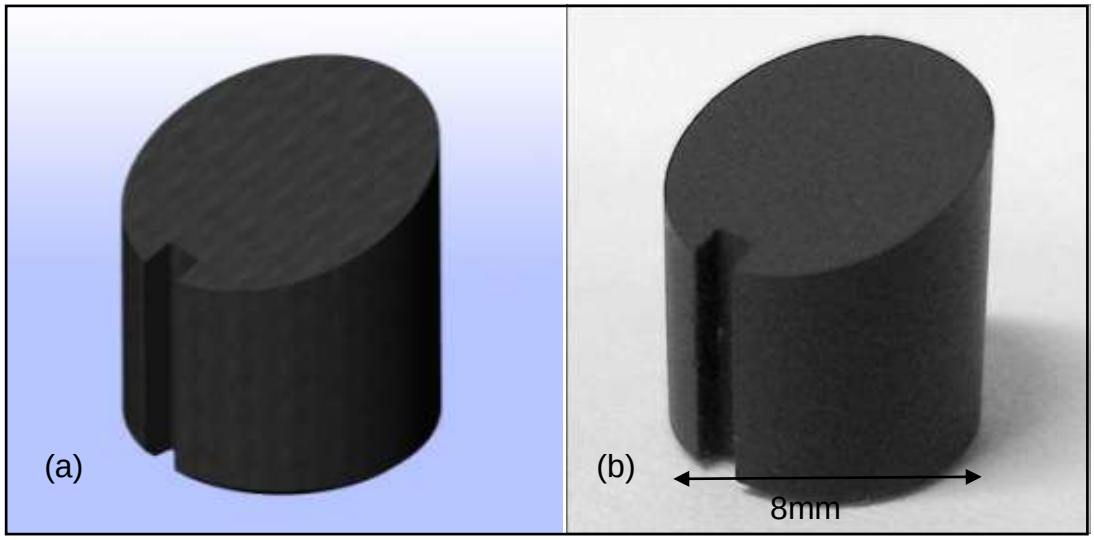

Figure 7.8 *(a) CAD design (b) machined backing*

Machining each insert is expensive and the accuracy of the detail depends on the tooling. A more attractive approach is casting the filled epoxy directly into shape. This means that multiple components can potentially be made consistently and the procedure can be more easily integrated into the complete transducer fabrication process. In addition the backing can be cast directly onto the active element, facilitating transducer assembly.

Initial fabrication trials were carried out by filling small rubber tubes with tungsten epoxy (~5mm diameter). It was found that it was necessary to degas the tungsten epoxy mixture before filling the tube to obtain material without large air holes and voids. Pictures of some of the samples from these trials are shown in Figure 7.9; the samples were obtained by adding the tungsten after the epoxy had been pre-cured for 30 minutes. Pre-cured samples that were not degassed showed large air voids (Figure 7.9a) and even when pre-cured samples were degassed, voids were obtained as the mixture was then too viscous to be degassed effectively (Figure 7.9b).

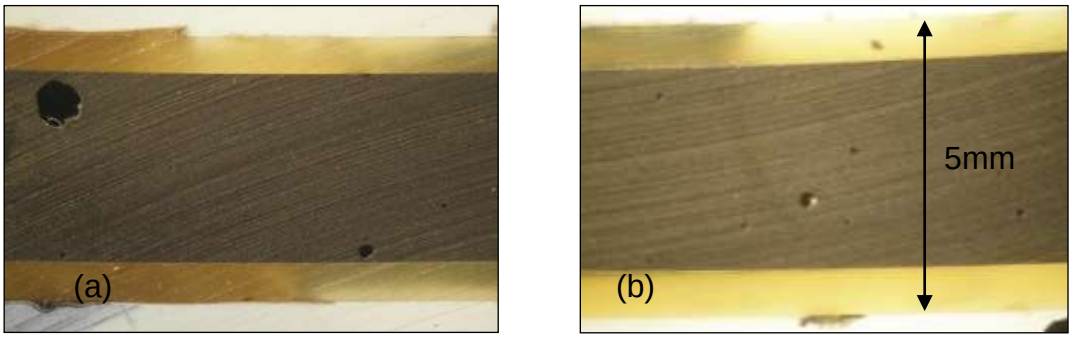

Figure 7.9 *Pre-cured tungsten epoxy cast into rubber tubes (a) without degassing (b) with degassing*

Samples where the tungsten and epoxy was mixed and degassed immediately showed less evidence of air holes, proving the method to be more suitable to cast transducer backings. The resulting samples with this fabrication method are shown in Figure 7.10, showing no small voids. There is one large void shown in Figure 7.10a at the top of the tube (right hand side in picture). This can be avoided with careful filling of the mould and removal of visible air bubbles.

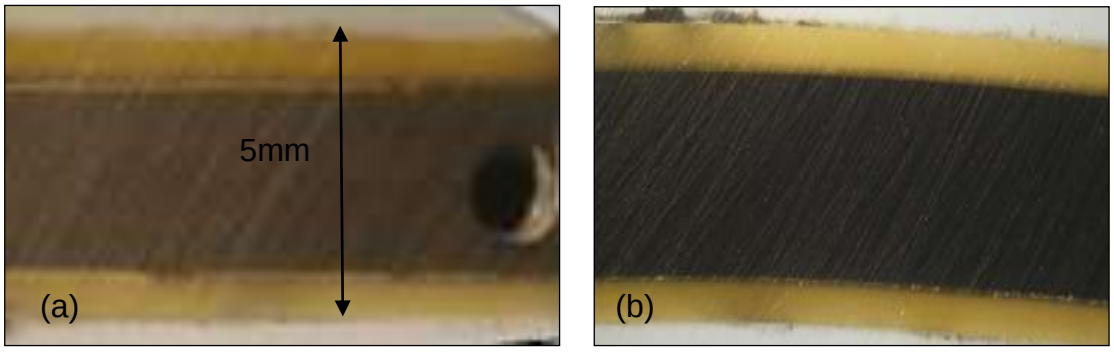

Figure 7.10 *Degassed tungsten epoxy cast into rubber tubes*

7.2.1.1 'Cast in Place' Fabrication

Following this preliminary work, a procedure was developed to mould the backing directly onto the active element of the transducer. [113] Wiring can also be incorporated so non conducting backing can be incorporated into the transducer design. Metal and PTFE mounts have been machined so that disposable silicone elastomer moulds can easily be made according to the transducer design. A flow diagram of the fabrication procedure is illustrated in Figure 7.11.

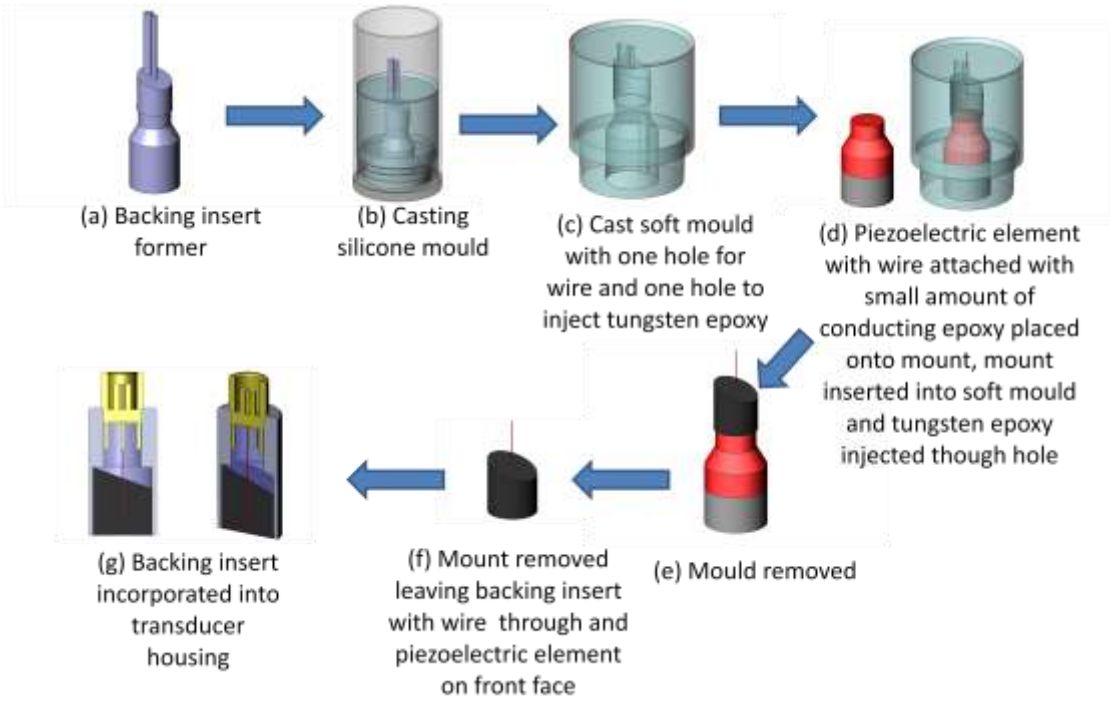

Figure 7.11 *Illustration of 'cast in place' fabrication process*

A soft mould is fabricated with a former, making the wedge shape of the final backing material with two holes; one to be able to inject the epoxy backing into the mould using a needle syringe and another for the wire to pass through the backing. shown in The piezocomposite disc (diameter 1.6mm) is attached to the mount with wax so it takes the shape of the former Figure 7.11d. A wire is then attached with a small amount of conducting epoxy (commercial Ag epoxy), as shown in Figure 7.12.

Figure 7.12 *Wired composite on top of mount*

The mount is then inserted into the soft mould made in Figure 7.11c and the wire is carefully threaded through the hole. Degassed tungsten epoxy is then injected into the mould. When the cavity is full with tungsten epoxy, any observed air bubbles are removed through the walls of the silicone mould using another syringe needle. The whole assembly is then left for 24 hours while the epoxy cures. After curing the whole mould is put into an oven at 40ºC to loosen the wax. The mount is then removed leaving the transducer element left on the tungsten epoxy, which is carefully removed from the silicone mould ready to be potted into a transducer casing (Figure 7.11e and 7.11f). A photograph of a tungsten backing cast directly onto a piezocomposite disc, using the method described, is shown in Figure 7.13.

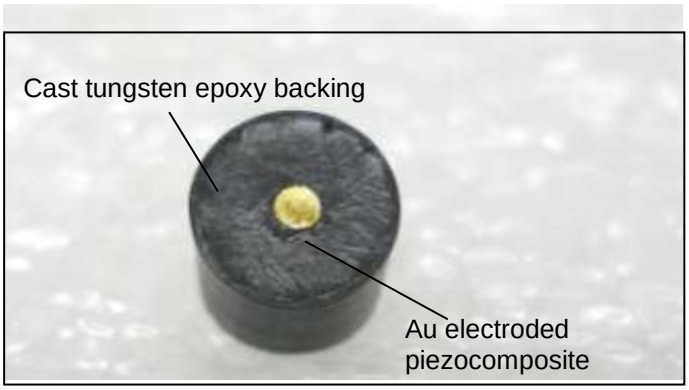

Figure 7.13 *1.6mm diameter piezocomposite disc cast onto tungsten epoxy backing*

An example of the final cured tungsten epoxy backing with wiring through the length is shown in Figure 7.14. There are associated problems with casting a wired element. Casting a backing onto a piezocomposite with a wire is difficult: adhesion between the composite and wire is weak so the wire can easily break away from the composite. This is a function of the electrode adhesion to the composite, which can be quite strong if proper film deposition and pre-cleaning are used. An additional problem is when the tungsten epoxy is cast into the mould: a column of tungsten epoxy can form around the wire up through the hole in the mould, as shown in Figure 7.14. This epoxy around the wire can be difficult to remove without damaging the wire, therefore this fabrication process does require skill. Examples of complete transducers fabricated using this method with custom casing are shown in Figure 7.15.

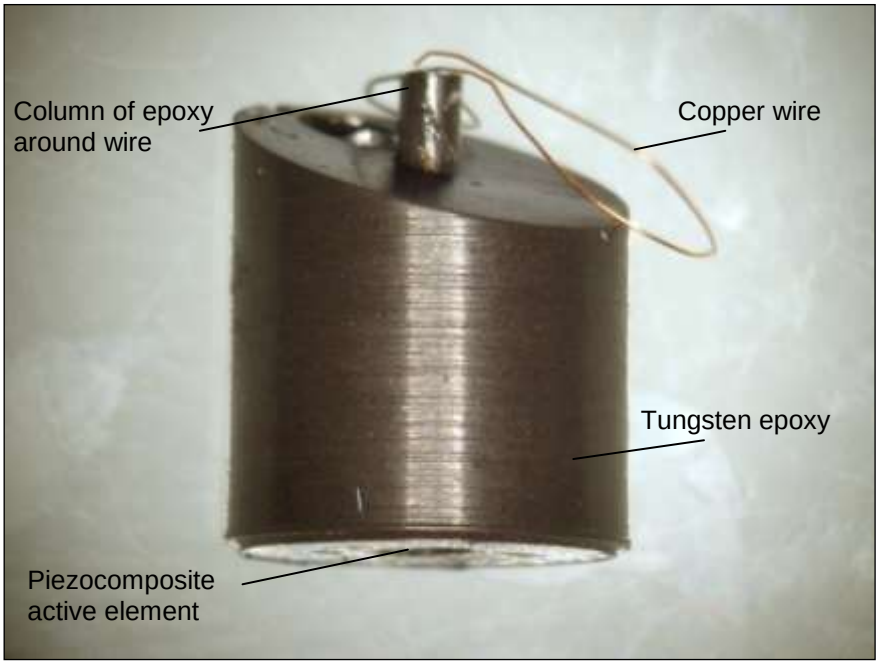

Figure 7.14 *Cast tungsten epoxy backing with wire*

A number of transducers have been made this way by AFM Ltd with curved and flat composite and PVDF active material; examples are shown in Figure 7.15.

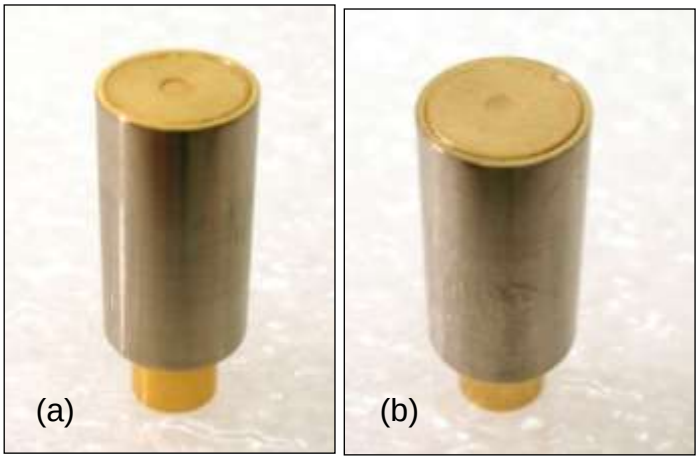

Figure 7.15 *(a) Flat composite transducer (AFMTH17) (b) Curved composite transducer (AFMTH16)*

7.3 Transducer Properties

The transducers made by AFM Ltd via the processes described and pictured in Figure 7.15 were backed with 0.10 volume fraction tungsten epoxy (Z ~4MRayl) and earlier prototypes made with a SMA housing were backed with the commercial silver epoxy discussed. Table 7.2 presents the properties of four transducers, two flat, and two focussed transducers, named AFMTH9, AFMTH10, AFMTH16 and AFMTH17.

Table 7.2 Transducer Properties

Transducer	Element Size (mm)	Element Thickness (µm)	Operational Frequency (MHz)	Focal Point (mm)	Transducer Housing	Backing Material
AFMTH9	1.7 ø	53	36	3.3	SMA	Ag Epoxy
AFMTH10	1.2x0.8	73	26	-	SMA	Ag Epoxy
AFMTH16	1.6 ø	48	43	2.4	Custom	W Epoxy
AFMTH17	1.6 ø	52	43.5	-	Custom	W Epoxy

These transducers have been tested in a pulse echo mode and the -6dB data is reproduced here in Table 7.3. [(107)]

Table 7.3 Transducer Data at -6dB Pulse Echo Mode

Transducer	Centre Frequency (MHz)	Bandwidth (MHz)	%	Pulse Length (ns)	Axial Resolution (μm)	Lateral Resolution (μm)	Depth of Field (mm)
AFMTH9 (SMA/Ag)	38	6	15.8%	165	127	145	3.3
AFMTH10 (SMA/Ag)	28	9	32.1%	101	78	-	-
AFMTH16 (Custom/W)	41.75	8.5	20.4%	91	70	100	2.4
AFMTH17 (Custom/W)	42	7	16.7%	103	79	430	-

The operating frequency of a transducer is determined by the piezoelectric properties of the active element material and the geometry, namely the thickness, of the element. Properties such as the pulse length and percentage bandwidth will be affected by the properties of the backing material. The data in Tables 7.2 and 7.3 can be used to compare the transducer properties of the SMA transducers backed with silver epoxy and the custom made transducers backed with tungsten epoxy. They appear to compare well, which is expected as the acoustic impedances of the silver epoxy backing and 0.10 volume fraction tungsten epoxy are similar. Using backing with different volume fractions may influence some of the transducer properties shown in Table 7.3 and is the main advantage of using tungsten epoxy over the commercial silver epoxy as the amount of tungsten can be altered.

7.4 Summary

Customised transducer housings have been developed to overcome the fabrication problems with the original SMA housing. Transducer prototypes have been made using non-conducting tungsten epoxy as backing. A transducer fabrication procedure has been developed to incorporate cast backing material straight onto the piezocomposite element, which is a preferred method to machining backing inserts as it is less expensive, can be done in house, reduces steps involved in the whole assembly process, and avoids potentially damaging effects of bondlines. Wiring has been successfully used to compensate for using a non-conducting backing although the wiring is fragile and easily damaged so other methods of electrical contact may be needed, although wiring should be sufficient with good electrodes. Initial experimental data suggests that the tungsten backing has a similar performance to other materials previously used as backing which cannot be altered to adjust for different acoustic impedance requirements. Therefore, it is expected that better performance properties can be achieved by optimising the backing loading and hence, acoustic impedance value.

CHAPTER 8

Conclusions and Further Work

8.1 General Overview

Ultrasound imaging is a very well established technique in diagnostic medicine, with conventional systems operating at frequencies < 20MHz. Recent advances in the manufacture of fine piezocomposite scale active material has led to the increased interest in high frequency transducer systems that are useful for applications in dermatology and ophthalmology amongst other applications. As a result, there is a need for accurate modelling of high frequency devices to aid the transducer design process. Important properties of passive materials in the transducer device are frequency dependent so it is necessary to obtain data for certain material properties at specific operating frequencies. Additionally the acoustic impedance requirements for these passive materials in piezocomposite devices are different to the requirements in conventional ceramic devices so knowledge of material properties is important to determine what materials are suitable.

This Thesis has described the fabrication and characterisation of materials conventionally used for backing and matching applications and how adjusting the amount of filler in the epoxy matrix can result in materials with acoustic impedance values suitable for use in high frequency piezocomposite devices. The theory of the characterisation technique for the acoustic properties of both longitudinal and shear waves through the material at high frequency has been discussed. The results presented detailed the measured material properties for both types of materials made; tungsten and alumina filled epoxy, particularly showing that a curve fitting technique to determine attenuation values gives a more accurate result as errors in the rotation angle of the sample in the experimental set up can be identified. It has also been shown how backing material made here can be incorporated into practical transducers

and transducer performance has been compared with previous transducer prototypes with other backing materials.

8.2 Fabrication of Materials

Filled epoxy samples were made using tungsten and alumina as filler particles. Mixing procedures were developed for each material so that materials with filler volume fraction up to approximately 0.3 could be made easily, without the filler particles forming a sediment or large agglomerates. Above this volume fraction the mixture proved too viscous to be degassed and cast properly. Attempts to fabricate higher volume fraction tungsten materials by reducing the viscosity with a solvent additive resulted in a lower volume fraction than expected as filler material was lost as the solvent evaporated. Higher tungsten volume fractions were made by milling the tungsten particles with epoxy or combining with PVB, but the milled mixture could not be degassed, resulting in porous material. The alumina was found to be more likely to form agglomerates than the tungsten, depending on the grade used. Three different alumina grades were used in two different epoxies. Higher loading was achieved in the Epotek 301 epoxy, which was slightly less viscous than the other epoxy used. A maximum volume fraction of 0.25 was achieved with the MA95 grade alumina, which had the largest particle size. Volume fractions up to 0.15 were made with the other grades of alumina investigated but SEM analysis showed that the nano grade was not fully dispersed, forming large agglomerates. Therefore it is predicted that if the nano grade alumina was fully dispersed in the epoxy the maximum loading achievable would be significantly lower. The nano grade material also contained porosity, which increased with increasing amount of filler.

8.3 Acoustic Characterisation of Materials

The longitudinal velocity was measured through the tungsten epoxy samples at 5MHz and 35MHz. There was no significant difference between the two sets of data, indicating that velocity is independent of frequency over this frequency range. The longitudinal and shear velocity was also found to follow the Devaney scattering model so the velocity and acoustic impedance may be estimated using this model. This is useful for transducer design as the acoustic impedance can be tailored by adjusting the amount of tungsten to achieve the required damping. Tungsten volume fraction up to 0.3 can be made easily using the final fabrication procedure described, corresponding to an acoustic impedance range of 3-10MRayl. A backing with an acoustic impedance value of 10MRayl may not be suitable for a conventional ceramic transducer but as piezocomposite has a lower acoustic impedance, the required impedance value for the backing is also lower. Therefore this range is highly suitable for backing a piezocomposite device. Tungsten is more suitable for backing than the alumina as a much higher loading of alumina is required to achieve similar acoustic impedance values.

The attenuation results for both the tungsten and alumina materials are higher than other values reported in the literature measured at lower frequencies, and similar to other work measured at 30MHz, [86] indicating attenuation does increase with frequency. Shear attenuation is greater than for longitudinal waves, and the trend of attenuation shows a familiar pattern with a peak in attenuation at approximately 0.05 volume fraction, as shown in other work. [56] The higher volume fraction tungsten achieved with the high shear milling does not follow this trend. It is predicted that different attenuation processes are acting in these materials, as the structure cannot be described as a 0-3 composite with discrete scatterers. At a certain volume fraction

(>0.3) the filler particles join together creating a network, and it is the attenuation properties of the filler material that are dominant. The attenuation results for the alumina material show the influence of particle size. It seems that the CR15 grade with a particle size of approximately 1μm is small enough not to influence the attenuation as the filler volume fraction increases, because the attenuation of this grade does not significantly change with increasing volume fraction. This is not the case with both MA95 and the nano grade which show an increase with a peak around 0.05-0.10 volume fraction. The porosity of the nano grade alumina filled material does not seem to affect either velocity or attenuation, although the attenuation does reduce more than the MA95 grade, indicating that something other than particle size may have an influence.

8.4 Improved Transducer Design and Packaging

The development of some piezocomposite transducer prototypes has been described. Tungsten backing made in this work has been incorporated into transducer devices and tested. The transducer design had to be changed to incorporate the non-conducting backing, introducing wire bonding to connect the active element electrically. Two approaches were used to fabricate the required backing insert; machining from a bigger block of material and casting the backing straight onto the active element using a disposable silicone mould. The material is suitable for casting in this way but including wiring can be difficult.

Transducers including 0.10 volume fraction tungsten backing were tested in pulse-echo mode along with earlier transducer prototypes that had silver loaded epoxy as backing. The transducer properties were similar, showing that the tungsten backing was comparable to the silver epoxy as a backing, which is expected as the measured

acoustic impedance values were also similar. It is expected that by using tungsten backing with different volume fractions and hence, acoustic impedance values, that the transducer properties can be improved by optimising the acoustic impedance of the backing so a compromise is reached so the transducer pulse length and sensitivity are improved.

8.5 Suggestions for Further Work

The results presented in this Thesis have highlighted the need for a more precise rotation mechanism for attenuation measurements using a through transmission characterisation technique. A calibration technique must be developed to ensure the a precise normal measurement and further accurate rotation. The use of a curve fitting approach rather than discrete incident angle measurements to determine attenuation meant that this problem could be easily identified. Future measurements should also be taken over a full range if incident angles to easily identify any errors and obtain accurate results.

This Thesis has mainly considered passive materials for single element devices. Array devices utilising a large number of elements on a piezocomposite array have an advantage over single element devices as the transducer can be scanned electrically rather than mechanically. The backing requirements for an array device are similar to a single element device, only the backing must be non-conducting so the elements are not shorted out. Therefore an investigation must be carried out to determine whether the tungsten epoxy material made here is suitable for backing array devices. Although this work has found that tungsten epoxy with a tungsten volume fraction <0.3 is non-conducting the size of the particles must also be considered. Depending

on the spacing of elements or electrodes the tungsten filler particles could short the system.

As discussed in this Thesis, the wire bonding of the transducer device may be unreliable and causes problems in manufacture. Therefore in future devices it is desirable to move away from wire bonding to electrically connect the active material. It is considered that along with the investigation of array devices the packaging will be improved using silicon based electronics to drive the transducer device.

This work has reported measurements at 5MHz and 35MHz showing particle sizes of about 1µm do not affect attenuation but larger agglomerates do have an influence. The frequency limitation of the measurements reported here mean that this work cannot be used to determine if this would be the case at higher frequency operation where at 100MHz the wavelength of ultrasound through these materials could be as low as 15µm. The use of nano particles as filler material for matching material has been reported in the literature. [90; 92] However, as shown in this work dispersion of the fine particles to prevent large agglomerates is difficult. It may be possible to obtain a dispersion of the nano particles using a dispersive agent in a suitable slurry. However, it would still be difficult to obtain a full dispersion in an epoxy, as used in this work. Additionally, as discussed in Chapter 6, it would be expected that only a very low volume fraction would be possible using the fabrication method described here. Therefore an alternative fabrication method should be investigated, such as spin coating. This method may be more suitable for making the thin films that are necessary for high frequency matching layers as casting epoxy, as described in this work, and then lapping down to thickness can be a costly difficult process.

The prototype transducers fabricated by AFM Ltd, described in this work did not have matching layers. As piezocomposite has a lower acoustic impedance value than conventional ceramic, it is intrinsically better matched to tissue and therefore may not require matching in the same way. An investigation should be carried out to determine the performance of matching on a piezocomposite transducer to assess whether it is an essential part of the transducer needed to improve performance. This may also be determined by commercial exploration regarding the additional benefits of such matching layers and whether the cost is acceptable.

APPENDIX 1

Derivations of Transmission Coefficients

Many entry level ultrasound textbooks give the expression for the transmission coefficient for two mediums at normal incidence. [1; 76] More advanced texts then go into more detail to give the coefficients across a range of incident angles. [114] This section will show the derivations for the transmission coefficients given in Chapter 3 for the "through transmission" set up, first at normal incidence, then at oblique incidence.

A1 Plane Wave Incident at Boundary at Normal Incidence

Following the analysis presented by O'Leary [101] consider a plane wave travelling through a medium of acoustic impedance Z_1 incident normally on a boundary with another medium of acoustic impedance Z_2, as shown in Figure A1.

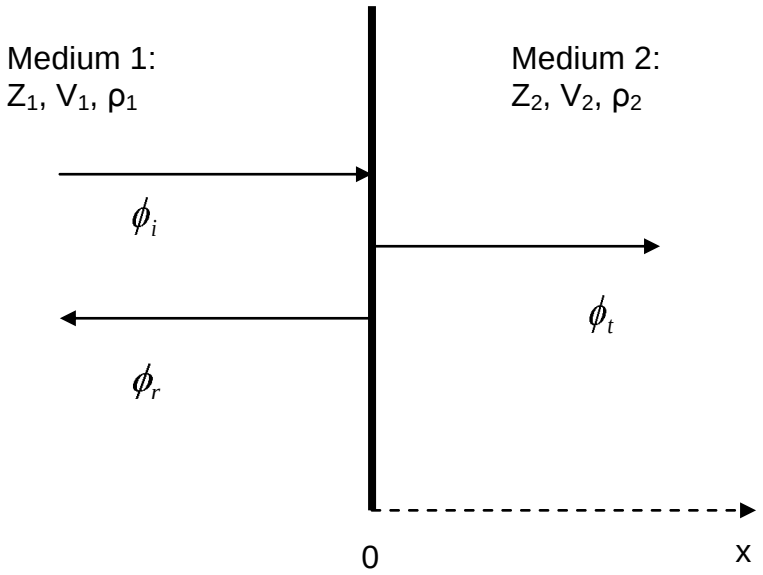

Figure A1 *Schematic of plane wave incident on boundary between two media*

Where

Z_n = the acoustic impedance of the medium

V_n = the longitudinal velocity of the medium

P_n = the density of the medium

n= 1 or 2 depending on which medium is being described

The incident, reflected and transmitted waves can be described in term of acoustic pressures, $\hat{\phi}_i$, $\hat{\phi}_r$ and $\hat{\phi}_t$ respectively

$$\begin{aligned}\hat{\phi}_i &= \phi_i \exp[j(\omega t - k_1 x)] \\ \hat{\phi}_r &= \phi_r \exp[j(\omega t + k_1 x)] \\ \hat{\phi}_t &= \phi_t \exp[j(\omega t - k_2 x)]\end{aligned} \qquad \textbf{Equation A1}$$

Where

ϕ_i, ϕ_r and ϕ_t = the amplitude of the respective waves

k_1 and k_2 = the wave numbers of the respective waves

x = the direction of wave propagation

For the incident wave the pressure transmission and reflection coefficients can be defined as follows

$$\begin{aligned}T_P &= \frac{\hat{\phi}_t}{\hat{\phi}_i} \\ R_P &= \frac{\hat{\phi}_r}{\hat{\phi}_i}\end{aligned} \qquad \textbf{Equation A2}$$

The corresponding power transmission and reflection coefficients can then be derived. Firstly, the intensity of each wave can be defined by

$$\begin{aligned}I_i &= \frac{\phi_i^{\,2}}{2}\frac{1}{Z_1} \\ I_r &= \frac{\phi_r^{\,2}}{2}\frac{1}{Z_1} \\ I_t &= \frac{\phi_t^{\,2}}{2}\frac{1}{Z_2}\end{aligned} \qquad \textbf{Equation A3}$$

The intensity transmission coefficient is given in Equation A4, similar to the pressure transmission coefficient.

$$T_I = \frac{I_t}{I_i} \qquad \textbf{Equation A4}$$

Substituting for I_t and I_i from Equation A3 gives

$$T_I = \frac{\frac{\phi_t^{\,2}}{2}\frac{1}{Z_2}}{\frac{\phi_i^{\,2}}{2}\frac{1}{Z_1}}$$

$$T_I = \frac{Z_1}{Z_2}\frac{\phi_t^{\,2}}{\phi_i^{\,2}} \qquad \textbf{Equation A5}$$

$$T_I = \frac{Z_1}{Z_2}T_P^{\,2}$$

Similarly Equation A6 gives the intensity reflection coefficient.

$$R_I = \frac{\frac{\phi_r^{\,2}}{2}\frac{1}{Z_1}}{\frac{\phi_i^{\,2}}{2}\frac{1}{Z_1}}$$

$$R_I = \frac{\phi_r^{\,2}}{\phi_i^{\,2}} \qquad \textbf{Equation A6}$$

$$R_I = R_P^{\,2}$$

As the two media are in contact the following boundary conditions must be satisfied.

The particle pressures on both sides must be equal.

The particle velocities on both sides must be equal.

Therefore at x = 0

$$\hat{\phi}_i + \hat{\phi}_r = \hat{\phi}_t \qquad \textbf{Equation A7}$$

$$\hat{u}_i + \hat{u}_r = \hat{u}_t \qquad \textbf{Equation A8}$$

Where u is the particle velocity and $\frac{\phi}{u} = \pm Z$ depending on the direction in which the wave is travelling so Equation A9 is obtained from A7 and A8.

$$\frac{(\phi_i + \phi_r)}{(u_i + u_r)} = \frac{\phi_t}{u_t}$$

$$= Z_2 \qquad \textbf{Equation A9}$$

Therefore

$$Z_1 \frac{(\phi_i + \phi_r)}{(\phi_i - \phi_r)} = Z_2 \qquad \textbf{Equation A10}$$

Solving for T_P and R_P in Equation A2 gives

$$T_{1P}^2 = \frac{\phi_t}{\phi_i}$$

$$= \frac{2Z_2}{Z_2 + Z_1} \qquad \textbf{Equation A11}$$

$$R_{1P}^2 = \frac{\phi_r}{\phi_i}$$

$$= \frac{Z_2 - Z_1}{Z_2 + Z_1} \qquad \textbf{Equation A12}$$

The corresponding intensity transmission and reflection coefficients are

$$T_{1I}^2 = \frac{4Z_1 Z_2}{(Z_2 + Z_1)^2} \qquad \textbf{Equation A13}$$

$$R_{1I}^2 = \left(\frac{Z_2 - Z_1}{Z_2 + Z_1}\right)^2 \qquad \textbf{Equation A14}$$

A2 Plane Wave Incident at Boundary at Oblique Incidence

The following analysis shows the derivation of transmission coefficients for oblique incidence by Brekhovskikh (103) used in Equations 3.29, 3.30, 3.31 and 3.32.

A2.1 Fundamental Equations and Boundary Conditions

The particle velocity in a medium can be expressed with a scalar and vector potential using Equation A15.

$$v = grad\phi + curl\psi \qquad \textbf{Equation A15}$$

In the case of a plane wave, assuming all quantities depend only on the coordinates *x* and *z*, and that the particle motion is in the *xz*-plane, the potential ψ can be chosen so only its *y*-component (denoted here by ψ) differs from zero. Then, according to Equation A15, v will be a vector with the components

$$v_x = \frac{\partial\phi}{\partial x} - \frac{\partial\psi}{\partial z},\ v_y = 0,\ v_z = \frac{\partial\phi}{\partial z} + \frac{\partial\psi}{\partial x} \qquad \textbf{Equation A16}$$

ϕ and ψ are the potentials of the longitudinal and shear waves respectively . It can be shown that these potentials satisfy the wave equations

$$\nabla^2\phi = \frac{1}{V_L{}^2}\frac{\partial^2\phi}{\partial t^2},\ \nabla^2\psi = \frac{1}{V_S}\frac{\partial^2\psi}{\partial t^2} \qquad \textbf{Equation A17}$$

Where V_L and V_S are the velocities of the longitudinal and shear waves respectively. They may be expressed in terms of Lame parameters λ and μ and the density ρ of the medium:

$$V_L = \sqrt{\left(\frac{\lambda + 2\mu}{\rho}\right)},\ V_S = \sqrt{\frac{\mu}{\rho}} \qquad \textbf{Equation A18}$$

The normal components of the stress and displacement must be continuous across the boundary. The tangential components of the stress tensor must also be continuous but as the tangential stresses in the liquid vanish the simple requirement is that the

tangential components of the stress tensor be zero at the boundary. The following expressions of the stress tensor components are important for in the case of a plane wave:

$$Z_z = \lambda\left(\frac{\partial u_x}{\partial x} + \frac{\partial u_z}{\partial z}\right) + 2\mu\frac{\partial u_z}{\partial z},\ Z_x = \mu\left(\frac{\partial u_x}{\partial z} + \frac{\partial u_z}{\partial x}\right),\ Z_y = 0 \qquad \textbf{Equation A19}$$

where u_x and u_z are the displacements along the *x*- and *z*-axes, respectively. The *z*-axis is assumed to be normal to the boundary. The displacements and stresses can be expressed in terms of ϕ and ψ using Equation A16. The displacement components u_x and u_z are obtained from the velocity components v_x and v_z by diving by $-i\omega$.

Quantities referring to the solid medium will be labelled with subscript 1 and quantities referring to the liquid phase will be left without subscripts. The boundary conditions between the solid-liquid medium at z=0 can now be written:

continuity of Z_z: $$\lambda\nabla^2\phi = \lambda_1\nabla^2\phi_1 + 2\mu_1\left(\frac{\partial^2\phi_1}{\partial z^2} + \frac{\partial^2\psi_1}{\partial x\partial z}\right) \qquad \textbf{Equation A20}$$

Z_x equal to zero: $$2\frac{\partial^2\phi_1}{\partial x\partial z} + \frac{\partial^2\psi_1}{\partial x^2} - \frac{\partial^2\psi_1}{\partial z^2} = 0 \qquad \textbf{Equation A21}$$

continuity of u_z $$\frac{\partial\phi}{\partial z} = \frac{\partial\phi_1}{\partial z} + \frac{\partial\psi_1}{\partial x} \qquad \textbf{Equation A22}$$

A2.2 Liquid-Solid Boundary

A plane sound wave incident on a liquid-solid interface can be described by the potential

$$\phi_i = A\exp[ik(x\sin\theta_i - z\cos\theta_i)] \qquad \textbf{Equation A23}$$

where θ_i is the angle of incidence and A is the amplitude of the wave. The reflected wave can be described with Equation A24.

$$\phi_r = RA\exp[ik(x\sin\theta_i + z\cos\theta_i)] \qquad \textbf{Equation A24}$$

Where R is the reflection coefficient. The total sound field in the liquid will be

$$\phi = A[\exp(-ikz\cos\theta_i) + \mathrm{Re}\,xp(ik\cos\theta_i)]\exp(ikx\sin\theta_i) \qquad \textbf{Equation A25}$$

A longitudinal and shear wave will be present in the solid and can be both described with

$$\phi_1 = T_{L1}A\exp[ik_1(x\sin\theta_L - z\cos\theta_L)] \qquad \textbf{Equation A26}$$

$$\psi_1 = T_{S1}A\exp[i\kappa_1(x\sin\theta_S - z\cos\theta_S)] \qquad \textbf{Equation A27}$$

where T_{L1} and T_{S1} and the longitudinal and shear wave transmission coefficients respectively. k, k_1 and κ_1 are the wave numbers:

$$k = \frac{\varpi}{V_i},\ k_1 = \frac{\omega}{V_L},\ \kappa_1 = \frac{\omega}{V_S} \qquad \textbf{Equation A28}$$

And θ_L and θ_S are the transmission angles of the longitudinal and shear waves respectively.

Substituting Equations A25, A26 and A27 into Equations A20, A21 and A22, and setting $z = 0$, three equations are obtained from which the angles θ_L and θ_S and the coefficients R, T_{L1} and T_{S1} can be found. For example, Equation A22 gives

$$k\cos\theta_i(R-1) = -k_1\cos\theta_L T_{L1}\exp[i(k_1\sin\theta_L - k\sin\theta_i)x] + \kappa_1\sin\theta_S T_{S1}\exp[i(\kappa_1\sin\theta_S - k\sin\theta_i)x] \qquad \textbf{Equation A29}$$

Since the left side of Equation A29 is independent of *x*, the right side must also be independent of *x*. This is only possible if Equation A30 is true where the directions of the waves in the solid medium are determined.

$$k\sin\theta_i = k_1\sin\theta_L = \kappa_1\sin\theta_S \qquad \textbf{Equation A30}$$

Now, Equation A29 can be rewritten as

$$k\cos\theta_i(R-1) = -k_1\cos\theta_L T_{L1} + \kappa_1\sin\theta_S T_{S1} \qquad \textbf{Equation A31}$$

Similarly, Equation A32 is obtained from A21.

$$k_1^2 T_{L1} \sin 2\theta_L + \kappa_1^2 T_{S1} \cos 2\theta_S = 0 \qquad \textbf{Equation A32}$$

The third equation is obtained from A20 by adding and subtracting $2\mu_1(\partial^2\phi_1/\partial x^2)$ on the right side and taking into account that

$$\nabla^2\phi_1 \equiv \frac{\partial^2\phi_1}{\partial x^2} + \frac{\partial^2\phi_1}{\partial z^2}\,.$$

Then the equation can be rewritten in the form

$$\lambda\nabla^2\phi = (\lambda_1 + 2\mu_1)\nabla^2\phi_1 + 2\mu_1\left(\frac{\partial^2\psi_1}{\partial x\partial z} - \frac{\partial^2\phi_1}{\partial x^2}\right),\ z = 0.$$

Furthermore, remembering that

$$\lambda = \rho V_i^{\,2} = \rho\frac{\omega^2}{k^2},\ \lambda_1 + 2\mu_1 = \rho_1\frac{\omega^2}{k_1^2},\ \mu_1 = \rho_1\frac{\omega^2}{\kappa_1^2} \qquad \textbf{Equation A33}$$

and also that, according to the wave equations,

$$\nabla^2\phi = -k^2\phi,\ \nabla^2\phi_1 = -k_1\phi_1,$$

the equation can be written in the simpler form

$$\frac{1}{m}\phi = \phi_1 - \frac{2}{\kappa_1^2}\left(\frac{\partial^2\psi_1}{\partial x\partial z} - \frac{\partial^2\phi_1}{\partial x^2}\right),\ z = 0 \qquad \textbf{Equation A34}$$

where $$m = \frac{\rho_1}{\rho}\ .$$

By substituting the values of ϕ, ϕ_1 and ψ_1 into Equation A34 the third equation for determining the coefficients R, T_{L1} and T_{S1} is found:

$$\frac{1}{m}(1+R) = \left(1 - 2\frac{k_1^2}{\kappa_1^2}\sin^2\theta_L\right)T_{L1} - \sin 2\theta_S T_{S1} \qquad \textbf{Equation A35}$$

Solving the system of Equations A31, A32 and A35 and making some transformations using Equation A30 the coefficients are found:

$$R = \frac{Z_L\cos^2 2\theta_S + Z_S\sin^2 2\theta_S - Z}{Z_L\cos^2 2\theta_S + Z_S\sin^2 2\theta_S + Z} \qquad \textbf{Equation A36}$$

$$T_{L1} = \frac{\rho}{\rho_1} \frac{2Z_L \cos 2\theta_S}{Z_L \cos^2 2\theta_S + Z_S \sin^2 2\theta_S + Z} \qquad \textbf{Equation A37}$$

$$T_{S1} = -\frac{\rho}{\rho_1} \frac{2Z_S \sin 2\theta_S}{Z_L \cos^2 2\theta_S + Z_S \sin^2 2\theta_S + Z} \qquad \textbf{Equation A38}$$

where Z, Z_L, and Z_S are the impedances of the wave in the liquid, and longitudinal and shear waves in the solid medium respectively:

$$Z = \frac{\rho V_i}{\cos\theta_i} \ , \ Z_L = \frac{\rho_1 V_L}{\cos\theta_L} , \ Z_S = \frac{\rho_1 V_S}{\cos\theta_S} \qquad \textbf{Equation A39}$$

A2.3 Solid-Fluid Boundary

A longitudinal wave with potential of amplitude A_L is incident on a solid-fluid boundary as illustrated in Figure A2. The wave will excite a reflected longitudinal wave (amplitude B_L), a reflected shear wave (amplitude B_S) and a transmitted longitudinal wave in the fluid (amplitude T_L).

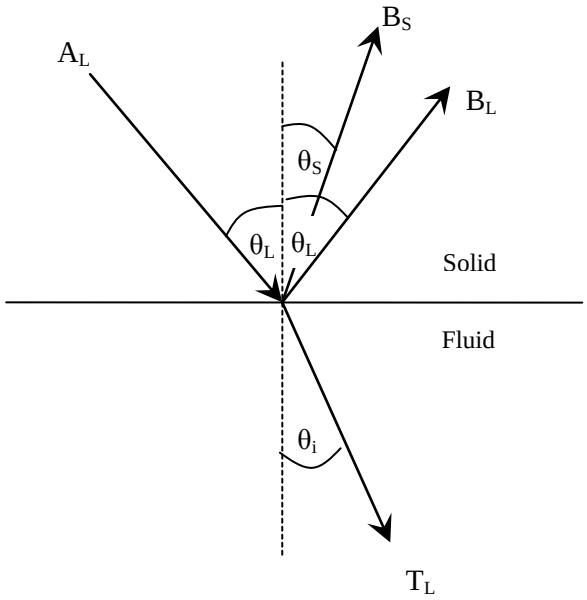

Figure A2 *Oblique incidence of a longitudinal wave at a solid-fluid interface*

The system of waves may be written in the form

$$\phi = T_L \exp[ik(x\sin\theta_i + z\cos\theta_i)$$

for the wave in the liquid;

$$\phi_1 = A_L \exp[ik_1(x\sin\theta_L = z\cos\theta_L)] + B_L \exp[ik_1(x\sin\theta_L - z\cos\theta_L)]$$

for the incident and reflected longitudinal waves and

$$\psi_1 = B_S \exp[i\kappa_1(x\sin\theta_S - z\cos\theta_S)]$$

for the reflected shear wave.

Using the boundary conditions A20-A22 as previously, it can be found that R', the longitudinal reflection coefficient for this interface is equivalent to Equation A40.

$$V' \equiv \frac{B_L}{A_L} = \frac{Z + Z_S \sin^2 2\theta_S - Z_L \cos^2 2\theta_S}{Z + Z_S \sin^2 2\theta_S + Z_L \cos^2 2\theta_S} \qquad \textbf{Equation A40}$$

Also:

$$\frac{T_L}{A_L} = \frac{V_i \cos\theta_L}{V_L \cos\theta_i \cos^2 2\theta_S}\left(1 - \frac{B_L}{A_L}\right) \qquad \textbf{Equation A41}$$

$$\frac{B_S}{A_L} = \left(\frac{V_S}{V_L}\right)^2 \frac{\sin 2\theta_L}{\cos 2\theta_S}\left(1 - \frac{B_L}{A_L}\right) \qquad \textbf{Equation A42}$$

The amplitude of the incident longitudinal wave in Figure A2 can be described by T_{L1} in Equation A37. Therefore Equation A41 can be rewritten to give T_L, the total transmission coefficient of the solid for longitudinal waves.

$$T_L = T_{L1} \frac{V_i \cos\theta_L}{V_L \cos\theta_i \cos^2 2\theta_S}\left(1 - \frac{Z + Z_S \sin^2 2\theta_S - Z_L \cos^2 2\theta_S}{Z + Z_S \sin^2 2\theta_S + Z_L \cos^2 2\theta_S}\right)$$

Equation A43

When a shear wave of amplitude A_S, in which the particle motion is in the *xz*-plane is incident from the solid onto the boundary, as shown in Figure A3, the system of waves can be written in the form

$$\phi = T_S \exp[ik(x\sin\theta_i + z\cos\theta_i)]$$

for the transmitted wave in the liquid;

$$\phi_1 = B_L \exp[ik_1(x\sin\theta_L - z\cos\theta_L)]$$

for the reflected longitudinal wave in the solid medium, and

$$\psi_1 = A_S \exp[i\kappa_1(x\sin\theta_S + z\cos\theta_S)] + B_S \exp[i\kappa_1(x\sin\theta_S - z\cos\theta_S)]$$

for the incident and reflected shear waves.

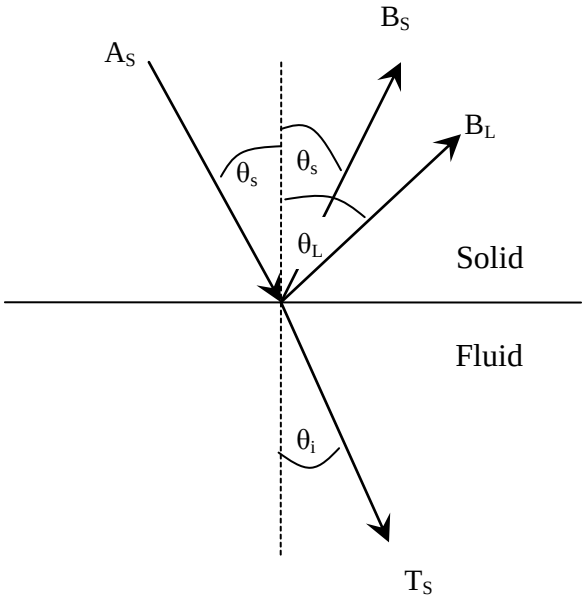

Figure A3 *Oblique incidence of a shear wave at a solid-fluid interface*

Again, using the boundary conditions A20-A22 it can be found that R'', the shear reflection coefficient for this interface is equivalent to Equation A44.

$$R'' \equiv \frac{B_S}{A_S} = -\frac{Z + Z_L \cos^2 2\theta_S - Z_S \sin^2 2\theta_S}{Z + Z_L \cos^2 2\theta_S + Z_S \sin^2 2\theta_S} \qquad \textbf{Equation A44}$$

Also,

$$\frac{T_S}{A_S} = \frac{\tan\theta_i}{2\sin^2\theta_S}\left(1 + \frac{B_S}{A_S}\right) \qquad \textbf{Equation A45}$$

$$\frac{B_L}{A_S} = -\left(\frac{V_L}{V_S}\right)^2 \frac{\cos 2\theta_S}{\sin 2\theta_L}\left(1 + \frac{B_S}{A_S}\right) \qquad \textbf{Equation A46}$$

As with the longitudinal wave, the amplitude of the shear wave incident on the solid-fluid boundary can be considered to be T_{S1} defined in Equation A38. Equation A45

can then be rewritten to give T_S, the total shear transmission coefficient for the solid medium.

$$T_S = T_{S1} \frac{\tan\theta_i}{2\sin^2\theta_S}\left(1 - \frac{Z + Z_L\cos^2 2\theta_S - Z_S\sin^2 2\theta_S}{Z + Z_L\cos^2 2\theta_S + Z_S\sin^2 2\theta_S}\right)$$

Equation A47

APPENDIX 2

Longitudinal and Shear Wave Attenuation Curves for Alumina Filled Epoxy Samples

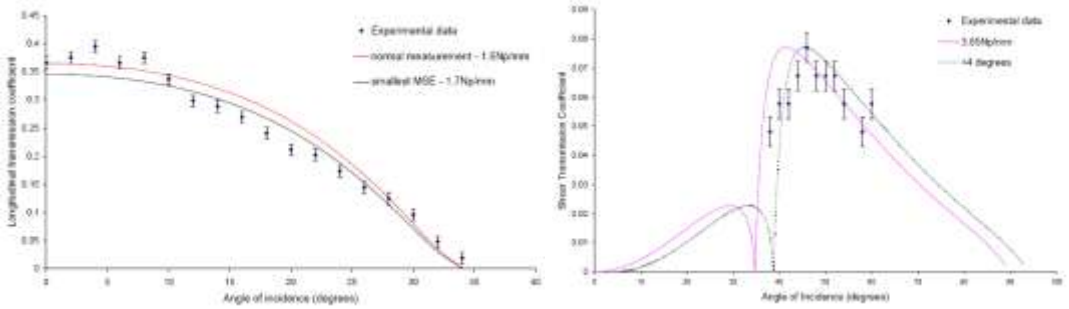

Figure A2.1 *Curve fitting data for 0.05 volume fraction MA95/Epofix sample (a) longitudinal attenuation (b) shear attenuation*

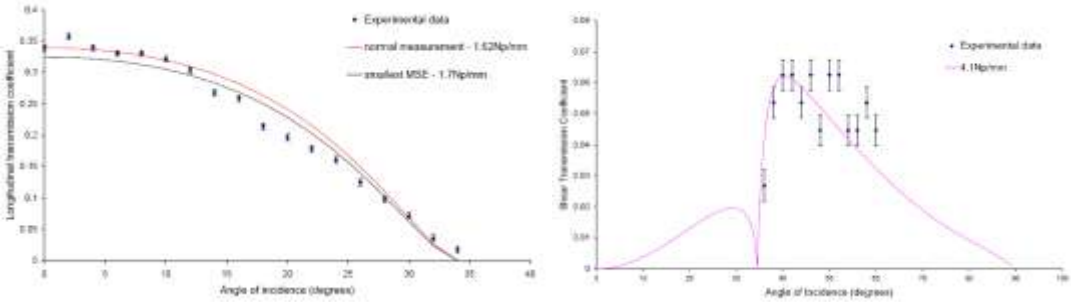

Figure A2.2 *Curve fitting data for 0.10 volume fraction MA95/Epofix sample (a) longitudinal attenuation (b) shear attenuation*

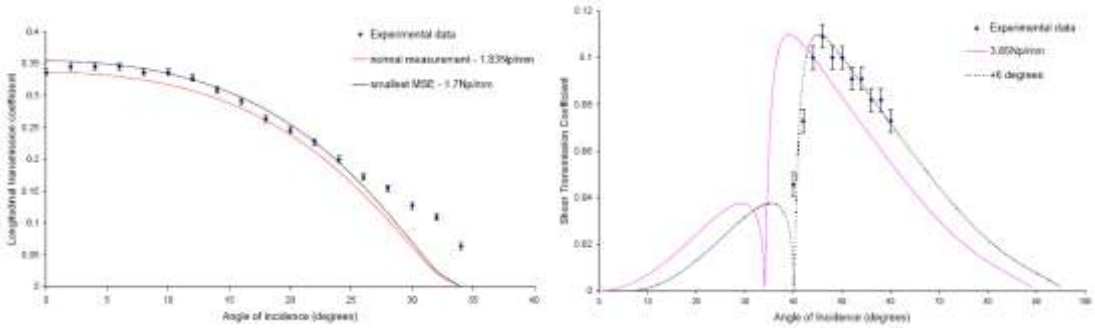

Figure A2.3 *Curve fitting data for 0.15 volume fraction MA95/Epofix sample (a) longitudinal attenuation (b) shear attenuation*

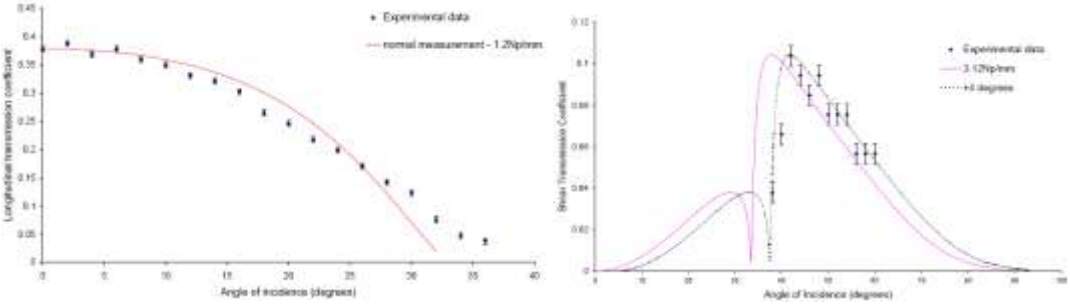

Figure A2.4 *Curve fitting data for 0.20 volume fraction MA95/Epofix sample*

(a) longitudinal attenuation (b) shear attenuation

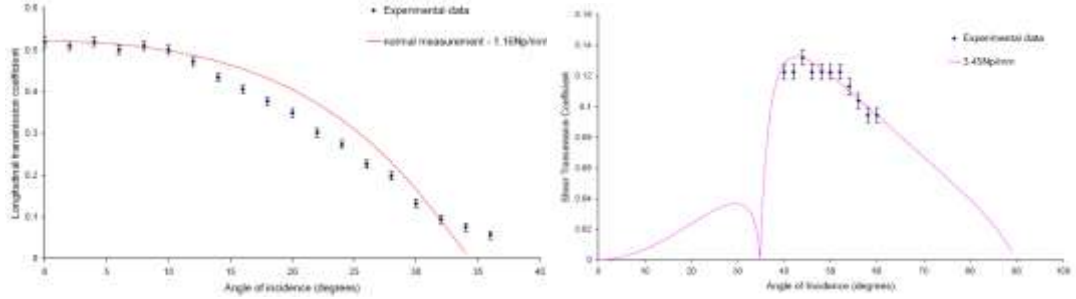

Figure A2.5 *Curve fitting data for 0.01 volume fraction CR15/Epofix sample (a) longitudinal attenuation (b) shear attenuation*

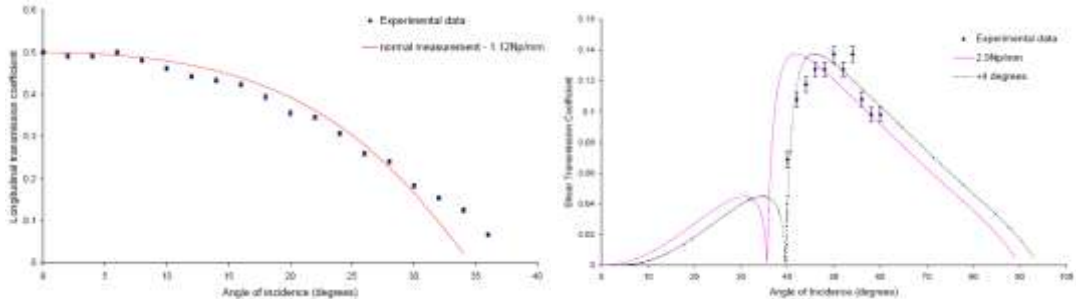

Figure A2.6 *Curve fitting data for 0.05 volume fraction CR15/Epofix sample (a) longitudinal attenuation (b) shear attenuation*

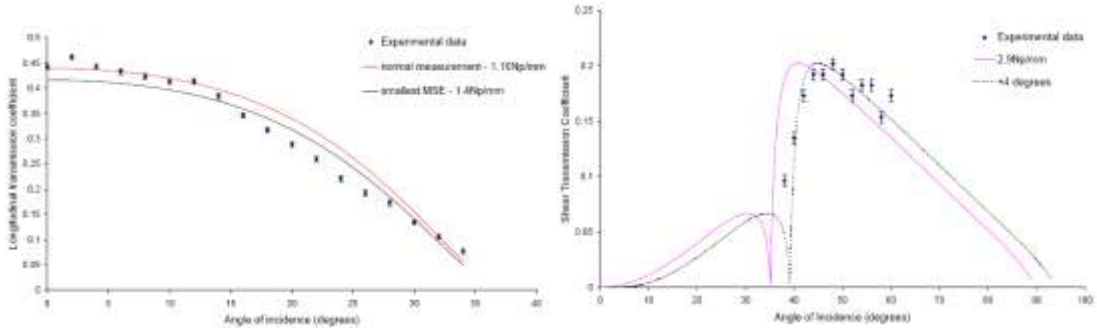

Figure A2.7*Curve fitting data for 0.10 volume fraction CR15/Epofix sample (a) longitudinal attenuation (b) shear attenuation*

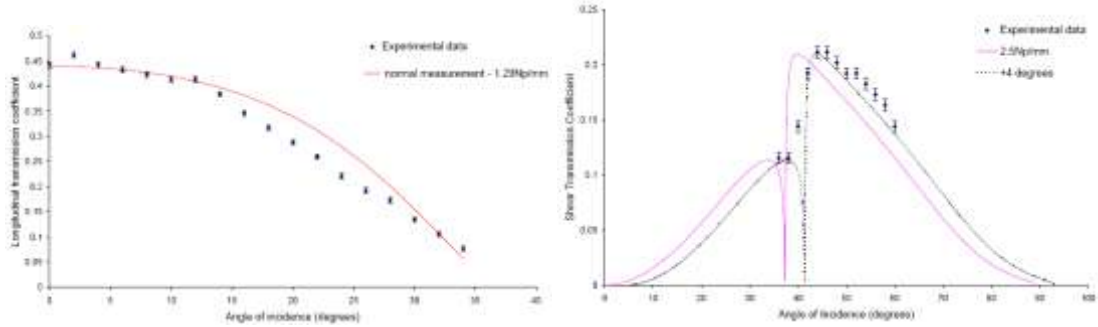

Figure A2.8 *Curve fitting data for 0.15 volume fraction CR15/Epofix sample (a) longitudinal attenuation (b) shear attenuation*

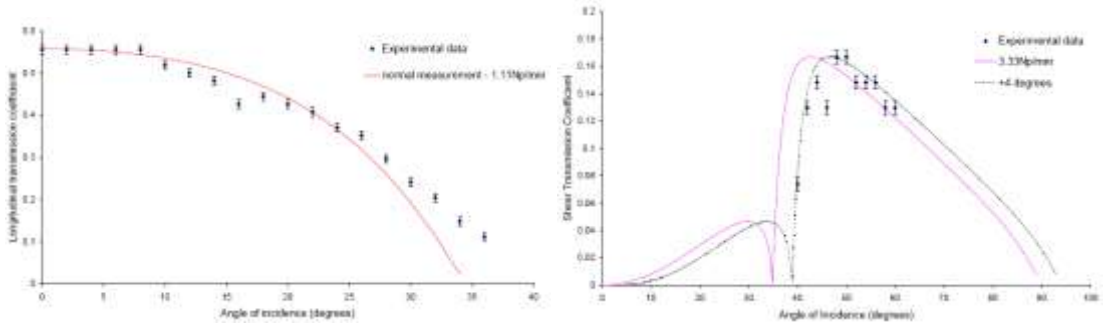

Figure A2.9*Curve fitting data for 0.01volume fraction Nano/Epofix sample (a) longitudinal attenuation (b) shear attenuation*

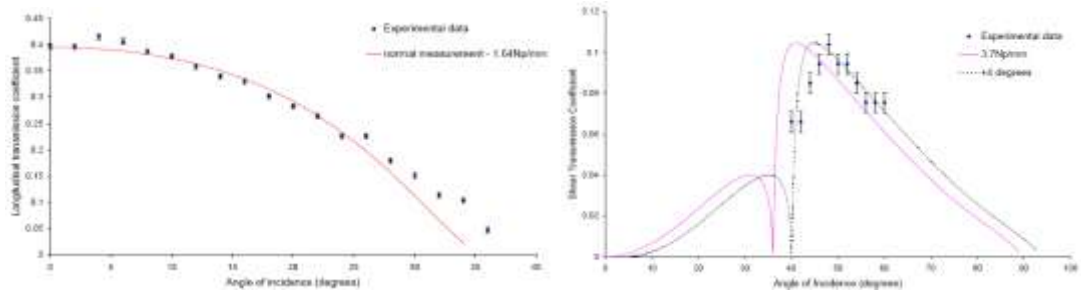

Figure A2.10 *Curve fitting data for 0.05 volume fraction Nano/Epofix sample (a) longitudinal attenuation (b) shear attenuation*

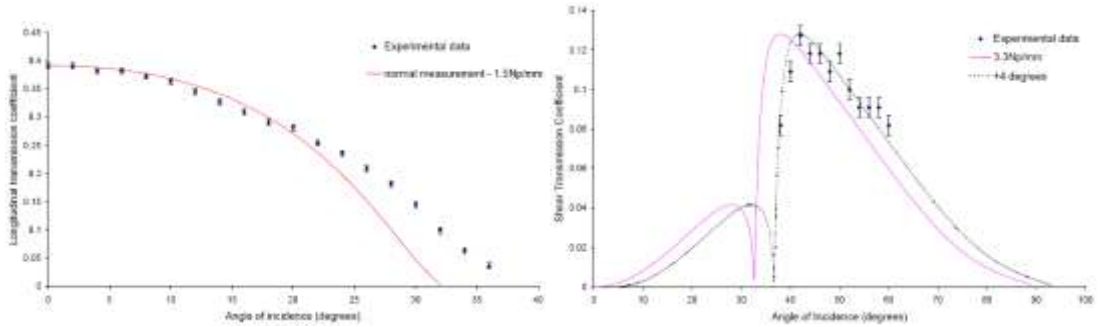

Figure A2.11 *Curve fitting data for 0.10 volume fraction Nano/Epofix sample (a) longitudinal attenuation (b) shear attenuation*

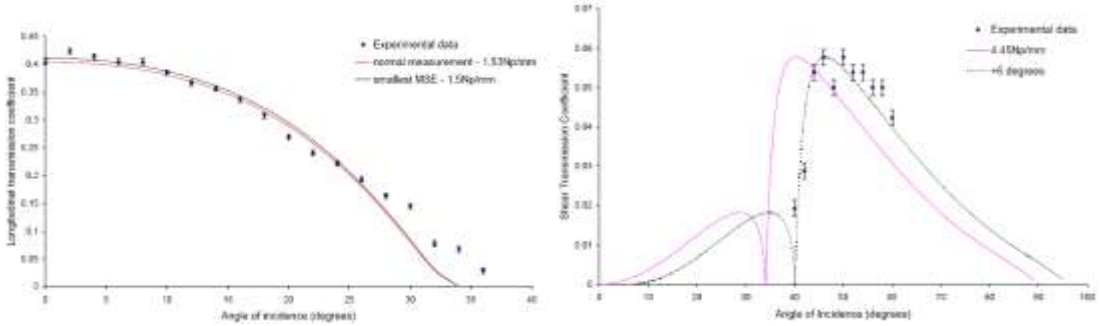

Figure A2.12 *Curve fitting data for Epotek 301 sample (a) longitudinal attenuation (b) shear attenuation*

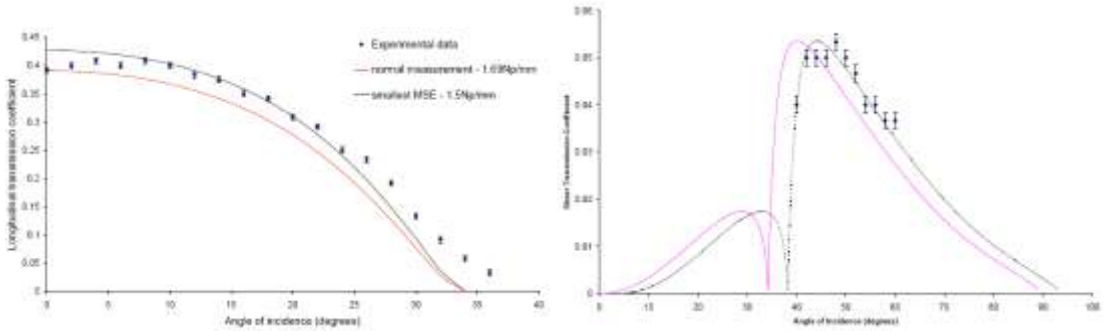

Figure A2.13 *Curve fitting data for0.01 volume fraction MA95/ Epotek 301 sample (a) longitudinal attenuation (b) shear attenuation*

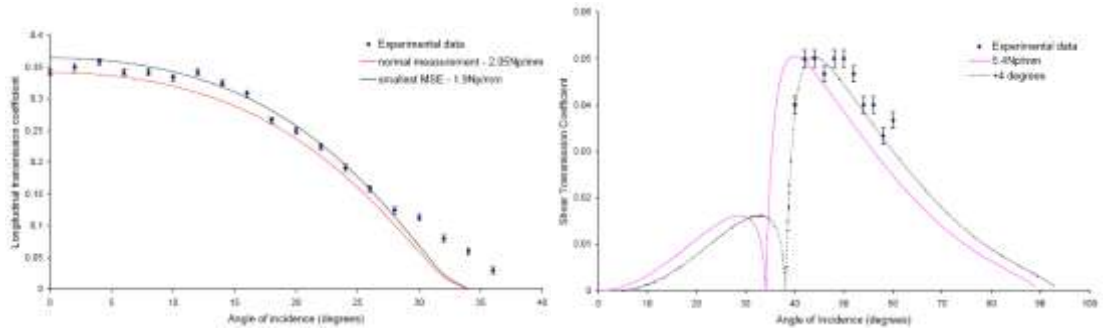

Figure A2.14 *Curve fitting data for0.05 volume fraction MA95/ Epotek 301 sample (a) longitudinal attenuation (b) shear attenuation*

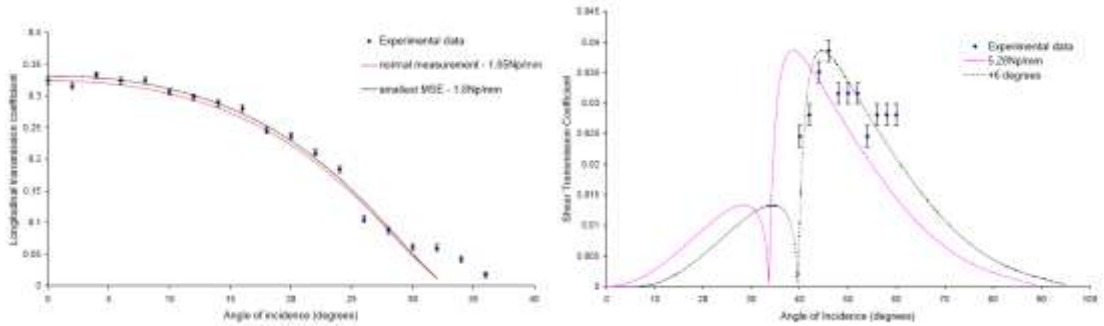

Figure A2.15 *Curve fitting data for0.10 volume fraction MA95/ Epotek 301 sample (a) longitudinal attenuation (b) shear attenuation*

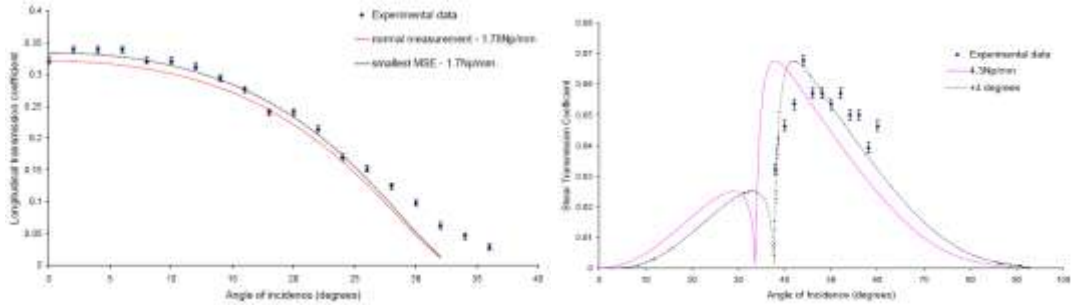

Figure A2.16 *Curve fitting data for0.15 volume fraction MA95/ Epotek 301 sample. (a) longitudinal attenuation (b) shear attenuation*

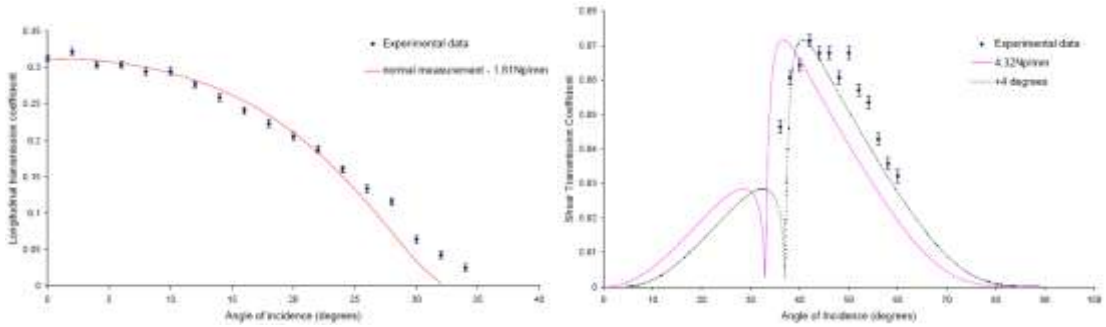

Figure A2.17 *Curve fitting data for0.20 volume fraction MA95/ Epotek 301 sample. (a) longitudinal attenuation (b) shear attenuation*

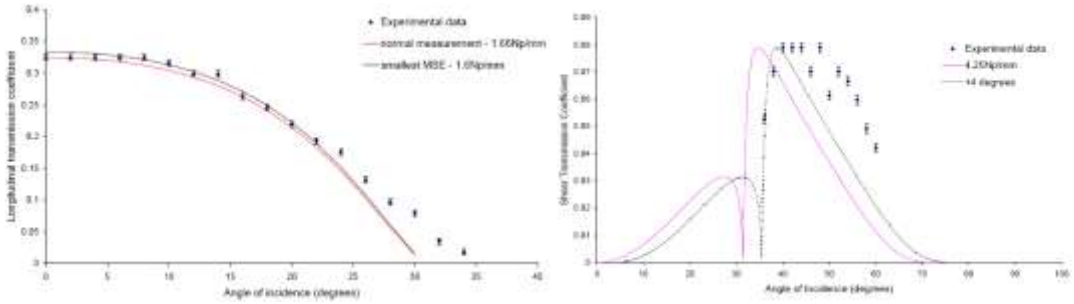

Figure A2.18 *Curve fitting data for0.25 volume fraction MA95/ Epotek 301 sample. (a) longitudinal attenuation (b) shear attenuation*

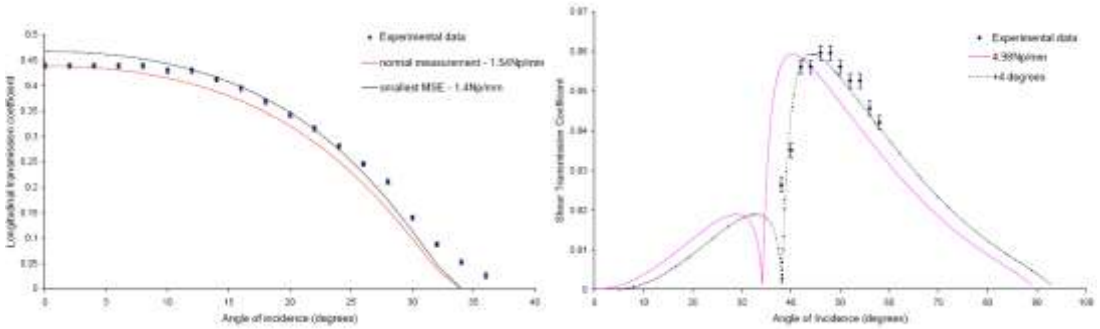

Figure A2.19 *Curve fitting data for0.01volume fraction CR15/ Epotek 301 sample. (a) longitudinal attenuation (b) shear attenuation*

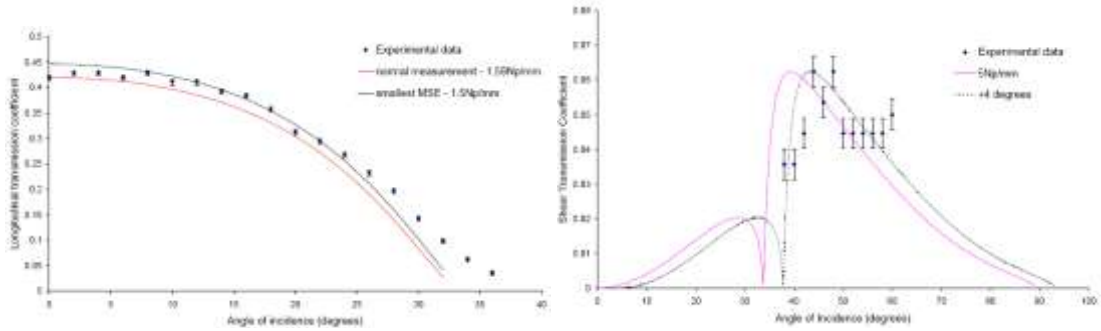

Figure A2.20 *Curve fitting data for0.05 volume fraction CR15/ Epotek 301 sample. (a) longitudinal attenuation (b) shear attenuation*

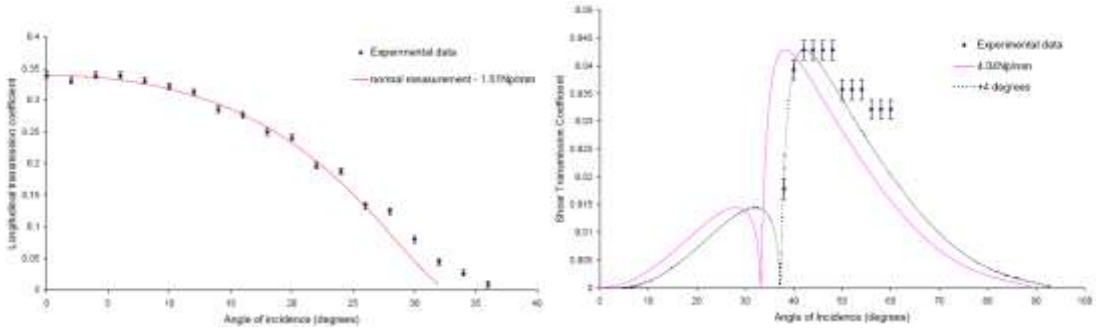

Figure A2.21 *Curve fitting data for0.10 volume fraction CR15/ Epotek 301 sample. (a) longitudinal attenuation (b) shear attenuation*

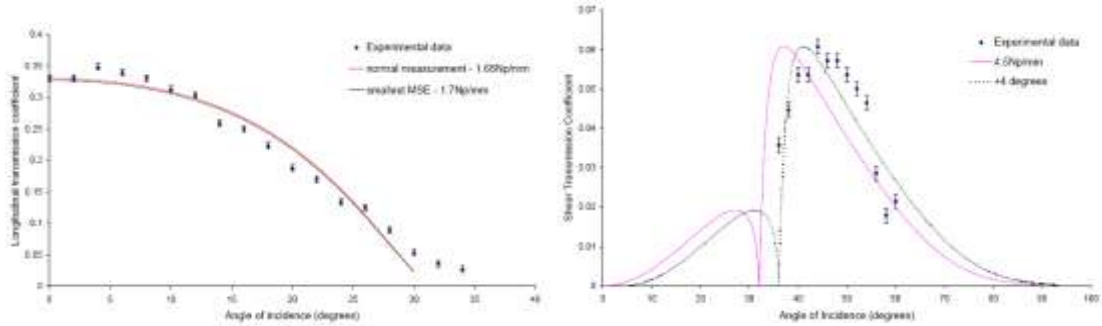

Figure A2.22 *Curve fitting data for0.15 volume fraction CR15/ Epotek 301 sample. (a) longitudinal attenuation (b) shear attenuation*

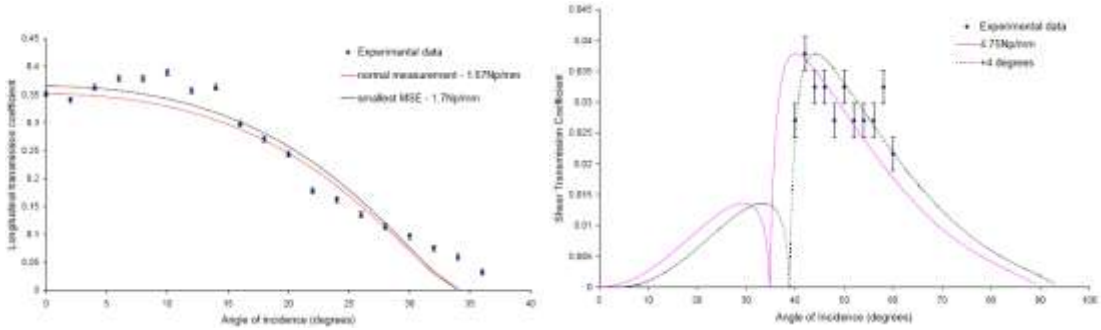

Figure A2.23 *Curve fitting data for0.01 volume fraction Nano/ Epotek 301 sample. (a) longitudinal attenuation (b) shear attenuation*

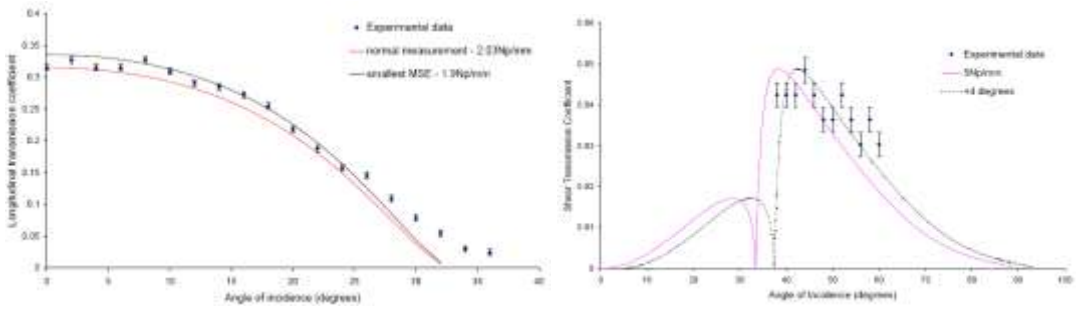

Figure A2.24 *Curve fitting data for0.05 volume fraction Nano/ Epotek 301 sample. (a) longitudinal attenuation (b) shear attenuation*

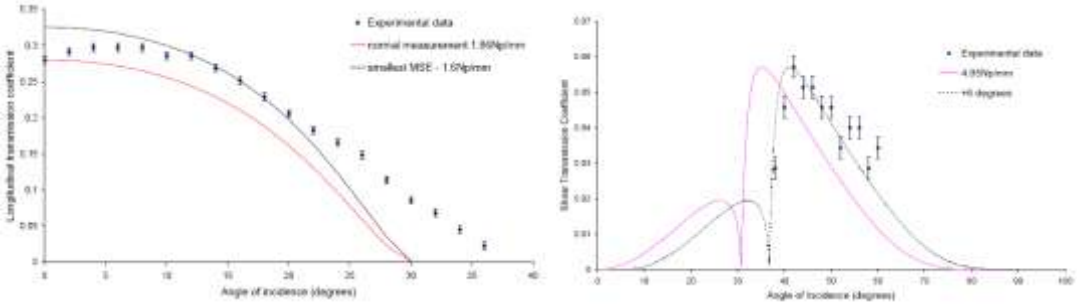

Figure A2.25 *Curve fitting data for0.10 volume fraction Nano/ Epotek 301 sample. (a) longitudinal attenuation (b) shear attenuation*

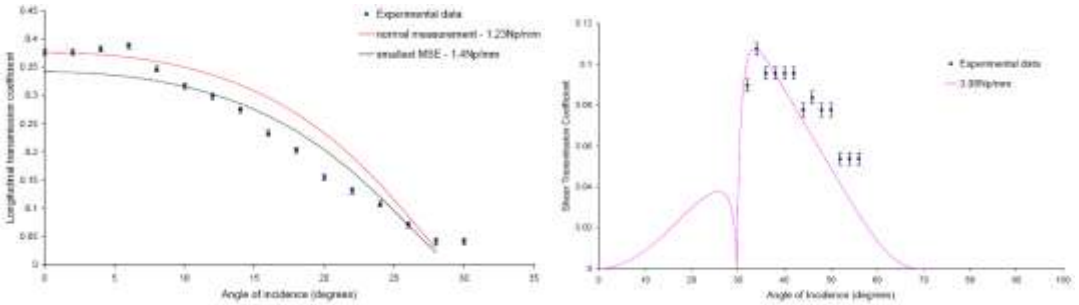

Figure A2.26 *Curve fitting data for0.15 volume fraction Nano/ Epotek 301 sample. (a) longitudinal attenuation (b) shear attenuation*

References

1. **W.R. Hedrick, D.L. Hykes & D.E. Starchman.** *Ultrasonic physics and instrumentation.* s.l. : Mosby, 1995.
2. **G.R. Lockwood, D.H. Turnbull, D.A. Christopher & F.S. Foster.** Beyond 30MHz: applications of high frequency ultrasound imaging. *IEEE Engineering in Medicine and Biology Magazine.* 1996, Vol. 15, p.60-71.
3. **D.M. Thoboutot.** *Dermatological applications of high frequency ultrasound.* SPIE Conference Proceedings, 1999.
4. **R.H. Silverman, J.A. Ketterling & D.J. Coleman.** High frequency ultrasonic imaging of the interior segment using an annular array transducer. *Ophthalmology.* 2007, Vol. 114, p.816-822.
5. **R.H. Silverman, D.J. Coleman, D.Z. Reinstein & F.L. Lizzi.** Clinical applications of very high frequency ultrasound in ophthalmology. *Journal of the Acoustical Society of America.* 2004, Vol. 115, p.2376.
6. **C.C. Harland, S.G. Kale, P. Jackson, P.S. Mortimer & J.C. Bamber.** Differentiation of common benign pigmented skin lesions from melanoma by high-resolution ultrasound. *British Journal of Dermatology.* 2000, Vol. 143, p.281-289.
7. **J.C. Bamber, N.L. Bush, M.C. Haddock, R.J. Ott, D. Rallan & C.C. Harland.** *Combining high frequency ultrasound reflex transmission imaging and imaging spectrophotometry for the diagnosis of skin cancer.* New York : IEEE Ultrasonics Symposium, 2007.
8. **W.A. Smith.** Composite piezoelectric materials for medical ultrasonic imaging transducers - a review. *International Symposium on Apllications of Ferroelectrics* . 1986, Vols. p. 249-256.
9. **A. Safari.** Development of piezoelectric composites for transducers. *Journal de Physique III.* 1994, Vol. 4, p.1129-1149.
10. **R. Guinovart-Diaz, J. Bravo-Castillero, R. Rodriguez-Ramos, F.J. Sabina & R. Martinez-Roasado.** Overall properties of piezocomposite materials 1-3 . *Materials Letters.* 2001, Vol. 48, p. 93-98.
11. **W.A. Smith, A. Shaulov & B.A. Auld.** Tailoring the properties of composite piezoelectric materials for medical ultrasonic transducers. *IEEE Ultrasonics Symposium.* 1985, p. 642-647.
12. **R.J. Meyer, Jr., T.R. Shrout & S. Yoshikawa.** Development of ultra-fine scale piezoelectric fibers for use in high frequency 1-3 transducers. *IEEE.* 1996, p. 547-550.
13. **D.Y. Wang, K. Li & H.W. Chan.** High frequency 1-3 composite transducer fabricated using sol-gel derived lead-free BNBT fibers. *Sensors and Actuators A.* 2004, Vol. 114, p. 1-6.
14. **L.J. Bowen, R.L. Gentilman, H.T. Pham, D.F. Fiore & K.W. French.** Injection moulded fine-scale piezoelectric composite transducers. *IEEE Ultrasonics Symposium.* 1993, p. 499-503.
15. **B.G. Pazol, L.J. Bowen, R.L. Gentilman, H.T. Pham & W.J. Serwatka.** Ultrafine scale piezoelectric composite materials for high frequency ultrasonic imaging arrays. *IEEE Ultrasonics Symposium.* 1995, p. 1263-1268.
16. **Y. Hirata, H. Okuvama, S. Ogino, T. Numazawa & H. Takada.** Piezoelectric composites for micro-ultrasonic transducers realised with deep-etch X-ray lithography. *Micro Electro Mechanical Systems.* 1995, p.191.

17. **S. Starke, A. Schonecker & W. Gebhardt.** 1-3 composites: a new approach of cost effective fabrication. *Proceesings of 11th IEEE Symposium on Applied Ferroelectrics.* 1998, p. 393-396.
18. **D. Zhang, B. Su & T.W. Button.** Preperation of concentrated aqueous alumina solutions for soft moulding microfabrications. *Journal of the European Ceramic Society.* 2001, Vol. 21, p. 2005-2009.
19. **A. Abrar, D. Zhang, B. Su, T.W. Button, K.J. Kirk & S. Cochran.** 1-3 connectivity piezoelectric ceramic-polymer composite transducers made with viscous polymer processing for high frequency ultrasound. *Ultrasonics.* 2004, Vol. 42, p. 479-484.
20. **S. Cochran, D. Zhang, N. Porch, T.W. Button, B. Su, C. Meggs, A. Abrar & K.J. Kirk.** *Net shape ceramic processing as a route to ultrafine scale 1-3 connectivity piezoelectric ceramic-polymer composite transducers.*IEEE Ultrasonics Symposium, Montreal : p. 1682-1685, 2004.
21. **D. Zhang, B. Su, T.W. Button, A. Abrar, K.J. Kirk & S. Cochran.** Piezoelectric 1-3 composites for high frequency ultrasonic transducer applications. *Ferroelectrics.* 2004, Vol. 304, p. 231-237.
22. **D. MacLennan, J. Elgoyhen, T.W. Button, C.E.M. Demore, H. Hughes, C. Meggs & S. Cochran.** Properties and application-orientated performance of high frequency piezocomposite ultrasonic transducers. *IEEE Ultrasonics Symposium.* 2007, p. 100-103.
23. **T.W. Button, S. Cochran, K.J. Kirk, D. MacLennan, A, MacNeil, K. McDonald, C. Meggs, D. Rodriquez-Sanmartin, R. Webster & D. Zhang.** Net-shape ceramic manufacturing as an aid to realize ulrasonic transducers for high-resolution medical imaging. *IEEE Ultrasonics Symposium.* 2005, p. 1625-1628.
24. **Rizzatto, G.** Ultrasound transducers. *European Journal of Radiology.* 1998, Vol. 27, S188-S195.
25. **R.E. McKeighen.** *Design guidelines for medical ultrasonic arrays.* SPIE International Symposium on Medical Imaging, San Diego, 1998.
26. **D. Waller, J. Chen & T.R. Gururaja.** Requirements of piezoelectric materials for medical ultrasound transducers. *IEEE Symposium on Applications of Ferroelectrics*, 1996, p. 565-568.
27. **G. Kossoff.** The effects of backing and matching on the performance of piezoelectric ceramic transducers. *IEEE Transactions on Sonics and Ultrasonics.* 1966, Vols. SU-13, 1, p. 20-30.
28. **W.A. Smith & B.A. Auld.** Modeling 1-3 composite piezoelectrics: thickness-mode oscillations. *IEEE Transactions on Ultrasonics, Ferroelectrics and Frequency Control.* 1991, Vol. 38, p. 40-47.
29. **K. Colquhoun, A. Alam & D. Wilson.** Basic science: ultrasound. *Current Orthopaedics.* 2005, Vol. 19, p. 27-33.
30. **P.J. White, G.T. Clement & K. Hynynen.** Longitudinal and shear mode ultrasound propagation in human skull bone. *Ultrasound Med Biol.* 2006, Vol. 32 , 7, p. 1085-1096.
31. **J.A. Gallego-Juarez.** Piezoelectric ceramics and ultrasonic transducers. *Journal of Physics E: Sci Instrum.* 1989, Vol. 22, p. 804-816.
32. **M. Lach, M. Platte & A. Ries.** Piezoelectric materials for ultrasonic probes. *NDTnet.* 1996, Vol. 1 , 9.
33. **E.L. Dove.** Notes on ultrasound - echocardiology. *Lecture Notes: Fundamentals of Bioimaging.* 2003.

34. **A.J. Moulsen & J. M. Herbert** *Electroceramics.* London : Chapman and Hall, 1990.
35. **N. Setter.** ABC of Piezoelectricity and Piezoceramic Materials. *Piezoelectric Materials and Devices.* s.l. : EPFL Swiss Federal Institute of Technology, 2002.
36. **F.S. Foster.** Transducer materials and probe construction. *Ultrasound in Medicine & Biology.* 2000, Vol. 26, p. S2-S5.
37. **J.Z. Zhao, G. Molingou, J. Zheng, W.H. Chen, T.A. Ritter & K.K. Shung.** High performance, high frequency ultrasound transducers incorporating PbTiO3. *IEEE Ultrasonics Symposium.* 2000, p. 973-976.
38. **J. M. Cannata, T.A. Ritter, W.H. Chen & K.K. Shung.** Design of focused single element (50-100MHz) transducers using Lithium Niobate. *IEEE Ultrasonics Symposium.* 2000, p. 1129-1133.
39. **J. M. Cannata, T.A. Ritter, W.H. Chen, R.H. Silverman & K.K. Shung.** Design of efficient, broadband single-element (20-80MHz) ultrasonic transducers for medical imaging applications. *IEEE Transactions on Ultrasonics, Ferroelectrics, and Frequency Control.* 2003, Vol. 50, p. 1548-1557.
40. **Q. Zhou, J.M. Cannata, H. Guo, C. Huang, V. Z. Marmarelis & K.K. Shung.** Half-thickness inversion layer high-frequency ultrasonic transducers using LiNbO3 Crystal. *IEEE Transactions on Ultrasonics, Ferroelectrics, and Frequency Control.* 2005, Vol. 52, p. 127-133.
41. **K.A. Snook, J.Z. Zhao, C.H.F. Alves, J.M. Cannata, W.H. Chen, R.J. Meyer, Jr. & T.A. Ritter.** Design, Fabrication, and evaluation of high frequency, single-element transducers incorporating different materials. *IEEE Transactions on Ultrasonics, Ferroelectrics, and Frequency Control.* 2002, Vol. 49, p. 169-176.
42. **K. Snook, S. Rhee, M. Robert, E. Gottlieb & K.K. Shung.** Development of P(VDF-TRFE) ultrasonic transducers operating at 50-120MHz. *?* ?, ?
43. **F. Levasorrt, L.P. Tran-Huu-Hue, D. Certon & M. Lethiecq.** *Piezoelectric materials for ultrasonic transucers: review of recent developments,* Laboratoire d'Ultrasons, Signaux et Instrumentation, GIP Ultrasons, 2002.
44. **K. Nakamae, Y. Hirata, H. Mizobuchi, A. Hashimoto & H. Takada.** Development of high-resolution and wide-band piezoelectric composite for ultrasonic probe. *SEI Technical Review.* 2004, Vol. 57, p. 26-30.
45. **A. Nguyen-Dinh, L. Ratsimandresey, P. Mauchamp, R. Dufait, A. Flesch & M. Lethiecq.** High frequency piezo-composite transducer array designed for ultrasound scanning applications. *IEEE Ultrasonics Symposium.* 1996, p. 943-947.
46. **T.R. Gururaja, W.A. Schulze, L.E. Cross, R.E. Newnham, B.A. Auld & Y.J. Wang.** Piezoelectric composite materials for ultrasonic transducer applications. Part I: resonant modes of vibration of PZT rod-polymer composites. *IEEE Transactions on Sonics and ULtrasonics .* 1985, Vols. SU-32, 4, p. 481-498.
47. **W.A. Smith.** The application of 1-3 piezocomposites in acoustic transducers. *IEEE Symposium on Applications of Ferroelectrics,* 1990, Vol. 6-8, p.145-152.
48. **T.R. Gururaja, W.A. Schulze, L.E. Cross & R.E. Newnham.** Piezoelectric composite materials for ultrasonic transducer applications. Part II: evaluation of ultrasonic medical applications. *IEEE Transactions on Sonics and Ultrasonics.* 1985, Vols. SU-32, 4, p. 499-513.

49. **D.H. Turnbull &O.T. Aristizabel.** 44-MHz LiNbO3 transducers for UBM-guided doppler ultrasound. *IEEE Transactions on Ultrasonics, Ferroelectrics and Frequency Control.* 2003, Vol. 50, p. 623-630.
50. **V. Bovtun, J. Doring, J. Bartusch, U. Beck, A. Erhard & Y. Yakymenko.** Ferroelectret non-contact ultrasonic transducers. *Applied Physics A: Materials Science and Processing.* 2007, Vol. 88, 4, p. 737-743.
51. **T. Ritter, K.K. Shung, X. Geng, P. Lopath, R. Tutwiler & T. Shrout.** Composite ultrasound transducer arrays for operation above 20MHz. *Proceedings of SPIE Conference.* 1999, Vol. 3664, p.67-75.
52. **E.J. Gottlieb, B. Lai, X. Xu, J. Cannata, J. Yen, Q. Zhou, P. Han, H. Ameri, T. Ratanapakorn, A. Barnes, M. Humayun & K.K. Shung.** PMN-PT high frequency ultrasonic needle transducers for pulsed wave doppler in the eye. *IEEE Ultrasonics Symposium.* 2005, p. 2227-2230.
53. **J.M. Canatta, J.A. Williams, Q. Zhou, T.A. Ritter & K.K. Shung.** Development of a 35-MHz piezo-composite ultrasound array for medical imaging. *IEEE Transactions on Ultrasonics, Ferroelectrics and Frequency Control.* 2006, Vol. 53, 1, p. 224-236.
54. **D.H. Turnbull & G.R. Lockwood.** Fabrication of high frequency sphaerically shaped ceramic transducers. *IEEE Transactions on Ultrasonics, Ferroelectrics and Frequency Control.* 1994, Vol. 41, p. 231-235.
55. **J.A. Brown, E. Cherin, J. Yin & F.S. Foster.** Fabrication and performance of a high-frequency geometrically focused composite transducer with triangular pillar geometry. *IEEE Ultrasonics Symposium.* 2007, p. 80-83.
56. **M.G. Grewe, T.R. Gururaja, T.R. Shrout & R.E. Newnham.** Acoustic properties of particle/polymer composites for ultrasonic transducer backing applications. *IEEE Transactions on Ultrasonics, Ferroelectrics and Frequency Control.* 1990, Vol. 37, p. 506-514.
57. **H. Wang, T.A. Ritter, W. Cao & K.K. Shung.** Passive materials for high frequency ultrasound transducers. *SPIE Proceedings.* 1999, p. 35-42.
58. **R. Zhang, W. Cao, Q. Zhou, J.H. Cha & K.K. Shung.** Acoustic properties of alumina colloidal/polymer nano-composite film on silicon. *IEEE Transactions on Ultrasonics, Ferroelectrics and Frequency Control.* 2007, Vol. 54, 3, p. 467-469.
59. **S. Thiagarajan, R.W. Martin, A. Proctor, I. Jayawadena & F. Silverstein.** Dual layer matching (20MHz) piezoelectric transducers with glass and parylene. *IEEE Transactions on ULtrasonics, Ferroelectrics and Frequency Control.* 1997, Vol. 44, 5, p. 1172-1174.
60. **Y.T. Zhang & S.H. Xiang.** Matching layer optimization between ultrasound transducer and human tissues. *IEEE Conference on Engineering in Medicine and Biology,* 1995, Vol. 1, p.623-624.
61. **B.T. Khuri-Yakub & B. Hadimioglu.** Polymer films as acoustic matching layers. *IEEE Ultrasonics Symposium.* 1990, p. 1337-1340.
62. **H. Savakus, K. Klicker & R.E. Newnham.** PZT-epoxy piezoelectric transducers: a simplified fabrication procedure. *Mat. Res. Bulls.* 1981, Vol. 16, p. 677-680.
63. **R. Lui, K.A. Harasiewicz & F.S. Foster.** Interdigital pair bonding for high f requency (20-50MHz) ultrasonic composite transducers. *IEEE Transactions on Ultrasonics, Ferroelectrics and Frequency Control.* 2001, Vol. 48, p. 299-306.

64. **L.F. Brown.** The effects of material selection for backing and wear protection/quarter-wave matching of piezoelectric polymer ultrasound transducers. *IEEE ULtrasonics Symposium.* 2000, p. 1029-1032.
65. **C.E. Tait & C.M. Sayers.** Ultrasonic properties of transducer backings. *Ultrasonics.* 1984, p. 57-60.
66. **W. Cao & M.R. Draheim** Finite element analysis on impedance matching layer thickness. *IEEE Symposium on Applications of Ferroelectrics,* 1996, p. 1015-1017, 1
67. **W. Cao & H. Wang** Charaterizing ultra-thin matching layers of high-frequency ultrasonic transducer based on impedance matching principle. *IEEE Transactions on Ultrasonics, Ferroelectrics and Frequency Control.* 2004, Vol. 51, 2, p. 211-215.
68. **T. Inoue, M. Ohta & S. Takahashi.** Design of ultrasonic transducers with multiple acoustic matching layers for medical applications. *IEEE Transactions on Ultrasonics, Ferroelectrics and Frequency Control.* 1987, Vol. 34, p. 8-16.
69. **A.R. Selfridge.** Approximate material properties in isotropic materials. *IEEE Transactions on Sonics and Ultrasonics.* 1985, Vol. 32, p. 381-384.
70. **K. Zell, J.I. Sperl, M.W. Vogel, R. Niessnar & C. Haisch.** Acoustical properties of selected tissue phantom materials for ultrasound imaging. *Physics in Medicine and Biology.* 2007, Vol. 52, N475-N484.
71. **C.H. Hertz & H.W. Persson.** Acoustic impedance matching of medical ultrasound transducers. *Ultrasonics.* 1985, Vol. 23, p. 83-89.
72. **S. Sherrit, S.P. Leary, B.P. Dolgin & Y. Bar-Cohen.** Comparison of the Mason and KLM equivalent circuits for piezoelectric resonators in the thickness mode. *IEEE Ultrasonics Symposium.* 1999.
73. **N.N. Abboud, G.L. Wojcik, D.K. Vaughan, J. Mould, D.J. Powell & L. Nikodym.** Finite element modelling for ultrasonic transducers. *SPIE Symposium on Medical Imaging.* 1998, p. 19-42.
74. **S. Ballandras, M. Wilm, P.F. Edoa, A. Soufyane & V. Laude.** Finite-element analysis of periodic piezoelectric transducers. *Journal of Applied Physics.* 2003, Vol. 93, 1, p. 702-711.
75. **K.K. Shung & J.M. Cannata.** A comparison of model and experiment for a high frequency (35MHz) linear ultrasonic array. *IEEE Ultrasonics Symposium.* 2003, p. 1658-1662.
76. **T.L. Szabo.** *Diagnostic ultrasound imaging: inside out.* London : Elsevier Academic Press, 2004.
77. **B. Budiansky.** On the elastic moduli of some heterogeneous materials. *Journal of the Mechanics and Physics of Solids.* 1965, Vol. 13, P. 223-227.
78. **B.A. Auld & J.A. Hossack.** Improved modeling of 0:3 composite materials. *IEEE Ultrasonics Symposium,* 1995, p. 945-949.
79. **T.N. Nguyen, M. Letiecq, F. Levassort & L. Pourcelot.** Experimental verification of the theory of elastic properties using scattering approximations in (0-3) connectivity composite materials. *IEEE Transactions on Ultrasonics, Ferroelectrics and Frequency Control.* 1996, Vol. 43, P. 640-645.
80. **S.A. Shtrikman & Z. Hashin.** Variational approach to the theory of the elastic behaviour of multiphase materials. *Journal of the Mechanics and Physics of Solids.* 1963, Vol. 11, p. 127-140.
81. **R.L. Smith & C.M. Sayers.** Ultrasonic velocity and attenuation in an epoxy matrix containing lead inclusions. *Journal of Physics D: Applied Physics.* 1983, Vol. 16, p. 1189-1194.

82. **V.K. Varadan, Y. Ma & V.V. Varadan.** A multiple scattering theory for elastic wave propagation in discrete random media. *Journal of Acoustical Society of Ameriva.* 1985, Vol. 77, p. 587-606.
83. **L.L. Foldy.** The multiple scattering of waves. *Physical Review.* 1945, Vol. 67, p. 107-119.
84. **M.N. Toksov & G.T. Kuster.** Velocity and attenuation of seismic waves in two-phase media: part 1. theoretical formulations. *Geophysics.* 1974, Vol. 39, p. 587-606.
85. **H. Levine &A.J. Devaney.** Effective elastic parameters of random composites . *Applied Physics Letters.* 1980, Vol. 37, p. 377-379.
86. **H. Wang, T.A. Ritter, W. Cao & K.K. Shung.** High frequency properties of passive materials for ultrasonic transducers. *IEEE Transactions on Ultrasonics, Ferroelectrics and Frequency Control.* 2001, Vol. 48, p. 78-84.
87. **K. Sugawara, M. Nishihira & K. Imano.** Experimental study of acoustic properties of (0-3) composite materials for intermediate layer or backing of ultrasonic transducers. *Japanese Journal of Applied Physics.* 2005, Vol. 44, p. 4347-4349.
88. **R.C. Chivers & L.W. Anson.** Ultrasonic velocity in suspensions of solids in solids - a comparison of theory and experiment. *Journal of Physics D: Applied Physics.* 1993, Vol. 26, p. 1566-1575.
89. **L. Wolgemuth.** *The surface modification properties of parylene for medical applications.* s.l. : Medical Device Manufacturing & Tecjnology, Speciality Coating Systems, 2002.
90. **Y. Hosono, Y. Yamashita & K. Itsumi.** Effects of fine metal oxide particle dopant on the acoustic properties of silicone rubber lens for medical array p robe. *IEEE Transactions on Ultrasonics, Ferroelectrics and Frequency Control.* 2007, Vol. 54, p. 1589-1595.
91. **Q.F. Zhou, J.H. Cha, R. Huang, W. Cao, J.M. Cannata & K.K. Shung.** Nanocomposite matching layers for high frequency ultrasound. *IEEE Ultrasonics Symposium.* 2006, p. 2365-2368.
92. **J. Zhu, W. Cao, B. Jiang, H. Zheng, Q. Zhou & K.K. Shung.** Fabrication and characterization of nanocrystalline TiO2-polymer composite matching layers. *IEEE Ulrasonics Symposium.* 2007, p. 1917-1920.
93. **D. Cheeke.** *Fundamentals amd Applications of Ultrasonic Waves.* New York : Academic Press, 2002.
94. **P. He.** Acoustic parameter estimation based on attenuation and dispersion measurements. *IEEE Annual International Conference*, Hong Kong, 1998. p. 886-889.
95. **V. Bucklin, B. O'Driscoll, C. Smyth, A.C. Alting & R.W. Visschers.** Ultrasonic spectroscopy for material analysis: recent advances. *Spectroscopy Europe.* 2003, Vol. 15, p. 20-25.
96. **H.J. McSkimmin.** Ultrasonic Methods for Measuring the Mechanical Properties of Solids and Liquids. [book auth.] W.P. Mason. *Physical Acoustics, Vol. 1 Part A.* New York : Academic Press, 1964.
97. **J. De Klerk, D.I. Bolef.** Some continuous-wave techniques for the measurement of velocity and attenuation of ultrasonic waves between 1 and 1000 Mc. *IEEE Transactions on Ultrasonics Engineering.* 1963, Vol. 10, p. 19-26.
98. **P.H.F. Nicholson, G. Lowet, C.M. Langton, J. Dequeker & G. Van der Perre.** A comparison of time-domain and frequency-domain approaches to ultrasonic velocity measurement in trabecular bone. *Physics in Medicine and Biology.* 1996, Vol. 41, p. 2421-2435.

99. **M.J. Lang, M. Duarte-Dominguez & W. Arnold.** Extension of frequency spectrum methods for phase velocity measurements in ultrasonic testing. *Review of Scientific Instruments.* 2000, Vol. 71, 9, p. 3470-3473.
100. **J. Zheng, P. He.** Acoustic dispersion and attenuation measurements using both transmitted and reflected pulses. *Ultrasonics.* 2001, Vol. 39, p. 27-32.
101. **R.L. O'Leary.** Investigation into the passive materials utilised within the construction of piezoelectric composite transducers. *PhD Thesis, University of Strathclyde.* 2003.
102. **J. Wu.** Determination of velocity and attenuation of shear waves using ultrasonic spectroscopy. *Journal of the Acoustical Society of America.* 1996, Vol. 99, p. 2871-2875.
103. **L.M. Brekhovskikh.** *Waves in Layered Media.* s.l. : Academic Press, 1960.
104. **R.L. O'leary, G. Hayward, G. Smile & A.C.S. Parr.** *CUE Materials Database Version 1.2.* s.l. : University of Strathclyde, Glasgow, 2005.
105. **I. Fankuchen, M.H. Jellinek.** X-Ray Diffraction of gamma alumina. *Industrial and Engineering Chemistry.* 1945, Vol. 37, 2, p. 158-163.
106. **A. Bernassau.** *Micro-engineering for high frequency ultrasound arrays.* PhD Thesis, University of Dundee, 2009.
107. **D. MacLennan.** *Fundamental charaterisation and basic testing of viscous polymer process micromoulded piezocomposites.* EngD Thesis, University of Strathclyde, 2009.
108. **J.M. Cannata, Z.J. Zhao, S. Ayyappan, T.A. Ritter, W. Chen & K.K. Shung.** Fabrication of high frequency (25-75MHz) single element ultrasonic t ransducers. *IEEE Ultrasonics Symposium.* 1999, p. 1099-1103.
109. **M.J. Winter.** Webelements. [Online] http://www.webelements.com/.
110. **S. Rhee, T.A. Ritter, K.K. Shung, H. Wang & W. Cao.** Materials for acoustic matching in ultrasound transducers. *IEEE Ultrasonics Symposium.* 2001, p. 1051-1055.
111. **R.A. Webster.** High frequency ultrasonic transducers with fine scale 1-3 piezocomposite structures. MRes Thesis, University of Birmingham, 2006.
112. **R.A. Webster & C. Meggs.** *Fabrication of single element and 1-3 PZT/polymer composite transducers using SMA standard straight coupler connectors.* AFM Ltd, 2006.
113. **C. Meggs.** *Fabrication Procedure for EPSRC Flat & Focussed 1.6mm Composite Transducers – Rev. 2* . AFM Ltd., 2007.
114. **H. Krautkramer & J. Krautkramer.** *Ultrsonic testing of materials.* Cologne : Springer-Verlag, 1983.
115. **K.K. Shung.** Novel materials and fabrication technology for medical ultrasonic transducers. *IEEE Bioengineering Conference.* 2002, p. 219-220.